

Methods for improving pan-European flood risk mapping

Paprotny, Dominik

DOI

[10.4233/uuid:35e33109-fb68-4949-a829-dd16e5e57e4a](https://doi.org/10.4233/uuid:35e33109-fb68-4949-a829-dd16e5e57e4a)

Publication date

2018

Document Version

Final published version

Citation (APA)

Paprotny, D. (2018). *Methods for improving pan-European flood risk mapping*. [Dissertation (TU Delft), Delft University of Technology]. <https://doi.org/10.4233/uuid:35e33109-fb68-4949-a829-dd16e5e57e4a>

Important note

To cite this publication, please use the final published version (if applicable).
Please check the document version above.

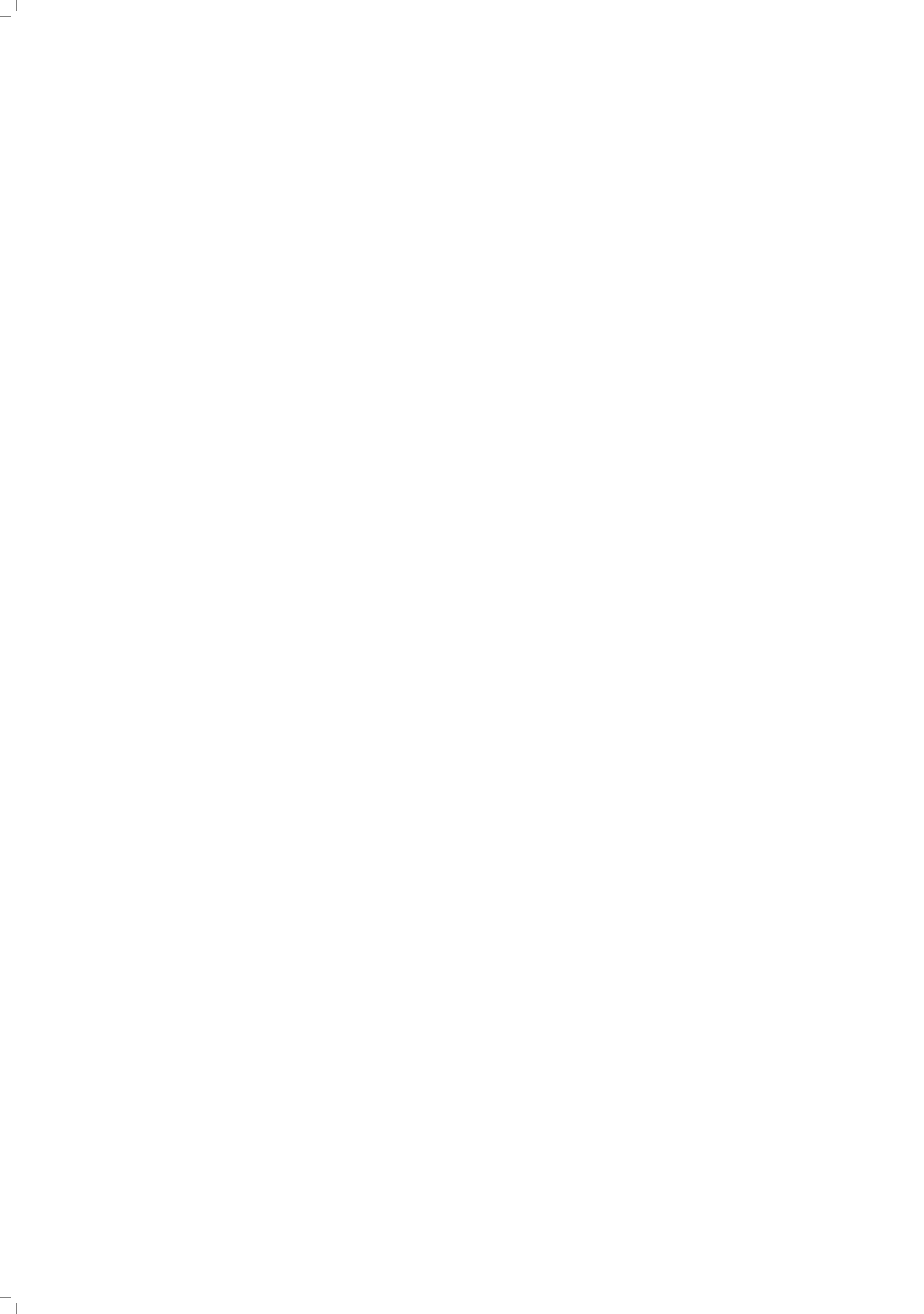
Copyright

Other than for strictly personal use, it is not permitted to download, forward or distribute the text or part of it, without the consent of the author(s) and/or copyright holder(s), unless the work is under an open content license such as Creative Commons.

Takedown policy

Please contact us and provide details if you believe this document breaches copyrights.
We will remove access to the work immediately and investigate your claim.

METHODS FOR IMPROVING PAN-EUROPEAN FLOOD RISK MAPPING



METHODS FOR IMPROVING PAN-EUROPEAN FLOOD RISK MAPPING

Proefschrift

ter verkrijging van de graad van doctor
aan de Technische Universiteit Delft,
op gezag van de Rector Magnificus prof. dr. ir. T.H.J.J. van der Hagen,
voorzitter van het College voor Promoties,
in het openbaar te verdedigen op
woensdag 14 November 2018 om 15:00 uur

door

Dominik PAPROTNY

Magister geografii,
Uniwersytet Szczeciński, Szczecin, Polen,
geboren te Szczecin, Polen.

Dit proefschrift is goedgekeurd door de promotoren.

Samenstelling promotiecommissie bestaat uit:

Rector Magnificus,	voorzitter
Prof. dr. ir. S.N. Jonkman	Technische Universiteit Delft, <i>promotor</i>
Dr. ir. O. Morales Nápoles	Technische Universiteit Delft, <i>copromotor</i>

Onafhankelijke leden:

Prof. dr. ir. P.H.A.J.M. van Gelder	Technische Universiteit Delft
Prof. dr. ir. M. Kok	Technische Universiteit Delft
Prof. dr. B. Merz	GFZ German Research Centre for Geosciences & University of Potsdam
Prof. dr. A.T. Vafeidis	Christian Albrechts University Kiel
Dr. P.J. Ward	Vrije Universiteit Amsterdam



This work was supported by the European Union's Seventh Framework Programme under "Risk analysis of infrastructure networks in response to extreme weather" (RAIN) project, grant no. 608166, and the European Union's Horizon 2020 research and innovation programme under "Bridging the Gap for Innovations in Disaster resilience" (BRIGAD) project, grant no. 700699.

Keywords: river discharge, storm surge, river flood, coastal flood, compound flood, hazard, exposure, vulnerability, climate change

Printed by: Gildeprint

Front cover: Rhône river flowing through Lyon, France.

Back cover: High water marks in Warsaw, Poland.

All photographs in this book (incl. cover) by D. Paprotny

Copyright © 2018 by D. Paprotny

ISBN 978-94-6186-970-8

An electronic version of this dissertation is available at
<http://repository.tudelft.nl/>.

To my parents



CONTENTS

Summary	xi
Samenvatting	xv
1 Introduction	3
1.1 Background	3
1.1.1 Floods	3
1.1.2 Floods in Europe	6
1.1.3 Historical outline of flood hazard and risk mapping	15
1.2 Research problems and objectives	19
1.3 Scope of the thesis	21
1.4 Thesis outline	24
2 Extreme river discharges	29
2.1 Introduction	29
2.2 Materials and methods	31
2.2.1 Workflow and outline of the method	31
2.2.2 River discharge data	32
2.2.3 Spatial datasets	34
2.2.4 Bayesian networks	37
2.2.5 Extreme discharge model	40
2.2.6 Return periods of discharges	42
2.2.7 Measures for validation of the model's results	43
2.3 Results	44
2.3.1 Validation of the model's results	44
2.3.2 Present and future river discharges in Europe	49
2.4 Discussion	53
2.4.1 Comparison with other models	53
2.4.2 Limitations and uncertainties	54
2.4.3 Applications and further developments	56
2.5 Conclusions	57
3 River flood hazard	61
3.1 Introduction	61
3.2 Materials and methods	63
3.2.1 Domain and overview of the methodology	63
3.2.2 River discharge scenarios	64
3.2.3 River water level modelling	65
3.2.4 Flood extent calculation	68
3.2.5 Reference flood maps	69

3.3	Results	72
3.3.1	Validation of flood maps	72
3.3.2	Present flood hazard in Europe	75
3.3.3	Future flood hazard in Europe	76
3.4	Discussion	78
3.5	Conclusions.	80
4	Storm surges and coastal flood hazard	85
4.1	Introduction	85
4.2	Materials and methods	88
4.2.1	Domain and overview of the methodology.	88
4.2.2	Storm surge heights	89
4.2.3	Extreme sea levels	93
4.2.4	Coastal flood extents.	96
4.2.5	Validation of coastal flood maps	97
4.3	Results	99
4.3.1	Model calibration and validation of modelled storm surge heights.	99
4.3.2	Validation of modelled extreme sea levels	102
4.3.3	Present and future storm surge heights and extreme sea levels in Europe.	104
4.3.4	Validation of coastal flood maps	108
4.3.5	Present and future coastal flood extents in Europe.	109
4.4	Discussion	115
4.4.1	Uncertainties related to extreme sea levels.	115
4.4.2	Uncertainties related to coastal flood extents	115
4.5	Conclusions.	118
5	Compound flood potential	121
5.1	Introduction	121
5.2	Materials and methods	123
5.2.1	Domain and data	123
5.2.2	Statistical analysis of dependencies between variables.	124
5.2.3	Composite indices of compound flood potential.	125
5.3	Results	126
5.3.1	Dependency structures in observational data	127
5.3.2	Validation of modelled data	128
5.3.3	Dependency structures in modelled data	132
5.3.4	Compound flood potential index	133
5.4	Discussion	136
5.4.1	Composite index and past records of floods	136
5.4.2	Time lags in joint occurrence	137
5.4.3	Uncertainties and limitations	140
5.4.4	Future research outlook	142
5.5	Conclusions.	142

6	Historical trends in flood exposure and losses	147
6.1	Introduction	147
6.2	Materials and methods	149
6.2.1	Domain and overview of the methodology.	149
6.2.2	Database of flood exposure	150
6.2.3	Database of past damaging floods	152
6.2.4	Methods for analysing trends in flood losses	154
6.3	Results	157
6.3.1	Trends in exposure.	157
6.3.2	Distribution of flood events in Europe	157
6.3.3	Trends in reported and normalized flood losses	161
6.3.4	Trends in flood losses corrected for missing records	161
6.3.5	Variation in flood loss trends by area and type of flood	163
6.4	Discussion	165
6.4.1	Estimation of underreporting of flood events	165
6.4.2	Validation of flood footprints	166
6.4.3	Other uncertainties in flood trends	169
6.5	Conclusions.	172
7	Conclusions and recommendations	175
7.1	Conclusions.	175
7.2	Recommendations	177
	APPENDICES	181
A	Diagnosis of underlying assumptions regarding the Non-Parametric Bayesian Networks	183
A.1	Introduction	183
A.2	Copulas.	183
A.3	Validation of the Bayesian Network	186
A.4	Conditionalizing the Bayesian Network.	188
B	Extreme river discharges under alternate climate models	191
C	Maps of extreme river discharges in Europe	199
D	Maps of river flood hazard in Europe	205
E	Maps of coastal flood hazard in Europe	209
F	Supplementary information on compound flood potential	213
G	Documentation of HANZE database	227
G.1	Introduction	227
G.2	Domain.	227
G.3	Contents of the database	227
G.4	Methodological aspects of HANZE-Exposure	230
G.4.1	Overview.	230
G.4.2	Step 1: baseline maps	232
G.4.3	Step 2: historical statistics	239

G.4.4	Step 3: land use and population change modelling	245
G.4.5	Step 4: disaggregated economic data.	250
G.5	Quality assessment of HANZE.	251
G.5.1	Accuracy of baseline maps	251
G.5.2	Validation of land use and population grids	253
G.5.3	Quality of flood event data	256
H	Supplementary information on trends in flood exposure and losses	257
I	Data availability	267
	Bibliography	269
	Acknowledgements	297
	Curriculum Vitæ	299
	List of Publications	301

SUMMARY

Floods are a major natural hazard in Europe, responsible for many fatalities and billions of euros of losses. Floods exist in many forms. In the past decade, there has been growing interest in analysing flood hazard and risk on European scale. Such maps allow assessment of climate change impacts, can be used at EU-level policymaking, enable consistent inter-country comparisons of flood risk and provide information on countries where local flood maps are not available. As various aspects of pan-European flood risk studies still need improvement, this thesis seeks to explore methods that can enhance their accuracy, efficiency, spatial, temporal and thematic coverage as well as data availability and reusability. It integrates statistical, hydrological and spatial (geographical) modelling approaches for a pan-European assessment of river and coastal flood hazard, compound flood potential and historical trends in flood losses and exposure.

Chapter 2 analyses extreme river discharges in Europe, which are a necessary input for large-scale hydrological modelling of flood hazard. Both physics-based and statistical models are being applied to compute discharges. The former require enormous computational power, while the latter are mostly limited in accuracy and spatial coverage. The chapter introduces an alternate, statistical approach based on Bayesian Networks (BN), a graphical model for dependent random variables. A non-parametric BN was used to describe the joint distribution of extreme discharges in European rivers and variables representing the geographical characteristics of their catchments. Annual maxima of daily discharges from more than 1800 river gauges were collected, together with information on terrain, land use and local climate. The (conditional) correlations between the variables were modelled through copulas, with the dependency structure defined in the network. The results show that using this method, mean annual maxima and return periods of discharges could be estimated with an accuracy similar to existing studies using physical models for Europe, and better than a comparable global statistical model. Performance of the model varies slightly between regions of Europe, but is consistent between different time periods, and remains the same in a split-sample validation. The BN was applied to a large domain covering all sizes of rivers in the continent both for present and future climate. Results show substantial variation in the influence of climate change on river discharges. The model can be used to provide quick estimates of extreme discharges at any location for the purpose of obtaining input information for hydraulic modelling.

Chapter 3 investigates river flood hazard, that is currently being researched on continental and global scales using models of increasing complexity. This chapter explores a different, simplified approach, which combines statistical and physical models in place of conventional rainfall-runoff models to carry out flood mapping for Europe. The model based on a Bayesian Network from chapter 2 was employed to generate return-period flow rates in European rivers with a catchment area larger than 100 km². The simulations were performed using a one-dimensional “steady-state” hydraulic model and the results

were post-processed using geographical information system (GIS) software in order to derive flood zones. This approach was validated by comparison with Joint Research Centre's (JRC) pan-European map and five local flood studies from different countries. Overall, the two approaches show similar performance in recreating flood zones of local maps. The simplified approach achieved similar level of accuracy, while substantially reducing the computational time. The chapter also presents the aggregated results on flood hazard in Europe, including future projections. The results indicate relatively small changes in flood hazard, i.e. an increase of flood zones area by 2–4 % by the end of the century compared to the current situation. However, when current levels of flood protection are taken into account, the flood-prone area increases substantially in the future (28–38 % for a 100-year return period). This is because in many parts of Europe the flood defences would not be able to withstand the increase in extreme river water levels caused by climate change.

Chapter 4 assesses coastal flood hazard in Europe. Firstly, it presents the calculations of return periods of storm surge heights and water levels for the European coast. The analysis utilized simulations by Delft3D hydrodynamic model driven by high-resolution meteorological data. The simulations were calibrated using sea levels from over 150 gauges. Resulting storm surge heights were transformed to extreme value distributions and combined with regional sea level rise and glacial isostatic adjustment projections. The study showed a good match between simulated and observed storm surge heights, also in comparison to existing studies. The analysis of the results indicated large differences in future trends of extreme sea levels in Europe, which were further used to generate coastal flood hazard zones by intersecting them with the digital elevation model. Then, the pan-European flood extents were compared with high-resolution local flood maps as in chapter 3, additionally contrasting the results with another pan-European model and one global assessment. It was found that large disparities exist between the large-scale flood maps and four local maps of flood extents from England, the Netherlands, Poland and France. Moreover, the accuracy of the underlying digital elevation model and assumptions about flood protection existing in a given area influence significantly the results. Additionally, the first pan-European projection of temporal trends in the size of flood zones is presented, with and without assuming flood protection levels.

Chapter 5 combines information from previous chapters to investigate the possible co-occurrence of riverine and coastal hazards, also referred to as “compound floods”. In Europe, several flood events of this type have been recorded in the past century. In this chapter the probability of joint occurrence of storm surges, precipitation, river discharges and waves is computed. A coincidence of those factors have a potential to cause compound floods. A large array of datasets, both observations and models, were used to carry out a statistical analysis based on copulas to assess the likelihood of joint occurrence. Further, the joint probability of occurrence of extreme compound events, and their intensity, was synthesized in the form of a composite index, thus identifying areas where compound floods could be of most concern. The results show considerable regional differences in the dependency structure and the resulting joint probability of extreme surge, precipitation and river discharge events. In southern Europe the probability of joint occurrence of storm surge and precipitation is relatively high due to significant flash flood hazard. In northern Europe, along the main corridor of winter storms,

dependency between surges and river discharges is higher than elsewhere, with large differences between west-facing and east-facing coasts. The occurrence of compound floods in most of the Nordic countries and along the Black Sea is very unlikely.

Chapter 6 looks into the historical trends in the occurrence of flood events and losses as well as changes in exposure. The analysis is a response to the lack of comprehensive, high-resolution data on historical changes in land use, population or assets available to study this topic. This chapter presents HANZE database, or “Historical Analysis of Natural Hazards in Europe”, which contains two parts: (1) HANZE-Exposure with maps for 37 countries and territories from 1870 to 2020 in 100 m resolution and (2) HANZE-Events, a compilation of past disasters with information on dates, locations and losses, currently limited to floods only. The database was constructed using high-resolution maps of present land use and population, a large compilation of historical statistics, and relatively simple disaggregation techniques and rule-based land-use reallocation schemes. Data encompassed in HANZE allow to “normalize” information on losses due to natural hazards by taking into account inflation as well as changes in population, production and wealth. Database of past events contains 1564 records (1870–2016) of flash, river, coastal and compound floods. The results show significant growth in flood exposure, though no increase in the percent of people or assets within flood zones (taken from chapters 3 and 4). Further, the results indicate that, after correcting for changes in flood exposure, there has been an increase in annually inundated area and number of persons affected since 1870, contrasted by a substantial decrease in flood fatalities. For more recent decades a considerable decline in financial losses per year was also found. It can be estimated, however, that there is large underreporting of smaller floods beyond most recent years, and shown that underreporting has a substantial impact on observed trends.

Datasets created during this study are available from public repositories, as described in Appendix I.



SAMENVATTING

Overstromingen vormen een belangrijke categorie van natuurrampen in Europa en leiden tot vele slachtoffers en miljarden euro's schade. In de afgelopen tien jaar is de belangstelling voor het analyseren van het overstromingsrisico op Europese schaal toegenomen. Overstromingsrisicokaarten zijn te gebruiken om de invloed van klimaatverandering te tonen, om op Europees niveau beleid te maken, om consistente vergelijkingen te maken tussen landen, en informatie te geven voor landen die niet over lokale overstromingskaarten beschikken. Diverse aspecten van onderzoeken naar pan-Europese overstromingsrisico's behoeven verbetering. Dit proefschrift heeft methoden onderzocht om de nauwkeurigheid, doeltreffendheid, en dekking in tijd en ruimte te vergroten, alsmede de beschikbaarheid en herbruikbaarheid van gegevens. Het werk integreert statistische, hydrologische en ruimtelijke (geografische) benaderingen voor een inschatting van rivier- en kustoverstromingen op pan-Europese schaal en geeft inzicht in historische trends in schades en blootstelling aan overstromingen. Hoofdstuk 1 geeft achtergrondinformatie over overstromingen, inclusief hun geografische oorzaken en geschiedenis, en schetst de ontwikkeling van het in kaart brengen van overstromingsrisico's tot op heden. In de volgende vijf hoofdstukken worden de diverse onderdelen van de analyse van overstromingsrisico's behandeld. Het laatste hoofdstuk bevat conclusies en aanbevelingen. De belangrijkste zijn hieronder samengevat.

In hoofdstuk 2 worden extreme rivierafvoeren in Europa geanalyseerd en deze worden gebruikt voor het op grote schaal hydrologisch modelleren van overstromingsgevaar. Zowel fysische als statistische modellen zijn toegepast om extreme afvoeren te berekenen. De eerstgenoemde vereisen zeer veel rekenkracht, de laatstgenoemde zijn vaak minder nauwkeurig en beperkter in geografische dekking. In dit hoofdstuk wordt een alternatieve benadering geïntroduceerd die is gebaseerd op Bayesiaanse Netwerken (BN). Gebruik werd gemaakt van een niet-parametrisch BN om de gezamenlijke kansverdeling van extreme afvoeren van Europese rivieren en variabelen die de geografische karakteristieken van hun stroomgebied vertegenwoordigen, te beschrijven. Jaarlijkse maxima van dagelijkse afvoeren van meer dan 1800 riviermetingen werden verzameld, alsmede informatie over het stroomgebied, het grondgebruik en het lokale klimaat. De (voorwaardelijke) correlaties tussen de variabelen werden gemodelleerd door middel van copula's. De resultaten laten zien dat met deze methode gemiddelde jaarlijkse maxima en herhalings tijden van afvoeren konden worden geschat. Dit resulteerde in een nauwkeurigheid die vergelijkbaar was met bestaande onderzoeken die fysische modellen voor Europa gebruiken, en beter dan met een vergelijkbaar wereldwijd statistisch model. De prestatie van het model varieert licht tussen Europese regio's, maar is consistent in verschillende tijdsperiodes. Bayesiaanse Netwerken zijn toegepast op een groot deel van het Europese continent met rivieren van allerlei grootte voor zowel het huidige als toekomstige klimaat. De resultaten laten een aanzienlijke variatie zien tussen gebieden in de invloed van de klimaatverandering op rivierafvoeren. Het model kan gebruikt worden

om snel een schatting te maken van extreme afvoeren op elke willekeurige plaats met als doel invoerinformatie te verkrijgen voor het maken van een hydraulisch overstromingsmodel.

In hoofdstuk 3 wordt het gevaar van rivieroverstromingen onderzocht. Dit wordt momenteel bestudeerd op continentale en wereldschaal met gebruikmaking van steeds ingewikkelder modellen. Een andere, eenvoudiger benadering is onderzocht waarbij statistische en fysische modellen werden gecombineerd als alternatief voor de gebruikelijke regenval-afvoermodellen om de Europese overstromingen in kaart te brengen. Het model, gebaseerd op het Bayesiaanse Netwerk uit hoofdstuk 2 is gebruikt om herhalings-tijden van afvoeren in Europese rivieren met een stroomgebied van meer dan 100 km² te bepalen. De simulaties zijn uitgevoerd met een ééndimensionaal “steady-state” hydraulisch model en de resultaten zijn nabewerkt met het geografische informatiesysteem (GIS) om overstromingszones af te leiden. Deze benadering is gevalideerd door deze te vergelijken met de pan-Europese kaart van het Joint Research Centre (JRC) en vijf lokale onderzoeken naar overstromingskaarten uit diverse landen. Beide benaderingen laten een vergelijkbare prestatie zien bij het opnieuw genereren van overstromingszones van lokale kaarten. De vereenvoudigde benadering resulteert in hetzelfde niveau van nauwkeurigheid met aanzienlijk minder rekentijd. In dit hoofdstuk worden ook de geaggregeerde resultaten gepresenteerd in de vorm van Europese overstromingskaarten, inclusief het effect van toekomstprojecties. De resultaten laten relatief kleine veranderingen op het gebied van overstromingsgevaar zien in de tijd, namelijk een toename van overstroombare gebieden met 2 % à 4 % aan het einde van de 21^e eeuw in vergelijking met de huidige situatie. Als echter rekening wordt gehouden met de huidige normen van overstromingsbescherming, neemt het gebied dat gevoelig is voor overstromingen, aanzienlijk toe in de toekomst (met 28 % tot 38 % voor gebeurtenissen met een herhalings-tijd van 100 jaar). In grote delen van Europa kunnen de waterkeringen namelijk de stijging van extreme rivierwaterstanden als gevolg van de klimaatverandering niet aan.

In hoofdstuk 4 is het overstromingsgevaar langs de Europese kust geanalyseerd. Allereerst zijn de berekeningen van herhalings-tijden van stormvloedhoogtes en waterstanden voor de Europese kust gepresenteerd. Voor de analyse is gebruik gemaakt van simulaties met het hydrodynamisch model Delft3D, gestuurd door meteorologische data met hoge resolutie. De simulaties zijn gekalibreerd met gebruikmaking van zee-waterstanden van meer dan 150 meetstations. De verkregen stormvloedhoogtes zijn getransformeerd naar extreme waardeverdelingen en gecombineerd met regionale zeespiegelstijgingsprojecties voor de glaciële isostatische aanpassing. Uit het onderzoek bleek dat de gesimuleerde en geobserveerde stormvloedhoogtes ongeveer even hoog waren, ook vergeleken met bestaande onderzoeken. De analyse van de resultaten gaf grote verschillen te zien in toekomstige trends in extreme zeeniveaus in Europa. De resultaten werden vervolgens gebruikt om overstromingskaarten voor kustgebieden te genereren door combinatie met een digitaal hoogtemodel. Vervolgens zijn de pan-Europese uitkomsten vergeleken met de lokale overstromingskaarten met hoge resolutie uit hoofdstuk 3. De resultaten zijn verder ook vergeleken met een ander pan-Europees model en een schatting uit een globaal model. Er bleken grote verschillen te zijn tussen de overstromingskaarten op grote schaal en vier lokale kaarten voor overstromingsgebieden in Engeland, Nederland, Polen en Frankrijk. Bovendien beïnvloedden de nauwkeurigheid van het on-

derliggende digitale hoogtemodel en de aannames met betrekking tot de overstromingsbescherming in een bepaald gebied de resultaten aanzienlijk. In deze studie is de eerste pan-Europese projectie van trends in de tijd en de omvang van overstromingsgebieden getoond, met en zonder effecten van waterkeringen.

In hoofdstuk 5 wordt de informatie uit de voorgaande hoofdstukken gecombineerd om het gezamenlijk voorkomen van rivier- en kustoverstromingen te onderzoeken, ook wel “compound flooding” genoemd. In Europa zijn diverse overstromingen van deze soort voorgevallen in de vorige eeuw. In dit hoofdstuk wordt de waarschijnlijkheid van het zich gezamenlijk voordoen van stormvloed, neerslag, rivierafvoeren en golven berekend. Het samenvallen van deze fenomenen kan tot een samengestelde overstroming leiden. Diverse datasets, zowel observaties als modellen, zijn gebruikt om een statistische analyse uit te voeren met copula’s om de waarschijnlijkheid van het gezamenlijk voorkomen in te schatten. Verder is de gezamenlijke kans op extreme “compound floods” en hun intensiteit geanalyseerd met een samengestelde index. Op deze manier zijn gebieden te identificeren waar samengestelde overstromingen het meest waarschijnlijk zijn. De resultaten laten aanzienlijke regionale verschillen zien in de afhankelijkheidsstructuur en in de kans van het zich gezamenlijk voordoen van extreme stormvloed, neerslag en rivierafvoer. In Zuid-Europa is de kans van het gezamenlijk voorkomen van stormvloed en neerslag relatief hoog en dit kan leiden tot aanzienlijke plotse linge overstromingen (flash floods). In Noord-Europa, in het gebied waar winterstormen dominant zijn, is de afhankelijkheid tussen stormvloed en rivierafvoeren hoger dan elders, waarbij de verschillen groot zijn tussen de op het westen en op het oosten gerichte kusten. Het optreden van samengestelde overstromingen in Scandinavië en langs de Zwarte Zee is erg onwaarschijnlijk.

Hoofdstuk 6 gaat over de historische trends in overstromingen, de resulterende schades en slachtoffers en de blootstelling aan overstromingen. Er is een gebrek aan hoge resolutie data op het gebied van historische ontwikkeling van landgebruik, bevolking en economische waarden en in deze studie zijn deze kennisleemten geadresseerd. Dit hoofdstuk introduceert de HANZE-database, oftewel “Historical Analysis of Natural Hazards in Europe”, die uit twee delen bestaat: (1) HANZE-Exposure (blootstelling) met kaarten voor 37 landen en gebieden tussen 1870 en 2020 met een resolutie van 100 m en (2) HANZE-Events (gebeurtenissen), een compilatie van historische rampen met informatie over data, getroffen gebied en verliezen door overstromingen. De database is opgebouwd met hoge resolutie kaarten met het huidige grondgebruik en de bevolking, een grote compilatie van historische statistieken, en relatief eenvoudige technieken voor het ruimtelijk herverdelen van het landgebruik. De in de HANZE-database opgenomen gegevens maken het mogelijk de informatie over schades als gevolg van natuurrampen te “normaliseren” omdat rekening wordt gehouden met zowel de inflatie als de veranderingen in bevolking, productie en rijkdom. De database van voorbije gebeurtenissen bevat 1564 records (1870-2016) met rivier-, kust- en samengestelde overstromingen. De resultaten laten een aanzienlijke toename in blootstelling aan overstromingen zien, hoewel er geen stijging is in het percentage mensen of bezittingen in overstromingszones (die zijn vastgesteld in hoofdstukken 3 en 4). Bovendien wijzen de resultaten er, na het corrigeren voor veranderingen in de blootstelling, op dat het jaarlijks overstroemde gebied en het aantal mensen dat eronder lijdt sinds 1870 toeneemt, dit in tegenstelling tot een belang-

rijke daling van het aantal slachtoffers door overstroming. De afgelopen tientallen jaren is ook een aanzienlijke afname van de jaarlijkse financiële verliezen vastgesteld. Echter, geschat wordt dat behalve voor recente jaren kleinere overstromingen vaak niet gemeld werden, wat van wezenlijke invloed blijkt te zijn op waargenomen trends.

De tijdens dit onderzoek gemaakte datasets zijn beschikbaar in openbare bewaarplaatsen zoals is beschreven in de bijlagen I.

This samenvatting was translated by Judith Schooneveld-Oosterling.



Previous page: Danube, the longest river in the study area, flows through Bratislava, Slovakia – one of the four European capitals along its shores.

1

INTRODUCTION

*"Just as winter occurs in the seasons of the year,
so in determined periods there comes a great winter
of a great year and with it excess of rain."*

Aristotle, *Meteorologica*, 352a (ca. 350 BC)

1.1. BACKGROUND

1.1.1. FLOODS

FLOODS have been affecting human populations for millennia. Legends of civilization-destroying floods were identified on all continents [1]. One example is the deluge of Deucalion mentioned by Aristotle in his treatise *Meteorologica* as an example of the effects of excessive rainfall [2]. The oldest recorded flood, on Huang He (the Yellow River) in China, occurred in year 2297 BC [3]. Floods are recurring phenomena and flood hazard is constantly evolving. This was already apparent to ancient Greeks [4]. Yet, while the history of flood management and prevention is as old as civilization, floods continue to menace many places in the world. In the last ten years only (2008–17) floods caused \$374 billion losses worldwide, of which \$53 billion in Europe, according to Munich Re [5]¹. Almost 64 000 fatalities were recorded in the same period, including 1165 in Europe, according to the same source. Attention given to the problem is growing, as evidenced by the relative share of flood-related phrases in the corpus of English books over the past two centuries (Fig. 1.1)².

But what constitutes a “flood”? The answer is not exactly straightforward. The European Union’s Floods Directive [8] defines it broadly as “the temporary covering by water of land not normally covered by water”. More plainly, flood “happens when water flows where it ought not to flow”, to quote Gumbel [9]. However, it is important to note that

¹Approximately €294 billion and €42 billion, respectively.

²It should be noted, however, that considerable bias towards scientific literature in more recent books weighs heavily on those results [6].

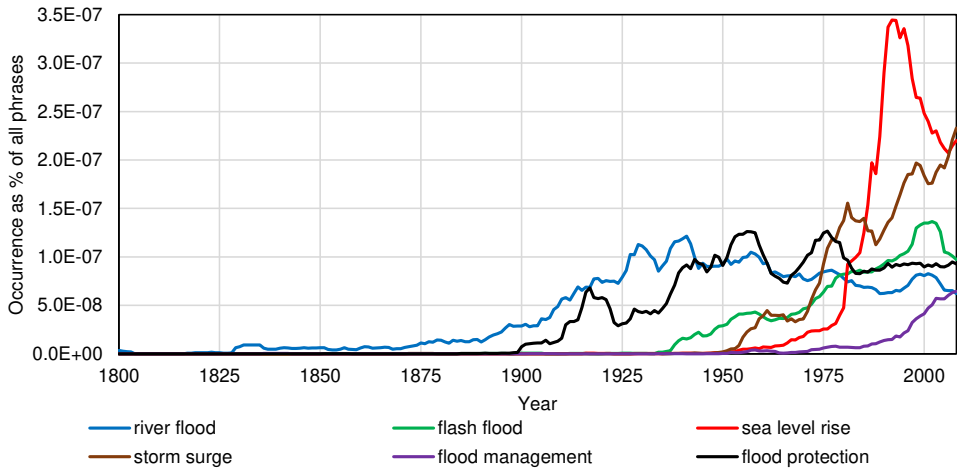


Figure 1.1: Relative occurrence of selected flood-related phrases in a corpus of English-language books, 1800–2008 (3-year running average). Source of data: Google Books Ngram Viewer [7].

such a wide definition of flood is specific for certain languages, such as English, and can be also referred to as a “hydrological flood” [10]. A flood defined hydrologically is usually mentioned in context of rivers only, and constitutes an increase in level or volume of water in a river channel. In most encompassing definitions, water does not even need to overflow outside the river channel to be considered a flood. This hardly fulfils the term “disaster”, with which “flood” is associated in public consciousness, and which is “a serious disruption of the functioning of a community or a society at any scale due to hazardous events...” [11]. Hence, floods that have “adverse impacts on the social system, the natural system or the built environment” [12] are termed “damaging floods”. In this thesis both hydrological and damaging floods are investigated³.

TYPES OF FLOODS

The complexity of floods goes further, as there are many causes and types of floods. The Floods Directive specifies that it includes floods “from rivers, mountain torrents, Mediterranean ephemeral water courses, and floods from the sea in coastal areas, and may exclude floods from sewerage systems”. River floods occur when water overflows the river bed onto the floodplain, for a number of reasons. High water level in rivers is usually caused by increased runoff in the river’s catchment, itself a result of either rainfall or snowmelt. In small catchments, especially in mountainous or dry areas, floods caused by very intense yet short rainfall are often referred to as “flash floods” due to their very

³Similar problem of an overarching definition of flood exists in e.g. French (*inondation*) and Spanish (*inundación*). Distinctions between hydrological and damaging floods, as exemplified by the wording of the Floods Directive, function in e.g. German (*Hochwasser* vs *Flut*) and Dutch (*overstroming* vs *vloed*). Practical use of the terms can be more complex, though. For instance, in Poland a flood (*powódź*) is considered “a surge (*wezbranie*) that causes economic, social or moral losses” according to Mikulski [13], yet the Polish version of the Floods Directive, as well as national law, use the term *powódź* also to mean a hydrological flood.

sudden nature and short duration. Otherwise, a flood can be caused by the inability of water to drain from the river basin due to blocked river flow. This blockage can be a result of accumulation of ice or frazil, and on very local scale also river silting, vegetation, animal activity or landslides [14]. Further, the drainage can be reduced in coastal areas by high sea levels, resulting in elevated water levels in the river's estuary, which can be referred to as "compound floods".

A separate group are coastal floods, which are a consequence of the sea inundating coastal areas. They are caused by storm surges, which are the increase in sea level due to strong winds and low atmospheric pressure. Frequently, storm surges alone are not high enough to cause a flood themselves, but submerge land when accompanied by a high tide and waves. The Floods Directive notes that it "may exclude floods from sewerage systems", which are more commonly referred to as "urban floods". They are caused by heavy precipitation exceeding the drainage capacity of urban areas⁴[15]. Floods can also originate from technical failures of dam and dikes, which are usually related to high water levels, but may as well be a result of ice drift, human and animal activity or even droughts [16]. Finally, there are floods of geophysical origin, such as tsunamis (waves generated by undersea earthquakes or landslides) or Icelandic *jökulhlaup* events (floods caused by melting of glaciers induced by volcanic activity). Yet, the focus of this thesis is only on floods of hydrological origin.

An important property of floods, which will be present in all chapters of this thesis, is that their occurrence can be described statistically. Among the continuous records of river discharges, or sea levels, at a specific location there is one that is the highest during a given year – it is known as the annual maxima, or "annual flood" in the hydrological sense [9]. Annual maxima from multiple years will form a probability distribution. From such distribution it can be calculated what is the annual probability of exceedance of a given discharge or sea level, in % per year. The reverse of the annual probability is the return period, or the average time between exceedances of a given discharge or sea level. Annual probability of 1 % becomes in this way a 100-year return period. The return period is often referred to as flood frequency. Floods considered as overflowing of natural river banks have, in general, a return period of at least 1.5 years according to Dunne and Leopold [17]. Damaging floods generally have higher return periods (or, lower probabilities of exceedance); Mikulski [13] noted that Polish rivers experience damaging floods on average every 3–3.5 years.

Yet, there are limitations in using the empirical distribution of observed annual maxima. The typical procedure of analysing flood data is called the "extreme value analysis". It involves fitting observations (say, sea levels) to theoretical probability distributions in order to be able to estimate probabilities of any given value of sea level, in particular extrapolating the most extreme values beyond the timespan of sea level records. The first known use of this approach is by Horton [18], though some attempts were apparently made already in the late 19th century [19]. However, it wasn't until the seminal study by Gumbel [20] when a probability distribution dedicated to extreme values and floods was devised. The Gumbel distribution is still commonly used in flood research, and is also applied throughout this thesis. Still, the limited amount of observations typically mean high uncertainty, and the distributions can shift substantially after large flood events

⁴A broader term "pluvial flood" is also used, encompassing both urban and flash floods.

[21].

1.1.2. FLOODS IN EUROPE

Flood hazard varies spatially and is driven by Europe's geographical characteristics, such as relative location of lands and seas, as well as topography and climate. In this section, after summarizing the most important geographical characteristics of Europe, the factors influencing the spatial distribution of floods in Europe are discussed. This description is largely based on Majewski [22] with additional sources as mentioned in the text. A general reference map of the continent supports this analysis in Fig. 1.2, though it omits the outermost parts of Europe that are not relevant for this thesis (outlying Atlantic islands and eastern European Russia). Afterwards, a historical overview of major flood disasters and flood protection in Europe is provided. Readers already familiar with those topics can move directly to section 1.2.

GEOGRAPHICAL CONSIDERATIONS

Europe is the second smallest continent (after Australia and Oceania), but that makes it no less geographically complex as bigger ones. Its area is about 10.5 million km², depending on the exact delineation of its border with Asia. It spans about 7000 km from the Azores (westwards of Spain, not shown on map) to the Ural Mountains and more than 5000 km from southernmost Greek islands to Franz Josef Land (northwards of Norway, not shown on map)⁵. The main land mass occupies approximately 70 % of the continent, with numerous peninsulas (the Scandinavian peninsula being the largest) taking up 23 % and many islands (largest of which is Great Britain) covering the remaining 7 %. The total length of the coastline is about 38 000 km excluding coasts of islands, and more than twice that number including the islands. Of the continents, only North America has more developed coasts than Europe⁶. Morphological types of coasts are also highly diverse throughout the continent.

Europe's average elevation is 292 m above sea level (a.s.l.), the lowest value among continents. In total, 1.4 % lays below sea level. Further 82.6 % of the continent is between 0 and 500 m a.s.l., and only 5.1 % above 1000 m a.s.l. Most of the depressions are encompassed in the Caspian Lowlands, which also contain the lowest point of Europe (27 m below sea level). This area is at the eastern edge of the continent (not shown on the map); the lowest point on the map, at 7 m below sea level, is located in the Netherlands. On the opposite end of scale, the highest peaks of Europe can be found in the Alps, with Mont Blanc reaching 4807 m a.s.l.

According to the Köppen-Geiger climate classification [27], the majority of Europe is located within warm temperate (C) climate zone 1.3. Portugal, Spain and most of the Mediterranean coasts have dry and hot summers (Csa), while other areas of the temperate zone are fully humid and with a warm summer (Cfa). Small areas of the Mediterranean region, mostly in south-eastern Spain, are so dry that they belong to arid (B) climate zone, usually of the cold steppe subtype (BSk). Eastern and northern Europe belong mostly to snow (D) climate due to cold winters. In eastern Poland and the for-

⁵Excluding islands, the values are about 5500 and 4000 km, respectively.

⁶In geography, coastal development is the ratio between a continent's coastline length and the circumference of a circle with an area equal to a continent's area.



Figure 1.2: General reference map of Europe. Rivers and lakes from CCM2 database [23], country borders from PBL [24], topography from SRTM DEM [25], cities from United Nations 2014 Urbanization Prospects (with estimated population in 2015) [26].

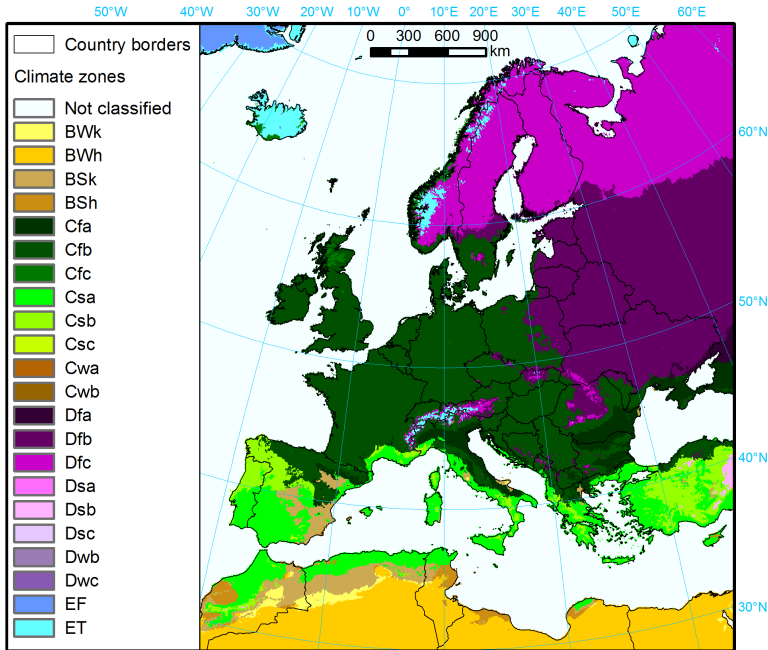


Figure 1.3: Climate of Europe according to Köppen-Geiger classification, for the period 1970–2000. Climate types, first letter: B – arid, C – warm temperate, D – snow, E – polar; second letter: W – desert, S – steppe, f – fully humid, s – dry summer, w – dry winter, F – frost, T – tundra; third letter: k – cold, h – hot, a – hot summer, b – warm summer, c – cold summer and cold winter. Zones calculated from monthly temperature and precipitation observations interpolated to a 5' resolution grid in WorldClim v2 dataset [28], using the Köppen-Geiger classification as presented by Kottek *et al.* [27].

mer Soviet Union⁷ the climate is fully humid and with a warm summer (Dfb). In Norway, Sweden (except southernmost part) and Finland the climate is also fully humid, but with cold summers (Dfc). Snow climate can be also found in mountainous areas throughout Europe, especially in the Alps and the Carpathian Mountains. Finally, most of Iceland and the highest parts of the Alps and the Scandinavian Mountains belong to polar (E) climate, of the tundra subtype (ET).

Topography and climate profoundly shape the hydrological network. Around 81 % of Europe drains to the Atlantic Ocean, with waters from the remainder (exclusively Russian territory) flowing into the Caspian Sea, a basin unconnected with oceans (not shown on map). Rivers in eastern Europe are the longest and have the biggest catchment areas, with Volga (3530 km and 1.36 mln km²) leading before Danube (2850 km and 817 000 km²), followed by Ural (not shown), Dnieper, Don, Northern Dvina and Pechora (not shown). In other parts of Europe, the biggest rivers are those draining to North and Baltic Seas, such as Rhine, Vistula, Elbe and Daugava. The network is supplemented by lakes, which dominate in post-glacial areas around the Baltic Sea. Overall, lakes cover 1.6 % of Europe, with the largest being Ladoga (18 400 km²), Onega and Vänern.

⁷Soviet Union successor states in Europe are Belarus, Estonia, Latvia, Lithuania, Moldova, Russia and Ukraine.

Topography and climate further influence the hydrological regimes of rivers, i.e. the variations of discharge during the year [29, 30]. The regimes are therefore an indicator of the season of the year in which floods tend to occur in a given river, and of the primary causes of such floods. Rivers in Ireland, the United Kingdom (UK), north-western France and Belgium, such as Thames and Seine, are of oceanic (or Atlantic) type. Precipitation is relatively uniform during the year, and they do not freeze, so their flows are regulated by changing evaporation during the year, reaching maximum discharge during winter (in Ireland/Scotland rather in autumn) and minimum discharge in the summer. Central European rivers such as Weser, Elbe, Oder and Vistula are of the nival-pluvial type: high discharges occur twice a year due to snowmelt (“nival”) during spring thaw and rainfall (“pluvial”) in the summer. Those rivers freeze during harsher winters and can therefore experience floods due to ice/frazil blockage. Moving eastwards, rivers such as Nemunas, Daugava, Dnieper or Volga develop entirely nival regime, as they freeze almost every winter up to 4 months and experience large increase of discharge during snowmelt in spring. In Scandinavian rivers, the regime is similar, but the peak discharge occurs later, rather in late spring or even early summer. Also, flows in Glomma, Torne, Kemi-joki and other northern rivers are typically smoothed due to a large number of lakes in their catchments. Rivers originating from the Alps, such as Rhine, Rhone, Po or Danube experience prolonged high discharge during late spring and summer due to the melting of snow and glaciers in the mountains. Smaller rivers in the Alps might have an entirely glacial regime, with high flow in the summer and very low discharge outside the melting season. In lower mountain ranges in Central Europe, such as the Carpathian Mountains, two peaks in late spring and summer occur close to each other. In the Mediterranean region, rivers such as Ebro, Tiber, Tagus or Guadiana have low discharge (and smaller run out water completely) during the dry and hot summer. They have typically two peaks during the rainfall season, in early winter and early spring.

It can be noticed from the above overview that hydrological regimes fall relatively neatly into climate divisions, with oceanic and nival-pluvial regimes connected to warm temperate and fully humid climates (Cf), nival regimes to snow climate with warm summer (Dfb), Scandinavian rivers to the snow climate with cold summer (Dfc), and Mediterranean rivers in warm temperate/dry summer or steppe climate (Csa, BS). Occurrence of heavy precipitation, which can lead to flash floods, is also tied to climate. As shown in 1.4, the highest daily precipitation is recorded in the Mediterranean region, with stations in Slovenia and northern Italy reporting an average annual maxima of 150 mm and more. Southern France, coasts of Spain and Greece are also affected by high daily precipitation, and in the whole region the maxima typically occur in autumn (September–November). This is connected to a rainfall season with convective storms that follows a dry summer. Other areas that experience extreme rainfall⁸ are the Carpathian Mountains and other mountain chains in central Europe as well as coasts of Ireland and Norway. In the mountains, heavy precipitation typically occurs in the summer when convective storms form. Norwegian coasts are the wettest location in Europe in general, as rainfall is discharged in the high mountains near the coastline; the interior of the country is much drier. Ireland is the first country on track of Atlantic storms, which move eastwards. Norway, Ireland, the UK and Atlantic coasts of France experience maximum daily precipitation in autumn. In central and northern Europe heavy precipitation decreases moving north-

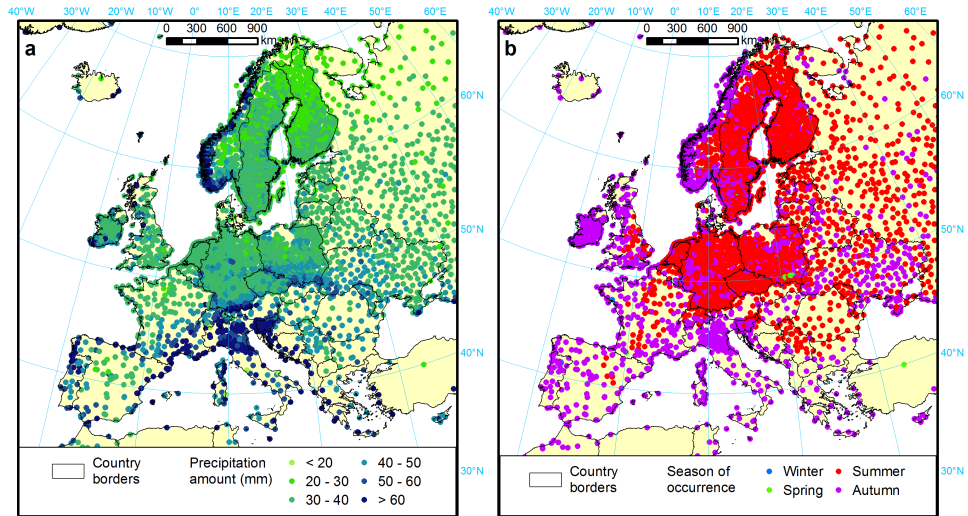


Figure 1.4: Annual maxima of daily precipitation at meteorological stations, for all available years (at least 10) between 1951 and 2010, (a) average precipitation amount and (b) season of the year in which the maxima most frequently occurred. Precipitation data from European Climate Assessment & Dataset [31].

wards, and the maximum rainfall most frequently occurs in the summer. Northernmost parts of Scandinavia (under tundra climate) record the lowest amount of average maxima of daily precipitation, down to 15–20 mm. However, interiors of Spain, Italy and the Balkans can also have low annual maxima of precipitation, as their climate is locally very arid (steppe or even desert type), though this makes such areas particularly prone to an odd violent cloud outburst.

Last but not least, occurrence of storm surges is largely regulated by the patterns of windstorms in Europe. They generally form in the North Atlantic, especially in autumn and winter, and move eastwards [32]. As a result, north-western Europe experiences the highest wind speeds [33]. The storms typically move along a rather narrow corridor from Ireland through the UK into the Netherlands, Denmark, northern Germany and southern Sweden into the Baltic Sea and northern Poland before reaching Lithuania and Latvia. The storms could deviate further north or south, reaching north-western Spain and France and move deeper into central Europe. In the Mediterranean and Black Seas, wind speeds are lower and surges as well, since convective storms are the dominant source of extreme weather in the south of Europe rather than Atlantic storms. Additionally, tides which can profoundly contribute to coastal floods are also the feature of primarily north-western Europe (see Fig. 4.3a in chapter 4). In the English Channel the amplitude of a spring tide exceeds 5 m, and is above 1 m in almost all coasts directly exposed to the Atlantic ocean. On the opposite side of the scale, in the semi-enclosed basins (Baltic, Black and Mediterranean Seas) the tides are below 0.5 m, according to

⁸Precipitation encompasses both rainfall and snowfall. However, daily snowfall's water amount doesn't get nearly as high as rainfall can, therefore in relation to extremes we can usually use the terms precipitation and rainfall interchangeably.

TPX08 tidal dataset [34]. Various morphological types of the coast determine the flood hazard, with low-lying deltas, estuaries and dune coasts more susceptible to floods than highly-elevated cliff or fiord coasts.

SIGNIFICANT PAST FLOODS

The oldest records of floods in Europe go back into antiquity, with information on inundations of Rome available since 414 BC [3] and Ebro river in Spain from 49 BC [35]. In most of Europe, however, records are available since the early medieval era in western Europe and usually late medieval era in eastern Europe [36]. For instance, there are known floods since the 6th century in the (present-day) Netherlands [37], the 9th century in Germany [38] and Switzerland [39] and 10th century in Poland [40]. Documentary evidence from centennial records of floods in various regions show no overall trend in flood frequency or severity in Europe, but rather many “flood rich” and “flood poor” periods, lasting several decades each [41, 42]. In many areas, the largest known floods (as indicated by maximum water level) have occurred before instrumental records began in the 18th or 19th century. This overview lists such flood events, selecting those which generated the most extreme water levels per major catchment or coastline, and a few other events of particularly large spatial extent. Major floods by total losses, recording of which is the topic of chapter 6, are presented in Table H.3 in Appendix H

In central Europe, the biggest flood ever is considered to be the “millennial” flood of July 1342, also known as the Magdalena Flood. It affected most of present-day Germany and was caused by heavy precipitation [43]. During the flood the Main and Rhine rivers reached highest-known discharge to date. In the Danube basin, the largest disaster is considered to be that of August 1501, when heavy rainfall caused a “millennial” flood lasting about 10 days, severely affecting Vienna and other towns in the upper parts of the catchment [44]. The same rainfall event also caused inundations along Main, Rhine and Oder rivers, and is also considered the largest ever on the Elbe and its Czech tributary, Vltava, that flows through Prague [36, 41]. Another notorious flood happened in January 1682, when a storm surge on the North Sea coincided with high discharges in Rhine and Meuse rivers caused by snowmelt and rainfall in Germany. Present-day Belgian and Dutch coasts were affected, as well as many areas in Germany along Main, Elbe and other rivers [41, 45]. One of the most geographically widespread in Europe was a series of floods between December 1783 and March 1784. A severe winter (attributed to the 1783/1784 eruption of Laki volcano in Iceland) affected many countries by causing snowmelt and ice-jams on rivers, from (present-day) Ireland, United Kingdom, northern France and Belgium to central Germany, Austria, Czech Republic, Slovakia and Hungary [46]. Other widespread floods were usually also a consequence of snowmelt and ice-jams between 16th and 19th century, but have become much less common due to the warming climate [41].

Other regions of Europe each have their own most extreme floods. In Catalonia (north-east Spain), where more than 1100 floods have been catalogued since the 11th century [35], flash floods are the primary hazard. The worst of them, as evidenced by reconstructed river discharges, occurred in November 1617 [47]. However, the highest rainfall extreme was likely recorded in October 1940, in eastern Pyrenees, when at least 840 mm fell in 24 hours, and almost 2000 mm in 5 days [48]. In France, Rhône river experienced its biggest flood in May 1856, the Loire the following month, and the Seine in



Figure 1.5: Recorded flood outlines in England, 1703–February 2017. Data from Recorded Flood Outlines, version May 2017, by the Environment Agency [54].

January–March 1910, when multiple waves of rainfall and snowmelt caused highest-ever water levels in Paris [36, 48, 49]. In Poland, though many significant floods were caused by snowmelt and ice jams, the largest in 1947, the highest water levels in its two main rivers were a result of exceptionally high summer rainfall. Along most of Vistula, the August 1813 event was the severest, and along Oder the “millennial flood” of July 1997 was the most intense [40, 50]. The biggest river of Italy, Po, had its maximum discharge during a October 1872 flood caused by persistent rainfall [51]. Similarly, multiday autumn rainfall caused the largest known discharge on Thames river in November 1894, though the snowmelt flood of March 1947 comes at close second [52]. Other British rivers usually experienced their most significant floods in the late 18th/early 19th centuries or earlier [53]. The Environment Agency in the UK has been recording flood outlines (for England only) since 1946 and has also compiled data on flood extents going back to 1703 (Fig. 1.5) [54]. In total, the Environment Agency records inundations covering almost 10 700 km², equivalent to 8 % of the size of England.

In Sweden, Norway or Finland, where floods are mostly the result of snowmelt, there is no particular “defining” episode of flooding. In Denmark, damaging floods are always coastal due to limited river flood potential, with the November 1872 storm surge in the Baltic Sea being the most extreme, also along the (present-day) German and Polish

coasts. Widespread coastal flooding of September 1497 is also a contender for the worst event to have ever reached the Polish coast [55]. Along the North Sea, the largest catastrophes of the modern era were the storm surges that inundated Hamburg, Germany, in February 1962 (347 fatalities), and eastern England, the Netherlands and Belgium in January/February 1953 with almost 2500 fatalities [56]. However, more significant disasters are known in the area from the early modern era. In November 1570, sea level reached record levels flooding (present-day) Belgian, Dutch and German coasts. South-western Netherlands were most severely affected, with upwards of 20 000 people killed. In the northern Netherlands, the biggest coastal flood was in December 1717, when an estimated 14 000 fatalities occurred [37, 45, 57].

FLOOD PROTECTION

With some many catastrophic floods throughout Europe, strategies of coping with floods have been developed through centuries. Ancient Romans have already observed and recorded extreme water levels at bridges⁹ and applied this knowledge in infrastructure design [36]. Dikes are one of the oldest flood protection measures and comprise of long earth berms aimed at keeping waters in rivers and the sea from inundating areas protected by dikes. In the Netherlands, dikes were constructed at least since the 2nd century BC [37]. Today, according to Rijkswaterstaat data (personal communication), primary dikes are 3379 km long and protect a hundred “dike rings”, which are areas protected against floods by a series of water defences (including dikes) and high grounds [58]. The total area of the dike rings is almost 19 900 km², or 57 % of land area of the Netherlands. There are also 14 000 km of secondary dikes in the Netherlands [59]. In other European countries, dikes were put into operations much later and are not as extensive. In Poland, dikes are known to have been constructed since the 13th century [60]. As of 2016, 8451 km of dikes protect around 10 900 km² of land, or 3.5 % of the national territory [61]. In urban areas with limited space, concrete walls sometimes replace dikes; some European cities also use temporary, mobile barriers installed during most extreme events [62].

The design of flood defences, initially based on past significant floods, moved to a probabilistic approach during the 20th century. The Netherlands has used extreme value analysis of sea levels in flood management as early as 1940 [63]. After the 1953 North Sea flood, with a death toll of almost 2000 people, Dutch researchers and managers worked on economic optimization of flood defences and implementing probabilistic design country-wide. An act of parliament from 1957 set out a goal of improving the flood defences in the Netherlands to water levels at given return periods by 1978. The most ambitious target was that of protecting South Holland against a 1 in 10 000 years flood. This target was achieved in 1997 [37]. At present, the Netherlands is moving from the probability of overtopping to a holistic analysis of dikes’ probability of failure including many mechanisms [64]. The new standards (return periods of flood) range from 100 to 100 000 years. The standards per dike section were chosen so that in any given area the probability of dying from flood (individual risk) is lower than 10⁻⁵ per year. The standards are expected to be met by 2050 [65].

⁹See chapter 4 cover photo, and the book’s rear cover, for two more contemporary examples of high water marks.

Other countries are less advance in using probabilistic approaches and hazard mapping in flood management. Also, the Netherlands has higher (nominal) protection standards than any other country in the world. In other European countries, the defences are usually expected to protect against water levels with a return period between 30 and 300 years [66]¹⁰. In Poland, the highest protection level is for a return period of 200 years, according to a government-imposed system in force since 1997, but defences designed for return periods as low as 10 years, or even 2 years, are not uncommon [67].

Barriers are another structural defence measure and are used to close off, permanently or temporarily, rivers and bays to prevent coastal floods. Such structures are again concentrated in the Netherlands. The most representative is perhaps the Afsluitdijk, a 32-km long permanent barrier that enclosed the bay of Zuiderzee in 1932 (north-east of Amsterdam), turning it into the IJsselmeer lake in order to prevent floods like the one in 1916. After the flood of 1953, the Deltaplan involved closing the estuaries of Rhine and Meuse rivers with moveable barriers, the last completed in 1997 in the New Waterway, west of Rotterdam [59]. Germany and the UK have two storm surge barriers each, including the Thames Barrier in London (see chapter 5 cover photo), while another one protects Saint Petersburg in Russia, and another is under construction in Venice [68].

Another method of taming river flows are reservoirs, which aim to smooth the flow of water during both rainy and dry periods. In Europe, there are more than 1400 large dams (above 15 m height), according to the GRaND database [69] and countless thousands of smaller reservoirs. River flow is regulated to the largest extent in southern Europe, particularly in Spain. Dams are much less common in central Europe or the British Isles (Ireland and United Kingdom). Most of large reservoirs are relatively new: few existed before the 20th century, while the highest intensity of dam construction was in the 1960s and 1970s. After the 1980s the number of new large reservoirs has dropped sharply, according to the GRaND database, so that by 2018 the construction of big dams has ceased altogether in Europe. However, smaller reservoirs for local-scale retention of water are still intensely built throughout the continent. River regulation and dredging is also used to improve flow conditions in rivers, and bypass channels like the New Danube in Vienna are also constructed to reduce extreme water levels [62]. Another possibility is withdrawing from endangered areas and even removing existing flood protection in order to make more room for floodwaters. This is because many rivers, e.g. the Rhine, have been artificially straightened and narrowed over the centuries in order to ease navigation. This had the negative effect of increasing flood hazard [70].

Some countries have put more stress on spatial planning, rather than hard engineering, by linking flood hazard zones with building restrictions. This connection is particularly strong and explicitly defined in e.g. Ireland [71], Switzerland [72] and the United Kingdom [73]. Similar regulations also exist e.g. in France [74] and Poland, but are much laxer and less strictly enforced. Presently, spatial planning also involves making more space for the river through moving the dikes back and creating more floodplains [59]. Other non-structural measures aimed at reducing flood losses, should inundation of populated areas occur, involve pre-flood preparedness of the citizens [75], emergency measures such as sandbags [76], and evacuation [77].

In practice, national and local authorities use mixtures of different flood manage-

¹⁰See Fig. D.3 in appendix D for a map of estimated flood protection standards in Europe.

Table 1.1: Flood management-related spending on fixed assets and completed works in Poland, total for 2004–16. Source: own calculations based on Central Statistical Office [61] and Ministry of Finance [81] data.

Category	Spending on fixed assets (current prices)	Completed works	Stock of structures (as of 2016)
Reservoirs and dams	€1374 mln	123 reservoirs with a total capacity of 134 mln m ³	Several thousand reservoirs, dammed lakes and polders with a capacity of approx. 4.5 bln m ³ [82]
Flood defences	€830 mln	2277 km of renovated or newly constructed defences	8451 km of dikes, protecting 10 912 m ² of land
River regulation, dredging etc.	€894 mln	4416 km of rivers and channels regulated, dredged etc.	43 442 km of channels and regulated rivers (58 % of total hydrographic network)
Coastal protection	€107 mln	79 km of the coast reinforced with seawalls, groynes, beach nourishment etc. (2009–16)	Approx. 25 % of the 500-km long coast is protected by structures, mostly groynes [83]

ment solutions. As pan-European data are not available, Table 1.1 shows example expenditure on flood-related structural protection schemes in Poland, with the number of structures constructed and their total inventory. Reservoirs and dams (€106 mln per year) have been most prominent, but they also have purposes not related to floods (water supply, environmental conservation etc.), while river dredging (€69 mln per year) is often made for maintaining inland navigation. Still, the structural measures applied are diversified and also more intense than in any point since the 1960s and early 1970s. On average, €64 mln per year allows to build or renovate approximately 2 % of the total stock of dikes in Poland. The same proportion of the coast is reinforced every year, mainly through beach nourishments. In the United Kingdom, the annual expenses of flood and coastal erosion management has averaged approx. €800 mln (fiscal years 2000/01–2016/17), of which slightly more than half was spent on fixed assets [78]. By contrast, annual economic consequences of floods are estimated at £1.35 bln, or approx. €1.7 bln [79]. In the Netherlands, the budget of the Delta Programme, which is responsible for the upkeep of the primary flood defences was €1.1 bln [80], compared with expected annual losses of about €600 million [64].

1.1.3. HISTORICAL OUTLINE OF FLOOD HAZARD AND RISK MAPPING

Mapping of flood hazard and risk, and designing the flood protection in accordance to frequency of extreme hydrological phenomena is still a relatively new activity in most of Europe. Incremental improvements of flood research and management practices developed over the span of many decades. The exact timeline varied substantially between countries, though some general observations could be drawn, and which are described below. As a more specific example, the experiences of Poland are summarized in Table 1.2.

Table 1.2: Milestones in development of flood hazard mapping and flood management in Poland. Adapted from Paprotny [67] unless otherwise noted.

Year	Development
1934	Catastrophic flood in southern Poland. The flood's outline is later published as a 1 : 500 000 scale map by the Military Geographic Institute
1936	First attempts of calculating return periods of river discharges for Polish rivers [84]
1967	A national atlas of extreme discharges is published [85]
1970	A manual on statistical methods in hydrology is published [86]
1975	Outlines of significant historical floods included in an 11-sheet, 1 : 500 000 scale hydrographic map of Poland (last sheet published 1980)
1997	A system of classifying flood defences based on flood frequency and area at risk of flooding is imposed by the national government. In July the "millennial" flood kills more than 50 people and inundates almost 7000 km ² [50]
1998	First sheets of a new edition of the 1:50 000 hydrographic map are published, which now include flood defences and other hydraulic structures as well as flood hazard zones (Fig. 1.6). Only 64 % coverage of the country achieved by 2010 [87]
2001	An act of parliament obligates the water management authorities to prepare flood maps that would include flood frequency. Local governments are also required to include 100-year flood extents in their spatial planning documents for areas of particular socio-economic importance
2007	The classification scheme of flood defences is amended to include socio-economic characteristics of the floodplains when assigning the protection level
2011	EU Floods Directive implemented in the national law, leading to country-wide flood mapping that for the first time utilized hydrodynamic modelling
2015	Final version of national flood hazard and risk maps is published, allowing their use in administrative processes such as spatial planning and granting construction permits [88]

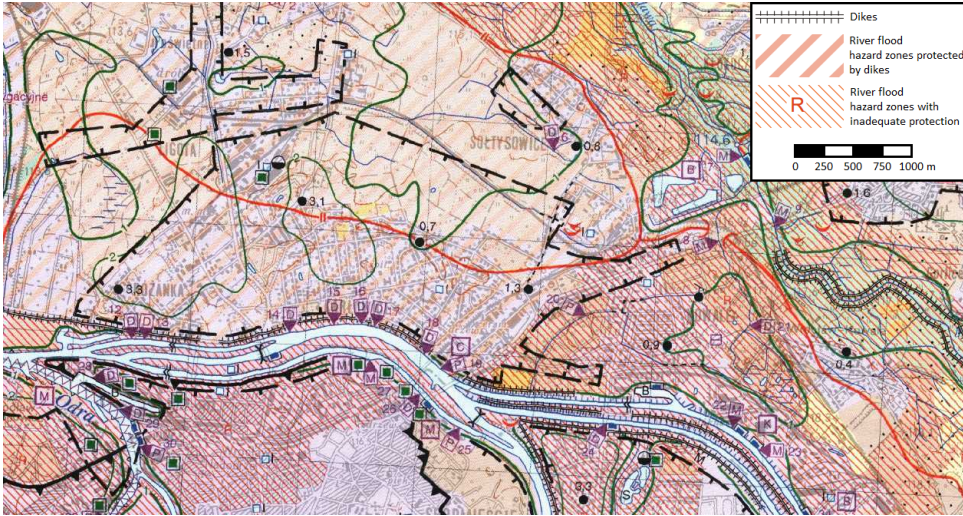


Figure 1.6: Fragment of a Polish 1:50 000 hydrographic map with marked flood defences and flood hazard zones, overlaying the city of Wrocław, which was severely affected by a flood in 1997. Map sheet M-33-35-C “Wrocław – Wsch.,” 1998, adapted from the Head Office of Geodesy & Cartography [87].

First flood maps were merely representing the outlines of areas actually inundated by past disasters. Sometimes they were published as stand-alone maps, otherwise with general hydrographic maps, or kept as administrative records. The latter is still carried out in some countries, noticeably in England (as shown in Fig. 1.5), but also e.g. in Finland and France. Remote sensing through satellites allows presently to map inundated areas worldwide, as it is done by the Dartmouth Flood Observatory [89]. The next step in flood hazard mapping was to use extreme value analysis to obtain water levels at given return periods and superimpose them over a topographic map. This technique was first applied in large scale in the United States in 1966 to produce 1 : 24 000 scale “flood inundation maps” [90]. In Poland, such maps started to be produced since 1998, an example of which is shown in Fig. 1.6. The same method of extrapolating water levels over the terrain (also known as the “planar approach”) can be applied to digital data [91]. In the past, flood maps were also produced based on the occurrence of alluvial and colluvial sediments [92].

Developments in computing and the production of digital spatial data, especially elevation models (DEMs) led to a new phase in flood mapping. In the 1980s computer models were created using de Saint-Venant equations, which preceded their implementation by over a century [93, 94]. At first, models were one-dimensional, providing water levels only at given cross-section of river valleys. This usually resulted in supplementing this method with the aforementioned planar approach; such an option was used for flood hazard mapping in chapter 3 of this thesis. From the 1990s two-dimensional models were used, allowing more detailed floodplain inundation mapping, also in coastal areas. However, since there is a large disproportion between river channel width and floodplain size, a combination of the two modelling modes (one- and two-dimensional) is some-

times applied. Due to the relatively high computational burden of two-dimensional computations, its use is often reserved for flood mapping of more economically valuable parts of countries (in Poland, only for larger cities).

Yet, in many European countries flood mapping was fragmentary or non-existent until recent years. Only in 2007 flood mapping was given adequate weight with the adoption of the European Union's Floods Directive [8]. It set out minimum requirements for flood risk assessments, flood hazard and risk maps as well as flood risk management plans. Implementation targets and cyclical reviews of those documents were all mandated upon member states. Before that, e.g. Estonia and Greece had only maps containing outlines of significant historical floods. Even in such flood-prone countries as Germany, Italy and Spain the hazard maps had only partial coverage of their territories [95]. At present, according to the directive, each EU country need to have a preliminary flood risk assessments (they were due in 2011 and are up for review in 2018). Those studies need to contain information on past floods and "an assessment of the potential adverse consequences of future floods for human health, the environment, cultural heritage and economic activity." Flood hazard and risk maps, which were due in 2013, ought to contain three flood scenarios, of low, medium, and high probability. The directive only specified the medium scenario as a return period of ≥ 100 years, which was interpreted differently across countries; in Poland return periods of 500, 100 and 10 years were used¹¹. The hazard maps should contain flood extents and water depths, while the risk maps should provide information on the number of people, economic activity and potentially-pollutive installations within the flood hazard zones. Finally, flood risk management plans (due in 2015) were mandated as policy documents on how to reduce flood risk.

Flood maps produced nationally typically have one considerable limitation: they do not include impact of climate change. Large uncertainty concerning local-scale climate impacts is a major obstacle preventing such studies. In the United Kingdom, guidance for local flood risk assessments provides only rough (upwards) modifiers that should be applied when analysing sea level, river discharge or wave heights [73]. In Poland, similarly to other European countries, impact of climate change of river floods has not been analysed nationally. A study on consequences of sea level rise, as a phenomena more uniform and somewhat easier to include in flood maps, was first published in Poland in 1990 [99], around the same time as in other European countries¹².

Amidst growing concern of climate change impacts and development of new European and global spatial datasets, efforts started on generating pan-European flood maps. Such maps allow assessment of climate change impacts, can be used at EU-level policymaking, and enable consistent inter-country comparisons of flood risk. Before the implementation of the Floods Directive, they also provided information on countries where national flood maps did not exist. Even at present, due to the limited dissemination of reusable data from national or local flood studies, pan-European maps are an important source of information. The first pan-European map, in 2006, was based

¹¹Examples of flood hazard map scenarios for other countries are as follows. Austria and Switzerland: 30, 100, 300 years [72, 96]; Czech Republic: 5, 20, 100 and 500 years [97]; Italy: 20–50, 100–200 and 500 years [98]; United Kingdom: 30, 100, 1000 years [54].

¹²For an overview of developments of coastal flood research in Poland see Paprotny and Terefenko [100].

on rough estimates of water levels based on catchment area superimposed over an elevation model with a 1 km resolution [101]. Afterwards, river floods were simulated using the two-dimensional LISFLOOD model, resulting in a map with a 100 m resolution [102]. At the same time, development of high-resolution climate models and climate change projections led to studies on precipitation extremes [103], followed by work on future trends in river discharges [104, 105]. This eventually resulted in pan-European estimates of changes in flood hazard area under a warming climate [106]. In parallel, studies on coastal flood hazard under climate change were made [107, 108], first based on available storm surge observations, global sea level rise predictions and static modelling approach, and later based on high-resolution hydrodynamic modelling of storms and inundation of coastal areas [109]. Finally, operational forecasting of river floods was developed by applying the same tools used to make pan-European flood maps [110]. Those studies were followed by many other, ever more extensive assessments utilizing improvements to models, computational power and data availability. Detailed information can be found in the introductions of chapters dealing with extreme discharges (chapter 2), river floods (chapter 3), storm surges and coastal floods (chapter 4).

1.2. RESEARCH PROBLEMS AND OBJECTIVES

Pan-European analyses of flood hazard and risk have become increasingly common in the past decade, as indicated in section 1.1.3. In this context, the title of this thesis defines both the research problem and the objective. The research problem is that various aspects of pan-European flood risk studies still need improvement, most importantly their accuracy; efficiency; spatial, temporal and thematic coverage; data availability and reusability. Below, the research problems are presented in more detail.

I. Accuracy Flood research involves a variety of physics-based or statistics-based models, which aim to recreate, as precisely as possible, the actual phenomena and processes of the Earth's environment. The most desirable outcome of flood analyses is an accurate delineation of flood hazard and risk zones, the probability of occurrence of floods, and trends in hazard and risk over time (especially future projections). Yet, only limited validation of flood maps has been presented in literature so far, mostly demonstrating needs for substantial improvements relative to detailed, local studies, especially in context of large uncertainty related to the reliability of flood defences. Also, limited availability of observations compared to the total length of the European river network and coastline requires pan-European modelling of river discharges, storm surge heights and extreme sea levels. Here, too, more can be done in order to achieve better match between modelled and observed data.

II. Efficiency Models can be simple or complex, including few or dozens of parameters. They also range from quickly computable to time-consuming. Therefore, "efficiency" can be understood as the model's complexity and computational time relative to the amount and accuracy of the results. Hydrological modelling of European river network, both to obtain river discharge estimates as well as flood zones is very computationally demanding. Simpler statistical methods for generating river discharge scenarios are fast, but have limited accuracy.

III. Spatial coverage and resolution In contrast to most other natural hazards, such as windstorms, temperature extremes or droughts, floods directly affect relatively small

areas, therefore they need to be studied in fine resolution. Pan-European studies now cover most of the continent with good resolution, but not for all types of floods (compound floods in particular), and not for all components of flood risk, especially flood losses and exposure. Further, due to the time needed to run hydrological models, relatively small rivers in Europe were not covered by existing flood hazard studies, but only rivers above a given threshold of catchment size. Also, in recent years many new pan-European datasets, including high-resolution climate models, have become available, but not yet applied in flood research.

IV. Joint probabilities in floods River, coastal and flash floods are usually analysed as if they were independent phenomena. Even when their co-occurrence, which can lead to compound floods, is analysed, it is done only for case studies. A comprehensive, pan-European compound flood assessment is therefore needed. Further, it is important to analyse the ability of climatic and hydrological models to recreate the dependencies between storm surges, river discharges, precipitation or waves identified using observational data.

V. Historical trends in flood risk components Changes in flood risk over time depend not only on evolving hazard, but also flood exposure and vulnerability. The actual consequences of floods are also not stationary, yet studies on this topic had limited spatial extent, resolution or temporal coverage. Most studies included periods from around 1970 to present, or even shorter timeframes, usually one country at a time. The topic needs to be explored on both pan-European and long-term scales, utilizing high-resolution spatial datasets, so that historical trends in flood occurrences, losses, exposure and vulnerability can be analysed.

VI. Data availability and reusability Data from flood analyses, especially those prepared by national or local authorities, is frequently not disseminated. Even if such flood maps are available, they are not reusable for research purposes, as they exist only as on-line visualizations or in other formats that are of limited use. Therefore, the aim of this study is to make all the results publicly available on reliable online repositories. Further, the results should be prepared in a common, universally-accepted format and disseminated with a proper documentation.

The overarching objective is to improve pan-European flood risk mapping and assessment through integration of statistical, hydrological and spatial (geographical) modelling approaches. Each chapter of this thesis covers different aspects from the aforementioned list of research problems, hence the chapter-specific objectives are as follows:

- Chapter 2: to provide pan-European extreme river discharge estimates using a statistical model instead of a hydrological rainfall-runoff model. Research problems: I (improving the accuracy of discharge estimation compared with other approaches), II (reducing complexity and computational time compared to rainfall-runoff models), III (providing the estimates in higher resolution and for many more rivers) and VI.
- Chapter 3: to create pan-European river flood hazard maps. Research problems: I (improving the accuracy of flood hazard zone representation compared to existing studies), II (reducing complexity and computational time compared to other approaches), III (providing flood maps for a larger number of river catchments) and

VI.

- Chapter 4: to generate pan-European estimates of storm surge heights and extreme sea levels, and prepare coastal flood hazard maps. Research problems: I (improving the accuracy of coastal flood maps and the boundary conditions for coastal hazard estimation), III (providing coastal flood hazard maps on European scale and using, for the first time, regional climate model data for coastal hazard estimation), and VI.
- Chapter 5: to investigate the probability of joint occurrence of precipitation, extreme river discharges, storm surges and waves in Europe. Research problems: III (calculating the joint probability estimates on European scale), IV (investigating the ability of climate and hydrological models to recreate the joint probabilities found in observational data and estimates of the possibility of compound flood occurrence) and VI.
- Chapter 6: to obtain pan-European, long-term historical trends in flood losses and exposure. Research problems: III (collecting high-resolution spatial and temporal data on flood events, losses and exposure on European scale), V (estimating long-term trends in flood losses and exposure) and VI.

1.3. SCOPE OF THE THESIS

The focus of this thesis, as stated in the title, is *pan-European flood risk mapping*. The four concepts indicated by the title require further description, as their meaning is specific to the purposes of both the thesis as a whole and individual chapters as well.

Pan-European. The study covers, and is limited to, the European continent. The exact delimitation of the domain varies between chapters, but is in any case smaller than the geographical extent of Europe. This caused by differences in scope of each chapter, and availability of data relevant to each analysis. The primary focus is on the European Union countries, while other territories are included depending on the feasibility of such analysis. In all chapters, almost all of the former Soviet Union territory is excluded. Furthermore, several outlying islands are omitted as well, namely the Azores, the Canary Islands, Madeira and Svalbard. However, all chapters cover Cyprus, which is geographically part of Asia, but nonetheless a member state of the European Union. More detailed information on the exact extent of the domain is provided in each chapter. It should be added that the boundaries and geographical names shown in the maps throughout this thesis do not imply a position on any territorial, sovereignty or naming dispute.

Flood. As noted in the introduction, there are many types of floods. In each chapter, a *flood* will be used as a shorthand encompassing different subsets of possible flood events. Chapter 2 deals only with extreme discharges in rivers, which are hydrological floods in the broadest sense. In chapter 3, only river floods caused by high discharges from rainfall or snowmelt are considered. Chapter 4 covers only coastal floods, i.e. caused by high sea levels caused by windstorms in combination with tides but excluding waves. Chapter 5 quantifies hydrometeorological phenomena (storm surges, precipitation, river discharges, waves) that lead to compound floods (considered here as the occurrence of a river/flash flood at the same time and place as a coastal flood. Finally,

the focus of chapter 6 are recorded flood events which have caused losses in land, population or assets (damaging floods), belonging to four types: river floods, coastal floods, flash floods (river floods caused by very short but intense rainfall) and compound floods (defined as co-occurrence of a river/flash flood and a coastal flood). In all cases, the thesis excludes urban floods, floods caused entirely by technical failures and floods of geophysical origin.

Risk. In natural disaster research, risk is understood as the product of a hazard and its consequences, with the latter further being the product of exposure and vulnerability [11, 112, 113]. This thesis, however, does not contain direct estimates of flood risk, but rather quantifies all the elements that risk is composed of. Firstly, hazard is the probability of occurrence of a threatening natural event. Most of this document is related to this component of risk. Chapters 2, 4 and 5 estimate the probability of occurrence of extreme hydrometeorological events that can result in floods: storm surges, heavy precipitation and river discharges, while chapters 3 and 4 provide flood hazard zones per given return period of extreme discharges or sea levels. The remaining chapter 6 looks into consequences, i.e. adverse effects on human health, society, the environment and assets. Consequences are investigated there using reported, quantitative information on flood losses: area inundated, fatalities, persons affected and monetary value of lost assets. Consequences can be direct (occurring in contact with flood waters) or indirect (e.g. economic and social disruption), of which only the former is considered here. Furthermore, chapter 6 provides estimates of exposure, i.e. inventory of elements that could potentially be affected by a flood (Fig. 1.7). The final component, vulnerability, i.e. propensity of exposed elements to be adversely affected (or, lack of resistance to damaging forces) is then calculated as the ratio of consequences and exposure. In case of compound flood analysis in chapter 5, the expression “flood potential” is used, as the hazard of compound floods is not directly computed, but only the hazard of co-occurrence of contributing phenomena.

Mapping. In all chapters, the analyses performed are essentially spatial analyses, as they concentrate on the inhomogeneity of space in terms of the components of flood risk. Flood hazard, losses and exposure are quantified and rendered on a map, where differences in the intensity of each variable can be assessed, and the spatial interactions between variables could be established. As a result, the thesis does not consider aspects of flood events that occur below a geographical scale and cannot be represented cartographically. For example, flood protection is considered in terms of spatial variation of dike heights, relative to local water levels, but not in terms of the processes that occur within dikes during a flood, and which could lead to dike failure. At the same time the large, pan-European domain of the study requires certain simplification and generalization of processes and phenomena related to flood events, in order to both maintain the accuracy of the study's outcomes and retain the computational feasibility of the analysis. It can be noted that flood risk mapping is not done in this thesis directly, i.e. the thesis does not result in producing flood risk maps, but instead maps the components of risk separately.

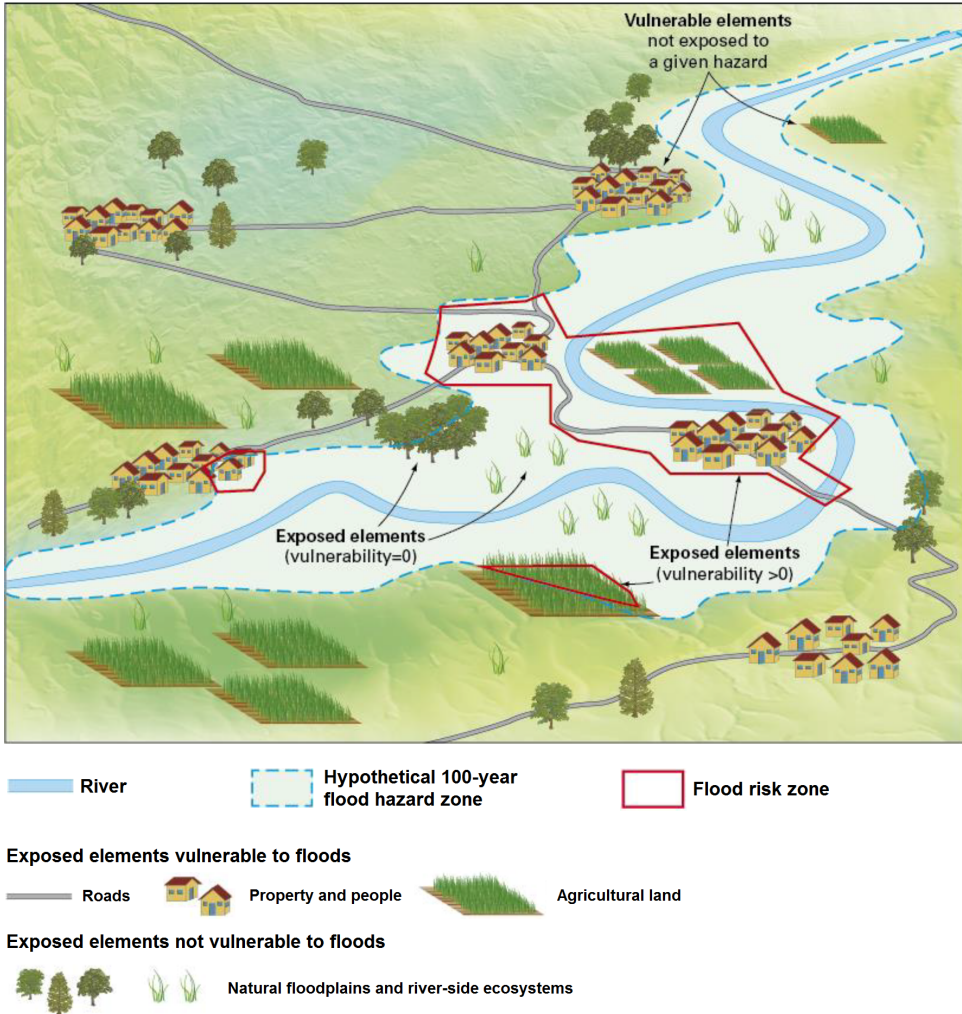


Figure 1.7: Graphical explanation of concepts of risk, hazard, vulnerability and exposure in context of floods. Adapted from INSPIRE Thematic Working Group Natural Risk Zones [111].

1.4. THESIS OUTLINE

This study consists of five connected chapters presenting the research, bookmarked by the introduction and conclusions (Fig. 1.8). This introduction has briefly examined what are floods, what factors determine their occurrence, where did they happen and what protection measures are deployed to reduce flood hazard. It has also outlined the history of flood risk mapping, and laid out the objectives and scope of the thesis. The research begins with an attempt to estimate extreme river discharges in Europe through a statistical model (chapter 2), presenting the study from theoretical background through the Bayesian Network model set-up to the analysis of the model's performance and a pan-European assessment of present and future discharges. Those results then are used in chapter 3, where they are transformed into river flood hazard zones, followed by pan-European estimates, projections and validation.

Separately, the other principal component of flood hazard – storm surges – is computed in chapter 4, where extreme sea levels are provided for all European coasts after calibration and validation of a hydrodynamic model. In the same chapter, sea levels are utilized to obtain coastal flood hazard zones for the continent, which are then compared with other studies. Hazard maps from chapters 3 and 4 are then an important component in the analysis of historical trends in flood losses and exposure since 1870 (chapter 6). This analysis involves a new database of past damaging floods and gridded socio-economic variables. Last but not least, compound floods are added to the analysis in chapter 5, which compiles data obtained for, and computed in, chapters 2, 4 and 6. The joint probability of hydrometeorological phenomenon is calculated based on their dependency structures and then used to create a composite index of compound flood potential. Overall conclusions and recommendations stemming from all research chapters close the thesis in chapter 7.

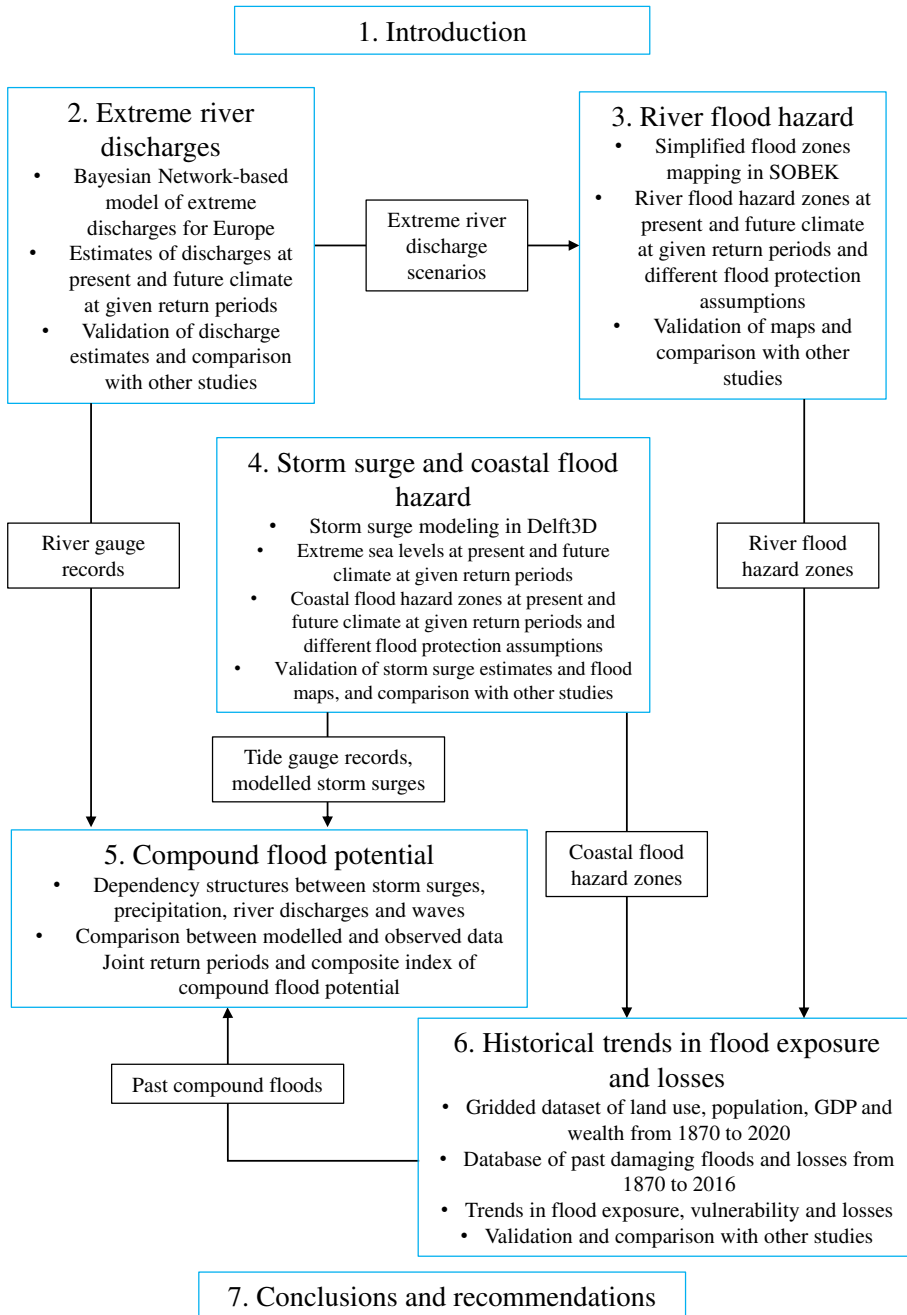
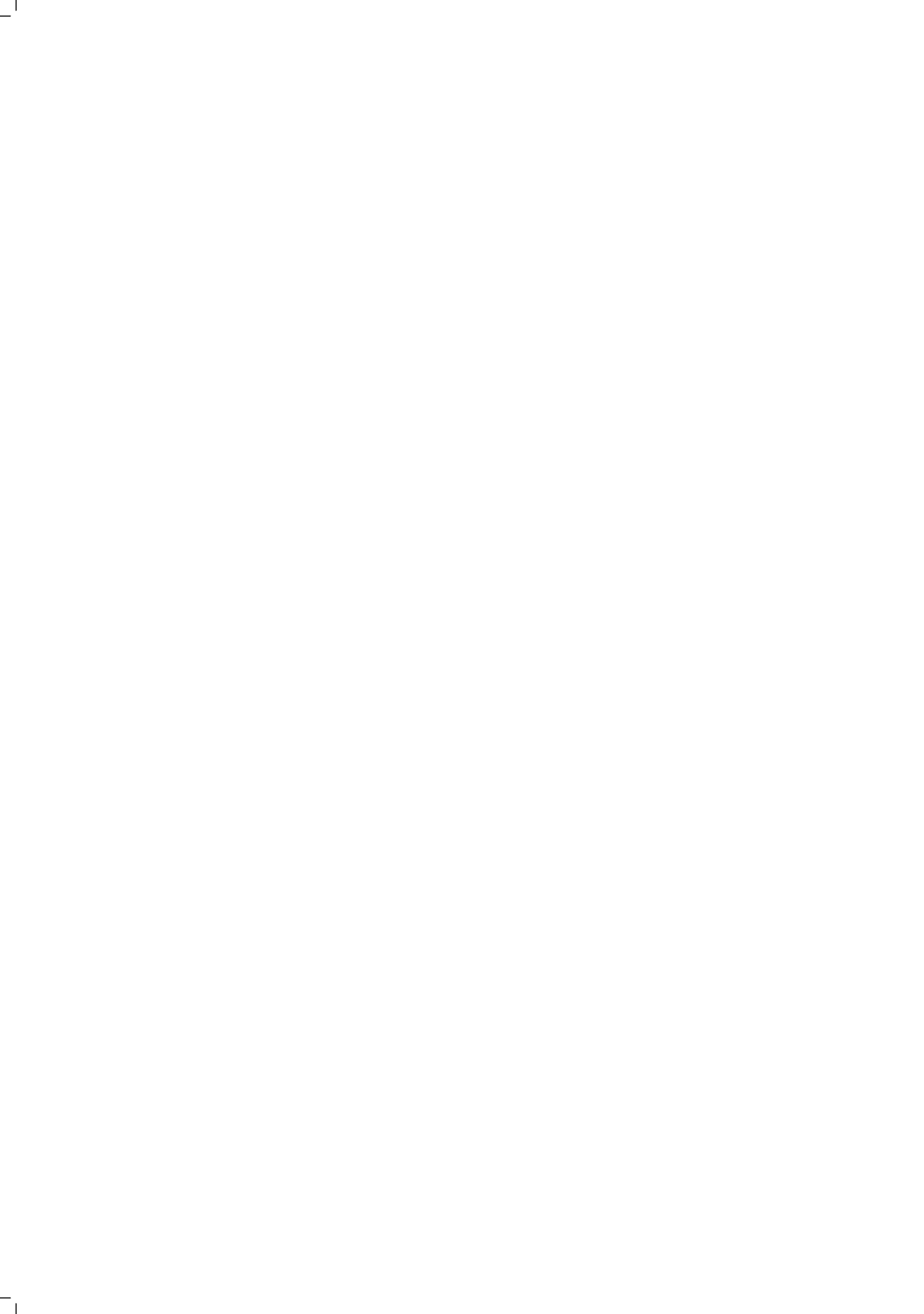


Figure 1.8: Outline of the thesis and connections between chapters.





84
E 88
82
E 81
80
E 79
78
E 77
76
E 75
74
E 73
72
E 71
70
E 69
68
E 67
66
E 65
64
E 63
62
E 61
60
E 59
58
E 57
56
E 55

Previous page: A traditional staff gauge used to provide a visual indication of water level, located in front of a modern digital gauging station. Oder river, Gartz, Germany.

2

EXTREME RIVER DISCHARGES

2.1. INTRODUCTION

THERE is currently substantial concern in Europe about increasing flood risk linked mainly to climate change. Available studies [106, 115, 116] predict that the severity of floods will increase, due to changes in extreme precipitation and socio-economic development. Abundant availability of continental and global climate, land-use, and elevation data result in many studies analysing floods in a similarly large domain. However, the amount of hydrological observations at our disposal is far from sufficient for comprehensive assessments of flood hazard. This is not only the result of the uneven distribution of measurement stations, but also of the limited dissemination of data by national or local bodies responsible for their collection. High-resolution historical measurements are critical for calculating hydrological event scenarios for the purpose of delineating flood zones. Those scenarios are typically values of extreme river discharge or water level with a certain return period, i.e. the average interval of time between the occurrences of an event with the same magnitude. Such calculation additionally requires long data series, further narrowing the number of locations where such analysis can be performed. In effect, to conduct large-scale¹ flood-hazard studies, it is necessary to fill the gaps in measurements with modelled river flows. There are two primary approaches used to obtain discharge values in ungauged catchments, i.e. catchments for which no discharge measurements are available.

The first approach is to use rainfall–runoff models. They utilize physical equations describing processes such as infiltration, runoff and retention in order to transform rainfall into river discharges. These models are typically used to model river flows on the catchment scale, although in recent years a few studies applied them on a continental or global scale. One series of publications [105, 117, 118] presented calculations

This chapter has been published in *Hydrology and Earth System Sciences* **21**, 2615–2636 (2017) [114].

¹This thesis uses the term “large-scale” in relation to assessments with a large spatial extent. However, it has to be noted that in cartography the usage of the term “scale” in cartography is reverse to the common usage. In effect, maps with a wide coverage (e.g. whole Europe) are known as “small-scale”.

using the LISFLOOD model. The simulation was set up for Europe with a 5 km resolution. Many different datasets of rainfall amount were analysed, including historical observations and future climate simulations, deriving daily discharge data for most of the continent. Another group of studies [119, 120] have introduced a global hydrological model GLOFRIS. This model has a much coarser resolution than LISFLOOD, as its rainfall–runoff module uses a 0.5° grid².

The aforementioned studies used the modelling results to perform an extreme value analysis of river discharges. Some also continued the research with flood-hazard estimation. The main drawback of this approach is the computational expense, which necessitates a reduction in resolution. Additionally, only a limited number of rivers are included in the models. For example, LISFLOOD-based studies used a threshold of 1000 km² catchment size, later reduced to 500 km², while GLOFRIS was prepared only for rivers with Strahler order 6 or above, which only accounts for about a third of the river length included in the aforementioned European model.

The second approach is to use statistical methods, of which a large variety exists. Several statistical models rely on the fact that catchments close to each other share many characteristics. River basins are therefore pooled into groups based on geographical proximity alone or also based on catchment size, climate data, terrain or soil type. However, the studies employing such techniques mostly covered a limited domain, typically single countries [121, 122]. The first global analysis was recently presented by Smith *et al.* [123]. The study applied regional frequency analysis (RFA) for all continents for the first time. Here, after clustering catchments based on size, climate type and average rainfall, a probability distribution of discharges is calculated for each region. Estimates of extreme discharges for a given ungauged catchment were derived by first assigning them to a proper region and then using data on catchment size and rainfall together with region-specific coefficients to solve a simple regression equation, in order to obtain an estimate of the mean of annual maxima of discharges in the catchment. Finally, a generalized extreme-value (GEV) probability distribution with region-specific parameters is used to calculate return periods of discharges. Flood scenarios (peak discharges) obtained through this method were then used in a global flood-hazard analysis by Sampson *et al.* [124].

There are also several statistical methods that rely solely on the geographical characteristics of catchments to estimate discharges. Many of them are simple equations that can be easily applied to quickly solve practical problems in engineering, such as estimating dike heights or calculating necessary channel or culvert capacity. Moreover, they are typically only applicable in small areas for which they were prepared. Usually, they are a variation of the “rational equation”, which states that river discharges can be calculated by multiplying the catchment area by the rainfall intensity and runoff coefficient [125, 126]. The first two elements are used in virtually all methods, but the remaining element is either left out due to the difficulty of estimating it, or is derived from a model table of coefficients, or additional factors are added as proxies. For instance, Stachý and Fal [127] developed an equation to calculate 100-year discharge in catchments above 50 km² in Poland which incorporates seven factors: catchment area, extreme rainfall (100-year return period), soil type, catchment slope, river slope, lake area and marsh

²Approximately 1000–2500 km² grid cells over Europe.

area. However, it also requires incorporating an additional empirical coefficient for each physio-geographic region of the country, while different return periods than the default 100 years are obtained by multiplying discharge by a region-specific factor, similar to the RFA method. Another example is the preliminary flood risk assessment in Norway [128], which utilized a simple regression between catchment area and 500-year water level. An “envelope curve” approach was then applied, in which a curve is constructed in such a manner that it contains all (or almost all) observations. This concept was long used to make crude estimations of maximum possible floods, also on a continental scale. Padi *et al.* [129], for instance, applied it to Africa. Some attempts have also been made to apply multiple linear regressions on global scale [130].

This chapter presents a new statistical method to calculate extreme river discharges under present and future climate in Europe. It was devised as an alternative to existing physical and statistical models; its purpose was to provide boundary conditions for hydraulic modelling that could be used in a pan-European flood-hazard analysis. The method is based on Bayesian networks (BNs) that combine probability theory and graph theory in order to build and operate a joint distribution. A BN is used to analyse and represent the dependencies between different environmental variables, including river discharges. This chapter also presents the quantification of the model based on a large dataset of river-gauge observations and pan-European spatial datasets. The model shows good performance across regions of Europe at different time periods. Further, a comparison of this new approach with other methods, both physical and statistical, is presented. Lastly, the method is applied over the entire domain to obtain a large database of extreme discharges, and analyse the influence of climate change on their return periods.

An early and preliminary variant of the method was originally reported in Paprotny and Morales Nápoles [131]. The BN presented there is superseded by an improved version described herein. Also, the work is part of a bigger effort to create pan-European meteorological and hydrological hazard maps under the “Risk analysis of infrastructure networks in response to extreme weather” (RAIN) project. This influenced the choice of the domain and input data, which is explained in section 2.2, although this does not limit the applicability of the method outside of the European domain.

2.2. MATERIALS AND METHODS

In this section, an overview of the model's framework and elements is given, followed by a description of how the model was prepared, what datasets were used to build it, what the underlying mathematical methods are, and how the model's accuracy and utility were assessed.

2.2.1. WORKFLOW AND OUTLINE OF THE METHOD

The basic elements of the procedure to derive extreme discharge estimates through a BN are presented in Fig. 2.1. The first step was to identify available data on annual maxima (Q_{AMAX}) of daily river discharge (I), and also the catchments which contribute to locations where the measurements were made (section 2.2.2), i.e. gauged catchments (II). Then, several large-scale (pan-European or global) spatial datasets were compiled

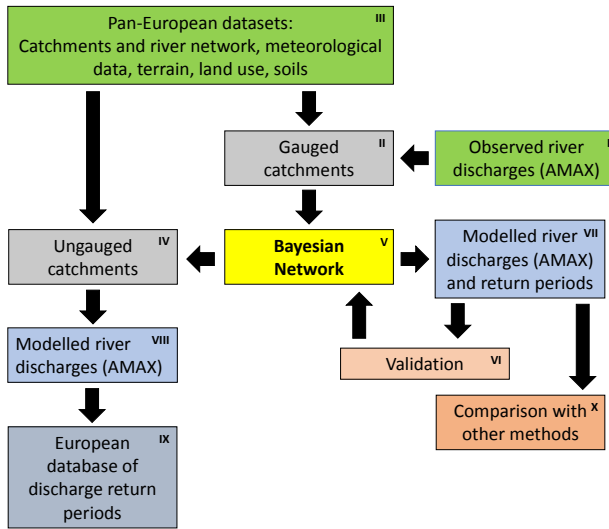


Figure 2.1: Schematic workflow of obtaining extreme river discharges from catchment characteristics. Q_{AMAX} = annual maxima of discharges. Roman numerals refer to the text.

(III), providing information on the most important variables influencing extreme river flow behaviour (section 2.2.3) both for gauged and ungauged catchments (IV). The dependence between those variables and river discharges were analysed through copulas and BNs (section 2.2.4) (V). After extensive testing of different configurations, an optimal model was constructed (section 2.2.5) that had the highest performance in validation in terms of the underlying statistical model and prediction capability (VI; section 2.2.7 and 2.3.1). The output of the model is annual maxima of daily river discharges (VII), which were then fitted to a probability distribution in order to obtain return periods (section 2.2.6). After the method was ready, it was applied for all catchments (IV) in the domain to create a database of discharges (VIII). Using frequency analysis, return periods of discharges under present and future climate in Europe (section 2.3.2) were obtained (IX). The accuracy of the BN model was also contrasted with alternate methods (X; section 2.3.1 and 2.4.1).

2.2.2. RIVER DISCHARGE DATA

Discharge data from measurement stations were collected over a domain covering most of Europe (Fig. 2.2). The study area includes the entire continent, plus Cyprus as a European Union (EU) member, with two exceptions. Out of the territory of the former Soviet Union, only river basins that are at least partially located within the EU were included. Also, the outlying regions of Madeira, the Azores and the Canary Islands were omitted because they are outside the EURO-CORDEX climate model's domain.

In total, data series for 1841 stations were compiled, not including a few dozen available stations whose tributaries could not be unequivocally identified and were therefore

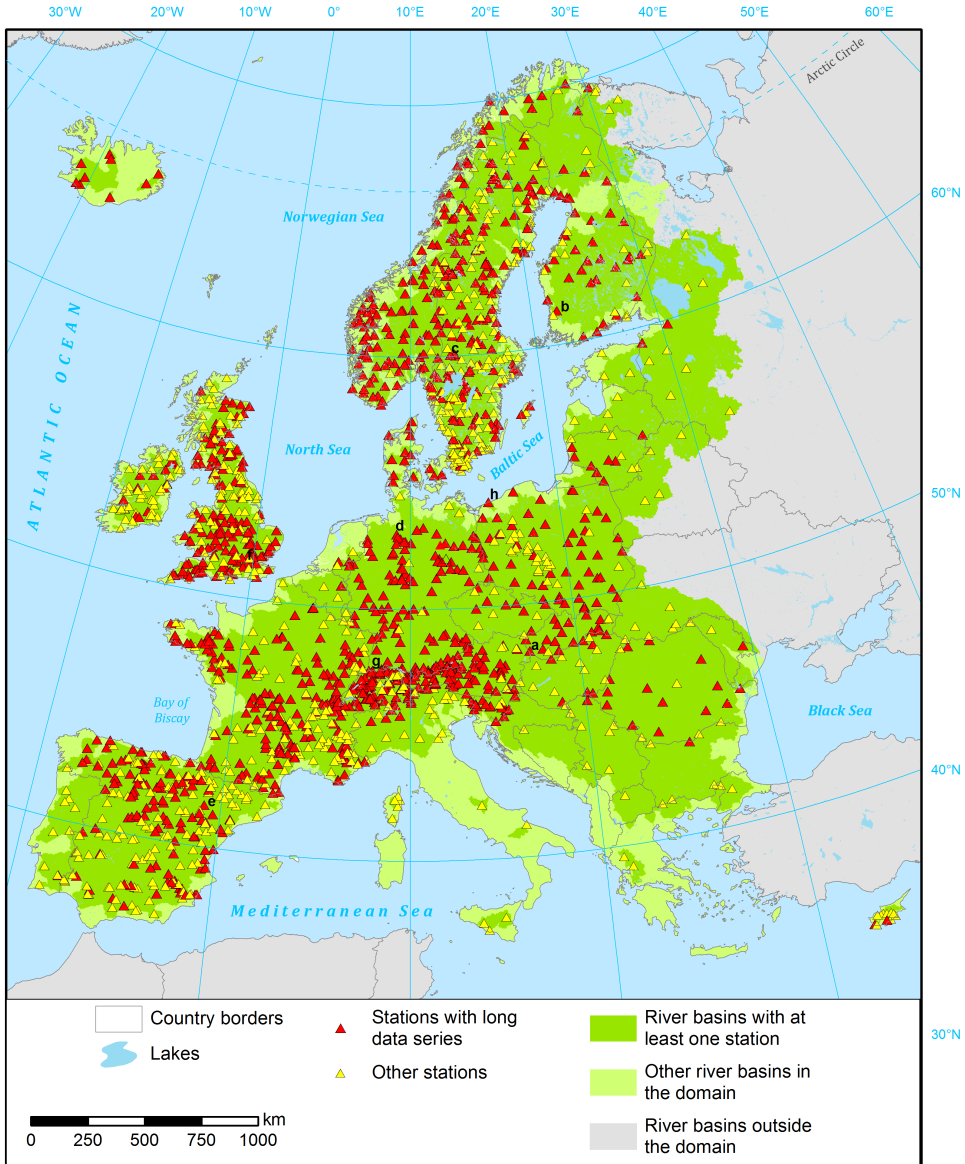


Figure 2.2: Measurement stations used in this chapter (“long data series” indicates stations with sufficient data for calculating return periods) and river basins included in the domain. Letters refer to gauges in Fig. 2.7.

excluded from the analysis. The data were collected from five sources, as follows:

- 1186 stations from the Global Runoff Data Centre [132]
- 82 stations from the Norwegian Water Resources & Energy Directorate [133]
- 284 stations from the Swedish Meteorological & Hydrological Institute [134]
- 239 stations from Centro de Estudios Hidrográficos [135]
- 50 stations from Fal [136]

The data collected were daily discharges observed between 1950 and 2013, though of primary interest were data up to 2005, since it was the maximum range of EURO-CORDEX climate models' historical scenario runs. All datasets were quality-checked by the providers; only a few cases of misplaced decimals in daily series were identified in the data after inspection. Daily discharges were transformed into annual maxima (Q_{AMAX}) for each calendar year, except for the last group of 50 stations, as Fal (2000) only reported the extreme and mean values. The total number of Q_{AMAX} values for the years 1950–2005 in the database was 74 757. The stations represent 37 countries and 439 different river basins (78 % of the domain's area of 5.67 million km²). However, the south-eastern part of Europe is substantially under-represented, with most stations concentrated in Scandinavia and western Europe. France has the highest number of Q_{AMAX} values in the database (14 %), followed closely by Spain, Sweden and the United Kingdom (UK), as can be seen in Table 2.1. However, the largest density of stations is in Switzerland, Austria and the UK. The catchments' sizes span from 1.4 to 807 000 km², with 43 % of them being in the 100–1000 km² range.

Long data series, i.e. at least three full decades of uninterrupted data (1951–80, 1961–90 or 1971–2000) were available for 1125 stations. These observations were used to validate the accuracy of the model in estimating mean Q_{AMAX} and return periods, while the complete database was used to quantify the BN model.

2.2.3. SPATIAL DATASETS

Several large-scale spatial datasets were collected for this study, even though not all of them were used in the final setup of the model. Nevertheless, all were useful for testing different configurations of the BN. The most important dataset was a map of the river network and catchments, which was derived from the pan-European CCM River and Catchment Database v2.1, or CCM2 [23, 137]. It was created by calculating flow direction and accumulation on a 100 m resolution digital elevation model (DEM), combined with land-cover information, satellite imagery and national GIS databases. CCM2 was utilized to delimit the domain used in this chapter. In total that area covers 831 125 river sections (almost 2 million km in length) in 70 638 river basins. Each river-gauge station was connected with a corresponding river section in CCM2. Each river section belongs to one primary catchment, whose attributes include the identifier of the next downstream catchment. Using this information, the whole tributary of a gauge station, or any other point in the domain, could be delimited. For each catchment, various statistics were calculated in GIS. A few indicators could be derived from this dataset alone: catchment

Table 2.1: Summary statistics of stations used in this chapter.

Country	Number of stations		Q _{AMAX} values (1950–2005)	
	Total	Per 1000 km ²	Total	%
France	273	0.50	10 642	14.2
Spain	247	0.50	10 602	14.2
Sweden	283	0.65	10 520	14.1
United Kingdom	228	0.92	9159	12.3
Germany	133	0.37	6996	9.4
Norway	104	0.32	5035	6.7
Switzerland	90	2.18	4093	5.5
Austria	73	0.87	3464	4.6
Poland	78	0.25	2807	3.8
Finland	53	0.16	2287	3.1
Ireland	40	0.57	1371	1.8
Other countries	239	0.10	7781	8.8
Total	1841	0.32	74 757	100.0
Catchment size (km ²)				
> 100 000	32		1303	1.7
10 000–100 000	207		8849	11.8
1000–10 000	513		20 826	27.9
100–1000	795		32 030	42.8
< 100	294		11 749	15.7
Total	1841		74 757	100.0

area, river network density (total river length divided by catchment area) and catchment circularity (catchment area divided by the area of a circle that has the same perimeter as the catchment), whereas others were derived using the datasets described below.

The next most relevant source of information is climate data, both historical and future projections. Two datasets for the former were analysed. E-OBS is a spatial interpolation of observations (starting in 1950) made by weather stations [138], while ERA-Interim is a global climate reanalysis going back to 1979 [139]. However, E-OBS has gaps in spatial coverage and includes few variables, whereas ERA-Interim has a relatively coarse resolution (0.75°)³. In effect, slightly better performance of the model was recorded using high-resolution control runs of a climate model under the EURO-CORDEX framework [140]; the results of this analysis can be found in Appendix B. EURO-CORDEX uses regional climate models (RCMs) for Europe, where boundary conditions are obtained from global-scale general circulation models (GCMs). This work utilizes simulations for the historical run (1950–2005) and two climate-change scenarios (RCP 4.5 and RCP 8.5 for 2006–2100). The necessary variables (precipitation, snowmelt and runoff) and resolution (0.11°) were included in a total of 14 model runs; of these, 8 model runs start in 1950. Of the model runs, one was made using GCM boundary conditions which came from a 12-member ensemble.

This model run, which was selected to carry out this study, was made by the Climate Limited-area Modelling Community utilizing the EC-Earth general circulation model

³Approximately 2000–6000 km² grid cells over Europe.

(run by ICHEC) with the COSMO_4.8_clm17 regional climate model [141], realization r12i1p1. This RCM also has relatively good model performance when estimating extreme precipitation in comparison with others [142]. No bias correction was performed, even though it is often considerable for extreme precipitation [143]. For the sake of simplicity and universality of the method, all input data are used unaltered. However, as an additional check on the method's performance, a different GCM-RCM combination was analysed, and the results have been added to Appendix B. From this dataset four variables were derived: total precipitation, snowmelt, near-surface temperature and total runoff. All data were daily values on a 0.11° rotated grid (spatial resolution of about 12.5 km).

Meteorological factors are the driving force behind floods, but more factors influence the runoff – terrain, land use and soils. Information on terrain was obtained from two DEMs. Most of the domain is available from EU-DEM, a dataset produced for the European Environment Agency. It was created by merging two sources of satellite altimetry data – Shuttle Radar Topography Mission (SRTM) and ASTER GDEM. It has a 25 m resolution and covers 39 countries [144], including areas north of 60° N, which are missing from SRTM-only datasets. For eastern Europe and some Atlantic islands which are not covered by EU-DEM, SRTM data were used instead [145]. SRTM has a 3 arcsec resolution⁴ and there are several versions available. The one used here is a void-filled derivative obtained from Viewfinder Panoramas [25]. Both datasets were resampled to a common 100 m grid matching the CCM2 dataset. The variables calculated from the DEMs included average elevation, average river slope and average catchment slope. The latter was derived either by averaging all slopes in the DEM or by calculating the slope S with the following equation:

$$S = \frac{H_{\max} - H_{\min}}{\sqrt{A}} \quad (2.1)$$

where H_{\max} is the maximum, and H_{\min} the minimum, elevation in the catchment and A is the catchment area. Another variable, the time of concentration, which is a measure of water circulation speed in the catchment, was calculated based on Gericke and Smithers [146]. Finally, we tested a terrain classification similar to one used in FLEX-Topo hydrological model [147]. In this approach, all grid cells in the DEM are classified based on height above nearest drainage, slope inclination and absolute elevation [148, 149]. Three classes – wetlands, hillslopes and mountains – were calculated as a percentage of total catchment area.

Land-use statistics for catchments were mainly based on CORINE Land Cover (CLC), another dataset produced by the European Environment Agency [150]. In this study, CLC 2000 edition, version 17 (12/2013), in raster format (100 m resolution) was used. It includes 44 land-cover classes with a minimum mapping unit of 25 ha and covers 39 countries. The main source material were Landsat 7 satellite images from the years 1999–2001 [151]. Similar to EU-DEM, the dataset does not cover some catchments in eastern Europe and in a few other areas. Missing information was supplemented using the Global Land Cover 2000 dataset, produced by the Joint Research Centre using algorithmic processing of SPOT 4 satellite images [152]. This product has a 30 arcsec

⁴Approximately 0.25–0.7 ha, or 2500–7000 m², grid cells over Europe.

resolution⁵ and includes 22 land-cover classes. The different classifications were synchronized to derive the area covered by forests, croplands (total and irrigated), marshes, lakes, glaciers, bare land and artificial surfaces. However, the data were only available for a single year for the whole domain, even though CLC was also produced for 2006, 2012 and, in some countries, for 1990. In contrast to terrain or soils, land use is dynamic and could influence the analysis for early time periods. Historical land-use reconstructions and projections (as in e.g. Klein Goldewijk *et al.* [153]) with sufficient resolution and thematic coverage were not available at the time of this analysis⁶. Therefore, fixed values of land-use percentages were used for all years, including the future climate-change scenarios.

Last but not least, soil property data were analysed. Occurrence of peat, unconsolidated and aeolian deposits, average water content, and soil texture were derived from the European Soil Database v2.0 [154], developed on a 1:1 000 000 scale, and Harmonized World Soil Database v1.2 [155], available at 30 arcsec resolution. Soil sealing (i.e. area covered by artificial impervious surfaces) was obtained from Revised Soil Sealing 2006, a dataset based on satellite imagery with a 100 m resolution [156]. Grain-size structure of the soil (gravel, sand, silt or clay) was calculated from SoilGrids1km database [157].

2.2.4. BAYESIAN NETWORKS

As noted in the introduction, BNs are graphical, probabilistic models [158, 159]. They have several advantages when compared against other methods, for the application described in this chapter. For one, their graphical nature makes the dependence configuration explicit, as evidenced in Fig. 2.3 in the next section. A BN takes into account, for example, dependencies between different environmental variables, which are not easily modelled with regression methods. Also, they can capture the often non-linear nature of those dependencies. The class of BNs used in this research includes several elements, whose specifics need to be explained before the actual hydrological model is presented.

First of all, consider a set of random variables (X_1, X_2, \dots, X_n) , which could be discrete, continuous or both. This distinction defines the different types of BNs. In this chapter, a continuous BN was built, since the environmental data used here are continuous. Furthermore, discrete BNs are only efficient for small models, whose variables have a limited number of states because of the way the (conditional) probabilities are calculated, as is explained later on. The random variables are represented as “nodes” of the BN, while the dependencies between them are represented as “arcs” joining different nodes. An arc represents the (conditional) correlation between two variables, and has a defined direction. The node whose arc points into the direction of another node is known as the “parent”, while the node on the “receiving” end of the arc is its “child”. A set of nodes and arcs forms the eponymous “network” of the BN. The arcs have to connect the nodes in such a manner that the graph is acyclic, i.e. if one chooses any node and follow strictly the direction of all arcs in a path, one will not end up at the same node. Each variable is conditionally independent of all its predecessors given its parents. Therefore, each variable has a conditional probability function given its parents, and the

⁵Approximately 25–70 ha, or 0.25–0.7 km², grid cells over Europe.

⁶This data deficiency is addressed in chapter 6.

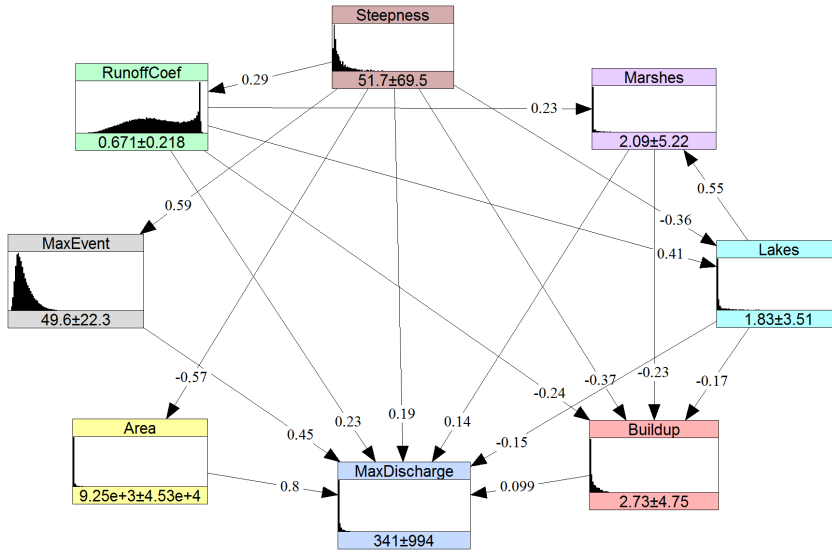


Figure 2.3: Bayesian network for river discharges in Europe. The nodes are presented as histograms, with numbers indicating the means and standard deviations of the variables. Values on the arcs are the (conditional) rank correlation coefficients.

joint probability can be expressed as follows [160]:

$$f_{X_1, X_2, \dots, X_n}(x_1, x_2, \dots, x_n) = \prod_{i=1}^n f_{X_i | \text{Pa}(X_i)}(x_i | \mathbf{x}_{\text{Pa}(X_i)}), \quad (2.2)$$

where $\text{Pa}(X_i)$ is the set of parent nodes of X_i , with $i = 1, \dots, n$. Naturally, if there are no parents, $f_{X_i | \text{Pa}(X_i)} = f_{X_i}$. It can be already seen that one of the purposes of BNs, perhaps the main one, is updating the probability distributions of subsets of nodes, when evidence (observations) of a different subset becomes available. Hence, it is important not only to properly set up the network with nodes and arcs, but also to choose a good method to describe the dependencies. In case of a discrete network, this is done using conditional probability tables. In the BN model, node “Max discharge” has 7 parents. In this case, if each continuous node was to be discretized into 5 states, a probability table with $5^7 = 390\,625$ conditional probabilities would be required. Of these, only $5^7 = 78\,125$ may be estimated by difference, as probabilities must add to 1. Thus, 312\,500 probabilities would need to be specified. Similarly, if one were to discretize each node into 10 states, 90\,000\,000 probabilities would need to be specified. Even a discretization into 5 states for each node in the BN model would make the quantification prohibitive given the data available. Considering other nodes (node “Buildup” has 4 continuous parents) would make it even more restrictive for the use of discrete BNs. Thus, in this chapter a continuous non-parametric BN was applied to avoid the use of probability tables.

By using a non-parametric continuous BN, one only needs to specify an empirical marginal distribution for each variable and a rank correlation for each arc [161]. The

usual estimator of the cumulative probability distribution was used:

$$\hat{F}(x) = \frac{1}{n} \sum_{i=1}^n 1_{\{x_i \leq x\}}, \quad (2.3)$$

where (x_1, \dots, x_n) are the samples of a random variable, while $1_{\{x_i \leq x\}} = 1$ over the set $\{x_i \leq x\}$ and is zero elsewhere. Spearman's rank correlations are used to parameterize one-parameter (conditional) copulas. A copula is, loosely, a joint distribution on the unit hypercube with uniform $[0,1]$ margins. There are many types of copulas, described in detail by Joe [162]. Here, bivariate Gaussian copulas are used, an assumption that was tested against alternate distributions (Clayton and Gumbel copulas). Details of this calculation and the validation of the whole BN can be found in Appendix A. The bivariate Gaussian copula C has the following cumulative distribution function:

$$C(u, v; \rho) = \Phi_\rho(\Phi^{-1}(u), \Phi^{-1}(v)), \rho \in [-1, 1][0, 1]^2, \quad (2.4)$$

where Φ is the standard normal distribution, Φ^{-1} is its inverse and Φ_ρ is the bivariate Gaussian cumulative distribution with (conditional) product moment correlation ρ between the two marginal uniform variates u and v in the interval $[0,1]$. In contrast to the copula specification, the non-parametric BN applied in this study is parameterized by (conditional) rank correlations. This is because they are algebraically independent; hence, any number in the interval $[-1,1]$ assigned to the arcs of the BN will warranty a positive definite correlation matrix. The rank correlation (denoted by r) of two random variables X_i and X_j with cumulative distribution functions F_{X_i} and F_{X_j} is the usual Pearson's product moment correlation ρ computed with the ranks of X_i and X_j :

$$r(X_i, X_j) = \rho(F_{X_i}(X_i), F_{X_j}(X_j)). \quad (2.5)$$

Conditional rank correlations are calculated as shown in eq. (2.5), except that the conditional distributions are used inside the arguments to the right of the equal sign. For the Gaussian copula, conditional correlations are equal to partial correlations and these are constant. For one-parameter bivariate copulas, eq. (2.5) becomes the following:

$$r(X_i, X_j) = 12 \int_0^1 \int_0^1 C_\theta(u, v) du dv - 3, \quad (2.6)$$

The conditional rank correlation of X_i and X_j given the random vector $\vec{Z} = \vec{z}$ is the rank correlation calculated in the conditional distribution of $(X_i X_j | \vec{Z} = \vec{z})$. For each variable X_i with m parents $\text{Pa}_1(X_i), \dots, \text{Pa}_m(X_i)$, the arc $\text{Pa}_j(X_i) \rightarrow X_i$ is associated with the rank correlation:

$$\begin{cases} r(X_i, \text{Pa}_j(X_i)), \\ j = 1 \\ r(X_i, \text{Pa}_j(X_i) | \text{Pa}_1(X_i), \dots, \text{Pa}_{j-1}(X_i)), \\ j = 2, \dots, m \end{cases}, \quad (2.7)$$

where the index j is in the non-unique sampling order. For more details on the non-parametric BNs the reader is referred to Hanea *et al.* [161]. After all the variables and

parameters of the BN are in place, the joint distribution is uniquely determined. Under the Gaussian copula assumption, exact inference is available as well as efficient sampling procedures (for details, see Hanea *et al.* [163]). Here, 1000 samples were used each time the BN was conditionalized in order to derive an estimate of river discharges for a given location in the dataset. This number of samples is adequate to approximate the conditional distributions of interest while keeping the procedure computationally feasible. The BN for river discharges presented here was implemented in MATLAB; however, the Uninet software for non-parametric BNs was also used to visualize and analyse the model during the study (for details, see Morales Nápoles *et al.* [164]).

2.2.5. EXTREME DISCHARGE MODEL

The final BN for extreme river discharges was derived by testing many configurations involving around 30 variables. It is important to note that a BN can neither be created uniquely in an automated manner nor is it desirable to do so. Therefore, the BN in this study was built stepwise and assessed using a set of statistical measures presented in section 2.2.7. The final model is based on eight variables and is presented in Fig. 2.3, with a histogram representing each variable's distributions. The position of the nodes shows their hierarchy relative to the annual maximum of daily river discharge (*MaxDischarge*); the order in which different variables conditionalize on the river discharge distribution (using eq. 2.7) is clockwise. The (conditional) rank correlation coefficients are indicated on the arcs. The variables and BN structure are described in more detail below.

Annual maximum of daily river discharge (*MaxDischarge*) in cubic metres per second (m^3/s). The parents of this variable are all the remaining variables in the BN. By far the most important is the **catchment area** (*Area*) in square kilometres (km^2), which determines the scale of the processes in a river basin and is largely dependent on **catchment steepness** (*Steepness*) in metres per kilometre (m/km). This is because mountainous catchments are very small, divided by ranges, and only grow in size when many rivers join along the way to its drainage basin, crossing more planar regions. Steepness was calculated here using eq. (2.1); it is a proxy for terrain characteristics that influence the speed with which the water from rainfall moves down the slopes [147].

The climate model from EURO-CORDEX framework delivered two variables to the BN. First is the **annual maximum of daily precipitation and snowmelt** (*MaxEvent*) in millimetres (mm). Both factors are relevant, though melting of snow cover is important only in some regions. Both events often occur concurrently (as evidenced in a list of large European floods by Barredo [56]), hence using a summation of the two improved the performance of the BN. The variable has one parent, catchment steepness, as hilly and mountainous areas receive more precipitation, also in the form of snow. The second variable is the **extreme runoff coefficient** (*RunoffCoef*), a dimensionless indicator. It was constructed to include meteorological factors influencing the circulation of water in a catchment. Every climate model needs to represent this variable to take into account factors such as soil moisture, evaporation and retention. The annual maximum of the climate model variable “total runoff” was obtained for each sample, and then divided by *MaxEvent*. This variable is dependent on catchment steepness, since in hilly or mountainous terrain, conditions limit evaporation or retention. It should be noted that the values of these climate variables were calculated as an average of annual maxima

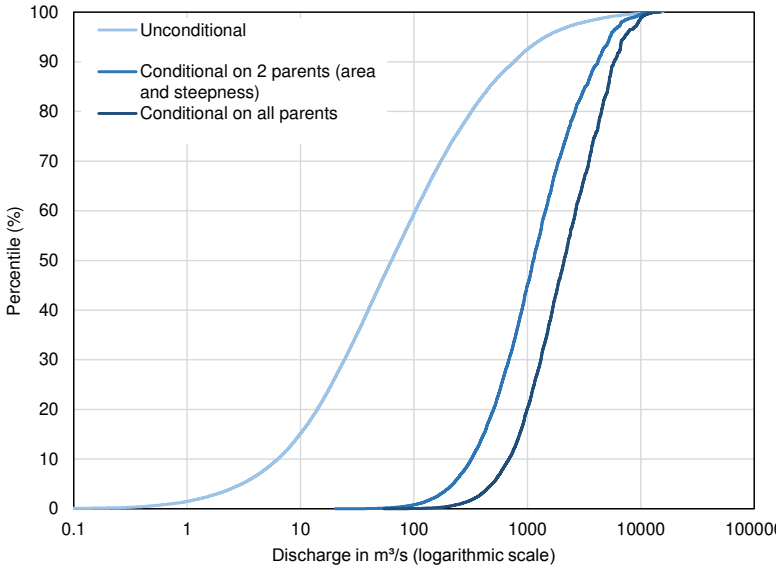


Figure 2.4: Cumulative probability distribution of river discharge: unconditional and conditionalized on two and seven nodes using values for Basel station in Switzerland (river Rhine, year 2005). This gauge is marked by letter “g” in Fig. 2.2

derived for each grid cell separately, and not by identifying the largest single event that occurred in a given catchment.

The BN is completed by three land-cover types, all expressed as a percentage of total catchment area. The statistics were obtained by choosing relevant classes from land-cover datasets. The first variable represents **lakes**, and was obtained using the “water bodies” class in CLC, with missing coverage supplemented by the water body layer in the CCM2 database. Lakes retain water from rainfall or snowmelt, thus reducing river discharge. This node has two parents: catchment steepness and extreme runoff coefficient. Lakes, especially large ones, are more prevalent in post-glacial plains of northern Europe, though increased lake cover is also observed in the mountains. In both of those areas, the runoff coefficients are higher, due to lower temperatures and more prevalence of impermeable soils. The second variable represents **marshes**, which are defined by CLC as three classes, “inland marshes”, “peat bogs” and “salt marshes”, while from Global Land Cover 2000 (GLC) the “regularly flooded shrub and/or herbaceous cover” class was used here. Similar to lakes, marshes increase retention in a catchment. They often occur in the same areas as lakes, with soils and climatology also having influence (as estimated by the runoff coefficient). Lastly, the **built-up areas** (*Buildup*) variable contains the “artificial surfaces” class from CLC or GLC. Construction increases the amount of impervious cover in a catchment, reducing infiltration, while water management systems collect the rainfall and route it directly to rivers. This variable is influenced, in order, by catchment steepness (flat areas are preferred for construction), runoff coefficient (which is higher in colder areas), lakes and marshes (less space available for construction).

In order to estimate river discharge in an ungauged catchment, the BN is updated,

that is, the value of the node or set of nodes (other than discharge) is defined based on the observations corresponding to that particular catchment, i.e. new evidence. Fig. 2.4 shows the effects of updating on the example of Basel station in Switzerland (meteorological data pertain to the year 2005). Conditionalizing on only two variables (catchment area and steepness) changed the mean of the distribution from 341 to 1740 m³/s. Knowing all seven variables that are parents of the river discharge node, one obtains an estimate of river discharge of 2819 m³/s. In this case, the estimate is fairly accurate, as discharge of 3212 m³/s was actually measured. The same procedure was applied to all rivers in the domain. Additional examples of conditionalization of the BN can be found in Appendix A. It should be noted that the discharge in each river section was estimated independently from another section in the same river using data for the entire upstream area.

In addition to validating the method, it is applied to model the influence of future climate predictions from EC-EARTH-COSMO_4.8_clm17 (Fig. 2.10) and EC-HadGEM2-ES-RACMO22E (Fig. B.5 in Appendix B) models. As noted before, land-cover statistics are fixed in time, and therefore only the climate variables change over time in the prediction. Future changes were calculated for two climate scenarios: RCP 4.5 and RCP 8.5. Those “representative concentration pathways” indicate changes in future physical and socio-economic environments that would cause, by 2100, an increase in radiative forcing of 4.5 or 8.5 W/m² [165].

2.2.6. RETURN PERIODS OF DISCHARGES

Annual maxima of daily river discharges calculated by the BN were used to perform a frequency analysis. Only stations with long data series were used, i.e. those with at least 30 years of discharge observations. To find an optimal model for estimating the marginal probability distribution of annual maxima of discharges, the Akaike information criterion (AIC) measure was used [166]. AIC values varied significantly between stations. On average, the AIC value was the lowest for the GEV distribution, indicating that it was the best fit over 15 other tested distributions, such as generalized Pareto, gamma, log-normal or Weibull distributions. This three-parameter distribution, however, gave very large errors for some stations. Therefore, to avoid completely unrealistic estimates in the database, the two-parameter Gumbel distribution is used, which is essentially the GEV distribution with the shape parameter equal to zero. This distribution was previously used in several large-scale flood-hazard studies [105, 118, 120, 167]. In order to calculate discharge Q with probability of occurrence p , the following equation is used:

$$Q_p = \mu - \sigma \ln(-\ln(1 - p)) \quad (2.8)$$

where μ is the location parameter and σ is the scale parameter. Parameters were fitted using maximum likelihood estimation [168, 169]. The extreme value analysis assumes the stationarity of the river discharge series. Using Spearman’s rank correlation, it was found that in 918 of 1125 gauges used to obtain return periods, the trend was not significant at level of significance of 0.05.

In order to maximize the number of stations available for validation, 30-year time periods were used in the calculation. 30 years were used because such a time period maximizes the number of stations available for validation. Also, this time span is com-

monly used in climate research. The main validation set consists of 958 stations with 1971–2000 data, 129 with 1961–90 data and 38 with 1951–80 data. That is 1125 in total out of 1841 used to quantify the BN. For further analysis, the calculation was made for all stations with data for a given time period; the 1981–2010 period was added as well, utilizing modelled discharge estimates based on the RCP 4.5 climate scenario for the years 2006–2010. Additionally, subsets comprising different regions of Europe and catchment size were also analysed.

2.2.7. MEASURES FOR VALIDATION OF THE MODEL'S RESULTS

Accurate estimation of return periods of extreme discharges, as well as mean annual maxima, are the desired outcomes of the BN model. Quality of return periods and average maxima simulations were evaluated using a set of three measures: coefficient of determination, Nash–Sutcliffe efficiency and RMSE-observation standard deviation ratio. Those methods were selected because they have also been used in other studies (e.g. Rojas *et al.* [143]) and were included in an overview of most important measures by Moriasi *et al.* [170]. First, the Pearson's coefficient of determination (R^2) was used to measure the correlation between observed and simulated values. In Kurowicka and Cooke [159] it is noted that R^2 actually factorizes into a function of the conditional rank correlations attached to the BN. Second, Nash–Sutcliffe efficiency (I_{NSE}) was applied to measure bias of the model. Its maximum value is 1, which means a plot of observed vs. simulated data fits the 1 : 1 line (no bias), while a value below 0 (down to $-\infty$) indicates that the mean of the observations is a better predictor than the simulated value. The relevant equation is as follows:

$$I_{NSE} = 1 - \left[\frac{\sum_{i=1}^n (x_i^{\text{obs}} - x_i^{\text{sim}})^2}{\sum_{i=1}^n (x_i^{\text{obs}} - x^{\text{mean}})^2} \right], \quad (2.9)$$

where x_i^{obs} is the i th observation of a variable, x_i^{sim} is the i th simulated value of that variable and x^{mean} is the mean of observations. The final measure is root mean square error (I_{RMSE})-observation standard deviation ratio (I_{RSR}). It standardizes the RMSE based on the standard deviation of observations ($I_{SD\text{obs}}$):

$$I_{RSR} = \frac{I_{RMSE}}{I_{SD\text{obs}}} = \frac{\sqrt{\sum_{i=1}^n (x_i^{\text{obs}} - x_i^{\text{sim}})^2}}{\sqrt{\sum_{i=1}^n (x_i^{\text{obs}} - x^{\text{mean}})^2}}. \quad (2.10)$$

To further investigate the relative accuracy of the method in light of alternate models, a RFA analysis was performed, as presented by Smith *et al.* [123]. This required us to obtain supplementary data. Each river-gauge station had to be assigned to one of five climate zones according to the Köppen–Geiger classification; a world map by Kottek *et al.* [27] was used for that purpose. Overall, 65 % of stations with long records in my sample are located in the temperate climate zone, with 30 % in continental, 4 % in polar and 1 % in arid zones. Additionally, mean annual rainfall was derived from CORDEX climate data. The final input information was catchment area, readily available from the datasets. In

order to estimate discharge in the RFA, a given station had to be assigned to 1 of the 82 clusters included in the RFA. The first criterion is the climate zone, which allocated a station to a group of clusters. Then, the Euclidean distance to each cluster centroid (defined through a logarithm of area and rainfall) was calculated. Afterwards, a “mean annual flood” equation (see Smith *et al.* [123]) was solved using the coefficients from the nearest cluster as well as catchment area and annual rainfall, providing us with Q_{MAMX} . Finally, cluster-specific GEV distribution parameters were then applied to obtain return periods of extreme discharges.

2.3. RESULTS

In this section, extreme river discharges calculated using the BN are compared with observed river discharges. Additionally, we present the results of applying the method to estimate the influence of climate change on discharges in Europe using EC-EARTH-COSMO_4.8_clm17 climate models. Results obtained with alternate climate models can be found in Appendix B.

2.3.1. VALIDATION OF THE MODEL'S RESULTS

Extreme river discharge estimates obtained from the BN are presented and compared with observed discharges in Figs. 2.5 and 2.6. The graphs include the mean annual maximum of daily discharge (Q_{MAMX}) and three return periods of discharges. In Fig. 2.6 a comparison of specific river discharges, i.e. runoff divided by the respective catchment areas [171], is shown. The former shows the highest performance, with both R^2 and I_{NSE} at 0.92, while accuracy of simulated discharge fitted to Gumbel distribution decreases with the probability of occurrence. The 10-year discharge (Q_{10}) has almost the same performance as Q_{MAMX} , while the 1000-year (Q_{1000}) discharge noticeably deviates from the 1:1 line, mainly for very large rivers. It should be also remembered that the return periods were based only on 30-year series, and therefore a 100- or 1000-year discharge includes the uncertainty of extrapolation of the return periods. However, the I_{NSE} value is still good, and R^2 changes moderately. The R^2 drops to 0.52 for Q_{MAMX} when considering specific river discharge and 0.44 for 100-year discharge, with I_{NSE} at 0.43 in both cases. Again, performance is slightly higher for 10-year discharge and drops approaching 1000-year discharge. It is also interesting to notice that the rank correlations for all four cases discussed previously (Q_{MAMX} , Q_{1000} , Q_{100} and Q_{10}) are in the order of 0.8 and their bivariate distribution does not present large asymmetries. This could be an indication that a method based on copulas could also be used for bias correction; however, further investigation of this observation is outside of the scope of this thesis.

Performance of the model by time period, region or catchment area was also analysed in more detail (Table 2.2). For four different time periods, where availability of stations varies, the results of the validation are almost identical. Only for 1981–2010 is it slightly lower because it is partially outside the timespan of the historical scenario of EURO-CORDEX; for 2006–2010, data from RCP 4.5 climate-change scenario run had to be used to fill the missing information. Much more variation in the quality of the simulations is observed when dividing the results by geographical regions (their definitions correspond to the regionalization of the CCM2 catchment database). Western Europe

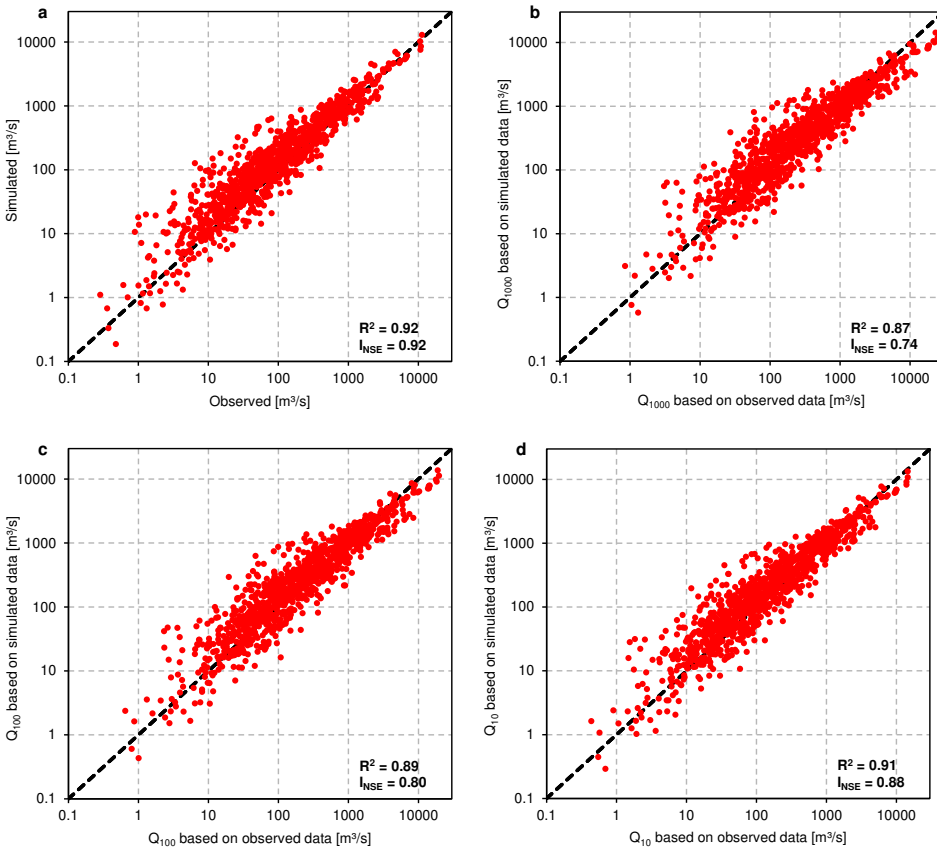


Figure 2.5: Simulated and observed average annual maxima of daily river discharges (a) and annual maxima fitted to Gumbel distribution to calculate 1000-, 100- and 10-year return periods (b–d), for 1125 stations. 30-year periods of annual maxima were used (the most recent available out of 1971–2000, 1961–90 or 1951–80).

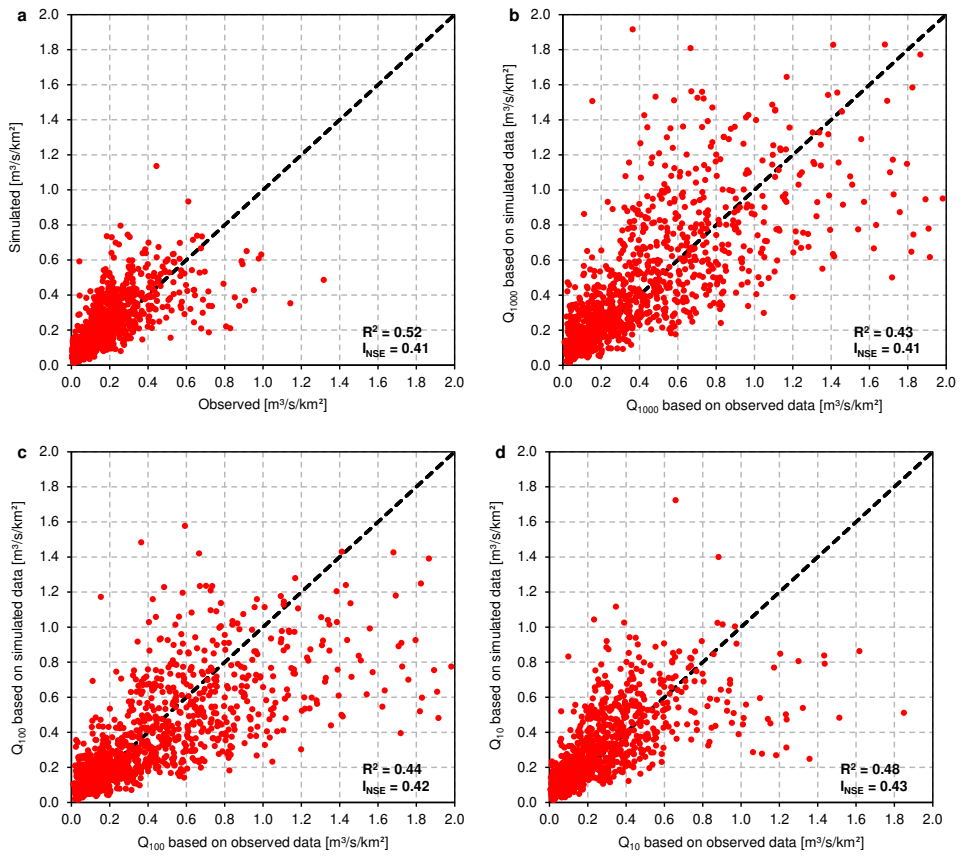


Figure 2.6: The same as Fig. 2.5, but for specific discharge, i.e. divided by catchment area.

(comprised mainly of France, Belgium, the Netherlands and the Rhine river basin) had particularly good results for Q_{MAMX} , followed by the Danube river basin and Scandinavia (roughly defined as Sweden and Norway). The lowest correlation for Q_{MAMX} was observed in the Iberian Peninsula (Spain and Portugal), while Central Europe (mainly Poland, Lithuania, Denmark and north-east Germany) had the highest I_{NSE} values. Iberia had the lowest performance for Q_{100} , while western Europe recorded the highest correlation, and Scandinavia had the best score in I_{NSE} and I_{RSR} . Central European and Scandinavian stations' error was lower and I_{NSE} values higher for the 100-year return period compared to Q_{MAMX} . No region dropped below acceptable levels (i.e. R^2 or I_{NSE} value of 0.5, according to Moriasi *et al.* [170]), albeit stations in the Iberia and "other regions" have noticeably lower performance. In the case of Spain, to which almost all stations collected for the Iberian Peninsula belong, discharges tend to be overestimated, which may point to the influence of reservoirs on river flow. Indeed, many Spanish stations with large errors were found to be just downstream of large dams. Finally, "other regions" is a grouping of a small number of stations scattered around Europe, mainly from Finland, Italy and Iceland. Those areas, containing many rivers in both arid and polar climates, are under-represented in the quantification of the BN, which may provide a potential justification for their lower performance.

In Fig. 2.5 it can be seen that the amount of scatter in the plot increases for rivers with smaller discharges. Detailed results in Table 2.2 show that the performance of the model drops for the smallest catchments, especially for those below 100 km² (177 catchments). For others, above 500 km², the R^2 and I_{NSE} values are mostly in the range of 0.5–0.6 for specific discharges, as when considering all stations. Additionally, to validate the robustness of the method, a split-sample test was carried out. Stations were randomly divided into two sets. Data from 917 stations were used to quantify the BN in order to simulate discharges in the remaining 924 stations. Of the latter, 586 stations had at least three full decades of discharge observations, which allowed us to make a comparison with simulated discharge. The validation result was almost identical with those reported for the full quantification, and even better results ($R^2 = 0.94$ and $I_{NSE} = 0.93$) were observed for Q_{MAMX} , while for Q_{100} the same value of I_{NSE} was calculated and R^2 equalled 0.90. Still, performance at individual stations varies. A selection of observed and simulated discharges, both annual maxima and those fitted to Gumbel distribution, is presented in Fig. 2.7. At some stations, there is a very close fit, while at others, either the discharge is overestimated or the distributions have different shapes. This is, however, not atypical even for more local studies.

The final analysis in this section is the comparison of the BN model and RFA. Using RFA, estimates of extreme discharge were obtained for all 1125 stations with long records and compared to discharges in Fig. 2.8. In the case of Q_{100} , Gumbel-distributed discharges were used, as the performance with GEV distribution was slightly lower. The performance of both BN and RFA models is visually similar, though the BN recorded higher correlation and less bias than the RFA. Less scatter can be observed in upper and lower ranges of discharges, with similar performance in the middle. Using specific river discharges (Fig. 2.9), the performance of both methods was lower, but still much better for the BN: I_{NSE} , for example, was negative for both Q_{MAMX} and Q_{100} when using RFA, in contrast to a value of 0.43 for the BN. RFA was devised as a global method instead of

Table 2.2: Validation results for simulated and observed average annual maxima of daily river discharges Q_{MAMX} and annual maxima with a 100-year return period Q_{100} .

Category		Stations	Q_{MAMX}			Q_{100}		
			R^2	I_{NSE}	I_{RSR}	R^2	I_{NSE}	I_{RSR}
	Total	1125	0.92	0.92	0.29	0.89	0.80	0.44
Regions	Central Europe	138	0.89	0.71	0.54	0.86	0.85	0.39
	British Isles	145	0.86	0.85	0.39	0.81	0.77	0.48
	Western Europe	261	0.97	0.96	0.19	0.94	0.79	0.46
	Iberian Peninsula	112	0.79	0.78	0.47	0.71	0.57	0.65
	Danube basin	167	0.93	0.92	0.27	0.92	0.83	0.42
	Scandinavia	227	0.92	0.83	0.42	0.91	0.90	0.31
	Other regions	75	0.79	0.82	0.43	0.72	0.70	0.55
Time period	1951–80	512	0.93	0.92	0.28	0.89	0.85	0.38
	1961–90	792	0.93	0.92	0.28	0.90	0.85	0.39
	1971–2000	958	0.93	0.93	0.27	0.90	0.84	0.40
	1981–2010	765	0.91	0.91	0.31	0.87	0.83	0.42
Catchment area	> 500 km ²	605	0.92	0.91	0.30	0.88	0.78	0.47
	< 500 km ²	520	0.59	0.52	0.69	0.56	0.55	0.67
	> 10 000 km ²	166	0.90	0.89	0.33	0.84	0.68	0.57
	1000–10 000 km ²	311	0.64	0.43	0.75	0.58	0.57	0.66
	100–1000 km ²	471	0.55	0.38	0.78	0.47	0.44	0.75
	< 100 km ²	177	0.47	0.41	0.77	0.42	0.40	0.77
Specific discharge by area	> 500 km ²	605	0.61	0.40	0.78	0.51	0.47	0.73
	< 500 km ²	520	0.36	0.23	0.88	0.27	0.23	0.88
	> 10 000 km ²	166	0.58	0.45	0.74	0.43	0.37	0.79
	1000–10 000 km ²	311	0.60	0.41	0.77	0.51	0.50	0.71
	100–1000 km ²	471	0.40	0.17	0.91	0.32	0.25	0.86
	< 100 km ²	177	0.29	0.20	0.90	0.20	0.12	0.94
	Total	1125	0.52	0.43	0.77	0.44	0.43	0.76

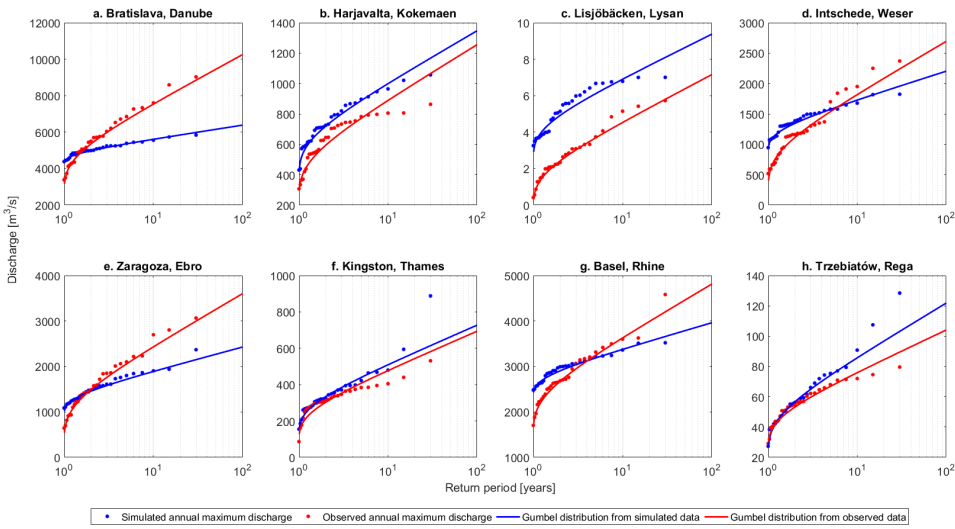


Figure 2.7: Simulated and observed annual maxima of daily river discharges fitted to Gumbel distribution at selected stations. Data refer to 1971–2000, except for panel (h), which refers to 1961–90. See Fig. 2.2 for the locations of stations.

a regional one, but at the same time it is in fact a set of 82 regional approximations of hydrological processes. Here, we analyse contributing factors of extreme discharges all together, achieving comparable or even better results.

2.3.2. PRESENT AND FUTURE RIVER DISCHARGES IN EUROPE

Calculation of river discharges utilizing data from EURO-CORDEX climate simulations was done for the years 1950–2100, and are presented here in three time slices: 1971–2000, 2021–2050 and 2071–2100. The first period is from the historical “control” run, while the other two were analysed for two emission scenarios: RCP 4.5 and RCP 8.5. Projected trends calculated from the data are presented in Fig. 2.10. For the sake of clarity, only rivers with catchment area above 500 km² are presented in the picture; full-scale maps of discharges have been included in Appendix C. Aggregate statistics by region and catchment size were included in Tables 2.3 and 2.4. The description focuses on 100-year discharge, but the trends are also representative of other return periods.

The projected trends in Europe are very diversified. For Europe as a whole, there is a slight 4–7 % increase in discharges with a 100-year return period (Q_{100}), with the biggest change observed in the 2021–2050 RCP 8.5 scenario. Along 34–44 % of river length in Europe, Q_{100} is projected to increase at least by 10 %, depending on scenario. Yet, along 16–21 % of river length a decrease by more than 10 % is expected, with only small changes (± 10 %) for the remaining 35–49 %. In RCP 8.5 both increases and decreases of Q_{100} are more prominent than in RCP 4.5. In effect, Q_{100} in the 2071–2100 RCP 8.5 scenario is projected to correspond to 176-year discharge under present climate (1971–2000) if we take the median value. This value is slightly lower in mid-century and in end-century for RCP 4.5, with the smallest change compared to present climate in the 2021–2050 RCP 4.5

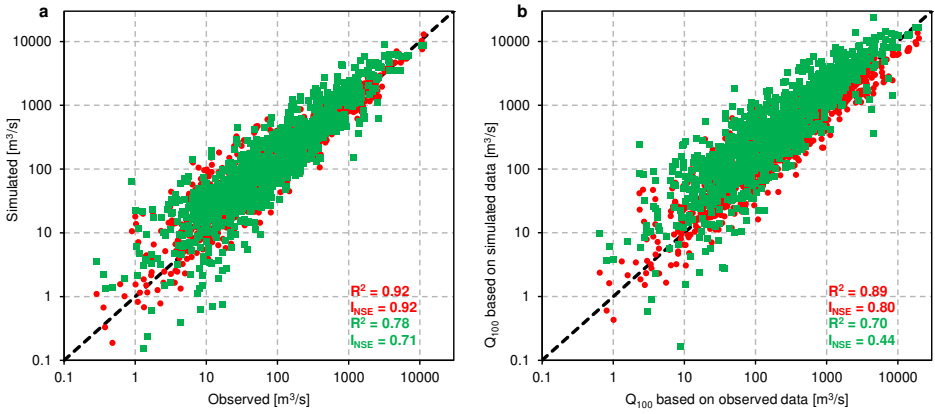


Figure 2.8: Simulated and observed average annual maxima of daily river discharges and 100-year discharge for 476 stations; Bayesian network model in red, regional frequency analysis in green. 30-year periods of annual maxima were used (the most recent available out of 1971–2000, 1961–1990 or 1951–1980).

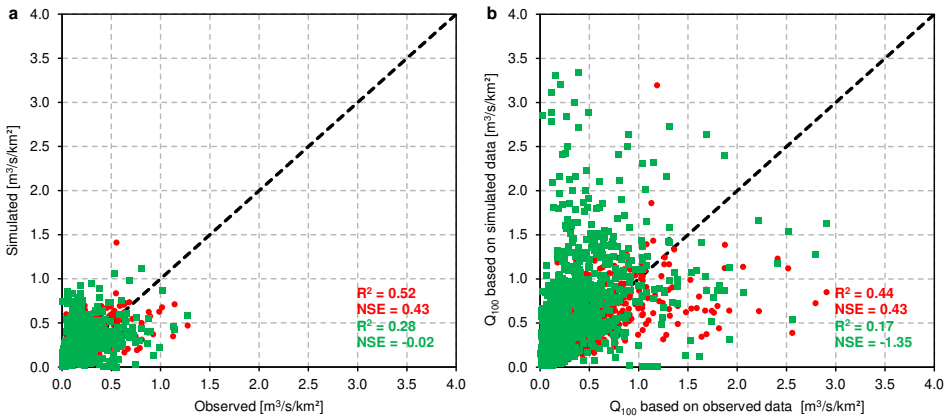


Figure 2.9: As Fig. 2.8, but for specific discharge, i.e. divided by catchment area.

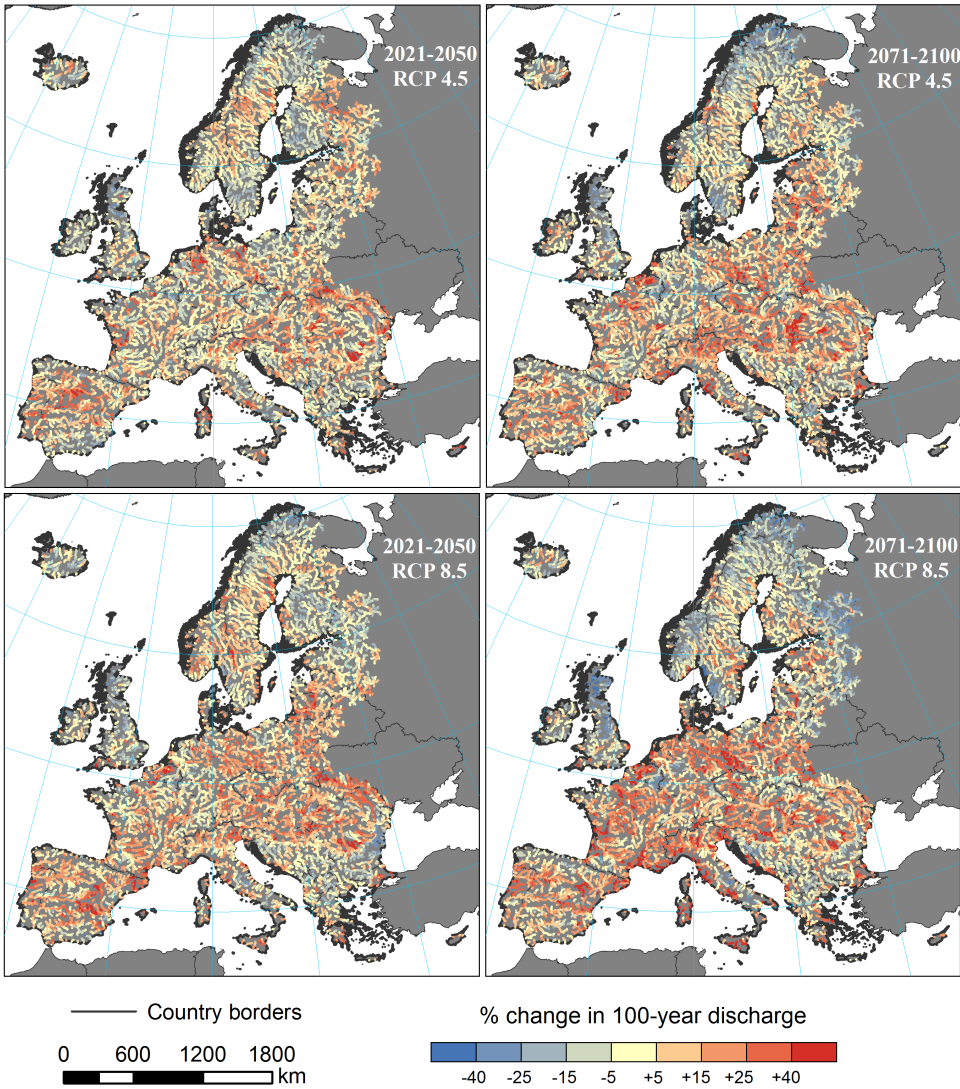


Figure 2.10: Predicted trends in daily river discharge with a 100-year return period (Gumbel distribution) under climate-change scenarios RCP 4.5 and RCP 8.5 (rivers with catchment area above 500 km² only). Projections based on EC-EARTH-COSMO_4.8_clm17 climate model run.

Table 2.3: Projected change in 100-year river discharge (Q_{100}) relative to 1971–2000 for two emission scenarios RCP 4.5 and RCP 8.5. Predictions based on EC-EARTH-COSMO_4.8_clm17 climate model run.

Category		Average change in Q_{100} weighted by length of river sections (%)			
		2021–2050	2071–2100	2021–2050	2071–2100
		RCP 4.5	RCP 4.5	RCP 8.5	RCP 8.5
	Total	+3.7	+5.7	+7.0	+5.9
Regions (selected)	Central Europe	+3.5	+9.6	+13.5	+12.2
	British Isles	−6.0	−6.5	−6.8	−13.5
	Southern Europe	+3.9	+12.1	+8.8	+17.7
	Western Europe	+1.1	+4.5	+5.8	+11.4
	Iberian Peninsula	+7.3	+8.1	+12.2	+11.0
	Danube basin	+6.5	+9.4	+9.3	+8.0
	North-east Europe	+1.2	−0.1	−1.5	−8.4
	Scandinavia	+1.8	−1.9	+4.6	−5.0
	South-east Europe	+1.2	+2.7	−1.2	+3.7
Catchment area	> 100 000 km ²	+2.9	+6.4	+8.2	+5.2
	10 000–100 000 km ²	+4.7	+7.4	+8.9	+7.2
	1000–10 000 km ²	+3.3	+4.3	+6.0	+5.1
	100–1000 km ²	+3.7	+5.1	+5.7	+5.7
	< 100 km ²	+2.9	+4.4	+3.8	+5.0

scenario.

Between regions, by mid-century, the largest average increases in extreme discharges are expected in the Iberian Peninsula and Danube basin (RCP 4.5), while Q_{100} in Central Europe (i.e. mainly the Elbe, Oder and Vistula river basins) is projected to surge even more in RCP 8.5. By the end of the century, however, southern Europe (comprised mostly of Italy) will experience the biggest average increase. Conversely, Q_{100} is projected to decrease on average in the British Isles in all four scenarios, in north-east Europe (Finland, north-west Russia and the Baltics) in three scenarios, in Scandinavia in two and in south-east Europe (mainly Greece) in one. Those discrepancies are the result of several trends, namely changes in extreme precipitation, snowmelt and runoff coefficient. The first is projected to increase across the continent, while the other two decrease at the same time with some exceptions. Decline in snowmelt, a consequence of thinner snow cover, will contribute to lower extreme discharges in parts of Scandinavia and Scotland. However, in most of Sweden, Finland and other areas, less snowmelt will be offset by more rainfall. Lower precipitation is expected only in small, scattered patches of Europe, most noticeably in southern Spain. At the same time, an increase of the runoff coefficient could be observed in predictions for the Iberian Peninsula and western Europe, with decreases in the remainder of the continent. Higher temperatures and less soil moisture are contributing factors to those trends.

In Tables 2.3 and 2.4 the projected trends in Q_{100} were also provided per catchment size. The differences in average increase of discharges are very small and partially caused by their uneven distribution in Europe. Median return periods show more diversity, since the relative increase in discharge by certain increment of return period typically gets smaller as the river grows in size. Most importantly, this breakdown shows that the

Table 2.4: Return periods of discharge equal to Q_{100} in 1971–2000 for two emission scenarios RCP 4.5 and RCP 8.5. Predictions based on EC-EARTH-COSMO_4.8_clm17 climate model run.

Category		Median return period of discharge equal to Q_{100} in 1971–2000 (years)			
		2021–2050	2071–2100	2021–2050	2071–2100
		RCP 4.5	RCP 4.5	RCP 8.5	RCP 8.5
	Total	133	168	163	176
Regions (selected)	Central Europe	138	200	225	276
	British Isles	59	62	58	42
	Southern Europe	142	311	209	492
	Western Europe	116	163	174	269
	Iberian Peninsula	181	177	215	206
	Danube basin	173	234	190	207
	North-east Europe	99	117	87	64
	Scandinavia	121	110	184	80
	South-east Europe	137	135	111	149
Catchment area	> 100 000 km ²	195	500	685	337
	10 000–100 000 km ²	168	205	269	227
	1000–10 000 km ²	133	156	173	162
	100–1000 km ²	128	163	170	159
	< 100 km ²	134	170	162	178

method is able to detect trends in discharge in both large and small rivers.

2.4. DISCUSSION

The results presented in the previous section, however encouraging on their own, have to be compared to other existing studies. Such analysis is presented in section 2.4.1. Section 2.4.2 presents a discussion of the limitations of the method and the uncertainties in the model's setup and results. Finally, in section 2.4.3, ongoing and planned developments of the BN are presented.

2.4.1. COMPARISON WITH OTHER MODELS

The accuracy of the BN model of extreme river discharges can be compared, directly or indirectly, with results of other statistical and physical models. In case of the former, a comparison with the RFA method was shown in section 2.3.1. For the latter, reported values of R^2 and I_{NSE} from several studies were obtained.

Studies with measures of model performance comparable with this analysis were summarized in Table 2.5. All of the publications were based on the LISFLOOD model forced by a large variety of climate models. The validation of those hydrological models was mainly based on Global Runoff Data Centre discharge data, similarly to this study. The correlation between observed and simulated mean annual maxima of daily discharges (Q_{MAMX}), measured by R^2 , was between 0.86 and 0.94. The corresponding value in this study is within this range. Only one other study [105] reported R^2 for discharge with different return periods (Q_{20} , Q_{50} and Q_{100}). When compared with the results using the BN model, the results are slightly higher. It should be noted that in the aforemen-

Table 2.5: Reported validation results for extreme discharge simulations for Europe.

Study	Description	Variable	Measure		
			R^2	NSE	
This study	Bayesian network model, 1125 stations	Q_{MAMX}	0.92	0.92	
		Q_{100}	0.89	0.80	
Dankers and Feyen (2008) [105]	LISFLOOD model, 2 different climate model resolutions, 1961–90, 209 stations, Gumbel or GEV distribution	Q_{MAMX}	0.90–0.91	–	
		Q_{100}	0.80–0.87	–	
		Q_{50}	0.84–0.88	–	
Dankers and Feyen (2009) [172]	LISFLOOD model, 8 different runs, 1961–90, 209 stations	Q_{20}	0.86–0.88	–	
		Q_{MAMX}	0.86–0.93	–	
Rojas et al. (2011) [143]	LISFLOOD, 1961–90, 554 stations	No bias correction of climate data	Q_{MAMX}	0.87	–1.89
		With bias correction	Q_{MAMX}	0.92	0.89
Rojas et al. (2012) [117]	LISFLOOD model, 12 bias-corrected runs, 1961–90, 554 stations	Q_{MAMX}	0.90–0.94	0.88–0.93	

tioned analysis, using Gumbel distribution (like in this study) yielded better correlation than GEV distribution. Only two studies reported I_{NSE} values. Most interestingly, Rojas *et al.* [143] show that the performance of the hydrological model changed significantly depending on how climate data were treated. The authors noted large biases in modelled precipitation data, and made a correction based on observational datasets. This modification of climate data output slightly improved the correlation, but most importantly the I_{NSE} went from a negative value, indicating poor performance, to a value close to perfect fit with a 1 : 1 line. In this study, no modifications to climate data were made and yet I_{NSE} values for the BN model are in the range of a physical model forced by bias-corrected climate data. Of course, the reported validation results are not perfectly comparable with this analysis, since the described studies focussed on relatively large rivers (those more than ca. 1000 km² catchment area) and used ENSEMBLES regional climate simulations, which are several years older than the CORDEX simulations employed herein. Additionally, R^2 and I_{NSE} are not the only measures available. Dankers and Feyen [105] report that the error in simulating Q_{MAMX} was bigger than 50 % in 24–25 % of stations and more than 100 % in 6–8 %. In this study, for comparable river size, i.e. with extreme discharge of ca. 100 m³/s and more, those values are 34 and 11 %. Still, overall the performance of the BN can be described as similar to the LISFLOOD model in estimating annual extremes.

2.4.2. LIMITATIONS AND UNCERTAINTIES

The BN model, despite its overall high performance, has lower accuracy over certain regions. Some of the uncertainties and limitations of the model are immanent properties of large-scale hydrological simulations, while others are specific to how the method was conceived and what assumptions and data were included. One of the foremost aspects belonging to the first category is that the method assumes natural flow in the catchment. Hydraulic structures, such as large dams, can have profound influence on extreme discharges, as many were developed as a flood-reducing measure. As mentioned in the results section, flows in Spanish rivers were generally overestimated and reservoirs may

provide a likely explanation. Continental- or global-scale models routinely omit this aspect, as there is not enough information available to incorporate the existence of reservoirs or their operation. The BN model includes reservoirs only indirectly; they count as lakes and contribute to the percentage of the catchment covered by water bodies and have a negative influence of extreme discharge. In total, 326 large dams are within the catchments of the stations used in this study, according to the GRanD database [69]. Additionally, the conditions in the catchment may change over the timespan of the analysis of discharge data (1950–2005), due to reservoir construction or river regulation, or simply because of land-use developments. Currently a single snapshot of European land cover is used (from around the year 2000), but the area covered by lakes, marshes and particularly artificial surfaces is dynamic. There was very little difference in performance between the various time periods, but this aspect could be relevant locally.

The configuration of the BN presented here was the best one found in this analysis, but may not be the only solution possible, or the best one there could be. The setup of the model was slightly different in Paprotny and Morales Nápoles [131], as unconsolidated deposits (calculated as a fraction of all soil types in a catchment) were used instead of the runoff coefficient. It can be noticed that despite several soil datasets being mentioned in the methodology (section 2.2.3), none made the final configuration of the model. Low resolution and limited thematic accuracy of global soil data are likely the cause. Several other variables describing terrain, climate or land cover mentioned in section 2.2.3 were not included, as adding them did not improve the model. However, one alternative configuration worth mentioning is a BN incorporating terrain classification based on height above nearest drainage. Replacing lake and marsh cover with “wetlands” and “hillslopes” identified in the DEM (see Gao *et al.* [149]) caused only a fractional drop in performance. Given that land-cover data for Europe have very high resolution and good accuracy, this approach may give better results in areas with less satisfactory data such as the developing countries.

Some issues are related to the datasets used. Discharge data are daily values, rather than absolute peak flows, as that variable was the only one available from the main source of information, i.e. the Global Runoff Data Centre. Yet, Polish data were only available as sub-daily maxima, which did not affect the accuracy for Poland or Europe much, but is nonetheless a slight inconsistency. More crucially, daily discharge is not adequate to model flash floods, floods of short duration or floods in small catchments. Flash floods can occur in matter of minutes and outside of river beds. Also, the model utilizes daily precipitation and snowmelt, which also may not be accurate for large catchments, where the biggest floods are caused by rainfalls lasting many days. Potential incorporation of different timespans of flood-inducing meteorological events is yet to be analysed. In some regions the amount of river-gauge station data was very limited, mainly in south-eastern Europe, while in others (northern and western Europe) it was abundant, making the sample less representative. The river-gauge observations might still contain errors, even though they were quality-checked by the providers; they could also be systematically inaccurate due to, for example, outdated rating curves.

Further concerns are related to the river and catchment dataset CCM2. It has lower accuracy in areas with low relief energy, otherwise known as plains. Slight inaccuracies in the DEM result in improper delimitation of catchments in such regions. Large numbers

of lakes in post-glacial parts of Europe can also result in sometimes substantial errors. For instance, the I_{NSE} value for Q_{MAMX} for mountainous Norway is 0.90, while for Sweden, with its lake-filled landscape, it drops to 0.71. River-gauge stations, for which there was a significant difference between catchment area in CCM2 and the corresponding value in the stations' metadata, were removed from the sample. The improperly divided basins still exist in my final database of simulated extreme discharges, though. This also involves omission of most artificial channels and all cases of bifurcation, river deltas included.

Climate data from CORDEX have the highest resolution available, yet biases in representing rainfall, snowmelt and runoff could influence the results. As addressed in section 2.4.1, bias-correction of precipitation significantly improved performance of the LISFLOOD hydrological model, leaving room for further enhancements of the method. Another issue is related to climate-change scenarios used to construct the database of discharges. The difference between RCP 4.5 and RCP 8.5 scenarios is sometimes very large, as witnessed in Fig. 2.7. This alone illustrates major uncertainty related to future projections of climate. For the historical period, the use of an alternative CORDEX model and a climate reanalysis has shown (Appendix B) that the BN model's performance depends on the climate model used, yet it is still considerably better than the RFA.

Finally, the underlying dependence structure requires further investigation since certain bivariate distributions of variables indicate that a non-Gaussian copula could be a better model (see Appendix A for details). Other copulas could potentially be used since, for some distributions, tail dependence and other asymmetries may be present, even though the normal copula works well most of the time. Skewness, for example, may be modelled by copulas based on mixture distributions. This would correspond to copulas with more than two parameters [162].

2.4.3. APPLICATIONS AND FURTHER DEVELOPMENTS

The method was originally conceived to provide extreme discharge estimates that could be used for pan-European hazard mapping. As shown in the previous sections, the BN provides similar results when compared to existing hydrological models, yet it is much faster. For hydrodynamic modelling of water levels (chapter 3), catchments with area greater than 100 km² were selected, both to further reduce calculation time and due to limited applicability of the BN model to very small catchments. The calculation of annual maximum discharge for 151 years, including 95 years in two climate-change scenarios, in a domain of almost 156 000 river sections above the threshold and obtaining return periods of flood events, takes less than a day on a desktop PC. The exact value depends on the number of samples used when conditionalizing the BN and the number of samples used to quantify the BN. Nevertheless, the method can reduce time needed to perform a flood-hazard analysis, both continental-scale and local, as long as annual extremes are relevant for a particular study.

The results of this chapter – extreme discharges with certain return periods under present and future climate for all river sections in the domain – are publicly available online [173]. The dataset was formatted in GIS in such a manner that it can be easily combined with the CCM2 river and catchment database. The files include a total of 10 different return periods of discharges (2–1000 years) and 5 scenarios, the same as de-

scribed in section 2.3.2. Additionally, for each future scenario, change in the return period of discharge compared to 1971–2000 was calculated and included in dataset. Flood-hazard maps that utilized those results are the topic of chapter 3). It should be noted, however, that all the databases were published with the intention of analysing them on a European scale, and users should be careful applying them on a local scale, especially for small and medium catchments (with an area of less than 500 km²).

Thus far, the model's domain has been limited to Europe, but investigation is also ongoing into applying the method to other regions, globally. Currently, data from the United States and Mexico are being analysed. There is a very large number of river-gauge observations available for the contiguous US, while for its southern neighbour the number and quality of historical records is limited. These case studies provide interesting challenges when compared to Europe. Mexico lays mostly within tropical and arid climate zones, which is in stark contrast to Europe. The United States is geographically diversified and its biggest river system – the Mississippi–Missouri basin – is almost four times larger than the Danube basin. For these countries, global spatial datasets will be used which have a lower resolution than those applied in this study. It is possible, for instance, to quantify the BN model with those datasets and analyse its performance relative to the European quantification presented in this chapter, as well as to combine those data. In this way, the model's configuration with seven variables can be challenged, as the risk is that the method is overfitting the data from Europe. But again, this could only be definitely resolved by testing the model in other geographical areas of the world. As a first check, Couasnon [174] applied the model for the contiguous United States, indicating that the European quantification performed generally well, though much less accuracy was observed for arid and hurricane-influenced parts of the country than in those with temperate climate. Quantification based on US or combined (US–Europe) data performed less well, though for any variant the results were better than when using RFA, which was originally validated for that area by Smith *et al.* [123]. Finally, the model could be potentially evaluated not only using all variables, but conditionalized only on some of them, as observations for all variables might not be available in a given location.

2.5. CONCLUSIONS

This chapter presented a first attempt to model extreme river discharges in Europe using BNs. The method revisits the old concept of estimating discharges using only geographical properties of catchments, but employing an entirely new approach. Instead of a usual regression analysis, the (conditional) correlations between different variables describing the catchments were determined with copulas and a non-parametric BN. It was shown that the model has comparable accuracy to other large-scale hydrological models in simulating mean annual maxima and return periods of daily discharges and better performance than a RFA. The data necessary to apply the method can be obtained from pan-European (or global) databases for any location in the continent (or other locations where global data are available). In this sense, the method can be used to create basic flood scenarios at any ungauged location where data for these variables are available. For that reason it was used to provide estimates of extreme river discharges for both present and future climate in all rivers in a domain covering most of the continent. However, the accuracy at different ungauged locations varies to some degree. The best performance

was found in Scandinavia, western Europe and the Danube basin, while the lowest was observed in southern Europe, especially in the Iberian Peninsula. Trends in discharges were found to be very diversified, while the database itself will be applied to delimiting flood-hazard zones in a separate study. Further research regarding discharge estimates with the BN model is recommended, especially for future climate scenarios.

There are several advantages of a BN approach. It has low computational expense, the method is flexible as its configuration could be easily modified, and the model can be used even if not all variables for a given location are available. At the same time it allows for sensitivity analysis of different variables on extreme discharges, as well as easy incorporation of changes in climate or land use over time. It relies purely on the statistical distributions and statistical dependence of catchment descriptors, without any empirical modifiers or clustering typical for other statistical methods. The model also has a graphical nature, which makes its formulation explicit. The aim was to make the method universal and, even though so far it was only comprehensively tested for Europe, its overall performance is encouraging. The accuracy of the model changes relatively little between regions and time periods, as well as when a split-sample test is applied. The disadvantages are mostly typical for other large-scale models, such as assumption of natural flow conditions in the rivers and lower performance in smaller catchments. Validation has shown that for catchments smaller than 500 km², and especially than 100 km², performance is significantly lower than for larger ones due to increasing influence of local factors. The method was also crafted only for annual maxima of discharges, with the purpose of accurately estimating return periods rather than discharges in a particular year. But again, this is the most relevant parameter in flood-hazard analysis.



Previous page: A dike along river Lek, a branch of the Rhine, in Kinderdijk, South Holland. Flood risk in this area is among the highest in the Netherlands.

3

RIVER FLOOD HAZARD

3.1. INTRODUCTION

RIVER floods are one of the most costly natural hazards in Europe. To identify the location and extent of flood risk, flood hazards have been mapped at the local and national scale. The maps provide high-resolution information for flood risk management; however they seldom include projected flooding under the influence of climate and socio-economic change. The EU Floods Directive requires revisions of flood maps every six years [8]. Yet, costs of detailed studies are high. For example, in England (2005–2013) the cost amounted to £ 7 million (approx. € 10 million), not including the necessary surveys and data collection, which amounted to more than £ 20 million [176]. The scope and extent of the studies vary across Europe, as does the level of dissemination, and few countries make the geospatial data underlying the flood maps easily available. Due to methodological differences, the comparability of the maps is limited and, consequently, the possibility of aggregating them and drawing Europe-wide conclusions is also hampered. Outside Europe, local flood maps are often not present at all.

To produce spatially consistent maps over large areas, several studies on European and global river flood hazard studies have been commissioned. In Europe a series of studies was recently made [106, 118, 177, 178] using the Lisflood model [179] to derive 100 m resolution maps for the continent. The same model has also been used in the European Flood Awareness System, or EFAS [110], as well as its global extension, Global Flood Awareness System GloFAS [180]. On a global scale, recent river floods studies include GLOFRIS [119, 120], SSBN [124] and analyses based on CaMa-Flood model [167, 181]. The resolution of the resulting maps ranges from 3 to 30 arcsec¹. Methodologies employed in the studies vary, but most start with coarsely gridded simulation of river flows based on meteorological and land surface data. Flood volumes calculated at 0.25–0.5° resolution² are typically downscaled and redistributed over finer grid cells to generate flood extents. In studies based on Lisflood model, a two-dimensional (2-

This chapter has been published in *Natural Hazards and Earth System Sciences* **17**, 1267–1283 (2017) [175].

¹Approximately 0.25–0.7 ha to 25–70 ha grid cells over Europe.

²Approximately 200–2500 km² grid cells over Europe.

D) hydrodynamic simulation was performed. However, validation of the models' accuracy has been limited over Europe. Few studies (e.g. Alfieri *et al.* [118], Sampson *et al.* [124], Winsemius *et al.* [182]) directly compare their estimated flood zones with local high-resolution studies. The practical use of the maps is also limited by rather small availability of the underlying data, which are mostly available as online visualizations or through direct contact with the authors. Additionally, the common assumption of the global maps is that there are no flood defences in place, thus constituting a worst-case scenario [183, 184]. On the other hand, an advantage of these models is that most of them do – or can – incorporate climate change and socio-economic developments needed to analyse changes in flood frequency over time.

However, calculating flood hazard for the whole continent or the globe is computationally demanding. Alfieri *et al.* [118] mentions using a 60-processor cluster to perform a 2-D simulation of flood zones at 100 m resolution for one scenario only. Sampson *et al.* [124] indicated that a similar calculation (3 arcsec grid, 2-D model) would take 3 months on a single processor core for an average $10^\circ \times 10^\circ$ grid box, which is roughly the geographical extent of metropolitan France. Using a 200-core cluster, the time is reduced to less than a day. Still, the question remains as to whether using complex models is necessary given the quality and resolution of the input data. Bates and De Roo [94] compared output from three different model types with extents of an actual flood for a case study in the United Kingdom. They found that at 100 m resolution a 2-D dynamic model performed almost identically to a one-dimensional (1-D) steady state and improved estimates only slightly when compared to floodplains generated by extrapolating water levels from observations over the digital elevation model (known as a planar approach). In another case study in Germany, Apel *et al.* [91] found only a small influence of model choice (water level interpolation, 1-D/2-D model, 2-D model) on the results of a flood risk analysis. Sampson *et al.* [124] replaced hydrological modelling of river discharges with a statistical method, known as the regional frequency analysis (RFA). Applying the same hydraulic model as in Alfieri *et al.* [118] to calculate flood extents, the researchers achieved a better fit to high-resolution flood maps of Thames and Severn river basins than the earlier study. A similar comparison for the two areas modelled using four global flood models was presented by Dottori *et al.* [180]. The results are not conclusive as to which modelling approach gives the best results.

In light of the above, it is not surprising that simpler approaches are still used for flood research. For the CFFlood data set [185], for instance, river flood extents were derived by using the planar approach based on water levels computed in Lisflood simulations from Feyen *et al.* [116], albeit no validation was presented for either study. As mentioned before, Sampson *et al.* [124] utilized a regional frequency analysis of river discharges that was presented by Smith *et al.* [123]. That study found that river discharges can be estimated by clustering gauge stations based on climate type, catchment area and annual rainfall. At any location, the discharge could be modelled through similarity of catchment parameters to those clusters. Similarly, in chapter 2 of this thesis a Bayesian network was employed to estimate extreme river discharges in Europe using seven geographical characteristics of catchments. The results have shown that similar accuracy to pan-European studies using hydrologic models could be achieved. Finally, for the lack of a better solution, flood defences have been omitted altogether in almost all studies.

Occasionally, an assumption that more valuable areas are better protected was used to compile databases of flood protection standards [66, 185].

The ultimate aim of the research presented in this chapter was to construct flood hazard maps for Europe under present and future climates. This chapter builds on the results of chapter 2. There it was shown how extreme river discharges can be derived for the whole continent using only a statistical model. This chapter extends this by calculating river flood extents over the same area. A relatively simple combination of one-dimensional hydraulic simulation of water levels and GIS-based planar approach is utilized to draw flood zones herein. Emphasis is placed on analysing the accuracy of the results in terms of match with local high-resolution flood maps. This is put in context of the performance of more advanced models in the same areas. Additionally, the aggregate results of the analysis are presented to show flooded areas at various return periods, the expected changes in the level of hazard due to climate change and the influence of flood defence standards on the modelling outcomes.

It should be noted that the work presented in this chapter was, just like chapter 2, a part of RAIN project's effort create pan-European meteorological and hydrological hazard maps. As a consequence, several design choices, such as the extent of the domain, source of input data or representation of the results, were made in order to synchronize the various hazard maps produced within the project [33].

3.2. MATERIALS AND METHODS

3.2.1. DOMAIN AND OVERVIEW OF THE METHODOLOGY

The analysis was performed over a domain covering most of the European continent, the same as in the previous chapter (see Fig. 2.2). In this area there are around 2 million km of rivers in more than 830 000 catchments, according to the CCM River and Catchment Database v2.1, or CCM2 [23, 137]. However, the smallest rivers are affected by flash floods and flooding cannot be represented using daily discharge extremes, as those phenomena last only a few hours or less. Therefore, a threshold of 100 km² upstream area was chosen, which reduces the domain to 155 664 river sections (19 % of the total), while retaining 26 % of river length (498 420 km). That is still more than double the 188 300 km of rivers analysed in Alfieri *et al.* [118]. Global studies mostly used higher thresholds: 5000 km² in Dottori *et al.* [180], which would have reduced the domain to 56 000 km (3 %), or Strahler number of at least 6 in Winsemius *et al.* [120], which would have had almost the same effect. The scope of the chapter covers river floods; therefore influence of tides and storm surges is not included. Also, flash floods in very small catchments (below 100 km²), which occur over a short period of time, are not covered here.

In this domain, flood extents were calculated using the procedure presented in Fig. 3.1. First, river discharges estimates from the Bayesian-network-based model (I) are collected, as described in section 3.2.2. Together with data on the river network and terrain (II), they serve as input data for a one-dimensional simulation of water levels using the SOBEK model (III). After the water levels (IV) have been calculated as per section 3.2.3, they are transferred to GIS software (V). Flood zones (VI) are then delimited utilizing the planar approach (section 3.2.4). The model in SOBEK is then adjusted (VII) based on

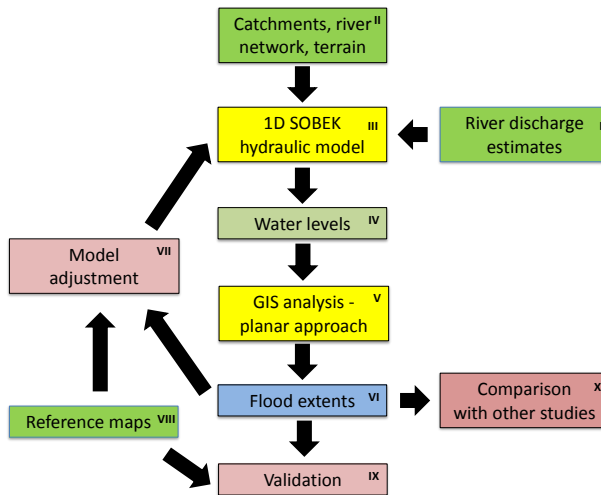


Figure 3.1: Schematic workflow of flood extent calculation. Roman numerals refer to the text.

the comparison with a set of reference maps (VIII), both local high-resolution studies and the Joint Research Centre's (JRC) map (section 3.2.5). If necessary, this step could indicate new runs of the SOBEK model that adjust the model's roughness coefficient. Afterwards, the resulting flood extents are validated (IX) with additional reference maps and contrasted with the outcomes of other studies (X), which are presented in section 3.3.1. Finally, flood extents are calculated both for the reference period (1971–2000) and climate change scenarios.

3.2.2. RIVER DISCHARGE SCENARIOS

In the approach chosen for this study, only the peak discharge value is used in the hydraulic model, rather than flood volumes or time series of discharges. This is because the steady-state simulation calculates the equilibrium water level, there time factor is excluded (see section 3.2.3). Estimates of annual maxima of river discharges were provided by the Bayesian-network-based (BN) model for three time periods 1971–2000, 2021–2050 and 2071–2100. The BN model was extensively described and validated in chapter 2. Future projections utilize the EC-EARTH and COSMO_4.8_clm17 climate model combination.

Yet, some additional work was necessary to use the extreme discharge estimates in the hydrodynamic simulation. All large-scale flood assessments face the problem of missing channel geometry data. Most of the time, the problem is solved by using the assumption that the satellite-derived digital elevation model represents the surface water at normal conditions. Thus, in this study, only the flow above the surface under normal conditions is considered. This baseline flow is therefore subtracted from the peak discharge estimates. It could be the mean annual discharge [118, 180] or the bankfull dis-

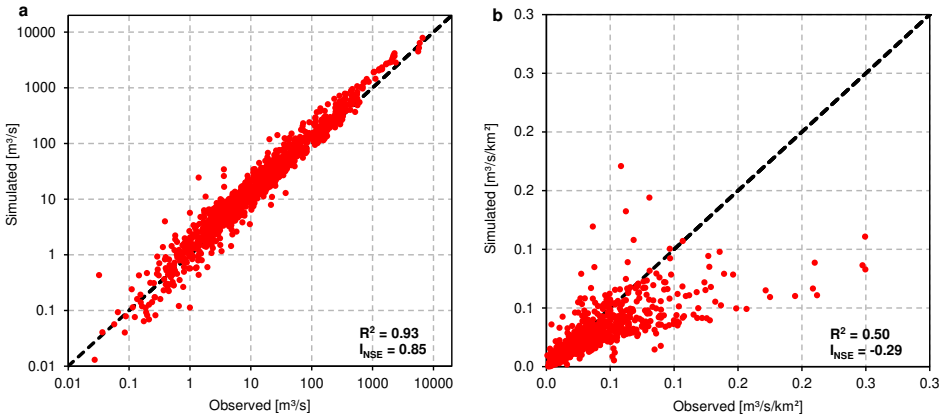


Figure 3.2: Comparison of simulated and observed mean annual river discharges using a Bayesian network: (a) actual values, (b) specific discharge (run-off divided by the respective catchment area).

charge, which is assumed to be equal to a 2-year return period [119, 124]. Here the mean-discharge approach was used, as it gave slightly better results than the other when comparing the flood extents with the reference maps. To estimate mean discharge, the BN model was modified by replacing the two variables representing the extreme meteorological events, namely annual maximum of daily precipitation combined with snowmelt and extreme run-off coefficient (annual maximum of total run-off divided by maximum of precipitation and snowmelt), with their equivalents for average climatology. Therefore, mean annual precipitation and average run-off coefficient (mean annual total run-off divided by mean annual precipitation) are considered. The BN was quantified for 1841 catchments using the same sources of data as before, and contrasted with the observations from gauge stations (Fig. 3.2). The coefficient of determination (R^2) is 0.93, which is the same value reported in Rojas *et al.* [143] for a hydrological model of Europe without bias-correction of climate data. For specific river discharge, i.e. run-off divided by the respective catchment areas, the R^2 is 0.60. The Nash-Sutcliffe efficiency (I_{NSE}), which measures the fit to a 1 : 1 line, equals 0.85. This is better than -0.39 reported in Rojas *et al.* [143], but only when the river discharge calculation was performed using climate data not corrected for bias. With bias-corrected climate data, the model by Rojas *et al.* [143] had almost perfect fit with the observations ($I_{NSE} = 0.99$).

3.2.3. RIVER WATER LEVEL MODELLING

Calculation of water levels was performed using the SOBEK v2.13 hydrodynamic model [186]. As noted in the introduction, the one-dimensional (1-D) module was chosen, as it is significantly less computationally demanding than a two-dimensional (2-D) model. One-dimensional flow is described by de Saint-Venant's continuity equation (eq. 3.1) and momentum equation (eq. 3.2), originally devised in 1871 [93]. In the case of the momentum equation, the four components describe inertia, convection, water level and bed friction, respectively [186]:

$$\frac{\partial Q}{\partial x} + \frac{\partial A_T}{\partial t} - q = 0 \quad (3.1)$$

$$\frac{\partial Q}{\partial t} + \frac{\partial}{\partial x} \left(\frac{Q^2}{A_F} \right) + g A_F \frac{\partial h}{\partial x} + \frac{g Q |Q|}{C^2 R A_F} = 0 \quad (3.2)$$

where Q – discharge (m^3/s); x – distance (m); A_T – total (flow and storage) area (m^2); t – time (s); q – lateral discharge per unit length (m^2/s); A_F – flow area (m^2); g – gravity acceleration (m/s^2); h – water level above reference level (m); C – Chézy coefficient ($\text{m}^{1/2}/\text{s}$); R – hydraulic radius (m). The momentum equation can be expanded with two more elements (wind friction and extra resistance), but neither was included in this calculation.

Also, a steady-state calculation was performed: the model iteratively performs the simulation until an equilibrium state of water level for a given discharge amount is found. This means that discharge is assumed to be non-variable in time, which reduces the computational effort compared to an unsteady calculation in which water levels are calculated for each defined time step. The hydraulic simulation was prepared utilizing six inputs: river network geometry, river cross sections, calculation points, upstream and downstream boundaries, lateral discharge and model parameters.

The geometry of the river network was obtained from the linear representation of the rivers in the CCM2 data set. As noted in section 3.2.1, river sections with catchment areas of at least 100 km^2 were selected. The network was divided into seven subsimulations based on the regional split of the original CCM2 data set (Fig. 3.3). The resolution of the geometry is about 100 m. Cross sections of the rivers were derived from the EU-DEM elevation model [144] at 100 m resolution. They vary in length depending on the characteristics of the topography (elevation differences) so that the maximum extent of the floodplain is captured. The density of the cross section along the rivers also varies. CCM2 data set splits rivers into segment whenever two rivers merge; thus, the number of cross sections per segment depends on its length. On average, the cross sections are 2.1 km apart. Due to the low resolution of the DEM two assumptions had to be made: first, that the DEM represents the average water level in the river, as discussed in the previous section, and second, that no flood defences or other discharge-control structures are present (unless dikes are large enough to be captured by the DEM). The latter assumption is featured in all continental and global studies and sometimes even in national studies, such as the flood assessment for England. The aspect of flood protection was dealt with outside the hydraulic computation itself (see section 3.2.4).

Another input element, calculation points, are locations along the digitized river network where the 1-D model computes the water levels. A 1-D model represents the rivers and channels as a linear object, therefore allowing movements of water along a single dimension. The dimensions of the river bed and floodplain are defined on the cross sections. The method utilizes de Saint-Venant's equations to calculate discharges in a longitudinal profile at calculation points. As another computational-time-conserving simplification, the lumped conveyance approach was used rather than vertically segmented approach. This means that it is assumed that velocity is uniform along the profile, as opposed to allowing different velocities in each defined vertical segment. Similarly to cross

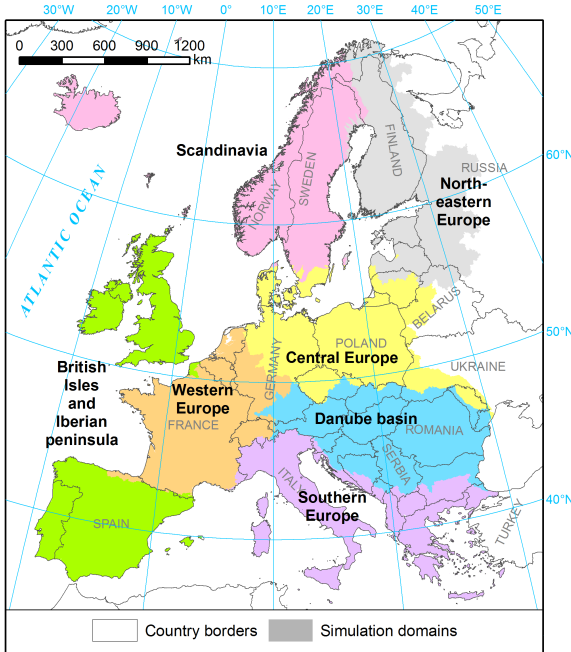


Figure 3.3: Division of the model into seven subsimulations, overlaid with political boundaries.

sections, calculation points vary in density and were defined in such a manner that they are located between the cross sections. Their total number is slightly higher so that the average distance between them is 2 km.

Computation of river flows in the network is limited by boundaries. Because a threshold of 100 km^2 catchment area is used, almost all upstream boundaries are located somewhere along the rivers and discharge values were drawn from the BN estimates for that particular location. In rare cases for which the source river section already has a catchment bigger than the threshold, the value of discharge was taken from the BN estimate made for that catchment. As noted earlier, average discharge was subtracted from the extreme discharge value for the purpose of the calculation. Meanwhile, the downstream boundaries are the locations where the rivers connect to the sea. The only exceptions are two rivers draining to lake Prespa in the southern Balkans. The boundary was defined as zero water level, representing the mean sea level unless the DEM indicated a value lower than zero. This could be due to a river moving through a depression, bias in the DEM or the difference between the mean sea level and modelled geoid underpinning the DEM.

Between the upstream and downstream boundaries the discharge increases as more catchment area contributes to the river flow; therefore more discharge had to be added along the river network. Lateral discharge nodes are used here so that water can enter the model at locations that are different to the boundaries. This is also necessary to properly represent the discharge scenarios in the network. At an intersection of two rivers, the water flow in both rivers is summed and continues downstream. However, extreme

discharges, for example with a 100-year return period, do not necessarily occur at the same moment in adjacent rivers. Hence, the 100-year discharge in the river segment below the intersection will be typically lower than the sum of the two contributing rivers. Using the lateral discharge option, the surplus water is withdrawn from the model, preserving a proper representation of flood scenarios.

The final aspect to be considered is the model parameters. The most important parameter is the roughness coefficient which was chosen through a relatively simple process. Other large-scale studies did not perform any calibration due to the lack of comparison material with sufficient spatial coverage. Here, the flood map for the historical scenario is compared, prepared as described in section 3.2.4, with the JRC map from Alfieri *et al.* [118]. Even though the JRC map was uncalibrated and by necessity only selectively validated, it used more advanced modelling steps which, most likely, resulted in higher accuracy. The roughness coefficient was assumed to be a constant value throughout each of the seven subsimulations. In five of them, the best results were achieved with a Manning's coefficient in the range of 0.13–0.15 s/m^{1/3}. Two remaining regions (both in northern Europe) had lower values, likely due to large lake cover. The methodology of map comparison is explained in section 3.2.5.

3.2.4. FLOOD EXTENT CALCULATION

Water levels obtained from the model were post-processed first by linearly interpolating them along the rivers to increase the density of estimates. For each point, located on average 250 m away from the next point, the nearest neighbourhood was defined with Thiessen polygons. For each polygon, a constant water level was assumed, therefore extrapolating the water levels over all terrain. Coastal segments were included in the nearest-neighbour calculation in order to avoid a situation where the water levels in a river are extrapolated along the coastline. Elevation from the DEM was then subtracted, per grid cell, from those water levels. From the whole area lying below water levels of the river, only those zones that were hydrologically connected with the rivers were included. In other words, high terrain completely surrounding a low-lying area prevents it from being inundated.

Similarly to the water level modelling approach, there are two main drawbacks. First is the lack of flood volume control, which has a large influence on the actual flood extent during an extreme event [91]. Second, it assumes that anything elevated above the water levels prevents inundation, which neglects the possibility of flood defence failure. However, flood defences can hardly be represented within the resolution of the model. Yet, due to high significance of this aspect, two sets of maps were produced. The first one directly uses the results of the analysis and can therefore be dubbed the “without flood protection” scenario. The second group corresponds to the maps “with flood protection”. To obtain them, flood defences were assumed to have the same protection standard as calculated by Scussolini *et al.* [66] in the FLOPROS database (Fig. D.3 in Appendix D). This data set provides protection standards defined as return periods of river floods. As a result, it was assumed that the return periods in those protection standards were equal to return periods of discharges calculated with the Bayesian-network-based model under historical climate scenario (Q_p in Fig. 3.4). If extreme discharge is higher than the protection standard ($Q_e > Q_p$), the terrain floods.

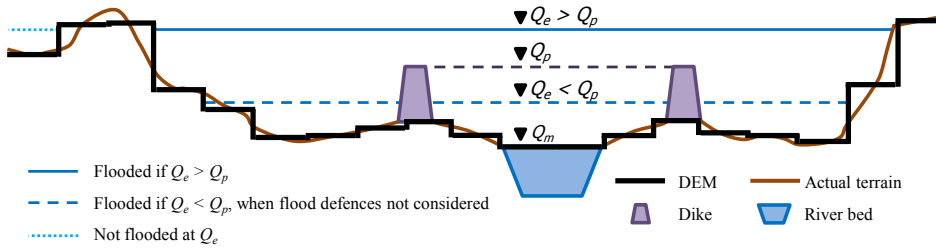


Figure 3.4: Cross section through a river valley and main model assumptions. The DEM is considered to represent terrain without flood defences and the river water surface at mean discharge (Q_m). Terrain represented in the DEM floods at extreme discharge Q_e if either no flood defences are considered or when $Q_e > Q_p$, i.e. when extreme discharge is higher than the discharge Q_p corresponding to the current level of flood protection.

Additionally, using the results of chapter 2, it was possible to calculate how the return period of discharge would change in the future for each climate scenario and river segment. This would indicate whether the current protection standard will remain sufficient under climate change. For instance, consider a dike that protects against a 200-year flood (Q_p) according to FLOPROS. It can be considered sufficient to withstand 100-year river discharge under the historical (1971–2000) scenario. If the extreme river discharges increase due to climate change, the future 100-year event will correspond to river discharge that currently has a return period of more than 100 years, say 250 years. In that case, discharges with a 250-year return period are higher than the present 200-year protection standard ($Q_e > Q_p$). Therefore, the area that is currently protected against a 100-year event will be at risk of inundation under climate change.

3.2.5. REFERENCE FLOOD MAPS

The results of this study (TUD map) were compared with six reference maps: one pan-European map and five regional flood maps. Below the main characteristics of those studies are briefly summarized (Table 3.1). The extent of local maps is presented in Fig. 3.5.

The pan-European map is available from the Joint Research Centre [187] and it is documented in Alfieri *et al.* [118]. The map was created by firstly running a rainfall-run-off simulation of river discharges based on interpolated climatological data for 1990–2010. Based on those results, 100-year discharges together with a flood wave hydrograph was estimated; this is the only scenario considered. Two-dimensional hydrodynamic model Lisflood was used to derive flood zones. The study utilized an SRTM terrain model and therefore does not include flood defences. The rainfall-run-off model was calibrated against river gauge observations, but the flood extent modelling was not calibrated. The resulting map covers 188 300 km of rivers (with a 500 km² catchment area threshold) in a domain that is slightly smaller than the one used in this chapter; it omits Cyprus, Iceland and parts of river basins that are located inside the former Soviet Union territory, except basins of the Danube, Vistula and Nemunas. The map's resolution is 100 m and it exactly matches the grid used in the TUD map.

The largest of the regional maps is the “Risk of Flooding from Rivers and Sea” map of

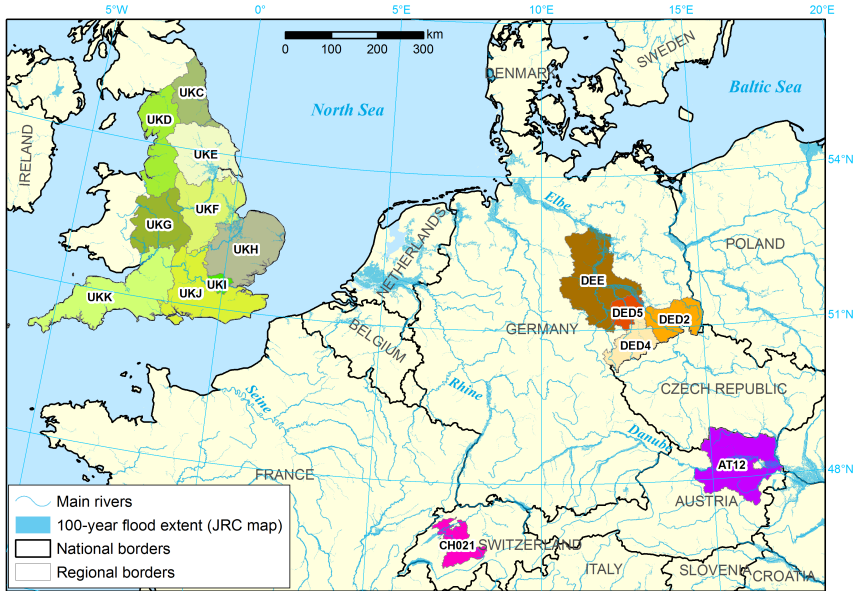


Figure 3.5: Location of the local reference maps with corresponding NUTS codes (see Table 3.2), with the JRC's flood map [118] presented in the background.

England from the Environment Agency [176]. This data set was produced during 2005–2013 utilizing local-scale modelling and takes into consideration the height, type and condition of the flood defences. The resulting maps were validated locally using experts' assessments. They are continuously updated; the version from April 2015 was used in this chapter. The data set's resolution is 50 m and for the use in this study the flood zones inundated directly from the sea were removed. The map was prepared in four thresholds defined by the flood extents corresponding to return periods: below 30, 30–100, 100–1000, above 1000 years. The largest flood zones are observed in the basins of rivers Great Ouse and Trent. Much lower hazard is indicated along the biggest rivers, Severn and Thames.

Two maps from Germany were collected, covering the federal states (*Länder*) of Saxony [188] and Saxony-Anhalt [189]. Both were prepared by the states' administration in 2015, but they followed certain national regulations. In both cases, the maps take into account the effect of flood defences and include 1-in-100-year flood scenario. The maps are provided in vector format, but their accuracy ought to be similar to a 1 : 25 000 map (> 25 m). Both regions are almost completely within the Elbe's river basin and most of the flood zone is along this river. Another map was obtained for the state of Lower Austria [96]. It is provided in vector format for three scenarios: 30-, 100- and 300-year floods. The impact of flood defence structures is included in this map which was produced in 2012 using 2-D modelling. Most of the flood zone is connected with the Danube or its tributary, Morava river.

The final map is from the Swiss canton of Bern [190] which is located within the basin

Table 3.1: Comparison of main modelling techniques and assumptions in the maps considered in this study.

Aspect	Pan-European map (TUD)	Pan-European map (JRC)	Local reference maps
River discharge model	Bayesian network for extreme river discharges (statistical model for Europe)	Rainfall-run-off model (Lisflood)	Mostly river gauge observations
Flood scenarios	Peak discharge with a return period assumed to follow Gumbel distribution	Flood hydrograph created with an empirical formula with a return period assumed to follow Gumbel distribution	Discharge with a return period; methodology varies between studies
Water level modelling	1-D hydrodynamic model (steady-state), no channel geometry	2-D hydrodynamic model (Lisflood-ACC), no channel geometry	1-D, hybrid 1-D/2-D or 2-D hydrodynamic model, depending on importance of a location and study
Calibration of river flow	Based on comparison with JRC map	None	Usually calibrated using river gauge observations
Flood zone modelling	Planar approach in GIS	2-D hydrodynamic model (Lisflood-ACC)	1-D, hybrid 1-D/2-D or 2-D hydrodynamic model, depending on importance of a location and study; occasionally GIS only for areas of low importance
Validation of results (flood extents)	With local reference maps	With local reference maps	Local knowledge and expertise
Output resolution	100 m	100 m	5–50 m
Flood defences	Included in post-processing of the maps (estimated protection standard)	Not included	Included in the river flow/flood zone modelling (dimensions, type of defences, sometimes their condition as well)
Simulation run time on a desktop computer	1 day per scenario	Computer cluster used (not feasible on a desktop computer)	From a few seconds (1-D) to a few days (2-D)

of Aare river, a tributary of the Rhine. It was prepared in 1 : 5000 scale from 1997 and 2011 multi-hazard assessments and takes into account the effect of flood defences. However, this is a flood risk map and, due to its graphical representation, only the 1-in-300-year flood scenario could be extracted from it. Additionally, this map only includes flood zones that incorporate populated areas. A map for the uninhabited zones exists in lower resolution (1 : 25 000), albeit it does not include information on return periods. Therefore, the risk map for the 300 years scenario was compared with our 1-in-300-year flood overlay, while the combination of all flood zones indicated in the two Swiss maps was compared with the 1-in-1000 year map.

The local maps required some modifications for the purpose of comparing them with the pan-European map. They were resampled to 100 m resolution and flood zones were removed if related to rivers with catchment areas below 100 km² (for comparison with the TUD map) and 500 km² (for comparison with the JRC map). The latter point was problematic in the sense that flood zones could be connected to multiple rivers, some of

which could be below or above the 100/500 km² threshold; flooding from a larger river can also spread over smaller tributaries. Therefore, as in Alfieri *et al.* [118], a 1.5 km buffer around the rivers bigger than the threshold was used for selecting flood zones from the full map.

The pan-European map was evaluated with two measures, the same as used by Bates and De Roo [94] and several later studies. Test for correctness (or hit rate) indicates what percentage of the reference map is recreated in the pan-European map (eq. 3.3). As this test does not penalize overestimation, the test for fit (or critical success index) is applied (eq. 3.4). They are calculated as follows:

$$I_{\text{cor}} = \frac{A_{\text{EM}} \cap A_{\text{RM}}}{A_{\text{RM}}} \times 100 \quad (3.3)$$

$$I_{\text{fit}} = \frac{A_{\text{EM}} \cap A_{\text{RM}}}{A_{\text{EM}} \cup A_{\text{RM}}} \times 100 \quad (3.4)$$

where A_{EM} is the area indicated as flooded in the TUD pan-European map and A_{RM} is the area indicated as flooded in the reference map. The TUD map was compared using the 100 km² threshold with the five local maps for all available scenarios and with the JRC map using the 500 km² threshold. Both pan-European maps were then compared with five local maps for the 100-year scenario (i.e. without the Swiss map) with a 500 km² threshold. The results for England and Saxony were split into smaller regions for a more detailed overview using the Nomenclature of Territorial Units for Statistics (NUTS) from Eurostat [191], 2013 edition. England is subdivided into nine statistical regions, while Saxony has three *Direktionsbezirke*, or districts. The comparison between the TUD and JRC map is presented for seven regions of Europe, the same as the seven subsimulations, as in Fig. 3.3.

3.3. RESULTS

3.3.1. VALIDATION OF FLOOD MAPS

The results of the comparison between the TUD map with reference maps are presented in Tables 3.2 and 3.3. Considering only flood zones connected with catchments with an area of at least 500 km², 84 % of the JRC's flood zone is also present in the TUD map (indicator I_{cor}). However, the JRC map indicates 246 000 km² at risk of flooding within the domain of the TUD map, which in turn shows almost 330 000 km² within the 100-year flood extent. The average fit (I_{fit}) is 56 %, with the lowest values observed in northern Europe, with more overlap observed in central Europe and the Danube basin.

In Table 3.3 the TUD map is compared with local reference maps in all available scenarios. A snapshot of the comparison for Trent river basin in central England is presented in Fig. 3.6. Large variability in the results is observed; most of the time 50–70 % flood zones from the detailed maps are recreated in the TUD maps. The highest value of I_{cor} (up to 80 %) was observed in Saxony-Anhalt and some parts of England, and the lowest values were in Switzerland and parts of Saxony (down to 30 %). I_{cor} decreases both in Austria and England between 30- and 100-year scenarios, but improves again for more extreme floods. I_{fit} is mostly below 30 %, but improves when moving from less

Table 3.2: Comparison of the TUD pan-European flood map (100-year return periods) with the JRC map per regions of Europe. Only for catchments $\geq 500 \text{ km}^2$.

Region	I_{cor} (%)	I_{fit} (%)
Full domain	80.2	51.1
Central Europe	81.2	57.7
British Isles and Iberian peninsula	76.7	43.5
Southern Europe	80.1	48.2
Western Europe	75.7	50.1
Danube basin	86.3	54.0
North-eastern Europe	69.1	41.7
Scandinavia	63.2	42.3

Table 3.3: Comparison of the TUD pan-European flood map with reference flood maps per NUTS region.

NUTS	Region	Flood map test measures (%) by return period							
		30 years		100 years		300 years		1000 years	
		I_{cor}	I_{fit}	I_{cor}	I_{fit}	I_{cor}	I_{fit}	I_{cor}	I_{fit}
UKC	North-east	57.9	21.9	59.7	33.7			60.1	40.0
UKD	North-west	48.5	23.0	47.7	26.7			51.8	39.3
UKE	Yorkshire and the Humber	73.1	20.5	69.5	36.6			68.2	48.7
UKF	East Midlands	62.8	17.7	73.5	46.0			73.6	57.8
UKG	West Midlands	66.2	38.7	64.2	42.6			65.7	47.0
UKH	East of England	58.3	15.8	80.4	59.1			78.1	63.2
UKI	London	68.8	13.8	64.8	17.4			70.9	49.4
UKJ	South-east	64.7	36.4	63.1	42.7			60.7	48.8
UKK	South-west	62.6	41.4	61.2	46.1			58.4	47.0
UK	England	62.7	24.0	69.6	44.9			68.5	52.8
DED2	Dresden			45.3	22.5				
DED4	Chemnitz			33.7	24.0				
DED5	Leipzig			60.8	33.8				
DED	Sachsen			50.3	27.4				
DEE	Sachsen-Anhalt			67.9	23.6				
AT12	Niederösterreich	55.0	21.9	49.5	24.3	61.8	34.4		
CH021	Bern					34.9	19.1	29.2	20.7

extreme to more severe scenarios. All local maps include effects of flood defences; therefore this exact pattern would be expected: flood zones expand rapidly with the increase of the return period of flood, as a declining number of defences can withstand the rising water levels. Hence, variation of the values of I_{fit} can be mostly explained by the differences in flood protection standards. In England, flood defences are mostly expected to protect against return periods of floods of about 75–200 years [192]. Hence, the protection structures should not influence the size of the 1000-year flood zone in England. Indeed, in this scenario and region the highest I_{cor} and I_{fit} values were observed at 68 and 53 %, respectively. Results were achieved in terms of alignment with the TUD map. The average value of I_{fit} is two times higher (53 %) than in the 30-year scenario (24 %). Furthermore, the highest protection level in England is expected in London [66], which had the lowest I_{fit} in the 30- and 100-year scenarios.

In other analysed regions, the flood protection standards are mostly higher in terms

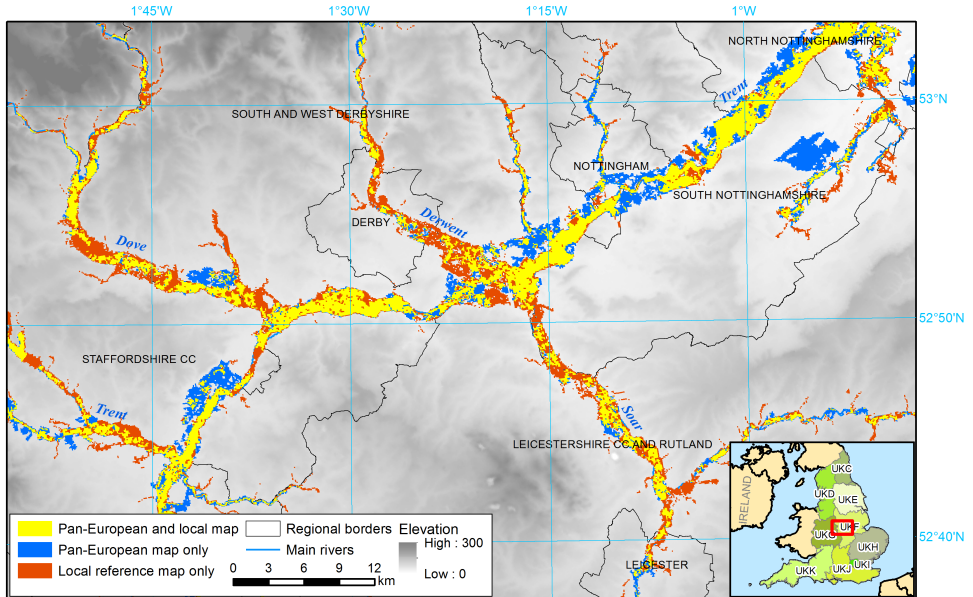


Figure 3.6: An example of the differences between the pan-European map from this study and the local reference map, in this case for the central part of England for the 100-year flood scenario [176].

of return periods than in England: 100–500 years in Germany, 100–1000 years in Austria (highest along the Danube) and 30–200 years in Switzerland [66, 193]. For the 100-year scenario, I_{fit} is only 24–27%. In Saxony, Dresden district had lower fit than the other two districts, which is consistent with the fact that the city of Dresden has an improved flood protection level of 500 years as opposed to 100 years in other areas. The test measures used also improve visibly in Austria between 100- and 300-year scenarios. On the other hand, the lowest performance of the TUD map in Switzerland can be explained with the characteristics of the flood map, rather than high protection standards. The 300-year flood layer could be extracted only for populated areas, which have much better protection than uninhabited areas. The 1000-year flood map is also incomplete, and was compiled for this comparison from flood zones with an unknown, but presumably high, return period.

Finally, both pan-European maps are compared with the local reference maps for the 100-year scenario for catchments with an area of at least 500 km² (Table 3.4). In England the performance of the TUD map was better than the JRC's map, but not in all parts of it. When comparing it with German and Austrian maps, the performance was similar or slightly lower. Summing up all flooded areas, the results show that the TUD map had higher values of both I_{COR} and I_{fit} . Yet, this results could be explained by some drawbacks of the GIS analysis. In particular, it was problematic to completely filter out from the TUD and local maps the flood zones below the threshold of 500 km² catchment area. That could have increased the overlap between TUD and local maps to a slightly higher degree than the overlap between the JRC and local maps. Also, in many areas of

Table 3.4: Comparison of the pan-European flood maps with the local reference flood maps for 100-year return period. Includes only rivers with catchment area of at least 500 km². 100-year flood zone area is for the reference maps.

NUTS NUTS	Name Name	100-year flood zone (km ²)	I_{cor} (%)		I_{fit} (%)	
			JRC	TUD	JRC	TUD
UKC	North-east	94	54.3	67.4	38.6	39.9
UKD	North-west	174	49.7	52.3	36.0	25.3
UKE	Yorkshire and the Humber	663	62.2	75.9	37.3	32.9
UKF	East Midlands	1014	54.4	77.6	42.3	37.0
UKG	West Midlands	312	73.6	74.2	55.5	45.8
UKH	East of England	1534	40.9	87.5	35.9	63.5
UKI	London	28	57.1	68.7	16.3	14.6
UKJ	South-east	489	54.2	68.0	38.8	39.4
UKK	South-west	471	38.3	71.5	33.6	44.1
UK	England	4780	50.6	77.5	38.6	43.4
DED2	Dresden	229	44.9	57.0	29.3	24.9
DED4	Chemnitz	64	49.9	49.0	30.0	30.7
DED5	Leipzig	254	70.3	67.3	41.1	35.4
DED	Sachsen	547	57.3	60.9	35.1	30.0
DEE	Sachsen-Anhalt	1035	68.5	73.4	25.2	23.3
AT12	Niederösterreich	632	54.2	59.6	23.9	26.3
	Total	6994	54.1	74.0	33.2	36.1

England better performance can be attributed to several large zones where both river and coastal floods occur, which favours overestimation of flooded area from the rivers. Lastly, English flood zones are twice as large as the remaining ones taken together. Still, the results of fitting both European maps in Saxony-Anhalt and Lower Austria are very similar. Substantial simplification of the methodology of making the European maps did not result in an equal drop in accuracy, but it was largely maintained. The computational time on a regular desktop PC was slightly less than a day per scenario.

3.3.2. PRESENT FLOOD HAZARD IN EUROPE

River flood hazard is analysed in this chapter in two variants: without flood protection or with flood protection as estimated in the FLOPROS database [66]. Full-size images of the maps were included in Appendix D. The total area identified within 1000-year flood scenario was almost 389 000 km², which is about six times more than the total for coastal flood hazard (chapter 4) if impact of flood defences is not included. In this section the outcomes of the historical scenario are briefly described (1971–2000).

The majority of the flood zones in the domain were 10-year zones, with only one-sixth belonging to other zones. More than half of the flood hazard was concentrated in only seven countries: Germany, Hungary, France, Romania, Italy, Russia (even though only a small part of this country is included in the domain) and Poland. Splitting the hazard zones by river basins, half of the endangered area is contained within only seven of them: Danube (mainly in Austria, Hungary, Serbia and Romania), Neva (Russia), Vistula (Poland), Elbe (mainly in Germany), Oder (mostly in Poland and Germany), Rhine (mainly in Germany) and Po (Italy). Twenty river basins with the highest area within

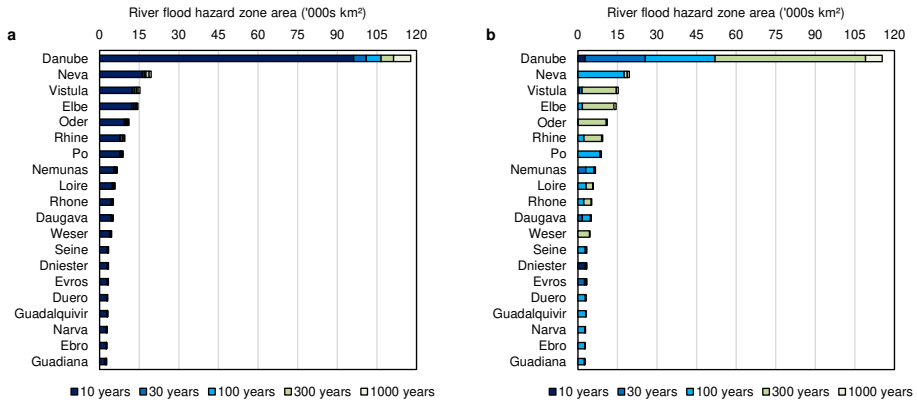


Figure 3.7: Area of flood hazard zones in 20 river basins with the largest hazard, (a) without and (b) with (estimated) flood protection. The basins listed here are highlighted in the maps in Appendix D.

flood zones are listed in Fig. 3.7. Taking into account flood defences, the estimated area of the 1000-year zone is revised downwards only slightly, to 376 000 km². A decrease in flood extent is noticeable only in the Netherlands, where the dike rings provide a high level of protection from both coastal and river floods, and Austria, where flood defences along the Danube are considered to have a high protection standard. On the other end of the scale, the 10-year flood zone is mostly constrained to the Dniester river catchment (6400 km²), while the 30-year zone is mostly present in the Balkans and former Soviet Union (basins of Danube, Nemunas, Evros and others).

The country with the largest hazard level proportional to its area is Hungary, as 37% of the country lies within the 1000-year zone. The Netherlands comes second when flood defences are not considered, with 26% of the territory in the flood zone. This value, however, drops to 1% when considering flood protection. Other countries with a high fraction of territory in the flood zone include Serbia (24%), Croatia (20%) and Slovakia (14%), all of which are located in the Danube basin. This river system does not have only the biggest basin in the domain and the largest flood extent, but also the highest proportion of flood area compared to total area (15%) among large river basins. Increased hazard is also present in the Po river basin (12%), Weser (10%) and Oder (9%). In contrast, Nordic countries have low levels of relative hazard, from 1% in Norway to 4% in Finland. Only 3% of the territory is in hazard zones in Ireland, Portugal, Spain and Switzerland, while in France, the United Kingdom and Austria the figure is 5%, in Poland 8% and in Germany 10%.

3.3.3. FUTURE FLOOD HAZARD IN EUROPE

The overall size of the river flood hazard zones in Europe increased for all four climate change scenarios considered. Yet, without considering flood defences the increases are small. By the mid-century (2021–2050), RCP 4.5 scenario adds 1.7% to the 1000-year zone, while RCP 8.5 adds 2.1% compared to 1971–2000. For 2071–2100, these figures are 4.4 and 2.5%, respectively (Fig. 3.8). This is largely a result of only a modest (on

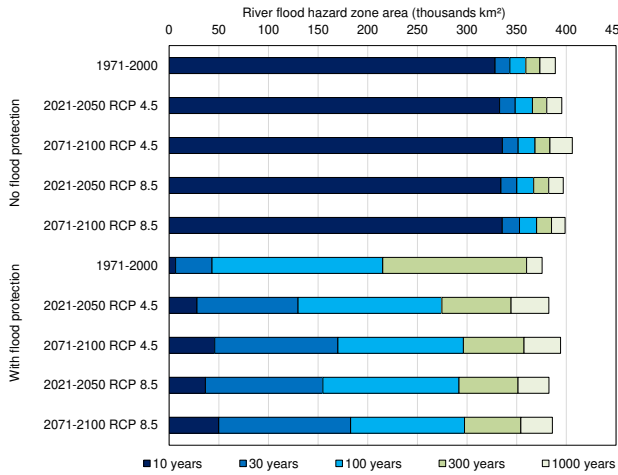


Figure 3.8: Flood hazards zone area in Europe by scenario, without and with (estimated) flood protection. Predictions based on EC-EARTH-COSMO_4.8_clm17 climate model run.

average) increase in river discharge in Europe. As a whole, this corresponds to 5–8 % depending on the scenario, according to the results in section 2.3.2. However, the significant implications of changes in discharge becomes apparent when taking into account present levels of flood protection. The 10-year zone, estimated at 6400 km² in 1971–2000, is projected to reach 28 000–50 000 km² (4–8 times more), depending on time period and emission scenario. The largest expansion in absolute terms was calculated for the 30-year zone, from 43 200 km² in the end of the 20th century to 130 000–183 000 km² (301–423 % increase). The 100-year zone is expected to be larger by 28–38 % compared to 215 000 km² in the historical scenario. Smaller changes are expected in flood hazards with a lower probability of occurrence: the 300-year zone is actually projected to decrease by 0.7–4.4 %, while the 1000-year zone could add 1.8–5 %.

Nevertheless, trends in river flood hazard will be very diversified across the European continent. Changes in flood extents presented in Fig. 3.9 were aggregated to a 50 × 50 km grid for the sake of clarity. It includes only one scenario (100-year flood), but the trends shown are also representative for other return periods. Fig. 3.10 shows the contributions of each country relative to the overall change in flood zone size. With or without flood defences, the largest increases in flood hazard area are projected in central Europe, particularly in Germany, Hungary and Poland. Trends in the Danube basins will be the main source of increase in hazard. The Elbe basin will contribute more than the Rhine, while in Poland flood zones along the Oder are projected to expand more than those along Vistula river. An increase in flood hazard is also projected in France. In the United Kingdom, increases are observed when flood defences are included, but a slight decrease is predicted without taking them into account. Decreases are mostly observed in northern Europe, particularly in Scandinavia, as a large decline of snowfall and, consequently, snowmelt is expected. To a lesser extent, a decrease of flood hazard is projected in many locations around the Mediterranean Sea, which is projected to receive less extreme rain-

fall in the future.

3.4. DISCUSSION

The results have shown that relatively simpler methods can give similar accuracy to more computationally demanding models for large-scale flood mapping. In this study, three main simplifications were applied: river discharges derived from a statistical model, river flow calculated using a one-dimensional steady-state model without channel geometry and flood zones derived in GIS based on water levels from the hydrodynamic model. The similarity in results to the more complex model used by JRC can be traced to the input data sets, which are mostly the same in various flood studies. For example, the SRTM-derived digital elevation models provides neither the river bed geometry nor the dimensions of flood protection structures. The former can only be obtained through local surveys, despite efforts to approximate river width or depth from global data [194]. Flood defences were incorporated here using nominal protection standards defined as flood return periods (from Scussolini *et al.* [66]), but this is only a rough approximation. Yet, as indicated, e.g. in Fig. 3.8, the difference between “without flood defences” and “with flood defences” scenarios is immense. Therefore, both present and future flood hazard and risk estimates need to take this aspect into account. More aspects are related to this issue, such as the influence of flood defences on river flow. Dams retain water from flood waves, while dikes constrain the river to a narrow space between them. Additionally, overtopping is just one of many dike failure mechanisms [195], while other flood control techniques exist such as bypass channels, e.g. the New Danube that protects Vienna [62]. All these analyses are currently feasible only at local or at most national scales, e.g. the recent flood risk assessment in the Netherlands [64]. At the European or global level, other techniques will have to be used, such as a formal statistical analysis of the differences between high- and low-resolution maps in order to derive indirect factors that determine the flood protection levels at given locations.

More comparison with local maps would also improve calibration of the large-scale models. So far, other studies have left the models uncalibrated, while here a step has been taken by using JRC’s – uncalibrated – flood map. Local maps were not readily available for all subsimulations, even though all EU countries do such studies. Intercomparison between the numerous global flood studies could also show which modelling approaches are most efficient. For example, Sampson *et al.* [124] achieved better results than Alfieri *et al.* [118] despite using a statistical model of river discharges as input. It was not possible, however, to obtain data from that study by the time the work described in this chapter had concluded.

Limitations of input data and models of river flow are not the only sources of uncertainty. Not all flood events are included in the study. Only rivers with catchments that have an area of at least 100 km² were included in the calculation. This omits very small rivers where dangerous flash floods can occur, especially in hilly or mountainous terrain [196]. Flash floods also appear in places where drainage is insufficient, mainly in urban areas [197]. Moreover, the estimates of extreme river discharge were based on two main factors causing flood – rainfall and snowmelt, while floods in northern Europe are also caused by ice and frazil blocking the river flow [36]. In estuaries, flood hazard is influenced by tides and storm surges, as they might occur at the same time as a river flood

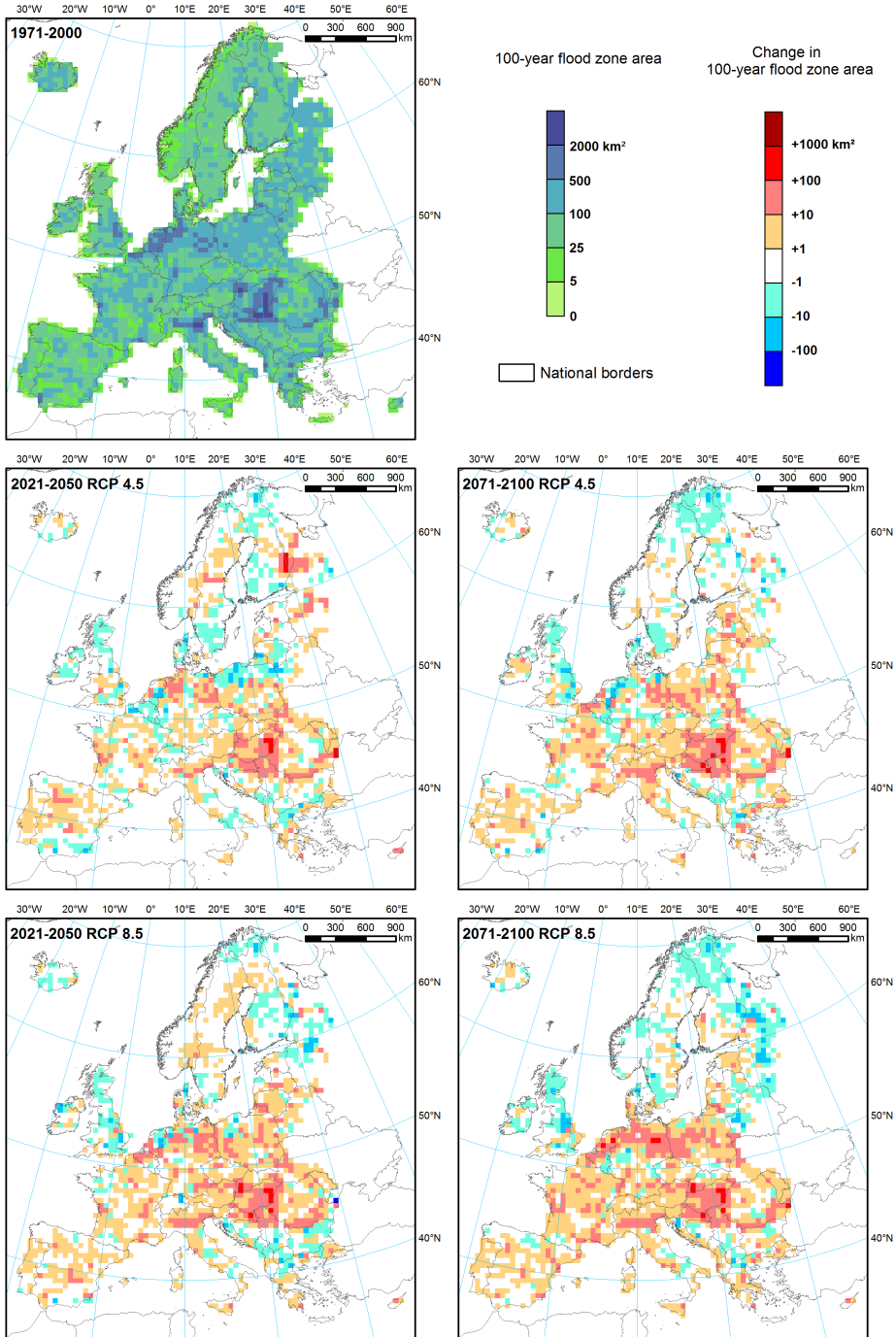


Figure 3.9: Total area of 100-year river flood hazard zones (no flood protection) aggregated to 50 × 50 km grid, and changes under climate scenarios. Predictions based on EC-EARTH-COSMO_4.8_clm17 climate model run.

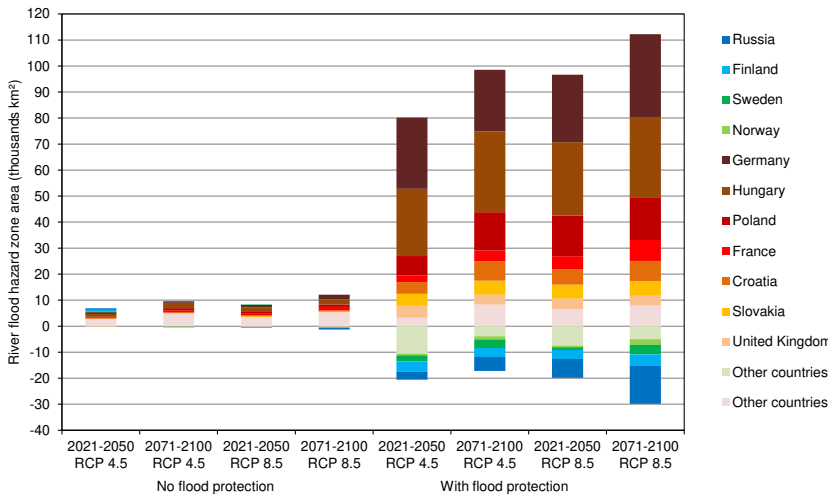


Figure 3.10: Contributions of selected countries to future changes in 100-year flood zone area in Europe by scenario, without and with (estimated) flood protection. Predictions based on EC-EARTH-COSMO_4.8_clm17 climate model run.

[198]. This aspect is the topic of chapter 5. Finally, disastrous floods could be caused by dam breaches [199].

Last, but not least, the uncertainty related to future climate projections should be mentioned. Only one climate model was used in the Bayesian network model for extreme river discharges. Also, as shown in Figs. 9–11 and the description, the difference between RCP 4.5 and RCP 8.5 scenarios is sometimes very large. The uncertainty is therefore significant and unavoidable as the differences between models and scenarios are considerable, especially concerning precipitation [142, 200]. Those aspects, however, do not affect the validation results in section 3.3.1.

3.5. CONCLUSIONS

This chapter has investigated the feasibility of creating pan-European flood maps using a simplified modelling approach. A one-dimensional steady-state hydrodynamic model of river flow was utilized to derive flood depths and flood zones were mapped in GIS. It can be concluded that this approach largely fulfilled its aims of reducing complexity while preserving an acceptable level of accuracy. First, the method has a low computational burden – performing a full simulation for Europe takes less than a day on a regular desktop PC, in contrast to months that would have been necessary if using a more advanced model. Second, the comparison with reference flood maps has shown that the method has similar accuracy to the JRC map, which was made by employing 2-D hydraulic models which are significantly more expensive computationally, but in general have shown a tendency to overestimate the size of the flood zones. Additionally, the river discharge data used in this study originated from a statistical model instead of a rainfall-

run-off model commonly used in other modelling approaches.

The results are also an indication that the resolution and completeness of input data have high importance compared to the choice of modelling approach. For instance, the flood protection standards as modelled in this research influence the size of the flood zones profoundly, both for the present and future scenarios. The assumption of perfect reliability of flood protection standards could be relaxed and further investigated in future research. Yet, the reliability of global flood defence data is rather low and considerable improvements need to be made. This aspect is where large gains in accuracy of continental or global-scale maps could be made. Then, more detailed digital elevation models are needed as well as data on river beds. Uncertainty of river discharge return periods and their future development should be further reduced by more research into statistical models.



Previous page: A storm surge hits the Polish Baltic Sea coast at the village of Łazy, during extra-tropical cyclone Xaver, December 2013.

4

STORM SURGES AND COASTAL FLOOD HAZARD

4.1. INTRODUCTION

THE main weather-related hazard in seaside areas are increases of water levels caused by windstorms, which may result in breaching of coastal defences and flooding. Though storm surges rarely cause such outcome, the consequences are often disastrous when they occur. Indeed, a list of large floods in Europe for 1950–2005 [56] includes only three coastal floods compared to 44 river and flash floods; yet, ranked by number of casualties, storm surges come first, third and sixth. The biggest was the 1953 North Sea flood, which caused over 2,000 casualties in the Netherlands and Belgium. That storm surge also resulted in 546 deaths in the United Kingdom, while the 1962 Hamburg flood killed 347 persons. The most recent large coastal flood occurred in 2010 in western France, with a death toll of 41 [203].

There is large concern that those rare events are becoming much more frequent because of the global climate change. One contributing factor would be an increase in storminess. Though no general trends have been detected in either historical data or climate projections, large regional variations are indicated [204, 205]. A crucial factor is the increase of the mean sea level (MSL), which is considered to translate directly into higher storm surge frequency [206–208]. Consequently, it may lead to a significant increase in the level of coastal flood hazard, even more than in case of river flood hazard [204, 209]. Between 1880 and 2009, global MSL increased by 21 cm [210], while IPCC projections show a further increase of 28–98 cm by 2100 [204]. However, sea level rise (SLR) is hardly uniform, according to recent satellite altimetry [211]. For instance in the North Sea the 1992–2015 trend was 1.8 mm per year, lower than the global average of 2.9 mm per year. In contrast, the trend in the Baltic Sea was 3.3 mm per year. Data from NOAA [211] indicate even negative trends for some small parts of the seas surrounding Europe.

This chapter was edited from papers published in E3S Web of Conferences 7, 02001 (2016) [201] and Journal of Flood Risk Management, e12459 (2018) [202].

Nevertheless, climate change is not the only factor influencing the level of hazard over time. One is glacial isostatic adjustment (GIA), the rebound of Earth's crust after the melting of ice sheets that covered vast areas during the last Ice Age. In Europe, its main effect is the vertical movement of the ground. In Scandinavia and in most other northernmost parts of Europe it causes an uplift, which can reach up to 1 cm per year in the northern part of the Gulf of Bothnia. For the time being, it effectively counters SLR along coasts of Sweden or Finland. More globally, ocean basins are becoming bigger due to GIA, slightly reducing sea level rise [212, 213]. Finally, there are various local factors generating vertical ground motion. More often than not, subsidence occurs, exacerbating the effects of SLR [214].

The main direct source of information on water levels during storm surges are high-frequency tide gauge measurements. Unfortunately, their availability is limited, not only because of the relative scarcity of the tide gauge network, but also due to limited dissemination of this data. Few countries consider this information as open data and make all the historical series freely available. Shortage is particularly acute when one considers that at least a 30-year series is considered necessary for calculating return periods from annual maxima.

In effect, various methods have been used in order to increase the coverage of extreme sea level estimates, so that a complete, continuous dataset along the coastline can be created. One group of approaches are statistical methods. The simplest is to make a geostatistical interpolation between tide gauges. One study [215] created maps of storm surge return periods in the Baltic Sea using this method. This basin, however, has the convenient feature of having negligible tides. Therefore, a study of the Atlantic coast of France [216] supplemented interpolation of surge levels with tidal amplitudes from a dedicated tide model. Then, there is a regional frequency analysis (RFA) method, which aims at identifying spatial patterns in the probability distribution of storm surges in nearby gauges. It was originally developed by Hosking and Wallis [217] and used in several studies, e.g. in France [218, 219] and the Netherlands [220].

Those methods, though, still require considerable amount of data from measurements. Therefore, many studies use hydrodynamic modelling instead. Here, such a model representing the basin in question is set up and then forced by wind and air pressure from observations or climate models. In this way, the water levels can be derived for the entire domain, including the influence of coastal features, bathymetry, climate or tides. Several studies of different parts of Europe have been performed. They used various techniques and model set-ups, with focus put on different aspects. For instance, one study made a general hindcast of water levels in the western coasts of Europe [221], while another concentrated on future climate change impacts on storm surges in the Netherlands [205]. Meanwhile, a different study [222] developed estimates of extreme sea levels along Great Britain's coast by correcting the output from the hydrodynamic model using a statistical analysis at tide gauges. Similarly, another group of studies [223] combined numerical models with RFA for the North Sea coast of Germany. Notwithstanding the method used, only a handful of studies analysed the subject on a European or global scale. Also, though some studies also computed coastal flood extents, none has so far used local flood hazard maps for validation.

The first attempt of creating an overarching collection on coastal hazard information

was made by Vafeidis *et al.* [108], who devised the Dynamic Interactive Vulnerability Assessment (DIVA) database. However, though it contains extreme sea levels with given return periods for 12,000 coastal segments (70 km each) around the world, the estimates were not derived through hydrodynamic modelling [224]. Additionally, the only validation of flood maps was done by comparing the number of people at risk of 1-in-1000-year flood with some national studies [225]. DIVA database has been more recently supplemented by the Coastal Fluvial Flood (CFFlood) database [185] for European countries. Yet, no validation was presented apart from stating that the flood zones delimited in that study were consistent with a national floodplain map for the United Kingdom. Only with the work of Muis *et al.* [226, 227] has a global dataset of storm surges, extreme sea levels and coastal floods become available (it will be referred to hereafter as the “GTSR model”). The study applied a Delft3D model forced by ERA-Interim climate reanalysis, covering years 1979–2014, but without future projections. Though it showed good accuracy for modelling the surge, the focus was put on the quality of sub-daily/daily predictions and the calibration was performed on the deep ocean. Only relatively limited validation for the European coast was presented. Also, no validation of the global coastal flood map was presented, though influence of the digital elevation model (DEM)’s vertical datum on the results was analysed [228].

On the European scale, Vousdoukas *et al.* [109, 229, 230] provided storm surge and extreme sea levels for both present and future climate, as well as coastal flood extent estimates for the present climate (it will be referred to hereafter as the “JRC model”). In Vousdoukas *et al.* [229], future projections of extreme sea levels are provided, taking into consideration variations in storm surge and wave regime, driven by general circulation models (GCMs), together with sea level rise. In Vousdoukas *et al.* [109] a comparative analysis of four methodologies of calculating coastal flood extents was presented, together with a juxtaposition of the pan-European maps with the actual inundation limit observed during Xynthia storm in France in 2010. Still, climate change projections were not yet published for coastal floods; even though a multi-hazard assessment for Europe by the JRC [209] did include future projections of coastal floods, they were made only by taking into account global sea level rise.

In light of the above, there is a need for a more detailed pan-European analysis of extreme sea levels, based on regional climate models. Also, a more systematic analysis of the accuracy of large-scale flood maps would be desirable, in context of their potential applications to flood risk management, as well as climate change mitigation and adaptation. Therefore, the objectives of this chapter were to (1) create a database of extreme sea levels (ESLs) in Europe under present and future climate based on a regional climate model, (2) create coastal flood hazard maps based on those ESLs and (3) compare the results of this study (they will be referred to hereafter as the “TUD model”) with JRC and GTSR models, as well as tide gauges measurements and local coastal flood maps.

It should be noted that the work presented in this chapter was, just like chapters 2 and 3, a part of RAIN project’s effort create pan-European meteorological and hydrological hazard maps. Consequently, this analysis is aligned in its design to the work on river flood hazard.

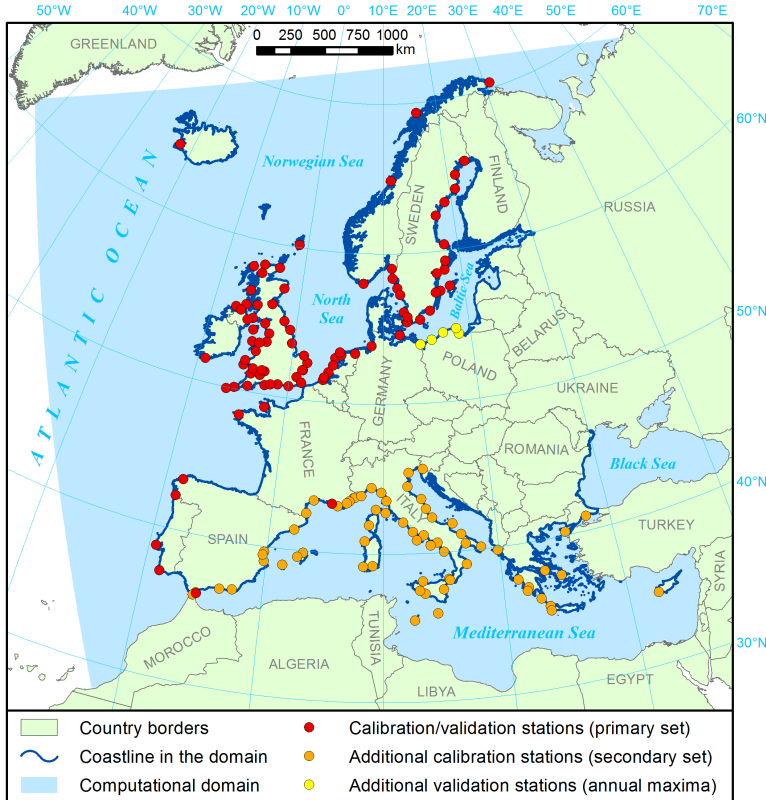


Figure 4.1: The domain used in Delft3D simulation and location of tide gauge stations used for calibration and validation.

4.2. MATERIALS AND METHODS

4.2.1. DOMAIN AND OVERVIEW OF THE METHODOLOGY

The domain in this chapter consists of two parts (Fig. 4.1). The computation of storm surge heights was completed in a regular gridded domain covering the seas surrounding Europe and a portion of the north-western Atlantic Ocean. The remaining analysis was done for sections of the coast that correspond to river basins used in chapters 2 and 3. Only very small sections along the White Sea, and Jan Mayen island were excluded.

The contents of this chapter is presented schematically in Fig. 4.2. Firstly, the meteorological forcing and bathymetry data (I) are used to set-up a Delft3D simulation (II) in section 4.2.2. The resulting modelled storm surge heights (III), i.e. extreme sea levels without the tidal component, are then compared with tide gauge observations (IV) to calibrate the model (V). Other components of past and future extreme sea levels, such as tides, GIA, SLR and baseline MSL (VI) are added from external datasets (VII) in section 4.2.3. A static inundation approach (VIII) is used to compute coastal flood extents (IX) in section 4.2.4. High-resolution local reference maps (X) are then utilized to validate the

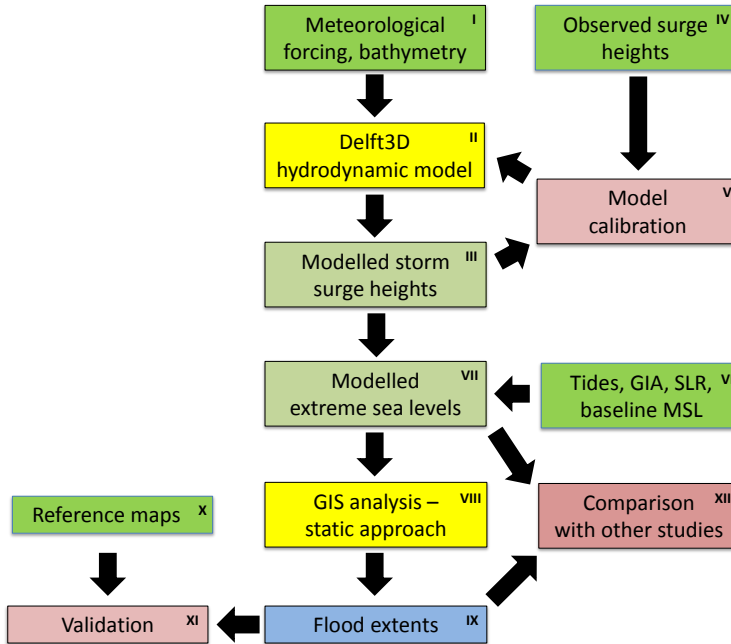


Figure 4.2: Schematic workflow of the analysis of coastal flood hazard. Roman numerals refer to the text.

European flood maps from this analysis and the other two models (XI), as described in section 4.2.5. Comparison with other studies was also done for storm surge heights (XII).

4.2.2. STORM SURGE HEIGHTS

METEOROLOGICAL FORCING

Two datasets were used to compute storm surge heights: ERA-Interim climate reanalysis and EURO-CORDEX climate simulations for past and future climate. ERA-Interim is a continuously-updated global atmospheric reanalysis [139] a spatial resolution of 0.75° and temporal resolution of 3 hours. This study applied it for the purpose of calibrating the hydrodynamic model. Since ERA-Interim uses data assimilation, it can provide sufficiently accurate information on temporal development of air pressure and wind speeds/direction, hence allowing for a direct comparison of modelled water levels with tide gauge observations. Meteorological data (u and v component of wind speed, and sea level air pressure) covering years 1979–2014 were used.

The other dataset applied here was generated within the EURO-CORDEX activities at the Rossby Centre of the Swedish Meteorological and Hydrological Institute (SMHI). It uses ICHEC-EC-EARTH general circulation model with SMHI-RCA4 regional circulation model [231], realization t12i1p1. This dataset includes 3-hour series of air pressure and 6-hour series of wind speed (u and v component). The subdaily resolution of the dataset, in contrast to daily resolution of other EURO-CORDEX simulations, was

achieved through SMHI's modelling work specifically for the purposes of RAIN project, including this study. The spatial resolution of the dataset is 0.11° (about 12.5 km). The model includes a historical run (1970–2005) and two climate projections (2006–2100) using RCP 4.5 and RCP 8.5 scenarios [165].

DELFT3D MODEL SET-UP

The study uses Delft3D model by Deltares [232], which was also employed in the JRC and GTSR studies. The model utilizes depth-averaged shallow water equations and allows to simulate both tides and surges. In this study, however, only the latter was calculated for a number of reasons. First of all, the model was intended to accurately represent the annual maxima of storm surges, so that return periods could be calculated. That requires long simulation periods and increased time steps, opposite to what is necessary for proper representation of tides operating in a predominantly semidiurnal cycle. Also, this study was mostly interested in the weather-related phenomena. There is, naturally, an interaction between surges and tides, though the calibration of the model was done on skew surge from tide gauge measurements, which includes this interaction. Furthermore, the statistical dependency of tides and surges for available stations was analysed, leading to the conclusion that the two factors can be safely assumed independent (see section 4.2.3).

The model used a structured grid of the same shape and resolution as the 0.11° EURO-CORDEX domain, with only slightly trimmed extent. That way, only interpolation of the ERA-Interim data was needed while maintaining reasonable resolution. For comparison, the GTSR study used an unstructured grid with a resolution of $0.05\text{--}0.5^\circ$, while the JRC analysis employed a regular 0.2° grid. Bathymetry was created from a digital terrain model covering all basins around Europe [233], originally at 0.125 arc minute resolution. The bathymetry was adjusted in several narrow straits in order to properly represent the flow of water through those passages.

It should be noted that the modelled surge heights were calculated as relative to local mean sea level. Thus, the boundary conditions and initial water level was set to zero. Meanwhile, the time step was set to 30 minutes to keep calculation time in check. For similar reasons the temporal resolution of the input data was chosen as 6 hours, despite air pressure data being available at 3-hour resolution. As a result, the output was also saved at 6-hour intervals.

Calibration was primarily done by adjusting two parameters. One is the wind drag coefficient, commonly known as Charnock [234]. Here, the coefficient increases with wind speed from 0.0013 to 0.007, slightly different than the default value. The other, more sensitive parameter is the bed roughness. Its formulation by Chézy is used here and was defined locally during calibration. International Hydrographic Organization's (IHO) maritime divisions as presented by Fourcy and Lorvelec [235] were used as a reference for that purpose. Particularly large influence of this parameter was recorded in the Danish and Turkish straits as well as Adriatic and North seas. On the other hand, most of the Mediterranean and Atlantic coasts were not too sensitive to it. The calibration runs encompassed years 1997–2000 and 2011–2014. Then, the model was validated with a full 1979–2014 run using ERA-Interim, and finally for 1970–2005 utilizing EURO-CORDEX data.

TIDE GAUGE MEASUREMENTS AND VALIDATION OF RESULTS

For comparison between modelled and observed water levels, data from available tide gauges were collected. The dataset compiled here consists of three parts. The primary set of research-quality high-frequency observations consists of 90 stations. That includes 21 stations from 12 countries obtained from University of Hawaii Sea Level Center [236], 42 stations (all but three located in the United Kingdom) from the British Oceanographic Data Centre [237], 19 Swedish stations from the SMHI [238] and 8 Dutch stations from Rijkswaterstaat [239]. Most of the stations have long series of data covering the entire period of interest (1970–2014). The secondary set consists of high-frequency raw data from 66 Mediterranean stations obtained from the Joint Research Centre (personal communication). They mostly cover years 2011–2014, with some series stretching back to 2008. Additionally, 5 Polish stations containing only information on annual maxima were used for validation of full model runs; they were obtained from Wiśniewski and Wolski [55]. The locations of all stations are presented in Fig. 4.1.

As mentioned above, surge heights are modelled as values relative to MSL. Therefore, sea level observations for each station were detrended and the long-term MSL was subtracted. A basic quality check was done for the stations from the secondary set, as some stations contained visibly erroneous observations. Afterwards, tides were removed from the water levels. Here, the skew surge approach was chosen, i.e. the difference between the predicted astronomical high tide and nearest observed high water [222]. This approach gives more certainty than using the residual, as even a very small difference in timing of the predicted and actual tide creates an “illusory” surge [240].

Predicted tide levels were obtained mostly through harmonic analysis using Matlab code by Grinsted [241]. However, tidal predictions by IHO (prepared via Delft Dashboard software) were used instead for some ocean-exposed stations, as they gave better results. Additionally, for some stations in Sweden (Stockholm and all other located northwards) water level data was applied directly, since a harmonic analysis actually created additional noise. This is likely because of the very low tidal amplitudes in that region. For the Mediterranean, JRC’s calculations were used for the tides, except for gauges where the quality check made for this analysis caused many modifications to the raw data.

During calibration three series of water levels were analysed: 6-hour values, daily maxima and monthly maxima. Each was evaluated with a set of measures. They are: Pearson’s coefficient of determination (R^2), Nash-Sutcliffe efficiency I_{NSE} , root mean square error I_{RSME} and RMSE-observations standard deviation ratio I_{RSR} . The measures are described with equations in section 2.2.7.

COMPARABLE STUDIES

A comparison between the TUD model set-up and the JRC and GTSR models is provided in Table 4.1. The three analyses are broadly similar, differing mostly in temporal and spatial resolution. The GTSR model differs most from the two European studies, as it includes tides directly in the hydrodynamic computation and uses an irregular grid. Also, the extreme value analysis was carried out by analysis the combined surge and tide timeseries in contrast to TUD and JRC models.

Table 4.1: Basic information on calculating extreme sea levels (ESLs) for coastal extent modelling by TUD and JRC. Based on Vousdoukas *et al.* [109, 229] for JRC and Muis *et al.* [227] for GTSR model.

Aspect	TUD analysis	JRC analysis	GTSR model
Hydrodynamic model	Delft3D, version 6.01.01.2856	Delft3D, version 6.01.07.4018	Delft3D
Processes simulated	Wind/pressure-driven ocean circulation	Wind/pressure-driven ocean circulation	Wind/pressure-driven ocean circulation and tides
Grid	Regular 0.11° (rotated relative to the geographical grid)	Regular 0.2° (40°W–47°E; 26°N–73°N)	Irregular, global
Spatial resolution	12.5 km	Varies depending on location	Varies depending on location
Atmospheric forcing	ERA-Interim, 6-hourly, 0.75° (calibration and validation); EURO-CORDEX, SMHI-RCA4 driven by EC-EARTH (r12i1p1), 6-hourly, 0.11° (validation and scenarios)	ERA-Interim, 6-hourly, 0.75°	ERA-Interim, 6-hourly, 0.75°
Climate scenarios	Reanalysis, historical, RCP4.5, RCP8.5	Reanalysis*	Reanalysis
Time range	1971–2000, 2021–2050, 2071–2100	1979–2014*	1979–2014
Output timestep	6-hourly	3-hourly	10-minute
Tide gauge data used for calibration or validation	161 stations with various data length	110 stations with various data length	27 stations in Europe, more globally
Calibration	Based on model runs for 1997–2000 and 2011–2014 with ERA-Interim, wind drag and bed roughness coefficients adjusted	No calibration	No calibration
Validation	ERA-Interim (1979–2014) and EURO-CORDEX (1970–2005) model runs	RA-Interim run, 1979–2014	ERA-Interim run, 1979–2014
Return periods of storm surges	Calculated using annual maxima and Gumbel distribution	Non-stationary extreme value statistical analysis with peak-over-threshold and Generalized Pareto distribution (with/without waves)	Calculated using annual maxima and Gumbel distribution (with tides)
Tides	Not included in the hydrodynamic simulation; mean high tide calculated from TPX08 model's tidal constituents	Not included in the hydrodynamic simulation; maximum tide based on TPX08 model's tidal constituents	Included in the hydrodynamic model (based on FES2012 model)
Inundation modelling	Static, without/with flood defences	Static/semi-dynamic/dynamic, with flood defences	Static, without flood defences

* CMIP5 simulations for future time periods were also carried out in Delft3D but they were not used to calculate flood extents.

4.2.3. EXTREME SEA LEVELS

After storm surge simulations have concluded, extreme sea levels were calculated taking into account several factors. Extreme sea level $E_{p,T,S}$ was considered here as:

$$E_{p,T,S} = R_{p,T,S} + D + M + L_{T,S} + G_T \quad (4.1)$$

where:

- p is the probability of occurrence (or, conversely, return period)
- T is the time period (1971–2000, 2021–2050, 2071–2100)
- S is the climate model run scenario (historical for 1971–2000, RCP4.5 and RCP8.5 for other periods)
- $R_{p,T,S}$ is the storm surge height (relative to local mean sea level) with a given probability of occurrence p , time period T and scenario S
- D is the mean high tide height
- M is the baseline mean sea level
- $L_{T,S}$ is the difference between mean sea level in time period T and scenario S compared to the baseline MSL (“sea level rise”)
- G_T is the accumulated effect of glacial isostatic adjustment between time period T and year 2000.

The first component of eq. 4.1 is the storm surge height $R_{p,T,S}$. It was calculated by fitting a parametric probability distribution to water levels from model simulations for all time periods. Two techniques were used: the block maxima method with Gumbel distribution as well as peak-over-threshold analysis with Generalized Pareto (GP) distribution [242, 243]. Gumbel distribution was chosen for the first method because it performed best in the Akaike Information Criterion goodness-of-fit test applied to our observational dataset [166]. The same method was used in the river discharge analysis in chapters 2 and 3. Meanwhile, peak-over-threshold method is used here to provide comparison with the JRC study. In this case, the surge series were declustered by first selecting surge heights above the 98th percentile in 6-hourly series and then further selecting only those surge peaks that were separated by at least 72 hours. The threshold values were chosen to recreate the methodology applied in Vousdoukas *et al.* [229]. The extreme value analysis was carried out as follows:

$$R_{p,Gumbel} = \mu - \sigma \ln(-\ln(1-p)) \quad (4.2)$$

$$R_{p,Pareto} = \mu + \frac{\sigma \left(\left(\frac{-1}{p-1} \right)^\theta - 1 \right)}{\theta} \quad (4.3)$$

where μ is the location parameter, σ is the scale parameter and θ the shape parameter (in GP only). In the Generalized Pareto distribution, μ is defined manually as a threshold value and it was set to the 98th percentile as in the declustering procedure.

The remaining four components were collected from external sources and are presented in Fig. 4.3. The second element of eq. 4.1 is the tide height D . Having in mind the possibility of tide-surge interaction, the dependency of the two was analysed through copulas (see Appendix A for information on copulas). A series of skew surge heights comprised of the 95th percentile of the whole set was compared with corresponding high tides for all 156 stations. Spearman's rank correlation coefficient was mostly near zero, with 129 stations indicating values less than 0.1. All but two of the remainder were Mediterranean stations where tidal amplitudes are very low and the amount of data was much smaller. It was also found that the value of tidal amplitude at a station had no influence on the strength of the tide-surge dependency. Therefore, independence of the tides and surges was assumed, and for calculating the coastal hazard the mean high tide was used. This information was obtained from TPXO8 tide model [34], which was shown to be the most accurate available [244]. It provides 9 constituents in 1/30° resolution (K1, K2, M2, M4, N2, O1, P1, Q1, S2) and 4 in 1/6° resolution (MS4, MN4, MF, MM). The same values are used for each time period. It should be noted that despite some studies showing influence of SLR on tides, most concluded that the effect is negligible (see Pickering *et al.* [245] for an overview).

The third element of eq. 4.1 is the “baseline” mean sea level M . Theoretically, mean sea levels should be aligned to the geoid. In practice, they deviate due to ocean circulation and atmospheric factors. This parameter is a correction for this fact and was obtained from MDT_CNES-CLS13 dataset [246, 247]. It is based on satellite altimetry observations and includes MSL averaged for years 1993–2012 at 0.25° resolution. Thus, the fourth constituent of eq. 4.1, which is the sea level rise $L_{T,S}$, had to be related to that baseline. SLR includes several factors: changes in dynamic sea topography, steric change (mainly thermal expansion) as well contributions of groundwater, glaciers and ice sheets. The dynamic and steric component were derived from CNRM-CM5 model [248]. It includes European inner seas (omitted in many other models) and has better accuracy for representing the dynamic topography compared to other models [249]. The horizontal resolution of the model is variable, but mostly ca. 0.5° over Europe. Remaining factors were obtained from studies on regional sea level rise [249, 250] through personal communication. The datasets provided estimates for years 1986–2100 at 1° resolution. 1986–2005 trend was extrapolated back to 1971 in order to provide data for the historical scenario.

The fifth and final component is the glacial isostatic adjustment G_T . The combined yearly rate of radial displacement and effects of the glacial rebound on the water level was obtained from ICE-6G_C (VM5a) model [213]. It is a global product with a 1° resolution. For each time period, the average displacement from the baseline elevation was calculated. This baseline is not the same as in the previous component, but is rather related with the specification of the digital elevation model EU-DEM, which was used to create flood hazard maps (section 4.2.4). EU-DEM was made using EVRS2000 vertical reference system, where the eponymous year 2000 is used as its epoch [251].

The calculation of ESLs was done for each coastal segment. Those were derived from CCM2 database [23], resulting in 70 292 coastal segments with a combined length of exactly 226 150 km. This source was used for consistency with the river flood maps from chapter 3. Since all datasets used in eq. 4.1 are grids of different resolutions, information

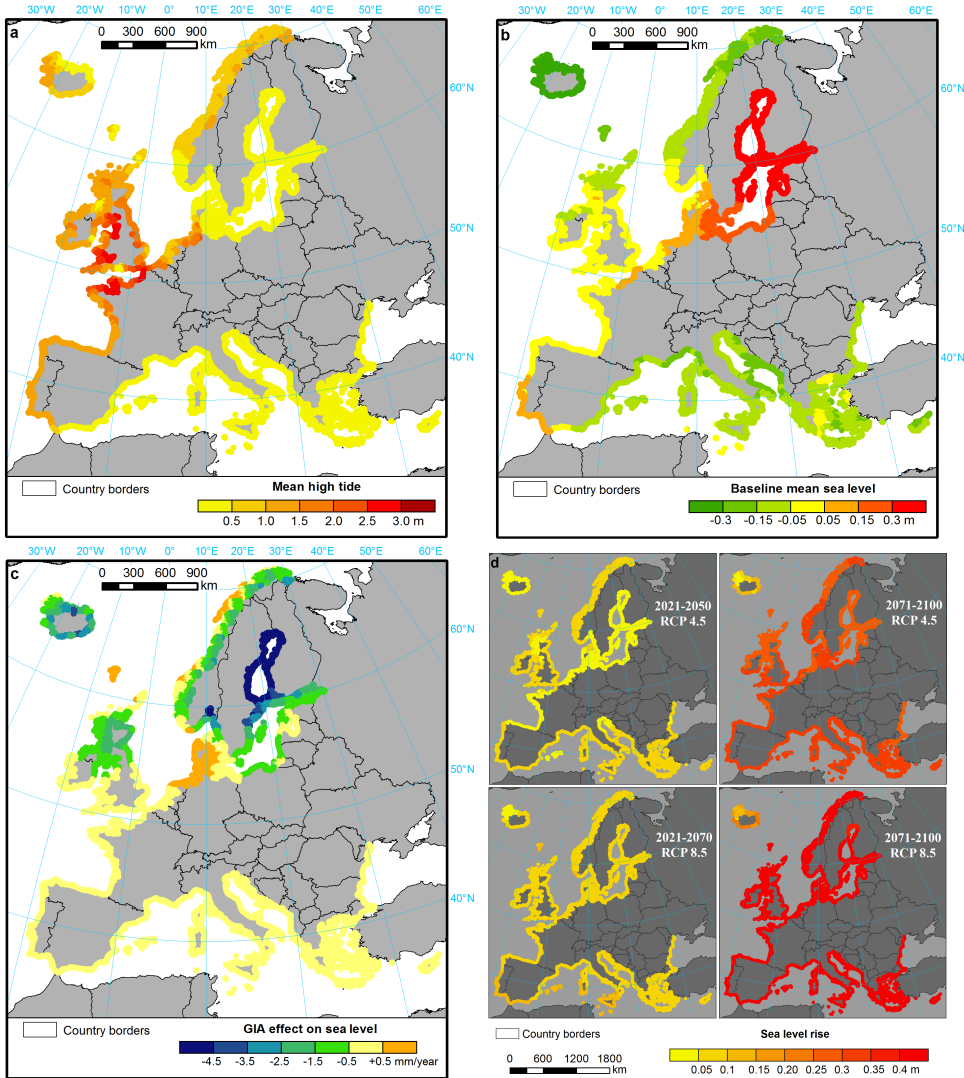


Figure 4.3: Components of extreme sea level other than storm surge height: (a) mean high tide in metres, (b) baseline mean sea level, 1993–2012, in metres above geoid; (c) glacial isostatic adjustment (GIA) effect on sea level in mm/year and (d) sea level rise in metres per time period and scenario, relative to 1993–2012 average. For underlying data sources, see text.

was assigned to each coastal segment from the nearest grid point of each dataset. Such a combined layer of water levels under present and future was used to calculate flood hazard along the coast.

It needs to be noted that the JRC's analysis of coastal flood extents utilized a different approach to ESLs. As it was done only for a historical reanalysis, it omits SLR and GIA, but adds another component, i.e. wave setup:

$$E_p = (R + 0.2W)_p + H \quad (4.4)$$

where R is the storm surge height, W is the significant wave height and H is the maximum high tide height. In the GTSR study, ESLs are a direct model output (combined surge and tide).

4

4.2.4. COASTAL FLOOD EXTENTS

After the boundary conditions have been obtained, they were applied to calculate flood extents. All model results analysed here used the same method, even if with a different setup. Static inundation approach, also known as “bathtub fill”, is the simplest applicable method [252]. In this approach, it is assumed that all land laying below the extreme sea level is flooded, as long as it is hydraulically connected with the sea.

TUD's study was carried out in two variants: with or without correction of elevation in the underlying digital elevation model (DEM). The model used here is EU-DEM (see section 2.2.3). It has a resolution of 1 arc second, but for the flood analysis it was resampled and projected to a 100 m resolution. Though the dataset is comprehensive and consistent, accuracy issues have been reported [144]. It is shown that the average error of the model is -0.56 m and root-mean-squared error of 2.9 m, while displaying significant diversity between countries. It was therefore decided to analyse floods not only on the original dataset, but also on a corrected one. The correction was based on an assumption that in the coastal zones the bias of the model is the same as averaged over the whole country, as indicated in the EU-DEM validation report.

To test this assumption, three nationally-produced DEMs were collected for:

- The Netherlands – Actueel Hoogtebestand Nederland [253]
- Poland – NMT 100 [254]
- United Kingdom – OS Terrain 50 DTM [255]

The first two datasets have a resolution of 100 m, while the last one – 50 m. All datasets were resampled to fit into the grid of EU-DEM, and the Polish dataset was modified by adding 18 cm [256] in order to move it from national vertical datum (Kronstadt) to EVRF-2000, which was used in EU-DEM. The comparison between the national and European DEMs was made for the coastal zone extending up to +3 m above mean sea level. In the Polish coast the bias of EU-DEM was found to be equal to -2.31 m, very close to country average of -2.38 m reported by DHI GRAS. In the Netherlands the values were -0.96 and -0.85 m, respectively, and in the UK +0.70 in the coast and +0.72 m for the whole territory. Due to the very close alignment of those figures, EU-DEM was corrected using country-specific values from the validation report.

Coastal flood extent estimates in the TUD analysis were done using the coastal segments from CCM2 database. For each coastal segment in CCM2, their nearest neighbourhood landward was calculated. Then, the nearest grid cell for each dataset representing a component of extreme sea levels (eq. 4.1) was assigned, so that the ESL could be calculated separately at each segment. It is important to note that existence of coastal defences was not taken into account at this stage. Instead, maps were post-processed by removing flood zones where extreme sea levels were below estimated protection standards. Those estimates were taken from two databases. Firstly, FLOPROS database [66] shows nominal protection levels in terms of return periods, which were assumed equal to ESLs in the historical scenario at a given coastal segments. The standards are either design levels of actual defences, or legal requirements for flood protection in a given area, or estimates based on expected annual damages. Secondly, a revised version of coastal protection levels from Vousdoukas *et al.* [109] were used, which are provided as heights above mean sea level, linking return periods with ESLs including tides. This database was constructed by considering all available information on flood extents and number of people affected known from past events and local studies. High-resolution population grid from JRC was combined with modelled flood zones to estimate affected population so that most probable protection standards for all return periods could be found.

The JRC study included approximately 11 000 segments of equal length (25 km), with the nearest neighbourhood extending 100 km landward. The elevation model used in the analysis was derived from CCM2, and is mostly based on Shuttle Radar Topography Mission (STRM) elevation model [257]. An important difference from the TUD approach was a modification the DEM using estimates coastal protection levels. The elevation in all DEM cells found on the coastline and having elevation lower than the one of the protection level. Those levels were estimated using high-resolution DEMs, information on flood protection standards, personal communication with national authorities etc. The JRC results analysed here are a revised version of those presented in Vousdoukas *et al.* [109]. Finally, the GTSR model used static inundation method on the original STRM DEM, with no coastal protection included.

4.2.5. VALIDATION OF COASTAL FLOOD MAPS

The validation of pan-European maps was done by comparison with four “reference” maps: two from official national flood studies, one from published research and one representing actual observed flood extent during an extreme event.

The map with the largest spatial extent is for England. “Risk of Flooding from Rivers and Sea” map [176], which was also used in the river flood analysis and therefore described already in section 3.2.5. However, as both river and coastal floods are represented in the same maps for different return periods, therefore for the comparison only those flood extent patches were selected that were connected to the coast, but no further than 25 km. This choice might have included some influence of rivers in the delimitation of flood zones, however there was no other possibility of disentangling the riverine and coastal phenomena from the map.

The other official study is “The National Flood Risk Analysis for the Netherlands” [64, 258], also known by the abbreviation VNK. Data underlying this analysis was ob-

tained from Rijkswaterstaat, the Dutch agency responsible for upkeep of primary flood defences through personal communication. In this dataset, the probability of failure of each dike section is provided together with a corresponding flood zone. Nine different failure mechanisms are considered, including four for dikes (overflow/overtopping, piping, instability, erosion), four for hydraulic structures (overflow/overtopping, seepage, structural failure, failure to close) and one for dunes (erosion). The inundation calculation was done using 1-D or 2-D dynamic models, depending on location, taking into account the development of breaches in dikes. Flood zones of 400 dike sections were combined into a single map, and the probability of flooding was added up when flood zones of different dike sections overlapped. It was therefore assumed that failure of each dike section would be mutually exclusive with failure of any other section. In this way, flood maps for 30-, 100-, 300-, 1000-year return period could be extracted at 100 m resolution. However, they only include flood zones inside the “dike rings”, which are continuous lines of defences completely surrounding a given area [259]. There are 100 dike rings in the country, of which 58 were included in the VNK study. Of these, 36 rings (numbered consecutively from 1 to 35 and ring 13b) solely or predominantly protect against high sea levels, therefore only these were selected for the comparison. The remaining rings protect against floods from river Rhine and Meuse; no ring exposed to coastal flood have been excluded from the VNK study. Only for the very small dike ring 13a the data could not be obtained, however the VNK study estimates that the defences have total probability of failure smaller than 1 in 1000 years.

The third dataset was obtained from a previous study on coastal floods and sea level rise in Poland [100]. In contrast to the previous two datasets it used only the static “bathtub” method, however it utilized a detailed 1 m-resolution DEM from lidar scanning. The same source material was used also in the official flood maps, which also used the static inundation method for direct flooding from the sea, though utilized hydrodynamic models areas of influence of both sea and rivers. The study analysed effects of floods for every 5 cm increase in water level, and the maps for specific return periods were obtained by assigning flood zones to one of 8 tide gauges in the coast for which extreme value analysis could be done. The map was obtained for all 5 scenarios considered in the pan-European TUD map. Validation presented in Paprotny and Terefenko [100] shows that number of the exposed population in main cities calculated in their study is very similar to the one indicated in the official flood maps.

Last but not least, one case study of an actual storm surge was used for validation. On 27–28 February 2010, an extra-tropical cyclone “Xynthia” caused a devastating flood in Vendée and Charente-Maritime departments of France, with a death toll of 41 [203]. The total flooded area was 413 km². Analysis of tide gauge data from La Pallice harbour in La Rochelle, which was located in the very centre of the event, shown that the water levels had a return period of more than 100 years [260]. Observed flood extent was digitized from maps presented by [261] for the purpose of this analysis.

All maps were projected and resampled to fit the same grid as the pan-European maps. For more detailed analysis, all flood maps were split into regions utilizing the Nomenclature of Territorial Units for Statistics (NUTS) from Eurostat [191], 2013 edition. The maps divided by regions are presented in Fig. 4.4.

The pan-European and global maps were evaluated with two measures, the same as

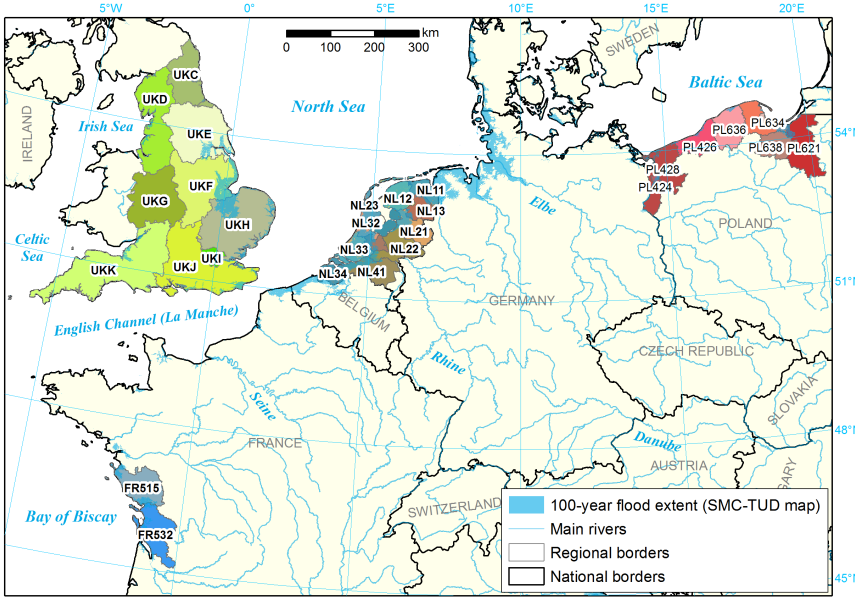


Figure 4.4: Location of the local reference maps with corresponding NUTS codes (see Table 4.5), with the TUD’s flood map presented in the background.

in chapter 3. The tests for correctness I_{cor} (or hit rate) and fit I_{fit} (or critical success index) are the same as described in section 3.2.5 and eqs. 3.3 and 3.4. However, the “false alarm ratio” is also analysed here, and which can be inferred from the other two measures:

$$I_{false} = \frac{I_{cor}}{I_{fit}} - 1 \tag{4.5}$$

4.3. RESULTS

4.3.1. MODEL CALIBRATION AND VALIDATION OF MODELLED STORM SURGE HEIGHTS

Summarized performance of the model after calibration with ERA-Interim climate data is presented in Table 4.2. “Timeseries” refers to the 6-hour model output compared with the full skew surge series from gauge stations. Results are very good for monthly maxima, less so for daily maxima and the full series. However, the former is most important in context of the work’s purpose of obtaining accurate surge levels at different return periods.

Most importantly, the model as a whole shows relatively little bias, as can be seen in Fig. 4.5a. Linear regression (indicated by a grey line) applied to monthly maxima deviates only slightly for the dashed black line representing the 1:1 relationship. However, the performance of the model is hardly uniform. Much lower alignment between observed and simulated surge heights was observed at Mediterranean stations 4.5b, though surges in those locations are also much smaller than elsewhere in Europe. The model

Table 4.2: Calibration results. See section 4.2.2 for explanation of measures. I_{RSR} value in meters.

Run	Series	R^2	I_{NSE}	I_{RSME}	I_{RSR}
2011–2014 primary stations	Timeseries	0.53	0.42	0.15	0.78
	Daily maxima	0.60	0.50	0.15	0.74
	Monthly maxima	0.75	0.72	0.15	0.53
2011–2014 secondary stations	Timeseries	0.23	-0.15	0.10	1.07
	Daily maxima	0.29	0.03	0.10	0.98
	Monthly maxima	0.43	0.29	0.10	0.86
2011–2014 all stations	Timeseries	0.48	0.36	0.13	0.81
	Daily maxima	0.55	0.48	0.13	0.74
	Monthly maxima	0.77	0.77	0.13	0.48
1997–2000 primary stations	Timeseries	0.52	0.42	0.15	0.78
	Daily maxima	0.61	0.52	0.15	0.72
	Monthly maxima	0.75	0.72	0.15	0.53
1979–2014 all stations	Timeseries	0.55	0.42	0.15	0.79
	Daily maxima	0.62	0.50	0.15	0.74
	Monthly maxima	0.77	0.73	0.15	0.53

performed best along the southern coasts of the North Sea and in the Danish Straits. Results along the coast of Great Britain are mixed, with relatively low performance observed along the Irish Sea.

Similarly to monthly maxima, calculations of annual maxima and return periods using the Gumbel distribution showed good performance, as presented in Table 4.3. 86 stations with at least 20 years of data were used for comparison with ERA-Interim results and 65 with EURO-CORDEX. Values of the measures change little between different return periods, though they are slightly lower for low probabilities of occurrence. Interestingly, simulation driven by EURO-CORDEX performed mostly better than one based on ERA-Interim data. The results in Table 4.3 are for different sets of stations, but they are very similar for a common set of 64 stations with sufficient data series. The difference in performance is likely caused by much finer resolution of the EURO-CORDEX model (0.11° versus 0.75°).

Performance for individual stations is mostly good, as can be seen in examples presented in Fig. 4. In Gedser, Denmark, as well as in many Baltic stations, there is close match of distributions of surges. In Brest there is a mismatch in water levels, both relatively little bias, while in La Coruña station there is noticeable bias. Nevertheless, the overall performance, as presented above, is satisfactory and the full-length simulations for present and future climate could be made.

Performance for individual stations is mostly good, as can be seen in examples presented in Fig. 4.6. In Gedser, Denmark, as well as in many Baltic stations, there is close match of distributions of surges. In Brest there is a mismatch in water levels, both relatively little bias, while in La Coruña station there is noticeable bias. Nevertheless, the overall performance, as presented above, is satisfactory and the full-length simulations for present and future climate could be made.

A further comparison could be made using directly the results from the JRC study, which utilized the peak-over-threshold Generalized Pareto distribution. The JRC model

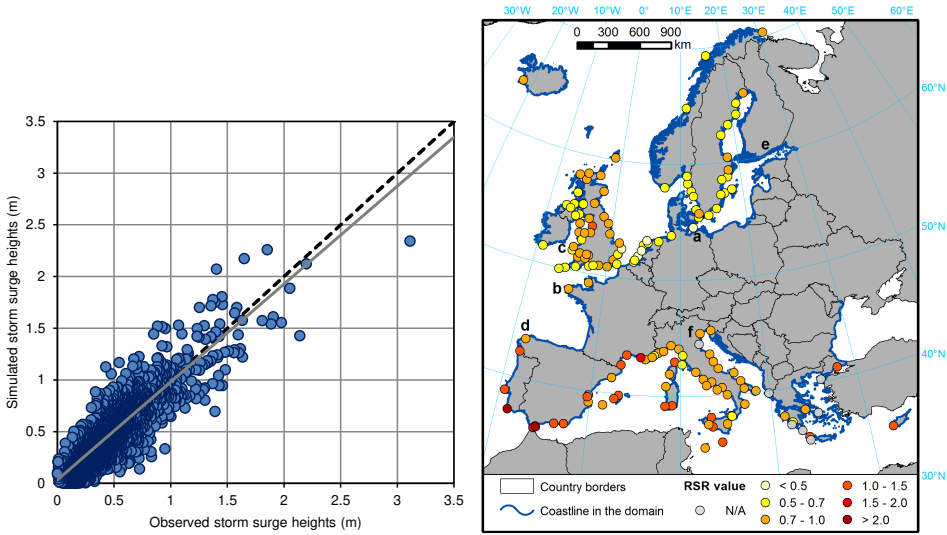


Figure 4.5: Comparison between simulated and observed monthly maxima (2011–2014): (a) Linear regression (grey line) and 1:1 line (black dashed line) and (b) RMSE-observations standard deviation ratio I_{RSR} . N/A = not available.

Table 4.3: Validation results (observed vs simulated storm surge heights). See section 4.2.2 for explanation of measures.

Return period (years)	ERA-Interim (1979–2014)			EURO-CORDEX (1970–2005)		
	R^2	I_{NSE}	I_{RSR}	R^2	I_{NSE}	I_{RSR}
1000	0.87	0.76	0.52	0.86	0.83	0.40
500	0.87	0.77	0.50	0.87	0.84	0.40
300	0.87	0.78	0.48	0.87	0.84	0.40
100	0.86	0.81	0.45	0.87	0.84	0.40
50	0.86	0.82	0.43	0.87	0.83	0.41
30	0.85	0.83	0.42	0.87	0.83	0.41
10	0.84	0.83	0.41	0.86	0.81	0.44
2	0.76	0.71	0.55	0.80	0.69	0.58

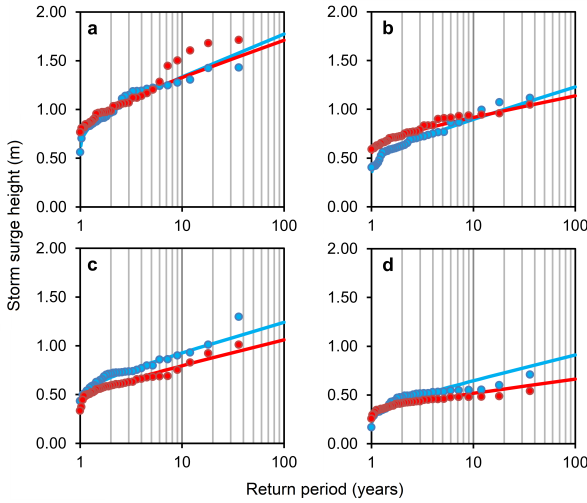


Figure 4.6: Comparison between simulated (red) and observed (blue) storm surge (1970–2005,) in selected stations. Dots are annual maxima and lines are their probability distributions fitted to Gumbel. Station are: (a) Gedser, Denmark, (b) Milford Haven, UK, (c) Brest, France, (d) La Coruña, Spain. For locations of stations see Fig. 4.5b.

covers a period from 1 December 1969 to 30 November 2004, which is a one month shift from the EURO-CORDEX simulation in the TUD model. Table 4.4 compares the results for a set of 71 stations using a similar methodology of extreme value analysis. For all return periods, I_{NSE} and I_{RSR} indicate better performance of the TUD model, though it decreases with the return period. Nonetheless, the performance is lower than in case of Gumbel distribution (Table 4.3).

4.3.2. VALIDATION OF MODELLED EXTREME SEA LEVELS

Extreme sea levels with a return period of 100 years obtained from TUD, JRC and GTSR models are compared with observations in Fig. 4.7. Data from 79 or 84 gauges, depending on time series availability, were used for this analysis. Results of all three studies in-

Table 4.4: Comparison of validation results (observed vs simulated storm surge heights fitted to Generalized Pareto distribution). See section 4.2.2 for explanation of measures.

Return period (years)	TUD model			JRC model		
	R^2	I_{NSE}	I_{RSR}	R^2	I_{NSE}	I_{RSR}
1000	0.48	0.42	0.76	0.38	0.12	1.57
500	0.50	0.46	0.74	0.41	0.10	1.75
200	0.52	0.49	0.71	0.43	0.08	1.98
100	0.53	0.50	0.70	0.43	0.06	2.16
50	0.53	0.51	0.70	0.43	0.05	2.32
20	0.53	0.50	0.71	0.41	0.04	2.53
10	0.53	0.49	0.73	0.39	0.03	2.67

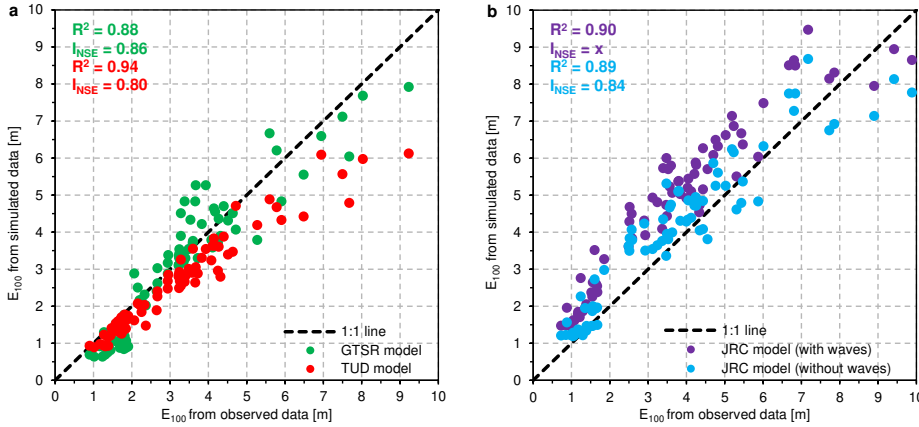


Figure 4.7: Comparison of 100-year extreme sea levels E_{100} calculated from water level timeseries from simulations and observations: (a) GTSR model (green) and TUD model (red), using Gumbel distribution, for 84 gauges and (b) JRC model with (violet) and without (blue), waves using non-stationary extreme value analysis with Generalized Pareto distribution for storm surges, with maximum tide added afterwards, for 79 stations. All simulations are 1979–2014 runs with ERA-Interim climate reanalysis. GTSR model results are from Muis *et al.* [227].

dicating similar performance for the historical reanalysis (1979–2014 with ERA-Interim climate model). The TUD model has the highest correlation ($R^2=0.94$), but also the highest bias as indicated by the lower value of Nash-Sutcliffe efficiency ($I_{NSE}=0.80$). It is visible that using mean high tide instead of combining surges and tide in the hydrodynamic model underestimates ESLs compared to extreme sea levels obtained by applying extreme value analysis to sea levels from tide gauges. In the case of the JRC model, ESLs (without waves) are slightly overestimated compared to tide gauge observations transformed with the same procedure. For reference, in Fig. 4.7b the JRC-calculated ESLs with and without waves are shown. For most gauges, inclusion of waves adds approximately one metre to the flood scenarios.

Flood scenarios for the TUD analysis were obtained from RCA4 model under EURO-CORDEX framework. The results are validated in Fig. 4.8. Number of gauges (63) with adequately complete records for 1970–2005 was smaller than for 1979–2014. In effect, though the correlation is higher and the bias is lower relative to the simulation using ERA-Interim, the comparison in Fig. 4.8 excludes most stations with very large tidal amplitudes. The tidal component is the same for analyses done with both climate models, therefore using EURO-CORDEX gave higher storm surge estimates than the ERA-Interim runs. Spatially, the distribution of error is very uneven: errors are low in the Baltic and North seas, and significantly higher for the coasts exposed directly to the Atlantic Ocean. No stations with long series could be found for the Mediterranean or Black seas. Also, some variability can be observed for analysing different return periods: the higher the return period, the lower the correlation and higher the bias: $R^2=0.94$ and $I_{NSE}=0.89$ for 10-year ESL compared to $R^2=0.89$ and $I_{NSE}=0.83$ for 1000-year ESL. This relatively minor

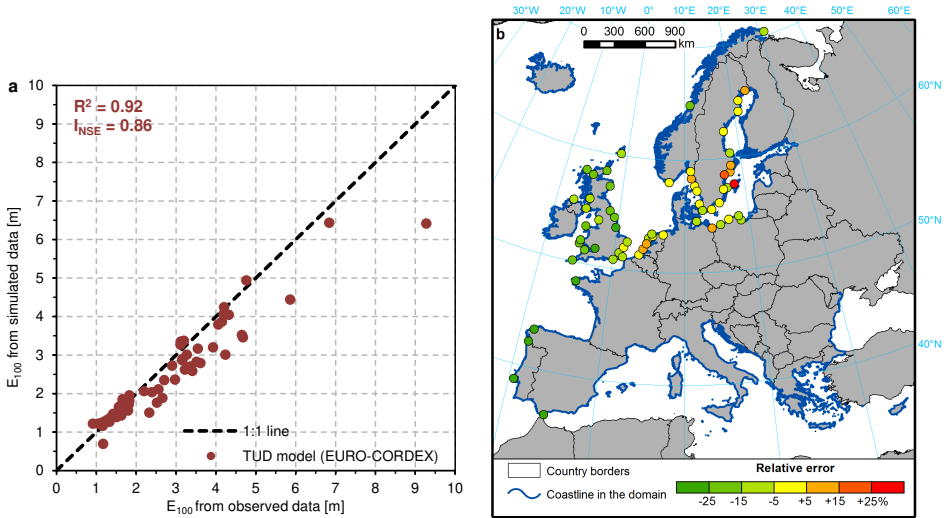


Figure 4.8: Comparison of 100-year extreme sea levels E_{100} calculated from water level timeseries from simulations with TUD model using EURO-CORDEX (1970–2005) model run, and observations at 63 gauges: (a) regression and 1:1 line and (b) results per each tide gauge.

decrease in accuracy for higher return periods can be largely attributed to the increasing uncertainty of the ESLs at a given return period.

4.3.3. PRESENT AND FUTURE STORM SURGE HEIGHTS AND EXTREME SEA LEVELS IN EUROPE

After validating the model, simulations of present (1971–2000) and future (2021–2050 and 2071–2100) storm surge regime were performed. Results for a 100-year surge are presented in Fig. 4.9a. Surges are the highest in the southern part of the North Sea, up to 4 m, though the average 100-year surge in the Baltic Sea is a bit higher, 1.69 m opposed to an average 1.57 m for all North Sea coasts. By contrast, in the western Mediterranean Sea and in the Black Sea it mostly amounted to half a metre. In most locations, a 1000-year surge is estimated to be about 50 % higher than a 10-year surge.

Future trends in storm surge heights are highly uneven. Fig. 4.10 presents result the change for a 100-year surge, but it is mostly representative for other return periods as well. The biggest increases are observed in the Norwegian Sea—a 20 cm rise by 2071–2100 in RCP 8.5, though almost no changes were found in this location in RCP 4.5. Relatively large increases were found in the Eastern Mediterranean and Black Sea by 2021–2050, though with large drops in surge heights in the next time period. Bigger storms are also expected in the Gulf of Cadiz, Bay of Biscay and most of British Isles' coast. In the North and Baltic seas, a decrease in storminess is projected. In the eastern part of the Mediterranean Sea and in the Black Sea there is noticeable increase in surge in the first half of the century, with a drop in the second half. Basically in all areas in RCP 8.5 simulations storms were higher than in RCP 4.5 scenario. Averaged over all coasts in our domain, a 100-year surge was 1.29 m during 1971–2000, declining to 1.20 m (RCP 4.5) or

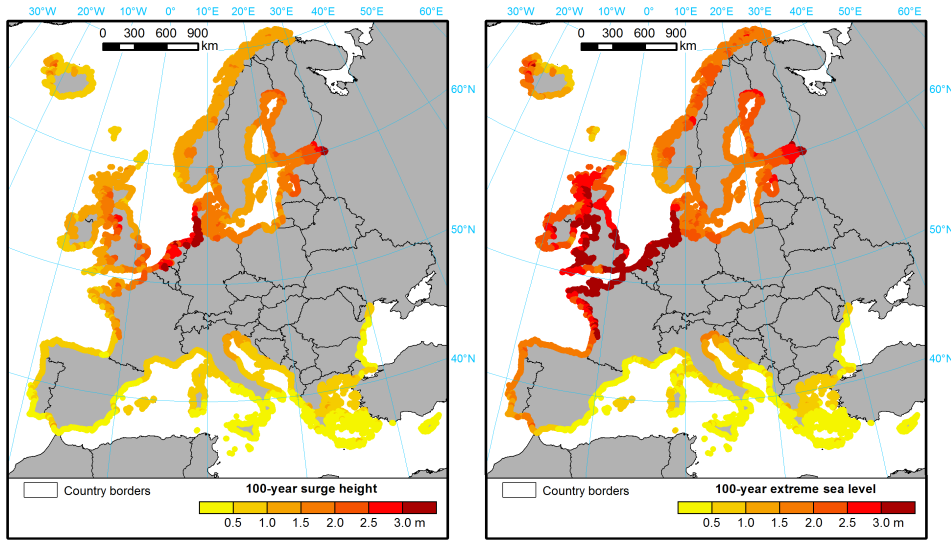


Figure 4.9: (a) 100-year storm surge heights and (b) extreme sea levels along European coasts, in metres above mean sea level, 1971–2000.

1.27 m (RCP 8.5) by 2071–2100. Only surges with low return periods (2–10 years) show a general, albeit small, increase in height by mid-century, with 2071–2100 almost the same as during 1971–2000. The same could be observed in most regions, even in the Baltic Sea, where the most extreme surges are projected to decrease.

After including all additional factors, extreme sea levels get significantly higher in north-western Europe due to the tides (Fig. 4.9b), where 100-year level can be even 6.5 m above mean. Still, in most of the Mediterranean region, water levels rarely increase by more than 0.5 m. In the almost non-tidal Baltic Sea, 100-year surge amounts to about 2 m.

Increase in ESLs is noticeably higher than surges alone in almost all of Europe (Fig. 4.11). Impact the glacial isostatic adjustment (GIA) is mostly very small, therefore the main source of change in extreme water levels is the sea level rise (SLR). Only in the Baltic Sea the GIA mostly offsets the impact of SLR, even in the RCP 8.5 scenario. Increases are also relatively modest in the northern coasts in the 2021–2050 timeframe, but by 2071–2100 they mostly increase by half a metre. Only the Dutch coast and in some parts of Great Britain will be less affected. It is also projected that along the Norwegian and Iberian coasts, together with the Mediterranean and Black seas, 100-year level will increase by around half a metre in RCP 8.5 by the end of the century. In the western Mediterranean it will cause a doubling of 100-year water levels, and almost tripling of 10-year levels. Largest absolute increases of 100-year levels are expected to be observed in Celtic and Irish seas, 60 cm and more. SLR is the main contributing factor almost everywhere, often the only one causing an increase, as opposed to the other two factors considered here (surges and GIA). Examples of influence of different factors for individual stations are presented in Fig. 4.12.

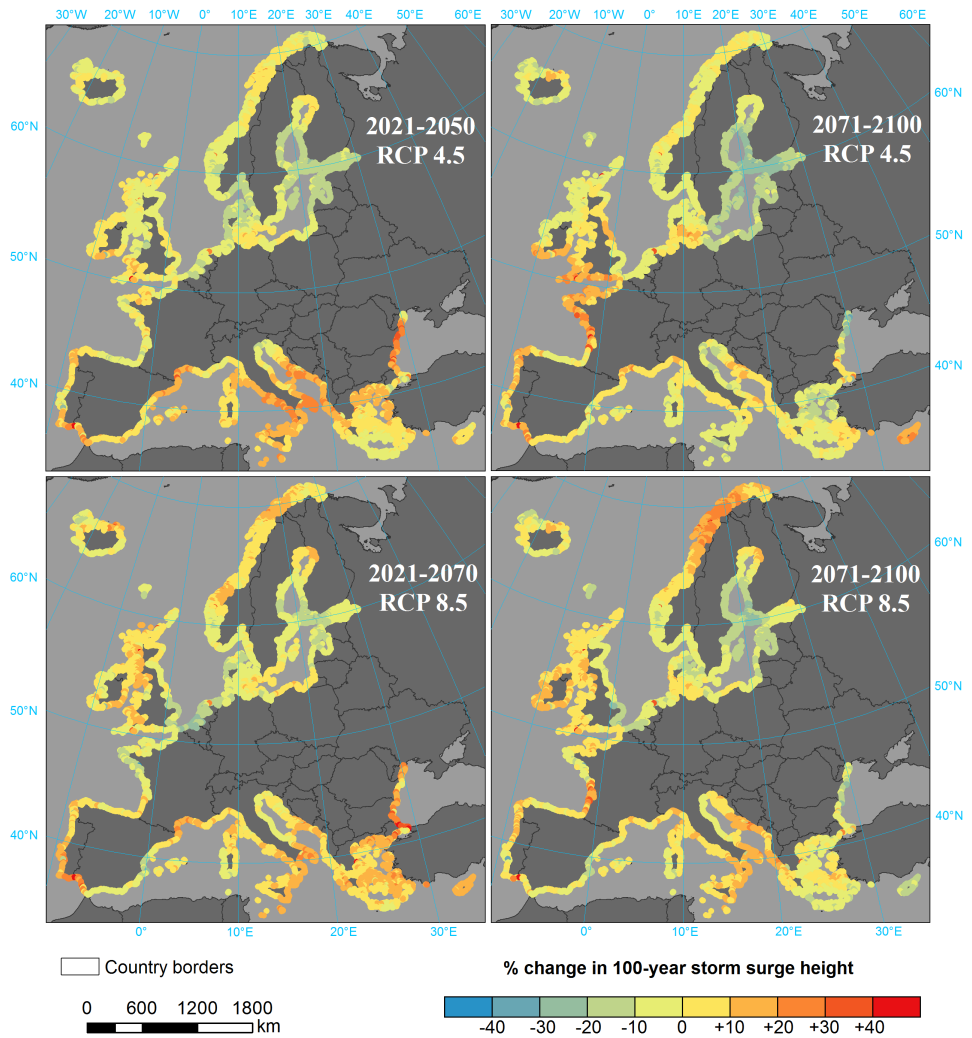


Figure 4.10: Changes in 100-year storm surge height along European coasts relative to 1971–2000 in %.

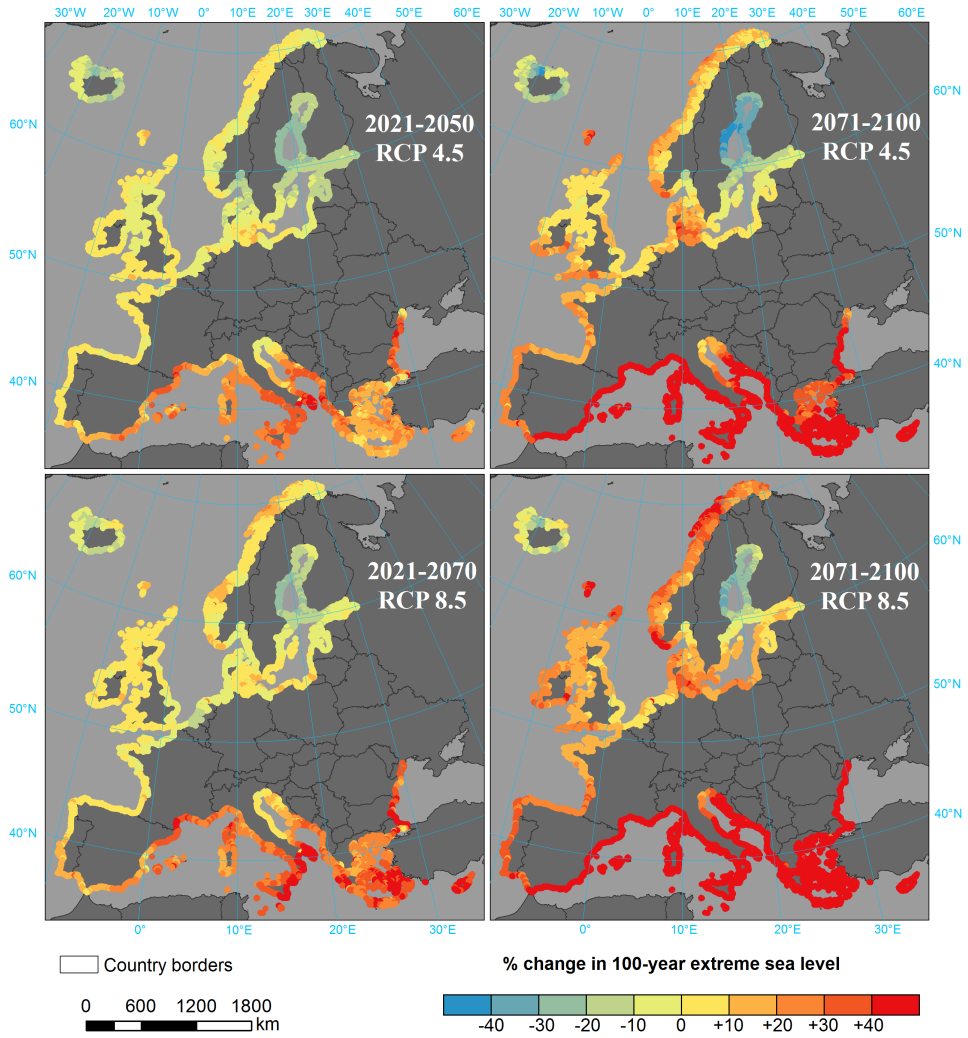


Figure 4.11: Changes in 100-year extreme sea level along European coasts relative to 1971–2000 in %.

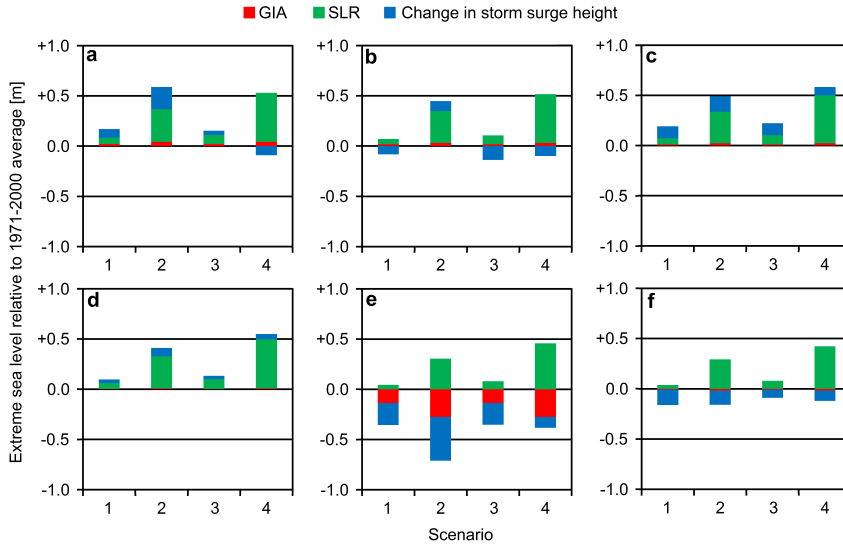


Figure 4.12: Change in 100-year water levels for selected stations. Stations are: (a) Gedser, Denmark, (b) Milford Haven, UK, (c) Brest, France, (d) La Coruña, Spain, (e) Helsinki, Finland, (f) Venezia, Italy. Scenarios: 1 - 2021–2050 RCP 4.5, 2 - 2071–2100 RCP 4.5, 3 - 2021–2050 RCP 8.5 and 4 - 2071–2100 RCP 8.5. For locations of stations see Fig. 4.5b.

4.3.4. VALIDATION OF COASTAL FLOOD MAPS

The results of the comparison between the TUD map with reference maps in five scenarios (10, 30, 100, 300 and 1000 years return period) are shown in Table 4.5 and all European-scale maps are validated for the 100-year event in Table 4.6. A snapshot of the comparison for the Humber river estuary on the eastern coast of England is presented in Fig. 4.13. National flood maps for England indicate more than 4000 km² at risk of a 1 in 100 years flood, the largest area of the four high-resolution studies. For that return period, 68 % of the flood zone is recreated in the TUD pan-European map (I_{cor}), however the “fit” (I_{fit}) is rather low, at 32 %. In effect, for each km² correctly predicted another km² is falsely indicated as being at risk of flood (111 % false alarm ratio I_{false}). Considering areas that are normally protected by flood defences against a 1 in 200 years event, the results for the pan-European map improve slightly. It improves further for the 1000-year event, but is very poor for a 30-year event. This is caused by the effect of flood defences, which are not included in the TUD map: most areas are protected against flood with a high probability of occurrence, but few are large enough to prevent a millennial flood. The same effect could be observed for the Dutch and Polish maps. In case of the former, the performance is very low for all return periods due to high level of flood protection in the Netherlands. In Poland, where the flood protection has lower standards (mostly below 100 years return period), the maps were prepared with the same methodology. Hence, the difference in flood zone delimitation compared to the pan-European map is caused primarily by the use a more detailed DEM. At the same time, there is noticeable influence of DEM correction on the results. This effect is lower in England, were the EU-

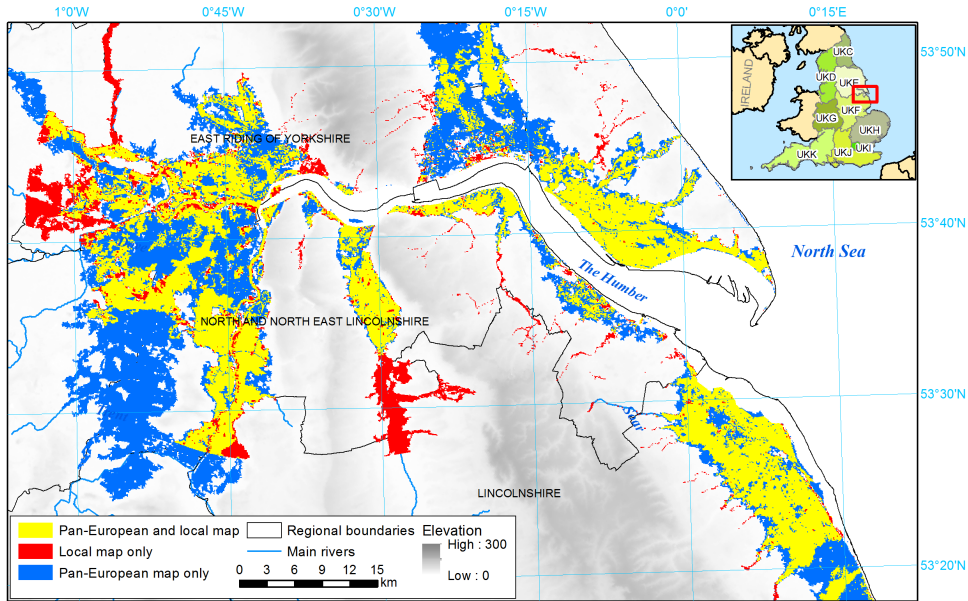


Figure 4.13: An example of the differences between the pan-European map from this study and the local reference map, for the Humber river estuary in England, both for the 100-year flood scenario [176].

DEM is less biased, and unnoticeable in the Netherlands, where flood zones are mostly depressions.

The performance of the GTSR model is, on average, similar to TUD analysis (for 100-year return period; Table 4.6). It also uses static inundation technique, with no flood protection is assumed, and only the ESLs and the underlying DEM are slightly different. However, at regional level disparities are sometimes significant, like for South East and South West of England. The bias in the global DEM over Poland reduces the accuracy of flood zone delimitation, similarly when the uncorrected EU-DEM is applied in the TUD analysis. Again, the whole low-lying territory of the Netherlands is indicated as flooded, and the extent of the Xynthia storm surge is substantially overestimated.

The JRC model included estimated flood protection levels in the calculation, generating smaller flood extents than the other two assessments. In general this leads to substantially lower overestimation: only 65 % false alarm ratio I_{false} for all study area together, compared to almost 300 % for remaining models. However, this is with the expense of missing many flood zones indicated in the local maps. Only for England the I_{cor} and I_{fit} measures are similar. In the case of the Netherlands, the no flood hazard in the 100-year scenario is indicated, as nominal protection standards are much higher.

4.3.5. PRESENT AND FUTURE COASTAL FLOOD EXTENTS IN EUROPE

Results of the coastal flood extent analysis using corrected DEM for present and future climate are visualized in Fig. 4.14 for the 100-year event. For the sake of clarity, the flood extents were aggregated in 50 km blocks from the original 100 m resolution maps, which

Table 4.5: Validation results for the pan-European TUD map, with and without DEM correction, by countries and regions. 100-year flood zone area is taken from the reference maps. The indicators for correctness (Cor) and fit (fit) are in %. For location of the regions, see Fig. 4.4.

NUTS	Name	100-year flood zone (km ²)	Map with corrected DEM (TUD-C)												Map with uncorrected DEM (TUD-U)											
			10 years		30 years		100 years		300 years		1000 years		10 years		30 years		100 years		300 years		1000 years					
			Cor	fit	Cor	fit	Cor	fit	Cor	fit	Cor	fit	Cor	fit	Cor	fit	Cor	fit	Cor	fit	Cor	fit				
UKC	North East	73.7	24	17	23	21	24	21	21	17	16	17	13	15	14	15	14	15	14	11	11					
UKD	North West	426.3	35	21	36	26	42	36	41	38	38	20	16	26	20	29	26	29	26	31	29					
UKE	Yorkshire and the Humber	660.5	70	10	74	42	76	54	74	67	67	64	12	63	41	63	49	63	60	63	60					
UKF	East Midlands	944.8	83	8	92	41	92	41	94	72	72	66	8	79	38	79	38	79	38	87	70					
UKH	East of England	826.4	78	15	81	23	83	30	84	37	37	74	15	78	23	79	29	81	37	70	37					
UKI	London	0.3	0	0	0	0	0	0	0	0	0	0	0	0	0	0	0	0	0	0	0					
UKJ	South East	530.8	77	24	75	40	81	61	77	59	59	73	25	72	42	78	63	74	60	60	60					
UKK	South West	700.7	36	25	33	25	36	30	37	32	32	16	14	14	12	16	15	19	17	17	17					
UK	United Kingdom	4163.5	60	15	68	32	70	39	71	50	50	49	14	58	30	60	36	63	47	47	47					
PL424	Miasto Szczecin	119.2	82	77	83	78	83	79	84	80	85	81	90	76	90	78	91	80	92	81	92	83				
PL426	Koszalin	149.4	62	51	67	56	65	66	71	66	64	57	73	41	87	49	87	49	87	52	87	52				
PL428	Szczecin	556.1	69	60	73	65	72	66	71	66	75	69	88	61	88	64	87	65	88	67	87	68				
PL621	Elbląski	355.5	90	76	92	78	93	86	93	89	94	92	99	76	99	78	99	86	99	89	99	92				
PL633	Trójmiejski	45.9	57	35	57	35	63	50	60	48	58	47	90	38	90	40	91	55	91	59	87	59				
PL634	Gdański	670.5	88	76	86	78	83	79	86	82	85	83	98	60	98	68	98	76	98	78	97	79				
PL636	Śląpski	207.5	0	0	0	0	54	54	51	51	49	49	62	49	63	53	68	53	68	55	67	54				
PL638	Starogardzki	80.3	85	71	89	66	87	72	87	75	82	76	100	21	100	23	99	27	99	30	99	32				
PL	Poland	2184.4	72	63	73	65	77	72	78	73	78	74	90	57	91	61	91	66	91	67	91	68				
NL11	Groningen	0.0	99	1	100	4	99	7	100	24	24	100	1	100	4	99	7	100	4	99	7	24				
NL12	Friesland	0.0	100	3	100	22	100	0	98	3	100	22	100	0	99	3	100	22	100	4	99	7				
NL13	Drenthe	0.1	100	0	98	3	100	22	100	0	99	7	100	0	99	3	100	22	100	4	99	7				
NL21	Overijssel	122.1	99	19	99	46	99	77	99	77	77	99	19	99	45	99	76	99	76	99	76	76				
NL22	Gelderland	0.5	78	1	77	1	98	75	98	75	75	98	1	87	1	87	1	98	74	98	74	74				
NL23	Flevoland	0.0	87	5	95	31	96	31	96	31	65	99	65	99	65	99	65	99	65	99	65	65				
NL31	Utrecht	30.5	87	5	95	31	96	31	96	31	31	94	5	98	31	98	32	98	32	98	32	32				
NL32	Noord-Holland	114.9	100	0	100	5	100	7	99	25	25	100	0	100	5	100	7	99	25	99	25	25				
NL33	Zuid-Holland	327.9	99	13	99	22	99	23	99	23	23	100	13	99	22	99	23	99	23	99	23	23				
NL34	Zeeiland	30.2	99	2	98	4	98	9	98	9	9	99	2	98	4	98	9	98	9	98	9	9				
NL41	Noord-Brabant	0.0	87	3	97	3	97	20	97	20	20	100	0	99	4	99	9	99	9	99	20	20				
NL	Netherlands	626.4	100	0	99	4	98	9	99	26	26	100	0	99	4	99	9	99	9	99	25	25				
FR515	Vendée	85.0	96	18	96	18	96	18	96	18	18	97	16	97	16	97	16	97	16	97	16	16				
FR532	Charente-Maritime	328.2	72	39	72	39	72	39	72	39	39	85	40	85	40	85	40	85	40	85	40	40				
FR	France	413.2	77	30	77	30	77	30	77	30	30	88	30	88	30	88	30	88	30	88	30	30				
TOTAL	TOTAL	7387.4	74	20	74	20	74	20	74	20	20	73	20	73	20	73	20	73	20	73	20	20				

Table 4.6: Validation results for the pan-European and global maps with a 100-year return period, by countries and regions. 100-year flood zone area is taken from the reference maps. TUD-C refers to the model with corrected DEM and TUD-U to the model with uncorrected DEM. The indicators for correctness (I_{cor}) and fit (I_{fit}) are in %. For location of the regions, see Fig. 4.4.

NUTS	Name	TUD-C		TUD-U		JRC		GTSR	
		I_{cor}	I_{fit}	I_{cor}	I_{fit}	I_{cor}	I_{fit}	I_{cor}	I_{fit}
UKC	North East	23	21	15	14	35	25	12	12
UKD	North West	36	26	26	20	54	30	25	18
UKE	Yorkshire and the Humber	74	42	63	41	34	25	74	41
UKF	East Midlands	92	41	79	38	96	42	93	41
UKH	East of England	81	23	78	23	70	29	71	21
UKI	London	0	0	0	0	0	0	0	0
UKJ	South East	75	40	72	41	61	30	52	29
UKK	South West	33	25	14	12	29	23	45	33
UK	United Kingdom	68	32	58	30	60	31	64	30
PL424	Miasto Szczecin	83	79	91	80	53	46	87	77
PL426	Koszaliński	65	56	87	49	64	45	70	54
PL428	Szczeciński	72	66	87	65	55	50	75	63
PL621	Elbląski	93	86	99	86	75	68	97	87
PL633	Trójmiejski	63	50	91	55	22	17	79	54
PL634	Gdański	83	79	98	76	39	35	96	76
PL636	Słupski	54	54	68	53	0	0	0	0
PL638	Starogardzki	87	72	99	27	39	30	99	31
PL	Poland	77	72	91	66	47	42	79	63
NL13	Drenthe	100	0	100	0	0	0	100	0
NL21	Overijssel	99	19	99	19	0	0	100	19
NL22	Gelderland	78	1	88	1	0	0	100	1
NL31	Utrecht	87	5	94	5	0	0	96	6
NL32	Noord-Holland	100	5	100	5	0	0	100	5
NL33	Zuid-Holland	99	13	100	13	0	0	100	13
NL34	Zeeland	99	2	99	2	0	0	99	2
NL	Netherlands	99	4	99	4	0	0	100	4
FR515	Vendée	96	18	97	16	99	13	98	15
FR532	Charente-Maritime	72	39	85	40	47	29	88	39
FR	France	77	30	88	30	58	20	90	29
	TOTAL	74	20	73	20	51	31	73	19

are presented in Appendix E. Those scenarios exclude flood protection; influence of such structures on the results is discussed in the next section. The maps are also indicative for regional distribution and future trends in flood extents with other return periods. In total, the static method with the corrected DEM indicated 68 000 km² at risk of flooding within the domain (100-year return period), which included all European coasts except for parts of Russian and Ukrainian coasts. That is approximately 1.2 % of the corresponding inland area of the domain. The flood zones concentrate around the North Sea, where ESLs are among the highest, and many low-lying areas occur. Other pockets of flood hazard are mostly located at river deltas, which often feature depressions, e.g. in Italy (Po), Spain (Guadalquivir, Ebro), Poland (Vistula), Lithuania (Nemunas), Romania (Danube).

4

Future coastal flood hazard was projected taking into account three factors, namely changing meteorological conditions, rising mean sea levels (SLR) and effects of glacial isostatic adjustment (GIA). On average, 100-year surges would decrease slightly in future (2–9 cm) according to projections based on RCA4 climate model, and GIA will also contribute negatively to ESLs (8–15 cm). In effect, by mid-century, mean ESLs would decline, only become bigger in the subsequent decades due to SLR, which would contribute 30–45 cm compared to the historical scenario. However, the trends will be very uneven around Europe, as complex coastlines of Finland, Norway, UK or Greece skew the average figures. In effect, also for the 2021–2050 an increase of the potential flood zones is expected, albeit very small, of about 0.4–0.6 %, depending on emission scenario. For 2071–2100, the growth will amount to 3–8 %. In the north of Europe, mostly reductions in flood hazard are projected for the near-term due to lower surge heights, while in the long-term only parts of Sweden and Finland around the Gulf of Bothnia will see a decrease in hazard as consequence of intense GIA. By contrast, in the Mediterranean GIA is negligible and surge are mostly below 1 m, hence sea level rise will be the predominant factor causing an increase of ESLs in the entire region.

The size of the flood zones and their changes in the future are highly dependent on the assumed current levels of flood protection, as can be ascertained from Fig. 4.15. Without considering them, most of the study area is already marked as inundated by a 10-year surge; relatively little is added for higher return periods or future time points. When adding protection estimates from FLOPROS database, the flood zones become much smaller: only 1000 km² is within the 30-year flood zone, and 21 000 km² in the 100-year zone. Under climate change projections, the 30-year zone would expand even up to 40 000 km², and 100-year to 48 000 km². 1000-year zone would decline by about 1 % around mid-century, but increase by 12–17 % by end of century. Using JRC's estimates of protection levels the inundation extents become even smaller: 2800 km² (10-year) to 12 600 km² (1000-year). In general, such reworked maps give a more complicated picture, with 100-year zone decreasing by 2021–2050 before increasing again above 1971–2000 levels by 2071–2100. However, the 1000-year would then be expected to expand by 48–67 % by 2071–2100. Influence of the different flood protection assumptions is also visible in Fig. 4.16, where only the effect of an uniform SLR is added to ESLs under historical scenario. The flooded area is the smallest when JRC's estimates are used, but also increase more steeply than when FLOPROS or no flood defences at all are used.

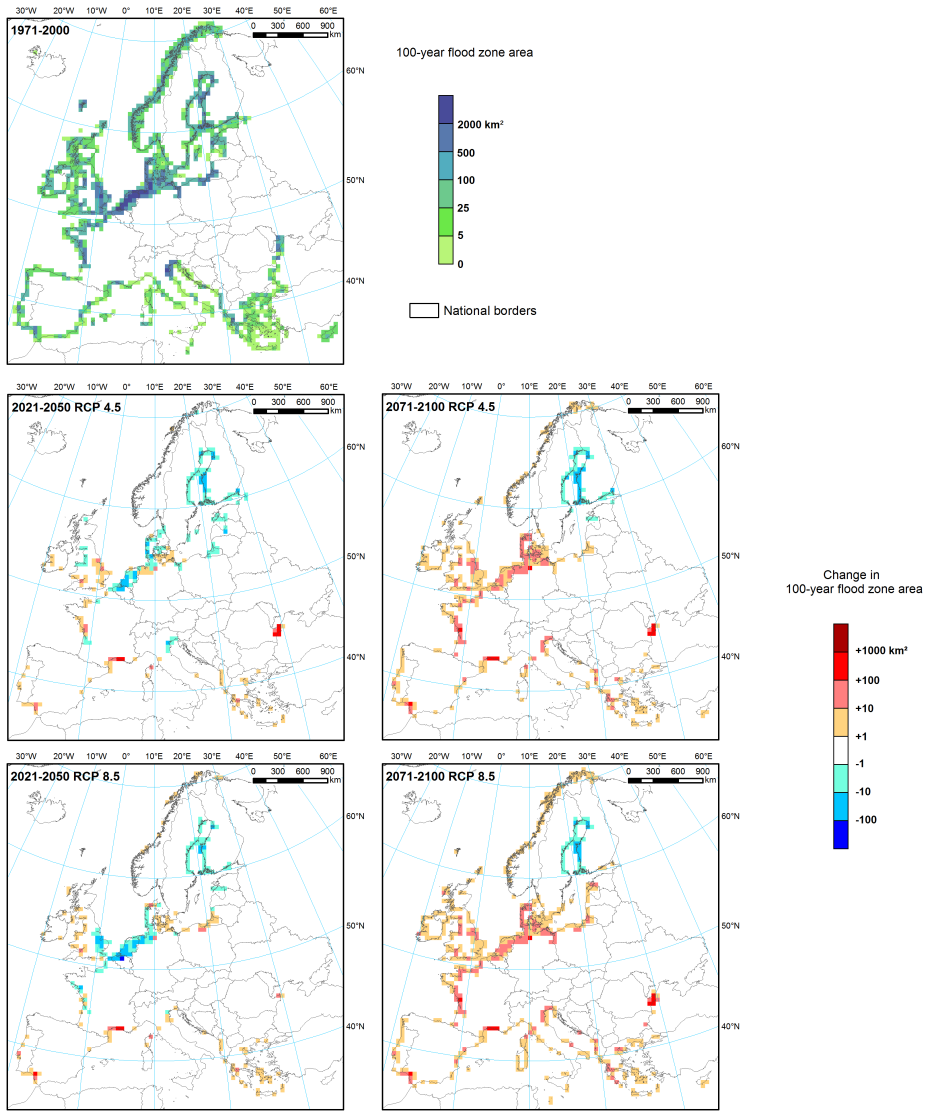


Figure 4.14: Flood extents under present and future climate (TUD method with corrected DEM, no flood protection). See section 4.2.4 for explanation of assumptions and climate models used in this assessment.

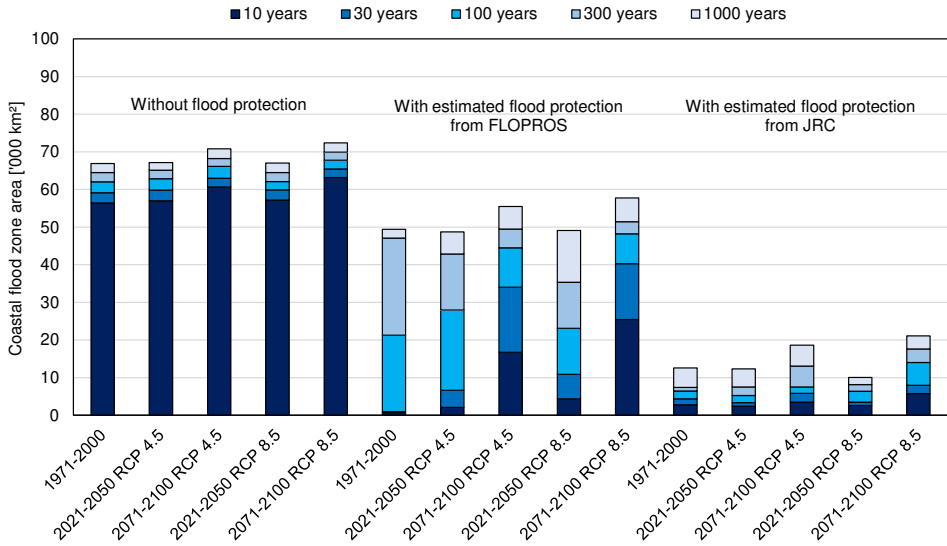


Figure 4.15: Coastal flood extents in Europe under present and future climate by return period, according to TUD model, using different assumptions of flood protection (from FLOPROS database and JRC). Only results for EU countries and Norway were included in this graph.

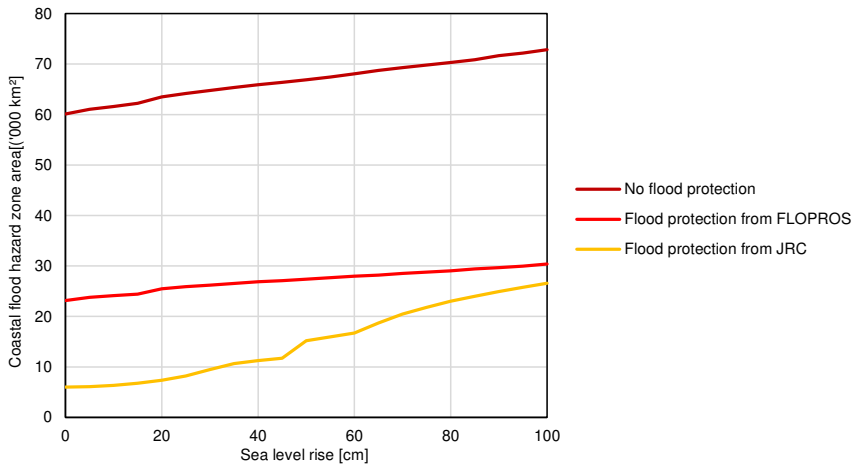


Figure 4.16: 100-year coastal flood zone area in Europe (EU plus Norway) assuming uniform sea level rise and using different assumptions of flood protection.

4.4. DISCUSSION

4.4.1. UNCERTAINTIES RELATED TO EXTREME SEA LEVELS

The analysis of ESLs includes several sources of uncertainties. Many are related to the input data. Storm surge heights are derived through a hydrodynamic model. Though it was shown that, as a whole, it has good accuracy, performance for individual stations was very diversified. Also, some regions, especially Mediterranean and Black seas or coast of France, had limited or no observational data for comparison. Moreover, the complicated shape of the coast could often not be incorporated, especially shores of Norway, Finland, Greece or Croatia, because the resolution of the model was not fine enough (ca. 12 km). Therefore, the error in deriving the surge height could be locally significant. Tides were obtained from a high-resolution model, yet it includes only 13 constituents and may not be as accurate in some regions with diversified coastline. Also, datasets on glacial isostatic adjustment and sea level rise have a resolution many times lower than the data on surges or tides.

Future changes in ESLs contain many uncertainties. The effects of ground subsidence were not taken into account due to lack of pan-European information, but could be locally significant. SLR could also have effects on tides and tide-surge interaction [262]. GIA is a very slow process, and the rate of vertical motion of the crust changes very little over time, though the resolution of available data is low [213]. Meanwhile, sea level rise is a combination of several climate-related factors, which are understood and quantified to a varying degree [214, 250]. Last but not least, there is uncertainty related with climate data, as the accuracy of storm surge estimates are dependent on the quality of air pressure and wind speed/direction data. The difference between RCP 4.5 and RCP 8.5 scenarios is sometimes very large, to the point that opposite trends are indicated. The projections used were generated by only one regional climate model - RCA4 driven by one global model EC-EARTH, which could give different results than other regional-global model combinations or the ensemble of general circulation models used in the JRC model.

An analysis of extreme wind speeds in Groenemeijer *et al.* [33] using an ensemble of EURO-CORDEX models has shown that there is good model agreement between climate hindcasts. However, it has also shown very little agreement on future trends – only for parts of North Atlantic and the Mediterranean Sea are a large decrease in extreme wind speeds is consistently being projected by different models. In effect, the are visible differences in the outcomes of the climate change simulations between TUD and JRC models. For instance, the TUD model predicts that extreme surges will mostly become lower in the Baltic Sea, opposite to the findings of the JRC study. On the other hand, JRC forecast a decrease in surge heights in most of the Iberia and British Isles, in contrast to this study, which mostly indicated increases.

4.4.2. UNCERTAINTIES RELATED TO COASTAL FLOOD EXTENTS

The analysis has shown that the results are very sensitive to different flood protection assumptions, especially in context of future projections. However, because information on dimensions and conditions of natural (dunes, cliffs, beaches) or artificial (sea walls, dikes) coastlines is only obtainable by detailed local studies; it is therefore not possible

to have complete information on the European scale. This information also changes relatively dynamically, compared to the climate or socio-economic situation, let alone underlying properties of the terrain: the coast erodes or builds-up by accumulation, flood defences deteriorate over time or are renovated and new ones are being constructed. Also, using nominal protection levels, for which some information could be found for selected countries or localities, also has pitfalls. For instance, the Netherlands have high protection standards, ranging from 1 in 1250 to 1 in 10 000 years in coastal dike rings [64]. When considering only overtopping of the dikes, indeed only 3 out of 400 dike sections in the study area have a probability of failure higher than 1 in 1000 years. However, when considering other failure mechanisms, 48 dikes segments are above this threshold according to the VNK study. Further, the different segments are not independent of each other. Hence, the probability of flooding in a given area is higher when failure of more than one segment can inundate it. In effect, the area of the 1-in-1000-years floodplain for the Netherlands is 3837 km², or more than a fifth of the area of dike rings included in the study.

More factors influence the performance of the European-scale maps. As Voudoukas *et al.* [109] and Ramirez *et al.* [263] have shown, the area with hazard is overestimated by the static method to a varying degree depending on the type of coast. Low-lying vicinities of estuaries and deltas are particularly prone to errors compared with steeper coasts. Part of the inaccuracy might stem from neglecting influence of river discharge in all European-scale assessments, but is included in English and Dutch flood hazard maps. Additionally, it may be noted that for England, the performance of the TUD coastal map was lower than in case of river phenomena. Here, the “correct” and “fit” measures are 68 % and 32 % for the 100-year flood map, respectively, in contrast to 78 % and 44 % reported in chapter 3. However, for the JRC coastal flood maps the figures are 60 % and 31 %, compared to 51 % and 40 % for rivers.

The construction of boundary conditions for flood modelling also influences the results: incorporation, or not, of waves into the model changed the flooded area estimate significantly. Comparing the flooded area by country (Table 4.7) shows that even with the static method and no flood defences, the models can yield very different results, depending on the forcing EWLs and underlying DEM. This is especially noticeable for countries around the Baltic Sea, Romania or Spain. Similarly, transposing the protection standards between models is not fully feasible. The estimates by JRC were based on EWLs including waves, therefore applying them to TUD model results in a very large drop in flood estimates. Only in the Baltic Sea, where waves are less significant, the protection standards are lower than the 100-year ESLs without waves. There is also large change in flood area when switching between JRC and FLOPROS databases of flood protection standards. This is because the two datasets were made using different assumptions and sources: FLOPROS was mostly focused on river flood protection, while the JRC study was dedicated to coastal floods only. Also, FLOPROS relied on available information nominal standards, while JRC’s estimates were made taking into account recorded flood damages and experts’ judgments. In context of future changes, coastal erosion/accumulation might change local protection levels, however no pan-European data are available on this aspect.

Table 4.7: 100-year flood hazard zone by country (EU countries and Norway only), according to different models and flood defence assumptions in km². TUD-C refers to the model with corrected DEM and TUD-U to the model with uncorrected DEM. (1) - protection standards from FLOPROS, (2) - protection standards from JRC's estimates.

Country	No flood defences			With flood defences		
	TUD-U	TUD-C	GTSR	TUD-C (1)	TUD-C (2)	JRC (2)
Belgium	1904	1772	2251	868	0	0
Bulgaria	66	63	0	63	0	38
Croatia	166	23	95	0	12	104
Cyprus	39	57	21	57	0	3
Denmark	3034	2386	2412	2378	140	2654
Estonia	83	465	20	465	465	49
Finland	1734	1401	871	1401	1369	566
France	5293	4155	4943	3139	0	4202
Germany	13 372	11 363	12 668	14	1207	8465
Greece	818	600	780	600	2	921
Ireland	481	444	136	2	0	622
Italy	5502	4580	5281	4576	0	4584
Latvia	436	111	74	111	111	77
Lithuania	501	237	493	237	237	497
Malta	4	3	0	3	0	0
Netherlands	17 839	16 816	18 006	0	0	0
Norway	1587	1648	1871	1637	0	1460
Poland	2854	1861	2313	1	1861	1319
Portugal	414	536	83	533	0	541
Romania	3296	163	0	163	0	2037
Slovenia	8	7	0	0	7	11
Spain	1138	1514	304	1502	1	368
Sweden	914	1154	760	1154	1003	443
United Kingdom	6929	8337	7785	102	24	8068
TOTAL	68 413	59 695	61 167	19 007	6 440	37 029

4.5. CONCLUSIONS

This chapter covered several aspects of present and future coastal flood hazards. Firstly, extreme sea levels along European coasts were computed, utilizing climate data with high temporal and spatial resolution. It was shown that using both climate reanalysis (ERA-Interim) and climate model control run (EURO-CORDEX), extreme storm surges could be accurately simulated in a hydrodynamic model. Also, the results show relatively higher accuracy of modelled data compared with observations than two other assessments (JRC and GTSR). The study found that sea levels under climate change have very diversified trends across different locations in Europe. Change in mean levels has the largest impact in most places in Europe. They will be compensated by ground uplift in Scandinavia, and by decrease in surge height in many other places. However, in areas where surges are small, such as the Mediterranean and Black seas, extreme sea levels could even double.

Secondly the accuracy in the pan-European EU-DEM elevation model was investigated in the context of its impact on flood modelling. It was found that vertical errors in the coastal floodplains of three countries analysed (UK, the Netherlands, Poland) were not negligible. In the case of Poland, the average error of -2. m in the coastal zone causes significant difference between inundation limits derived without and with correction of the DEM. Similar disparity in results was found for several other countries, mainly along the Baltic Sea (Table 4.7). It is therefore recommended to analyse the accuracy of DEMs underlying the flood analysis before calculating coastal flood extents.

Further, the three large-scale models were juxtaposed with four case studies in Europe, where the 100-year flood hazard zone covers more than 7000 km². Performance of the static method in all models was not satisfactory. For England, the accuracy of flood zone delimitation was similar in all variants, and was lower than in river flood maps over the same territory analysed separately by TUD and JRC. For Poland the performance was better, as the flood maps for that country come from research which also used static inundation, albeit utilizing a high-resolution DEM. For the Netherlands, either the whole low-lying area of the country was indicated as at risk of inundation or not at all, due to the difficulty of recreating the dike rings system in large-scale models. All models largely overestimated flood zones recorded during Xynthia storm surge in France. This area includes extensive low-lying areas and during the actual event they could not have been flooded because of the short duration of the phenomena, while the static method indicates the whole area as being at risk of flooding.

Finally, projections of future changes in flood zones from the TUD assessment were presented. Depending on time period and climate change scenario, different factors are the main contributors to future trends: storm patterns, mean sea level rise or glacial isostatic adjustment. However, it was shown that the results are highly influenced by the flood protection levels that were assumed. Both external databases of flood protection levels used different sources and methods, yielding widely disparate results in terms of future flood extents. As noted above, relying on protection standards can lead to underestimation of hazard due to neglecting dike reliability. Overall, continental analyses are useful because they are homogenous and allow drawing conclusions on larger scales. However, for the time being, they are not a good alternative for local assessments when high accuracy is the priority.



Previous page: Thames Barrier, constructed in 1982 to protect London from storm surges, might not be as effective if a surge coincides with a river flood wave, like during the 1928 disaster.

5

COMPOUND FLOOD POTENTIAL

5.1. INTRODUCTION

COMPOUND floods occur when high discharge in the rivers coincide with a storm surge, resulting in water levels higher than if they would have happened separately, consequently resulting in a flood. However, this compounding effect needs to be studied locally due to its limited geographical extent and the physical interactions involved. It is therefore necessary to firstly quantify the joint probability of co-occurrence of storm surges (including waves) and flood-inducing inland phenomena (high river discharges and extreme precipitation). This chapter analyses the dependency between these hydrometeorological phenomena to identify areas with the highest potential for compound flood occurrence. Consequently, for the purposes of this analysis, a compound flood will be defined as any occurrence of both extreme sea levels and high river discharges or extreme precipitation at the same time and location.

Presently, growing consideration is given to possible co-occurrence of hazards previously considered independently [265]. This attention is drawn primarily by damages caused by both coincidence of surge and excessive rainfall during tropical cyclones in the United States, including the \$150-billion deluge in Houston during hurricane Harvey in August 2017 [21]. Yet, climate of Europe differs substantially from American coasts, which are often affected by tropical storms. Even in the US, along coasts outside the paths of hurricanes there is very little dependency between coastal water levels and heavy precipitation [266], while correlation between river flows and surges is spatially diverse [267]. European coasts are affected by extra-tropical cyclones, with diverse mechanisms of fluvial and pluvial floods. Climate change is expected to increase the level of hazard in many parts of the continent through increased sea levels [229], river discharges [178] and extreme precipitation [268]. At the same time, several large European cities located in river estuaries are prone to coastal floods, such as Antwerp, Hamburg, London and Rotterdam.

This chapter has been submitted to Hydrology and Earth System Sciences [264].

Historical information on past damaging floods in Europe reveal that compound events have occurred in many locations. According to HANZE database (see chapter 6), out of 1564 floods that occurred in 37 European countries between 1870 and 2016, 23 (1.5 %) were compound floods, recorded in six countries (see also Fig. F.1 in Appendix F). The highest number of compound events, nine, were observed along the northernmost coast of the Adriatic Sea – Italian regions of Veneto and Friuli-Venezia Giulia (1927, 1951, 1952, 1953, 1957, 1966, 1986, 2008, 2012). In those situations, the events' river and coastal components merely occurred at the same time, generally without directly exacerbating total water levels. For instance, the November 1966 coastal flood in Venice (phenomena locally known as *acqua alta*), during which the highest water level ever recorded there was reached (194 cm), happened at the same time as high water in the Po river basin (137 km² inundated). Altogether, Adriatic Sea surges and coinciding high flows in the Po river resulted in approximately 25 fatalities altogether and several thousand people affected.

Another “hotspot” for compound events is the Mediterranean coast of France. Five damaging compound floods could be identified (1872, 1997, 2005, 2006, 2013). In 1872 the surge coincided with eight days of rain, resulting in 18 fatalities. The December 1997 event affected the vicinity of the Rhône river estuary, which was swelled by 669 mm of rainfall in four days and a storm surge. The other three were flash floods caused by more than 200 mm of rain in 24 hours at the time of very strong winds and high sea levels, each causing one fatality and many losses in several locations in the southern coast (and Corsica in 2013). The Western coast of France witnessed compound floods as well, for example along the Charente river in 1962 (1600 persons affected) and several rivers in the Brittany region in 2000 (600 persons affected). In both cases, a storm surge appeared during a particularly wet period, causing river flows to be elevated for a long period of time.

Remaining compound events across Europe are similar to those occurring in the western coasts of France. Surges and long periods of rainfall elevating river water levels caused compound events in Ireland in 2004 (200 persons affected) and 2009 (6800 affected), in England along The Humber in 1954 (4000) and the Bristol Channel in 1999 (1200), as well as on the river Scheldt in Belgium in 1928 (10 000). On the contrary, the causes of the 1928 Thames flood which resulted in 14 deaths in London and affected 4000 people, were unusual as high river discharge was a consequence of snowmelt, and the relatively moderate storm surge was exacerbated by a high tide. In the Baltic Sea, the only known instance of compound events was the storm surge along the Polish coast in 2009. There, the storm surge was not extreme, but unusually strong northerly winds pushed seawater upstream of the Odra and Vistula rivers at the time of increased runoff from rainfall. This caused inundation along Odra as far as the city of Szczecin, 70 km upstream.

Compound flood hazard in Europe was studied before, but in a variety of case studies using a wide array of methods and variables, covering Italy [269], the Netherlands [270], Sweden [271] and United Kingdom [198, 272]. There is, therefore, a clear need for pan-European assessment of compound flood potential that includes both extreme rainfall events and high river discharges.

In this chapter, a large number of observational datasets and climate reanalyses was

utilized to investigate dependency between hydrometeorological phenomena which contribute to compound floods along European coasts. Dependency was analysed using copula theory. The goals of this chapter's analysis, all undertaken for the first time on European scale, are (1) establish dependency patterns in observational data between storm surge heights, river discharges, precipitation and wave heights, (2) evaluate the ability of climatic and hydrological models to recreate the dependencies found in observations, (3) synthesize the information on joint probability and intensity of compound flood-inducing phenomena into an indicator of areas, where compound flooding is most likely to occur and more detailed, local analysis of flood hazard should be carried out.

5.2. MATERIALS AND METHODS

The study described in this chapter was carried out in three phases – each introduced in this section. Firstly, pan-European datasets on storm surge heights, precipitations amounts, river discharges and significant wave heights were collected. Then, pairs of variables for the same, or nearest available, location were analysed through copulas to obtain correlations and dependency structures. Both observational and modelled datasets are used, with modelled data validated based on observations. Finally, areas with the highest and lowest potential for compound flood occurrence are identified using two composite indices. The analysis builds extensively on the data from chapters 2, 4 and 6.

5.2.1. DOMAIN AND DATA

Datasets collected for this study are summarized in Table 5.1. Fundamental for the analysis were direct measurements (observations). Hourly records of sea levels were taken from 156 gauges, the same as used in chapter 4. The tidal component was removed from the data using a skew surge approach, i.e. the difference between the predicted astronomical high tide and nearest observed high water [222]. Detailed sources of the sea level data and information on how the data can be found in chapter 4. Records of daily river discharges were collected from 1791 gauges and are the same as in chapter 2. Finally, daily precipitation was drawn from two sources, both being gridded interpolations of measurements taken at weather stations: E-OBS v16.0 with a 0.25° resolution¹ [138], and EFAS-Meteo with a 5 km resolution [273]. Wave heights from 48 buoys were taken from Vousdoukas *et al.* [230].

For a full pan-European analysis, data from several models were collected. Daily river discharges in a gridded, 5-km network were obtained from the European Flood Awareness System (EFAS), which utilizes the Lisflood hydrological model driven by meteorological data from EFAS-Meteo [274]. Sub-daily storm surge heights were simulated in chapter 4 using Delft3D [232] with a 0.11° regular rotated-pole grid (ca. 12.5 km) driven by wind and air pressure data from ERA-Interim climate reanalysis [139]. Sub-daily significant wave heights were obtained from WaveWatch III simulations [275] driven by ERA-Interim and carried out by Mentaschi *et al.* [276], with results presented per 25 km coastal segments. Precipitation was taken directly from ERA-Interim, which has a 0.75°

¹Approximately 200–600 km² grid cells over Europe.

Table 5.1: Summary of data collected for the study described in this chapter, by variable, input climate forcing, temporal resolution and timespan. See text for details and sources of datasets.

Climate forcing > Variable v	Observations	EFAS-Meteo	ERA-Interim	EURO-CORDEX (RCA4)
River discharges	daily 1950–2013	daily 1990–2013	–	daily 1970–2005
Storm surges	hourly 1970–2014	–	6-hourly 1979–2014	6-hourly 1970–2005
Precipitation	daily 1950–2017	daily 1990–2013	3-hourly 1979–2016	6-hourly 1970–2005
Wave height	subdaily 1989–2013	–	3-hourly 1980–2012	–

resolution².

Lastly, data were collected from simulations utilizing hindcasts from regional climate models within the EURO-CORDEX framework [140]. To be comparable, the different variables would need to originate from the same climate model run. Here, storm surge and river discharge simulations, made with Delft3D and EFAS, respectively, were only both available for the RCA4 regional model [231] coupled with the ICHEC-EC-EARTH general circulation model, realization r12i1p1. Details of those simulations can be found in chapter 4 and Alfieri *et al.* [178]. Precipitation was obtained directly from the RCA4 historical run at 0.11° resolution (1970–2005).

The study area is the same as in chapter 4, which is comprised of all European coasts with the exception of outlying islands (the Azores, Madeira, the Canary Islands and Norwegian Arctic dependencies) as well as majority of Russian and Ukrainian coastline. Grid cells of the Delft3D model were connected with the geographically nearest grid cell of the other datasets. A different method was only used for linking river gauges and EFAS grid cells. For each river gauge, an EFAS grid cell with the smallest difference in catchment area within 10 km radius was considered corresponding to the river gauge in question.

5.2.2. STATISTICAL ANALYSIS OF DEPENDENCIES BETWEEN VARIABLES

The dependency between the different variables is analysed here using copulas, which are an important tool for studying dependency between hydrological and meteorological phenomena, such as relationship between flood volume and peak discharge [277], precipitation at two different locations [278] and precipitation amount and duration [279]. Copulas were used also in chapter 2 and are described in Appendix A. However, the analysis was extended to cover seven copula types, instead of only three described in Appendix A, in order to include more possible dependency structures. A summary of the copulas used in this chaoter and their cumulative density functions are presented in Table 5.2. The table also indicates what type of tail dependence is captured by each copula type.

As a diagnostic tool to choose the copula that best represents the dependency structure, one of the test statistics in the “Blanket Test” class discussed by Genest *et al.* [280],

²Approximately 2000–6000 km² grid cells over Europe.

Table 5.2: A summary of copulas used in the analysis. Based on Joe [162].

Copula	CDF for copula C	Tail dependence
Gaussian	$C(u, v; \rho) = \Phi_\rho(\Phi^{-1}(u), \Phi^{-1}(v)), \rho \in [-1, 1]$	No
Gumbel	$C(u, v; \delta) = \exp(-([-\log(u)]^\delta + [-\log(v)]^\delta)^{1/\delta}), \delta \geq 1$	Upper
Clayton	$C(u, v; \alpha) = (u^{-\alpha} + v^{-\alpha} - 1)^{-\alpha}, \alpha \in [-1, \infty)$	Lower
Frank	$C(u, v; \theta) = -\theta^{-1} \log\left(\frac{1 - e^{-\theta} - (1 - e^{-\theta}u)(1 - e^{-\theta}v)}{1 - e^{-\theta}}\right), \theta \in (-\infty, \infty)$	No
t	$C(u, v; P; f) = \int_{-\infty}^{t_f^{-1}(u)} \int_{-\infty}^{t_f^{-1}(v)} \frac{\Gamma(\frac{f+2}{2})}{\Gamma(\frac{f}{2})\sqrt{(\pi f)^2 P }} (1 + \frac{\mathbf{x}' P^{-1} \mathbf{x}}{f})^{-\frac{f+2}{2}} 2\mathbf{x}$	Upper and lower
Plackett	$C(u, v; \vartheta) = \frac{1}{2}\eta^{-1}(1 + \eta(u + v) - [(1 + \eta(u + v))^2 - 4\vartheta\eta uv]^{1/2}), \vartheta \geq 0$	No
Joe-Clayton (BB7)	$C(u, v; \kappa, \beta) = 1 - (1 - [(1 - \bar{u}^\kappa)^{-\beta} - (1 - \bar{v}^\kappa)^{-\beta} - 1]^{-\frac{1}{\kappa}})^{\frac{1}{\beta}}, \kappa \geq 1, \beta > 0$	Upper and lower

Symbols: $u, v \in [0, 1]$, Φ is the bivariate Gaussian cumulative distribution with Pearson's correlation coefficient ρ , $\eta = \vartheta - 1$, t_f^{-1} denotes the quantile function of a standard univariate t_f distribution, f are the degrees of freedom, \mathbf{x} is a random vector, and the remaining symbols are copula-specific parameters.

which is the Cramèr–von Mises statistic (M), was utilized. The test is described in Appendix A. A copula that had the lowest M statistics for a given pair of variables for a given location was considered the “best-fitting” copula and used for subsequent analyses. However, if the correlation was very weak, i.e. in the interval [-0.1,0.1], the copula type was not calculated, except for the purpose of calculating a synthetic index of compound flood potential in section 5.3.4. Furthermore, full marginal distributions of all variables were used to compute correlation coefficients and best-fitting copula types, rather than only the most extreme values of the distribution above a given percentile. The rationale for this important assumption is related to an analysis of the resulting dependencies and discussed in section 5.4.3.

5.2.3. COMPOSITE INDICES OF COMPOUND FLOOD POTENTIAL

The various dependency structures found in the many data series of storm surge heights, precipitation amounts and river discharges are presented in the results section. Those translate into return periods of compound events, which also involve a variety of intensities along the joint distributions' margins. In order to synthesize this information to identify areas with highest potential for a hazardous compound event, two composite indices were constructed . The first is intended to represent the potential of joint occurrence of a storm surge and a flash flood, using three subindices: extreme precipitation amount, storm surge height and joint return period. The other is for the joint occurrence of a storm surge and a river flood and combines three subindices: extreme river discharge, storm surge height and joint return period. Thus, by combining two boundary conditions and joint probability, the indices distinguish areas favourable for compound flood occurrence.

The indices are an average of a set of subindices $S_{i,c}$ for each data point c along the

coast:

$$S_{i,c} = \frac{v_{i,c} - \min(V_i)}{\max(V_i) - \min(V_i)} \quad (5.1)$$

where v_i is a variable that is used to construct the subindex, with $i = 1, 2, 3, 4, 5$, and $V_i = \{v_{i,1}, v_{i,2}, \dots, v_{i,n}\}$ is a set of all observations of v_i . Each variable v_i is a decimal logarithm of the following indicators:

- v_1 is the joint return period (in years) of a 10-year precipitation event occurring on the same day as a 10-year storm surge. This is calculated using the best-fitting copula.
- v_2 is the daily precipitation amount (in mm) with a return period of 10 years.
- v_3 is the storm surge height (daily average in m) with a return period of 10 years.
- v_4 is the return period (in years) of a 10-year extreme high river discharge occurring on the same day as a 10-year storm surge. This is calculated using the best-fitting copula.
- v_5 is the river discharge (daily average in $\text{m}^3 \text{s}^{-1}$) with a return period of 10 years.

In other words, each indicator was transformed into decimal logarithm and standardized in the interval $[0, 1]$. The subindices were aggregated by a simple average into a composite index for a storm surge-flash flood combination I_p and storm surge-river flood combination I_d :

$$I_p = \frac{(1 - S_1) + S_2 + S_3}{3} \quad (5.2)$$

$$I_d = \frac{(1 - S_4) + S_2 + S_5}{3} \quad (5.3)$$

The composite index can have values in the interval $[0, 1]$. I_p was computed for all coastal segments in Europe, while I_d only for estuaries of rivers with a catchment area of at least 500 km^2 . The indices were calculated from 1990–2013 data. Precipitation amounts for the index were taken from EFAS-Meteo, river discharges from EFAS/EFAS-Meteo and storm surge heights from Delft3D/ERA-Interim.

5.3. RESULTS

In this chapter, only results calculated using a daily temporal resolution for all datasets are presented. This is for the sake of clarity and brevity, as the dependency structures in daily and 6-hourly data were found to be very similar. Appendix Fig. E2 compares Spearman's rank correlation coefficients computed from daily and 6-hourly series for a few example pairings of variables and datasets. When correlations calculated from different data sources are compared throughout the paper, only data from overlapping time periods are used for the analysis, e.g. observations from 1990–2013 are used when comparing with results from EFAS, rather than full series starting in 1950. There were very few overlapping time series for observed surges and waves in our dataset, hence those results are excluded.

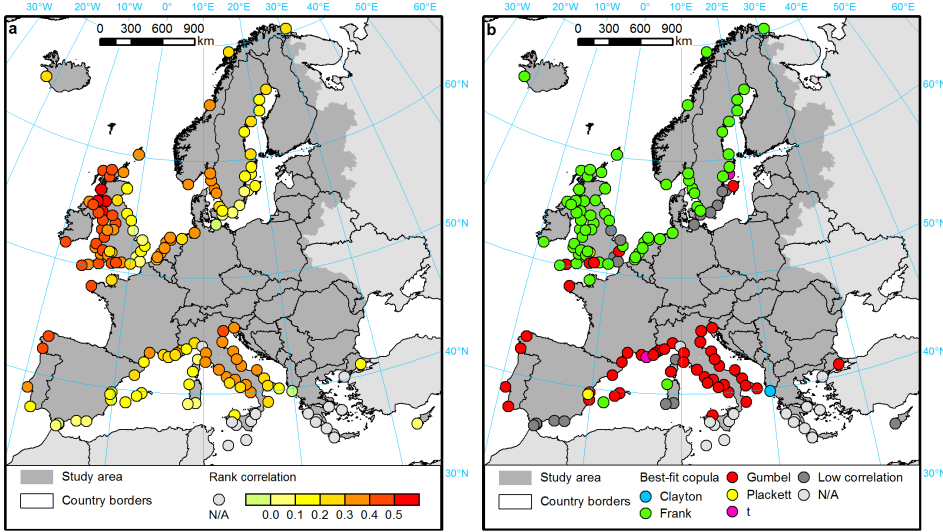


Figure 5.1: (a) rank correlation between observed daily storm surge and precipitation; (b) best-fitting copula type for dependency between observed daily storm surge and precipitation.

5.3.1. DEPENDENCY STRUCTURES IN OBSERVATIONAL DATA

Dependency between storm surge heights and precipitation amounts is presented in Fig. 5.1. Strongest dependency (rank correlation 0.3 and more) is observed in the west-facing coasts, such as western Great Britain, the Netherlands, western Sweden and Norway, and western Iberia. Along the coasts on the opposite side (eastern Great Britain, Sweden or Spain) the correlation is much weaker, mostly below 0.2. A notable exception is the eastern coasts of the Apennine Peninsula, where the correlation is stronger than in other parts of the Mediterranean Sea. Indeed, the highest correlation in that basin was calculated for Venice tide gauge, where, as noted in the introduction, compound events are particularly frequent. Further, there is a sharp divide in dependency structure between northern and southern Europe. In total, out of 120 gauges for which a copula type was calculated for the period 1970–2014, Frank copula was the best-fitting type for 56% and Gumbel for 40% (some gauges did not have comparable E-OBS precipitation grid points nearby or the rank correlation was too low). However, gauges in northern Europe show almost exclusively Frank copula dependency, while those in the south – Gumbel copula dependency. Other types of copulas appear only in a few gauges, exclusively in the south.

Dependency structures observed between storm surges and river discharges are more complex (Fig. 5.2). Similarly to precipitation, high correlations are observed in west-exposed coasts. Yet, higher correlation is also very noticeable along the main storm corridor in Europe, which goes from Ireland and Great Britain through the Netherlands, northern Germany, Denmark, southern Sweden, and ending in the eastern Baltic Sea coasts. In Scandinavia, the correlation visibly weakens moving north, while in Great Britain it lowers moving east. Naturally, moving from the coast to the interior of the con-

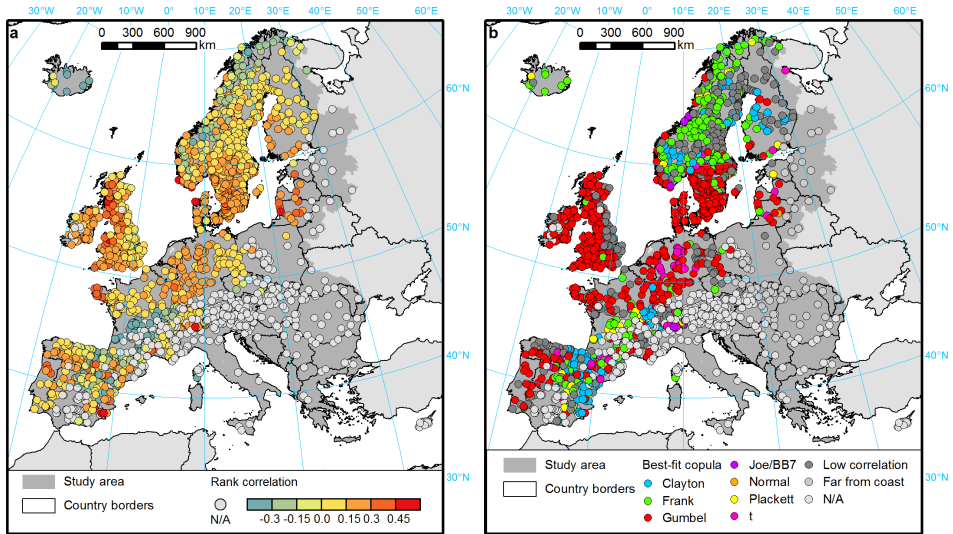


Figure 5.2: (a) rank correlation between observed daily storm surge and river discharge (river gauges compared with the closest tide gauge); (b) best-fitting copula type for dependency between observed daily storm surge and river discharge (river gauges compared with the closest tide gauge).

tinent the dependency also weakens, to the point that in central France or north-eastern Spain, where discharges are compared with Mediterranean tide gauges, the correlation mostly turns negative. Stark spatial patterns are also visible for best-fitting copula types. Along the aforementioned storm path the Gumbel copula dominates, and is also most frequent among all river gauges for which data is available (56%). In Scandinavia, except southern Sweden, Frank copula is most common, and best-fitting for 20% of all gauges in Europe. Clayton copula (12%) occurs in stations in Spain and France, usually for those with negative correlation, but also in some locations in Scandinavia. Remaining copula types (12%) are spread without clear pattern across Europe, but appear more often in France and Spain, in gauges located further away from the coast. Examples of two most common dependency types in this analysis, Gumbel and Frank, are shown in Fig. 5.3.

5.3.2. VALIDATION OF MODELLED DATA

Analysis of model's performance was first carried out by validating the marginal distributions of variables obtained through ERA-Interim and EFAS-Meteo. They were compared with observed daily time series of precipitation, surges and river discharges. EURO-CORDEX data are a hindcast, hence those time series are not directly comparable with observations. The performance of models (or alternative observational data from EFAS-Meteo) for different variables is similar. Average rank correlation for storm surge heights from tide gauges compared with data calculated from Delft3D/ERA-Interim is 0.64 (1979–2014). Overall, surges in northern Europe were modelled more accurately than those in the Mediterranean. For river discharges in EFAS, the average rank correlation with river gauge observations is 0.68 (1990–2013). For precipitation (evaluated at tide gauge loca-

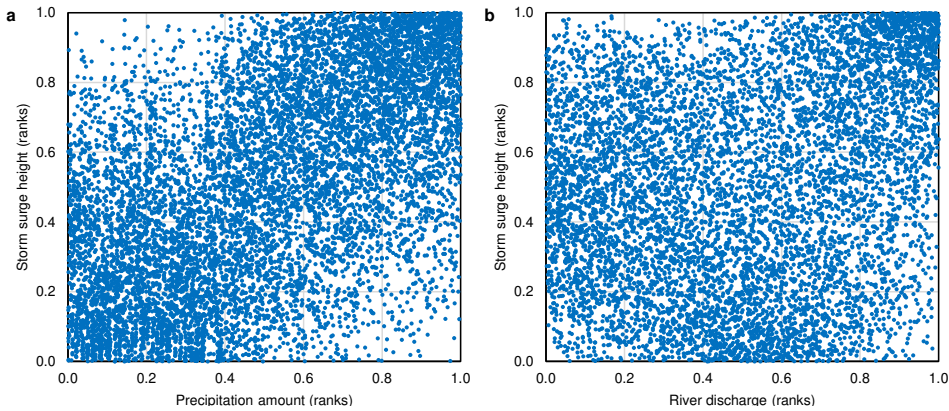


Figure 5.3: Examples of highly correlated storm surges and precipitation (a) or river discharge (b). In the left example, station Millport in Scotland shows Frank copula-type dependency, while in the other example, surges from Tredge, southern Norway, exhibit Gumbel copula-type dependency with discharges at river station Haugland.

tions), the correlation between E-OBS and EFAS-Meteo is 0.65 (1990–2013), and between E-OBS and ERA-Interim is 0.56 (1979–2014). In case of precipitation, the result is affected by large differences in grid sizes (ERA-Interim is much coarser, and EFAS-Meteo much finer than E-OBS) and noticeable inaccuracies of interpolated data sets in coastal areas. Finally, the average rank correlation of observed and modelled discharges is 0.65. Results for individual stations are presented in Appendix Figs. E3, E4 and E5.

Three combinations of models were used to compute dependency between storm surges and precipitation, and were compared with rank correlations obtained from observations (Fig. 5.4). Performance of all three model combinations is similar and relatively good, with R^2 in the range of 0.6–0.67. Also, in all three configurations the correlation between modelled surge and precipitation is overestimated on average compared to the observations. EURO-CORDEX data indicate the best performance, but with some visible bias, in contrast to the other two model combinations. Spatially, the differences between modelled and “observed” rank correlations are distributed very unevenly. The largest overestimation of correlation is noticeable in southern Great Britain, the Netherlands and western Iberia, with much better performance for northern Great Britain, Scandinavia and eastern coast of Italy (Appendix Fig. E6). However, the dependency structure is largely preserved, with the best-fitting copula types being very consistent between modelled and observed data. Stations in the Mediterranean Sea with insufficient data in Fig. 5.1 were indicated by models as belonging to Gumbel copula type, which is consistent with other stations in southern Europe. As a result, the share of Gumbel and Frank copulas indicated as best-fitting type is estimated at 46–49% and 47–53%, respectively.

Models’ performance in recreating the dependency between storm surges and river discharges is not as good as for precipitation. Combination of surge heights from Delft3D with ERA-Interim forcing and discharges from EFAS is very badly correlated with depen-

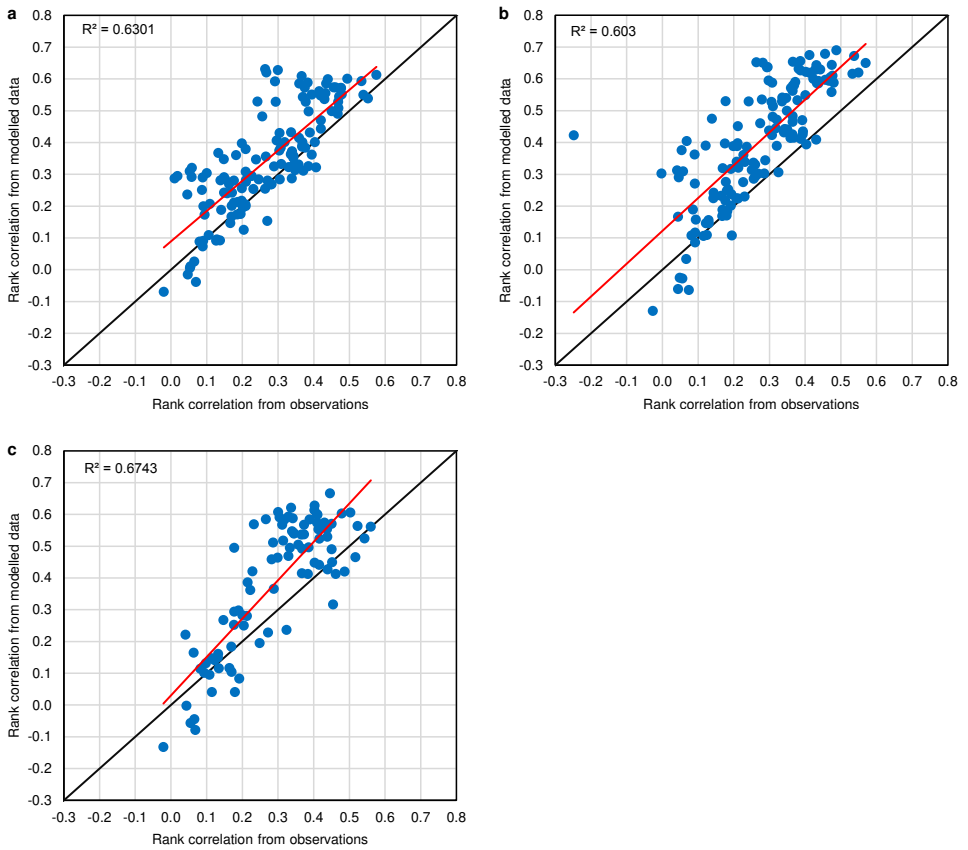


Figure 5.4: Comparison of rank correlations between daily storm surges and precipitation: (a) Delft3D/ERA-Interim + EFAS-Meteo, (b) Delft3D/ERA-Interim + ERA-Interim and (c) Delft3D/CORDEX + CORDEX.

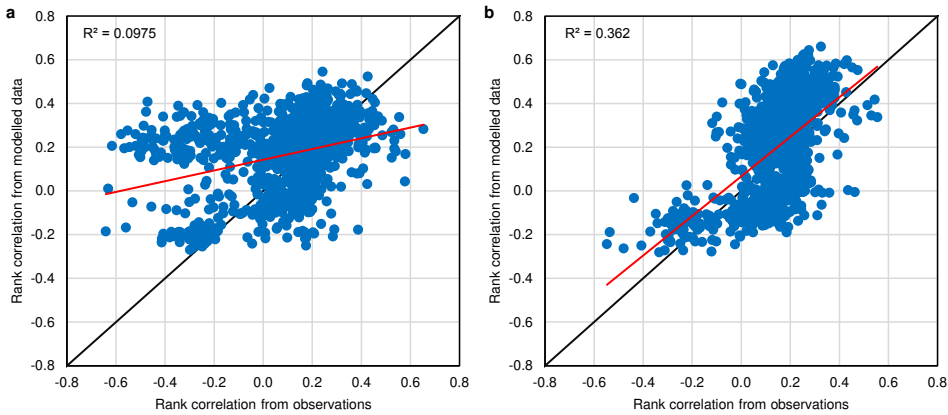


Figure 5.5: Comparison of rank correlations between daily storm surges and river discharge: (a) Delft3D/ERA-Interim + EFAS/EFAS-Meteo and (b) Delft3D/CORDEX + EFAS/CORDEX.

dependencies found in observations (Fig. 5.5), with R^2 equalling only 0.1. On the other hand, surges and discharges forced by CORDEX hindcast perform much better, with R^2 equal to 0.36. This is because there is a lack of sea level observations for 1970–2005 along the Mediterranean coasts of France and Spain. Models have shown particularly poor performance for river gauges in proximity to the Mediterranean Sea (Appendix Fig. F.7). Without those stations, the R^2 between ERA-Interim/EFAS data and observations would be 0.39. Otherwise, there is no clear pattern in the distribution of errors, though in areas most frequently affected by winter storms (corridor from Ireland to southern Sweden) the models' performance is somewhat better. The rank correlation for stations in Scandinavia is lower for models than for observations, while in France and Spain it is, in most cases, substantially larger. It should be noted that the errors originate rather in the storm surge model than in the river model, as the rank correlations from tide gauge-EFAS combination compared with rank correlations from observations give an R^2 of 0.44, while for Delft3D-river gauge combination the R^2 is 0.17. It can be due to the fact that a large number of river stations, mostly in France and Spain, are paired with tide gauges where storm surge series are modelled much less accurately than in the North or Baltic Seas. Exclusion of those stations (ca. 20% of total) increases R^2 for Delft3D-river gauge combination from 0.17 to 0.60.

At coastal gauge locations, model performance is also unsatisfactory in relation to river discharges. Only a limited number of stations had comparable data (78 or 43), but the relatively poor R^2 (0.15–0.28) and substantial bias is noticeable (Fig. 5.6). In the first comparison, tide gauge series are replaced by reanalysis using Delft3D and ERA-Interim, with EFAS discharges used for both dependency calculations. CORDEX-generated data series mostly underestimate it. Also, the majority of modelled dependencies show Frank copula-type dependency, in contrast to Gumbel being most frequent in the “observations”. Out of the stations available, gauges in Great Britain indicate the largest error, and those in Scandinavia relatively smaller (Appendix Fig. F.8).

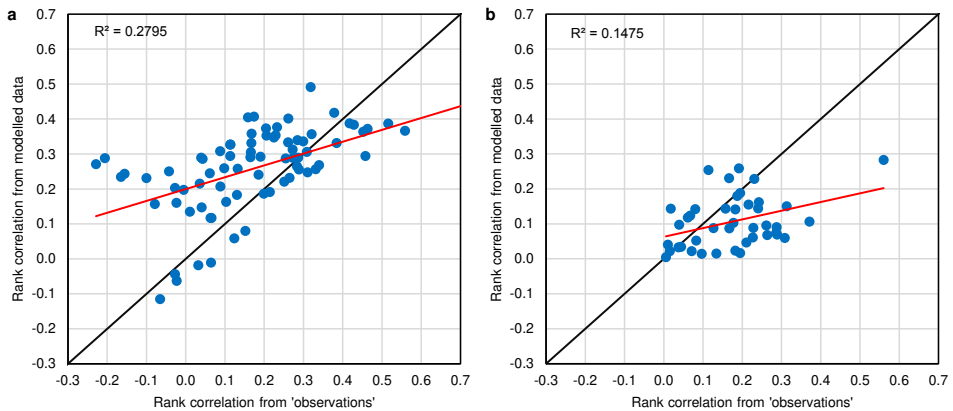


Figure 5.6: Comparison of rank correlations between modelled and “observed” (tide gauges + EFAS/EFAS-Meteo) daily storm surge and river discharge for closest river with catchment area of at least 500 km². (a) Delft3D/ERA-Interim + EFAS/EFAS-Meteo; (b) Delft3D/CORDEX + EFAS/CORDEX.

5

5.3.3. DEPENDENCY STRUCTURES IN MODELLED DATA

Using modelled storm surges, precipitation, discharges and waves provides full coverage of European coasts, not attainable with scattered observations. Fig. 5.7 presents rank correlations and best-fitting copula types calculated using storm surge heights from Delft3D/ERA-Interim and precipitation from EFAS-Meteo. In general, correlations from observations (Fig. 5.1) blends well with model outputs, so that the geographical distribution of rank correlations between daily surge and precipitation is very similar to the observations. Highest correlations observed in west-exposed coasts and Italy, the lowest in eastern Great Britain, Iceland and south-west Baltic Sea. The distribution of best-fitting copula types is also similar, with Frank copula dominating in northern Europe (and 56 % of all coastline) and Gumbel dominating in the south (38 %). Using ERA-Interim reanalysis instead of EFAS for precipitation gives very similar results both in terms correlation and best-fitting copula types. Hindcast data from EURO-CORDEX are slightly less aligned, with some overestimation in northern Europe and eastern Mediterranean relative to the reanalysis (Appendix Fig. F9a). Nonetheless, there is an overall good match between the hindcast and the reanalysis with EFAS-Meteo, with $R^2 = 0.75$ (Appendix Fig. F9b).

Dependency between storm surge heights and river discharges from Delft3D/ERA-Interim and EFAS/EFAS-Meteo, respectively, is shown in Fig. 5.8 (rank correlations) and Fig. 5.9 (best-fitting copula types). The geographical distribution of correlations for all coastal catchments is similar to those between storm surges and precipitation described in the previous paragraph, as the vast majority of storm surge data points were connected with very small, one-grid cell catchments (25 km²). Still, the average correlation is almost a third lower. Therefore, the second set of figures uses only EFAS grid cells (within 25 km distance) that have at least 500 km² catchment area. This largely weakens the correlations with storm surges, hence no distinct patterns could be observed, though still more correlation is visible in western Spain and Portugal, along the Irish Sea

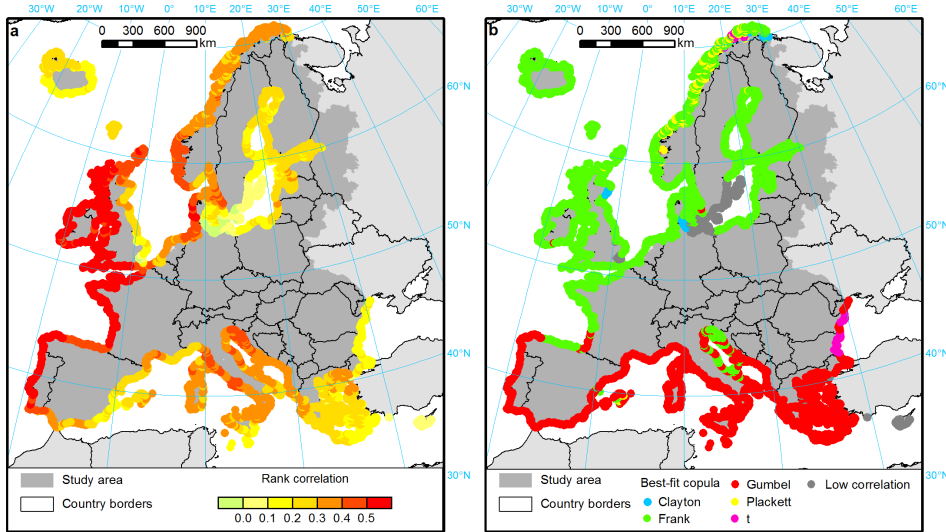


Figure 5.7: (a) rank correlation between modelled daily storm surge (Delft3D/ERA-Interim) and precipitation (EFAS-Meteo); (b) best-fitting copula type for dependency between modelled daily storm surge and precipitation.

and central Italy. In the vast majority of data points (84–87 % of coastline) the Gumbel copula is indicated as the most optimal to model dependency between surge and river discharge. However, using data from EURO-CORDEX, the pattern of best-fitting copula types is closer to that found in observations, with Gumbel being most optimal for 55–66 % of coastline. EURO-CORDEX data show higher rank correlations than the reanalysis in general (Appendix Fig. E10), but both model configurations are relatively aligned, with R^2 of 0.65–0.67 (Appendix Fig. E11).

Finally, modelled significant wave heights were used to analyse correlations with storm surge heights. This combination of events does not generate a compound flood, but nonetheless could be an important contributing factor. The resulting patterns are similar to other combinations, with west-facing coasts having the highest dependency (Fig. 5.10). However, Icelandic and Italian coasts also stand out with high correlation. In relatively sheltered locations, such as the western Baltic Sea, Aegean Sea and Alboran Sea (westernmost part of the Mediterranean) the correlation is the lowest and mostly negative. Gumbel copula is the best-fitting dependency structure for the vast majority of the coastline (84 %). Frank copula (10 %) can be found only in some east-facing coasts and in the far north of Europe.

5.3.4. COMPOUND FLOOD POTENTIAL INDEX

The two variants of the compound flood potential index – for storm surges combined with either extreme precipitation (as a proxy for flash floods) or high river discharges (as a proxy for river floods) – are presented in Fig. 5.11. Higher values of the index should be interpreted as an indication that local hydrometeorological conditions are

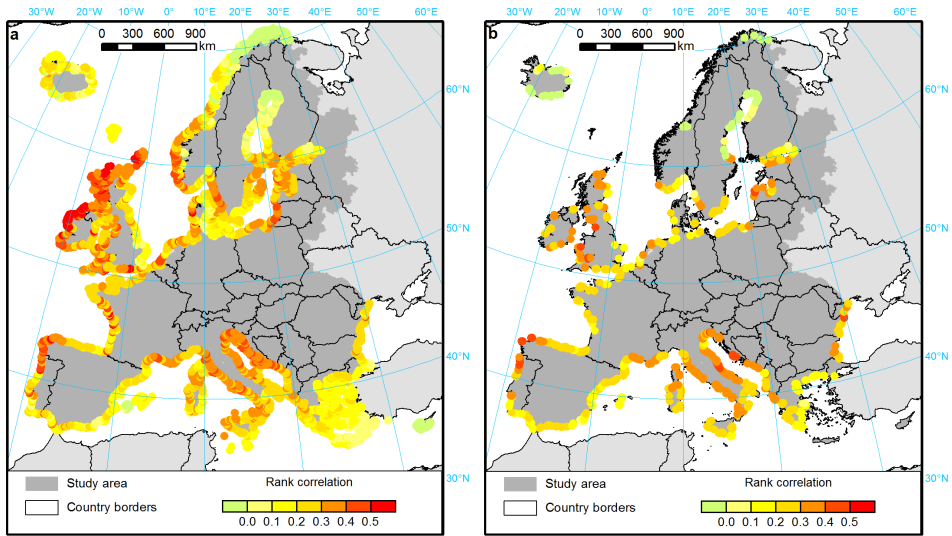


Figure 5.8: Rank correlation between modelled daily storm surge (Delft3D/ERA-Interim) and river discharge (EFAS/EFAS-Meteo), for (a) any closest river and (b) for closest river with catchment area of at least 500 km². For rank correlation between observed surge and EFAS/EFAS-Meteo-modelled river discharges in outlined circles see Appendix Fig. F.12).

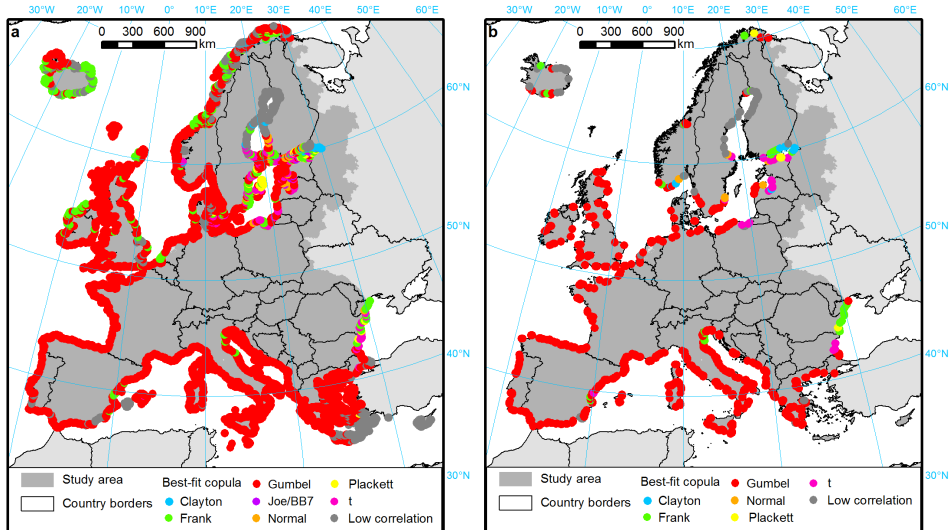


Figure 5.9: Best-fitting copula type for dependency between modelled daily storm surge (Delft3D/ERA-Interim) and river discharge (EFAS/EFAS-Meteo), for (a) any closest river and (b) for closest river with catchment area of at least 500 km². For best-fitting copula types for observed surge and EFAS/EFAS-Meteo-modelled river discharges see Appendix Fig. F.13.

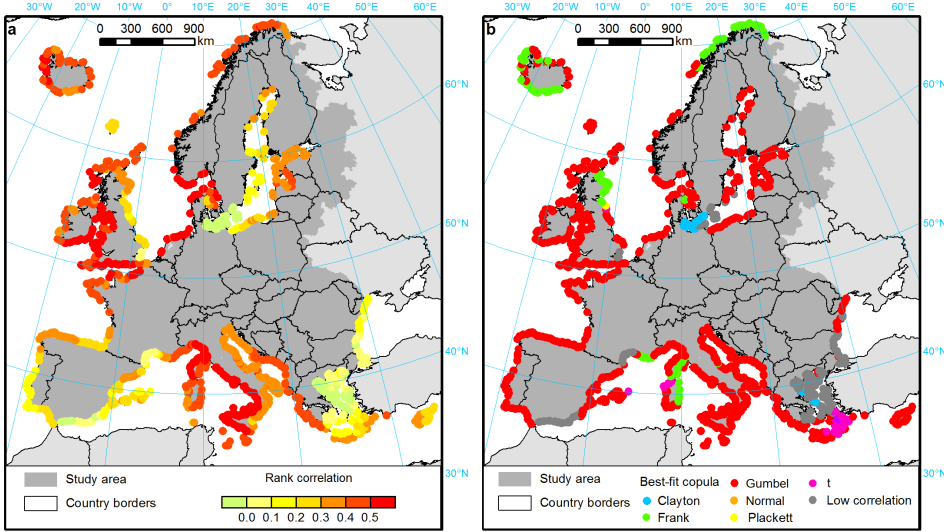


Figure 5.10: (a) rank correlation between modelled daily storm surge and significant wave height (Delft3D/ERA-Interim + WW3/ERA-Interim). Rank correlation between observed surge and modelled wave height in outlined circles; (b) best-fitting copula type for dependency between daily storm surge and significant wave height.

more favourable for occurrence of compound flood events than in other locations. The individual components, i.e. return periods of joint occurrence and intensity of marginal events, are shown in Appendix Fig. E14 and E15, respectively. Storm surges are the highest along the North Sea and Baltic Sea coast, and lowest in the Mediterranean region, while for extreme precipitation essentially the reverse is true – smallest precipitation amounts with a 10-year return period are recorded in northern Europe, and the highest in southern France, eastern Spain, Italy and Greece. River discharges are, very roughly, proportional to catchment size.

Return period of joint occurrence of a 10-year storm surge and 10-year extreme precipitation event differs substantially between southern Europe, where it is below 500 years (often less than 100 years), and northern parts of the continent, where it is above 1000 years. This is a result of different copula types indicated as best-fitting in the two regions (see section 5.3.3), with upper tail dependence in the data series from the Mediterranean region being the reason for relatively high probability of occurrence of compound flood events. The return periods of co-occurrence of surges and high water in rivers is more evenly spread, and are mostly less than 500 years along the majority of southern and western Europe's coasts. Only in the far north of the continent (Iceland, Norway, northern Baltic Sea) and along the Black Sea it is much higher, above 1000 years.

Combining the subindices together brings a complex picture (Fig. 5.11). Flash flood-storm surge co-occurrence is indicated as having most potential to cause a compound flood in north-western Spain and Portugal, southern France, north-west and southern Italy, Adriatic Sea coasts and Greece, and the lowest potential along the Finnish, Swedish and Icelandic coasts. It is also relatively higher along the southern and eastern shores of

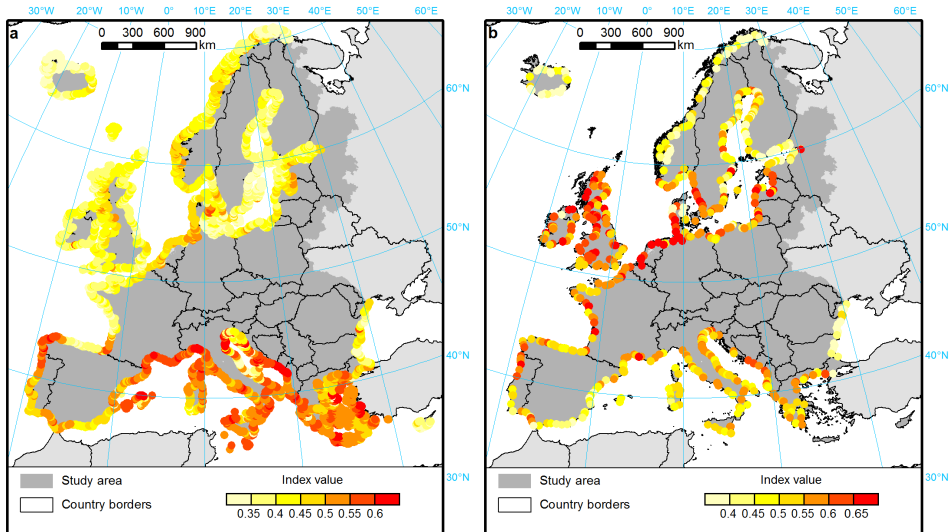


Figure 5.11: Compound Flood Potential Index for (a) flash flood-storm surge co-occurrence and (b) river flood-storm surge co-occurrence, for the 1990–2013 period. Note that the index for river floods was computed for rivers with catchment area of at least 500 km², with the locations being actual estuaries, rather than Delft3D grid cells as shown in previous figures.

the North Sea. In case of rivers with catchment area of at least 500 km², the potential for compound events is the highest along the corridor from Ireland through Great Britain, the Netherlands, north-west Germany, southern Sweden to Lithuania and Latvia. Western and southern coasts of France, north-western Portugal and Spain, and some of the rivers in the Balkans also have elevated potential for compound floods; much less so for southern parts of the Mediterranean region, and far north of Europe.

5.4. DISCUSSION

5.4.1. COMPOSITE INDEX AND PAST RECORDS OF FLOODS

Compound floods are rare and diverse events, therefore it is difficult to synthesize at European scale. In the composite index, events with a 10-year return period were used, which are not particularly extreme by themselves. Yet, even with such a low threshold, actual co-occurrence of compound flood-inducing phenomena is exceedingly rare. Using Delft3D/ERA-Interim reanalysis of storm surge and EFAS river discharges, merely three compound events could be identified for years 1990–2013 using the aforementioned threshold. Combining surge reanalysis with ERA-Interim precipitation gives only six events with at least 10-year return period on both margins for years 1979–2014, and a further two with EFAS-Meteo precipitation (1990–2013). Out of those 11 events, seven are known to have caused damages (see Table 5.3). Most damaging was the 1986 Venetian *acqua alta*, with five fatalities. Most of the compound events found in the reanalysis were located in the south of Europe, where flash floods are most common and damaging [281]. North-western Spain and Portugal, where both variants of the index have high

values, is featured three times, and in each case there known direct losses from flood. South-western Spain (by the Gulf of Cádiz) occurs in Table 5.3 twice, both with recorded losses; this region has also relatively high values of both composite indices. Three events were indicated in Greece, though no information on losses were identified. Remaining compound events were found in areas with rather low values of the composite index of flash flood-storm surge co-occurrence: Iceland and north-western France.

In a further investigation into the utility of the composite index, a list of river estuaries with the highest value of the index was compiled together with past records of damaging floods (Table 5.4). The rivers are of variety of sizes, but all were affected by both coastal and river floods in the vicinity of their estuaries. Two (Scheldt and Ouse) have known past compound events, and flash floods were records around some of the estuaries. Further, reanalysis data has shown that some of the river floods co-occurred with minor storm surges (return period below 10 years). Hence, all 12 estuaries with the highest compound flood potential have caused damages several times in the past and could likely be affected by a compound event. All are located in north-western Europe, which can be connected with specific regional climate features. As it happens, the storm season (November–March) is also the period when flows in rivers in France, UK, Benelux countries are elevated, which a characteristic of the oceanic river regime type [30]. Snowmelt-related floods with long flood waves also occur in that period. It can be added that due to high coastal flood hazard, two estuaries (Meuse and Rhine) can be closed by storm surge barriers, similarly to the Thames (not featured among top 12), where a compound flood occurred in 1928, while others might be not as well protected [66]. On the other hand, closure of a barrier during high water in the river might not prevent a flood [270, 284].

5.4.2. TIME LAGS IN JOINT OCCURRENCE

The analysis presented here only included co-occurrence of surge, precipitation or discharges at the same time, while there might be a no less hazardous situation when events occur one immediately after the other. For instance, in area affected by a flash flood, and therefore with reduced resilience, a storm surge might have more serious consequences than during a standalone occurrence. To investigate this aspect, the correlations between the different variables were recalculated, with a lag inserted into one of the series in every pair. Values of the lag, in days, that provided the highest correlation at a given location, are shown in Fig. 5.12, with additional 6-hourly analysis presented in Appendix Fig. E16. In case of daily precipitation, the series without any lag gave the highest correlation with storm surge heights in 50 % of locations. In 39 % of data points along the coast, precipitation from the day before a surge had the highest correlation. However, using 6-hourly series from ERA-Interim, the largest dependency was obtained with no lag in 81 % of cases, and with a 6-hour lag in 14 % of cases. Synchronization of surges and precipitation is, therefore, very high, except for some regions, like the southern coasts of North Sea and Baltic Sea, where the arrival of high sea levels from the ocean is delayed by the coasts of Great Britain and Denmark.

The situation is different for discharges in rivers with catchment area of 500 km² or more, as no lag results in the highest correlation only in 6% of estuaries. A lag of +1 day is observed in 44 % of rivers, +2 days in 25 % and +3 days or more in 15 %. The highest lags

Table 5.3: Compound flood events, defined by occurrence on the same day of a storm surge with at least 10-year return period and extreme precipitation or river discharge also with at least 10-year return period, identified in reanalysis data (Delft3D/ERA-Interim surge with EFAS/EFAS-Meteo discharge, EFAS-Meteo precipitation or ERA-Interim precipitation). Historical records of losses from HANZE database [282], Meteo France [48] and Dirección General de Protección Civil [283].

No.	Type	Date	Location	Historical records of losses
1	Surge-river discharge	07-12-2000	Minho river, Portugal/Spain; Duero river (Portugal)	Flash flood in Spain recorded further upstream (ca. 600 persons affected)
2	Surge-river discharge	27-12-2002	Duero river, Portugal	Flash floods recorded in several regions (ca. 100 persons affected)
3	Surge-river discharge	24-12-2009	Guadalate river, Spain	River floods in recorded further upstream (ca. 600 persons affected)
4	Surge-precipitation	22-01-1981	Central Greece region, Greece	No records
5	Surge-precipitation	31-01-1986	Venezia province, Italy	Large compound flood, 5 fatalities, 50-70 mln euro damages in 2011 prices
6	Surge-precipitation	15-10-1987	Galicia region, Spain; Loire-Atlantique, Vendée and Morbihan departments, France	Some houses damaged in Galicia (no quantitative data)
7	Surge-precipitation	22-12-2000	Andalusia, Spain	Some houses damaged (no quantitative data)
8	Surge-precipitation	25-01-2009	Thessaly and Western Macedonia regions, Greece	No records
9	Surge-precipitation	06-01-2012	Eastern Macedonia region, Greece	No records
10	Surge-precipitation	10-09-2012	Northern Iceland	No records (very scarcely populated area)
11	Surge-precipitation	24-12-2013	Charente-Maritime, Loire-Atlantique, and Vendée departments, France	Windstorm and floods recorded (no data on losses)

Table 5.4: Top 12 river estuaries in Europe ranked by compound flood potential. Return period is of a 10-year surge and 10-year river discharge occurring on the same day. Past damaging floods from HANZE database [282].

Rank	River	City/country	Catchment area (km ²)	Return period (years)	10-year storm surge (m)	10-year discharge (m ³ /s)	Past damaging floods in the region of the estuary		
							Coastal	River	Com- pound Flash
1	Weser	Bremerhaven, Germany	44 700	182	1.86	2128	1973, 1976	1909, 1956, 1998*	
2	Scheldt	Antwerp, Belgium	19 400	52	1.57	1179	1906, 1953, 1976		1928 1998
3	Meuse	Dordrecht, Netherlands	34 700	129	1.29	2823	1953**	1926, 1993, 1995	1998
4	Elbe	Hamburg, Germany	138 300	2632	2.23	4356	1962, 1973, 1976	1888, 2002, 2016	
5	Rhine	Rotterdam, Netherlands	164 100	1639	1.28	11 082	1953**	1926, 1993, 1995	1998
6	Garonne	Bordeaux, France	80 800	217	0.78	5248	2010	1930, 1981	
7	Eden	Carlisle, UK	2300	71	1.35	635	1977	2005*, 2012, 2015	1953, 2009*
8	Loire	Saint-Nazaire, France	116 200	382	0.81	4679	1924, 1937	1910, 1995, 2001	
9	Lune	Lancaster, UK	900	63	1.33	303	1927, 1977	1903, 2012, 2015	2009*
10	Ouse	Hull, UK	10 600	109	0.81	1215	1921, 1953, 1947, 1982, 1999, 1976, 1978, 2013	2007, 2012	1954 1910
11	Wye	Chepstow, UK	3800	65	0.90	651	2014	1998, 2000*	
12	Severn	Gloucester, UK	10 700	104	0.90	880	2014***	1947, 1982, 2007, 2012, 2013, 2014	1968

Notes: * minor storm surges (return period <10 years) during river/flash flood were identified in the hydrometeorological data used in this study, ** estuaries currently protected by storm surge barriers; *** storm surge occurred between waves of river floods (2013/2014).

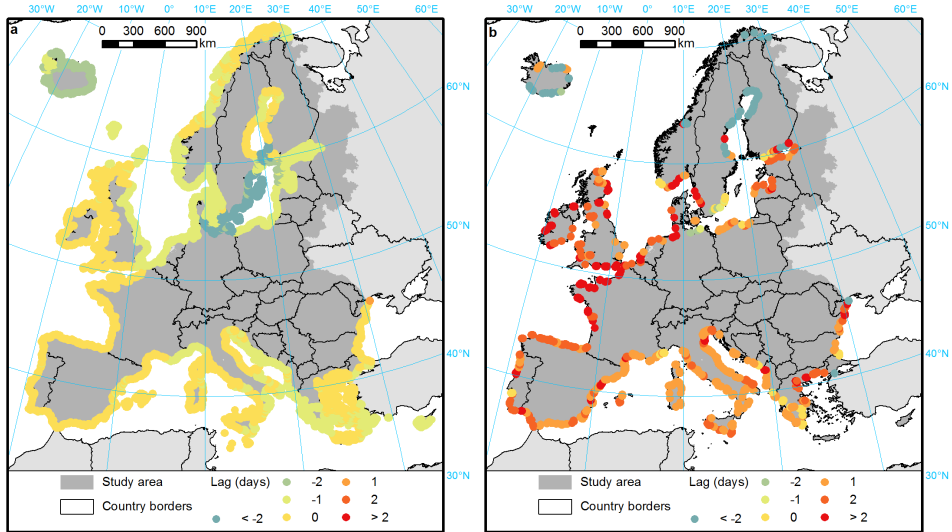


Figure 5.12: Lag between storm surge height (Delft3D/ERA-Interim) and (a) daily precipitation from EFAS-Meteo or (b) daily river discharge from EFAS for catchments with an area of at least 500 km², that has the highest correlation with storm surge height series.

are observed in north-western Europe, including France and the United Kingdom. Only in the far north of Europe (Iceland and northern Scandinavia) a negative lag gives the largest correlations. Similarly, lags for 6-hourly significant wave heights are mostly positive: in 50 % of cases, waves occurring 6 hours or more after the surges are most highly correlated. The lag is slightly higher at coasts exposed directly to the Atlantic Ocean, though the highest values were obtained for Greece. Negative lags are confined to the Baltic Sea, where the storm surges are delayed by the time needed by the basin to fill up through the Danish Straits during windstorms.

5.4.3. UNCERTAINTIES AND LIMITATIONS

For the dependency analysis, the full marginal distributions of storm surge heights, precipitation, river discharges or wave heights were used. This is different approach than taken in some other studies. For instance, Wahl *et al.* [266] only utilized annual maxima of surge heights or precipitation and corresponding values of the other variable within ± 1 day range. However, there are several reasons for opting for another approach. On the theoretical level, using only the upper tail of the marginal distribution of one variable and the corresponding values on the other margin gives two separate results, themselves not independent of each other. Wahl *et al.* [266] argued that they represent different mechanisms, namely moderate surges during extreme precipitation events, and moderate precipitation events during extreme surges, as evidenced by different weather patterns during those two variants of combined floods. However, such approach limits severely the number of data points, which likely caused the large variety of dependency structures observed in the aforementioned study's results.

Here, a comparison was made of the same analyses based on both the full dataset and only the upper 95th of one of the margins. In case of precipitation, 96 % of storm surge-precipitation pairs at tide gauges indicated Frank or Gumbel copula as best-fitting, split neatly between northern and southern Europe (see Fig. 5.1 and Fig. 5.7), but when the upper 95th of the distribution was used, this value went down to only 60–67 %, scattered without a clear pattern around the continent (see Appendix Fig. E.17). For storm surge-river discharge pairs, the corresponding values are 76 % and 59–66 %. The contrast is even stronger for reanalysis data (Delft3D/ERA-Interim storm surges, ERA-Interim or EFAS precipitation and EFAS river discharges) which have much less gaps in their time series compared to observations. At the same time, those modelled data represent the correlations between two marginal distributions poorly when the upper 95th of the data series is used. In case of storm surge-precipitation pairs, the R^2 between rank correlations from observations and modelled data is 0.60 for the whole marginal distributions and 0.19–0.31 for the upper 95th (see Appendix Fig. E.18). For storm surge-river discharge pairs, the corresponding values are 0.38 and 0.19–0.31, respectively (see Appendix Fig. E.19).

The lower performance of the upper tail in recreating dependency can be largely attributed to lower performance of models regarding extreme events [285]. Indeed, rank correlations between modelled and observed 95th percentiles of the margins are in the 0.34–0.36 range, except between E-OBS and EFAS-Meteo (0.50), in contrast to 0.56–0.68 for the full marginal distributions. Importantly, return periods are also mostly lower when using the upper 95th compared to the full distribution. For instance, at the Schelde estuary in Belgium, the location of a large compound flood in 1928 as well as many coastal and river floods, the return period of a joint event consisting of a 10-year storm surge and 10-year river discharge occurring at the same day was estimated at 52 years using the full marginal distributions, but at 4000 and 25 000 years using the upper 95th of one of the variables (with Delft3D/ERA-Interim and EFAS). If surge and discharge would be completely independent, the return period of such a compound event would be approximately 36 500 years. In general, the variation of return period between neighbouring coastal segments is higher when using the upper 95th rather than the full margins.

In the presented analysis, there are two principal source of uncertainty. First is the data availability: the length of most series is only just enough for a univariate extreme value analysis (>30 years), and some observational data series are even shorter (including EFAS covering only 24 years). The relative rarity of compound floods, as evidenced in the introduction and section 5.4.3, leads to reduced confidence in the resulting correlations. This fact also forbids an analysis of long-term changes to compound flood probability of occurrence. The second source of uncertainty is the choice of copula. Here, seven among the most popular copula types were used, but many more exist. Also, as a parametric model of dependency, it doesn't perfectly recreate the joint probability, and due to limited amount data the copula type might not be assigned correctly, leading to great differences in return periods, e. g. between Frank and Gumbel copulas. However, the relative spatial homogeneity and rather clear spatial patterns in distributions of copula types gives good confidence in the results. Upper tail dependence is most frequently observed, which means that high sea levels and high precipitation or river discharges are usually more correlated with each other than those variables at moderate or low in-

tensity. This is particularly relevant in the Mediterranean region, where precipitation is concentrated in a smaller number of days – mostly less than 80 days during average year – compared to northern Europe, where it rains above 110 days on average [31].

5.4.4. FUTURE RESEARCH OUTLOOK

Still, more work is needed in applying the joint distribution of flood-inducing events to flood hazard mapping. One important local factor omitted completely from the analysis are tides. A high tide can contribute significantly to a compound event (like in London in 1928), but tides are, barring for nonlinear effects on local sea level [205, 286], an independent component. Additionally, they need to be analysed with a good temporal resolution, in contrast to 6- and 24-hourly data utilized here. After a pan-European analysis have been performed, local case studies should be carried out. Hydrodynamic modelling in good resolution would be required to assess the influence of joint occurrence of high water levels in both river and coastal side of an estuary [174]. Such a model would have to take into account time-varying sea level (including tidal component), river discharge and wave heights. Detailed topography and bathymetry of the estuary would also be necessary. By modelling the dependency between hydrological events with copulas, the joint distribution could be sampled to provide a range of possible set-ups of simulations. That requires observational data from gauges located at the coast and in the river above the zone of influence of tides and surges on river water levels. An additional gauge on the river should be located in the area where the increase of water level caused by a compound event could be found, so that the model's validation can be performed. Further, the model should be run iteratively based on samples of the joint distribution, so that the local probability of flooding could be obtained that incorporates compound flood possibility. Finally, the analyses should be linked with historical events to fully to assess the circumstances that lead to compound flooding.

5

5.5. CONCLUSIONS

This chapter analysed the joint occurrence of hydro-meteorological phenomena that have the potential to cause a compound flood event. The analysis has identified areas with various patterns of dependency. Europe can be essentially divided in three regions. Southern Europe, with Portugal, Spain, Italy and Greece where the probability of joint occurrence of storm surge and precipitation is relatively high, and the intensity of the latter very large. Northern Europe, along the main corridor of winter storms that spans from Ireland and United Kingdom through the Netherlands, Denmark, southern Sweden and across the Baltic Sea. Here, dependency between surges and river discharges is higher than elsewhere, with large differences in flood potential between west-facing and east-facing coasts. The correlation between surges and precipitation can be very high, but there is also a lack of tail dependence, i.e. extreme events are not more likely to co-occur than more moderate events. This results in relatively high return periods for compound events. Finally, the far north of Europe (Iceland, Norway, Finland and northern Sweden) and Black Sea countries show very little potential for compound flood occurrence.

Performance of models in recreating observation dependencies is good in relation

to precipitation, but much less so in case of river discharges. Simulations driven by the RCA4 regional climate model had mostly similar performance compared with the re-analysis, albeit the latter with a much coarser resolution. Therefore, there is potential for making relatively accurate future predictions of the dependency between surges and precipitation. River discharge estimations, on the other hand, still need improvements before such predictions can be confidently made.

The composite index of compound flood potential identified areas of most interest for further studying the topic. A few European estuaries have experienced damaging compound floods in the past, and many more could be affected, especially in view of the projected rise in extreme sea levels [230] and river flood hazard [287]. Those need to be analysed in detailed case studies with the use of hydrodynamic modelling.

CITY OF YORK FLOOD HEIGHTS AT OUSE BRIDGE

2000  17' 8"

1636  17' 6"

1831  16' 8"

1982  16' 7"

1947  16' 4 $\frac{1}{2}$ "

1763  16' 2 $\frac{1}{2}$ "

1978  15' 11"

1892  15' 8"

1991  15' 6"

1995  15' 5"

Previous page: High water marks in York, England, UK, highlight floods that affected the city over the span of nearly four centuries.

6

HISTORICAL TRENDS IN FLOOD EXPOSURE AND LOSSES

6.1. INTRODUCTION

EXTRME hydrological events are generally predicted to become more frequent and damaging in Europe due to warming climate [178, 182, 209, 225, 230, 288]. Though consensus seems to exist regarding the trajectory of future climatic developments seem certain, there is less confidence in the changes in flood losses as a result of climate change so far [41, 289–291]. Qualitative and quantitative hydrological studies for Europe have indicated no general continental-wide trend in river flood occurrences, extreme precipitation, or annual maxima of runoff [292–294]. However, substantial variations between different catchments have been observed, ranging from an increase in north-western Europe to no trend or a decrease in other parts of the continent [36, 42]. Similar findings were reported for storminess along the European coasts [295, 296].

Natural hazards take place when recurring extremes of the Earth’s environment collide with human activities. Beyond the natural or anthropogenic changes to the environment, the extent of those activities has profound effect on the consequences of disasters. Even in a space of a few decades, social, economic and technological developments drive the constant evolution of exposure and vulnerability to hazards. Therefore, there is growing interest in how much the number of persons and assets at risk has changed over time worldwide [297–299], and what consequences those findings have for observed trends in natural hazards-related losses [300–304].

Without correcting reported losses for spatial and temporal changes in exposure, previous studies report a significant upward trend in losses [305–307]. Applying correction for exposure changes (often referred to as “normalization”) results in a different outcome. Barredo [292] found that correcting reported flood losses for inflation and economic growth yields no trend for 1970–2006, in contrast to steep rise in originally-

This chapter was edited from papers published in *Earth System Science Data* **10**, 565–581 (2018) [282] and *Nature Communications* **9**, 1985 (2018) [281].

reported losses. Similar findings were presented for the United Kingdom, covering years 1884–2013 [308]. Other studies on trends in flood exposure were carried out, e.g. for Austria [309], Italy [310], the Netherlands [311], Spain [312], Switzerland [313], and the United Kingdom [314]. The importance of not only population or economic growth, but also land use distribution has been emphasised [315, 316]. Such “normalization” processes have also proven to be important for explaining trends globally [300, 303] and for other natural hazards [302, 317, 318].

Yet, there are several limitations of the aforementioned studies and databases. Exposure datasets were derived at a variety of spatial and temporal resolutions with different thematic coverage. Within a given country, typically one series of population, gross domestic product (GDP), housing stock, or other variable were used to normalize reported flood losses. This approach neglects substantial variation in development within countries. The timespan of the studies on exposure is usually limited to the most recent decades, given the lack of adequate data.

A typical source of gridded historical population and land use is HYDE [319], which has a 5 arc minute resolution¹ and a very long time span, from 10 000 BC to 2100 AD. HYDE utilizes historical population estimates combined with a set weighting maps for land use to generate gridded reconstructions of the past anthropogenic environment. Other time-varying datasets of gridded population include GPW v4 for years 2000–2020 [320] and GHSL for years 1975–2014 [321]. Disaggregated GDP is provided for years 1990–2005 by GEcon 4.0 [322] and for years 1980–2100 by a dataset by Murakami and Yamagata [323]. Finally, relatively detailed, 1 km resolution maps of European land cover were created for 1900 [324] and 1950–2010 [325]. Still, there is a lack of a comprehensive dataset that would allow to normalize losses from past natural hazards, especially those needed to be analysed in a very fine resolution, like floods.

In effect, almost all studies consider socio-economic variables at the national level; only Munich Re [303] utilized a coarse $1^\circ \times 1^\circ$ grid² of exposure data. High resolution is of particular importance for analysing flood exposure, which is relatively limited in space: at present time less than 10 % of European territory is at risk of river or coastal flooding as shown in chapters 3 and 4. A few national studies that have analysed changes in exposure found different trends in population or housing stock inside and outside hazard zones [298, 309, 311, 313], which shows the importance of using a sufficient resolution of the analysis. Furthermore, trends in exposure and normalization of reported losses have been carried out with many different economic variables depending on the study, such as GDP, variously-defined wealth or housing stock.

Also, the availability of past flood damage information is very uneven between countries. Further, international databases of natural hazards, such as EM-DAT [326], Nat-CatService [5], Dartmouth Flood Observatory [89] or the collection of data from European Union-mandated preliminary flood risk assessments from the European Environment Agency [327] provide reasonable coverage only beginning with the 1980s. As the number of flood events for which quantitative information is available declines quickly when moving back in time, the starting point for many studies on flood trends is in the vicinity of the year 1970 or later [328, 329]. Comprehensive and publicly-available na-

¹Approximately 40 to 60 km² grid cells over Europe.

²Approximately 5000 to 9000 km² grid cells over Europe.

tional repositories of disaster loss data are few in Europe and, those that are available, focus on flood and landslide events [283, 330–333]. Moreover, the completeness and extent of information contained in existing data sets varies to a significant degree. In effect, large-scale studies usually rely entirely on the contents of global or continental databases, while national studies are shaped by the specifics of locally-available data. This leads to considerable uncertainties when examining trends at the continental scale or comparing trends between countries.

This chapter aims to address the aforementioned limitations (short time series and low spatial resolution) of previous assessments of flood trends for Europe through a new comprehensive dataset. The study draws from recent developments in European demographic and land use mapping, as well as new studies on historical changes in population, production and wealth. HANZE, or “Historical Analysis of Natural Hazards in Europe”, is a database enabling the study of historical trends and driving factors of vulnerability to natural hazards, with a particular focus on floods. It has two components, namely HANZE-Exposure and HANZE-Events. HANZE-Exposure consists of high-resolution gridded data with information on land use, population, production and wealth per 100 m grid cell from 1870 to 2020. It allows to derive potential damages for any past natural hazard with a defined spatial extent. The other component, HANZE-Events, contains information on location, time and quantitative data on consequences of past natural disasters, currently limited to floods (1870–2016). It is supplemented by economic data necessary for converting nominal monetary losses to a single benchmark. Both components are then combined into a pan-European analysis of trends in flood exposure, losses and, implicitly, vulnerability.

6.2. MATERIALS AND METHODS

6.2.1. DOMAIN AND OVERVIEW OF THE METHODOLOGY

HANZE database covers 37 European countries and territories constituting approx. 70 % of the continent’s population [334]. Included are all 28 European Union (EU) member states, all four European Free Trade Agreement (EFTA) members (Iceland, Liechtenstein, Norway and Switzerland), four microstates located in Western Europe (Andorra, Monaco, San Marino and the Vatican) and one Crown Dependency of the United Kingdom (Isle of Man). Excluded are, therefore, non-EU successor states of the Soviet Union or Yugoslavia, as well as Albania and Turkey. However, some EU territory is also excluded, namely:

- Canary Islands, Ceuta and Melilla (parts of Spain)
- The Azores and Madeira (parts of Portugal)
- All dependent or overseas territories of EU states, except the Isle of Man

Data for Cyprus exclude areas controlled by the Turkish Republic of Northern Cyprus, but include the Sovereign Base Areas of Akrotiri and Dhekelia and the United Nations Buffer Zone. The composition of the domain was chosen based on data availability. The domain is shown in Appendix Fig. G.1.

Majority of work in this chapter was related in creating the HANZE database. As presented in Fig. 6.1, the starting points for constructing HANZE-Exposure database were a gridded land cover/use map (100 m resolution) and a population map (1 km resolution), both referring to the situation in Europe ca. 2011. Based on previously published methods, demographic and economic data were disaggregated to 100 m resolution, and changes in historical land use and population were modelled utilizing a large compilation of historical statistics at the regional level. Due to the very large amount of technical details involved in this work, the methodology is described only synthetically in section 6.2.2, while the full description was included in Appendix G. HANZE-Events was created from a wide array of published sources and databases, as described in section 6.2.3. The end-date of HANZE-Exposure is different from HANZE-Events, because exposure data are prepared with a 10-year timestep for 1870–1970 and a 5-year for 1970–2020. Therefore, a short-term projection for 2020 is necessary to calculate exposure for post-2015 events. It should be noted that the starting year of 1870 was chosen mainly due to data availability.

The two components of HANZE database are the combined to analyse flood trends since 1870. For that purpose, the spatial extent of each flood event, or ‘footprint’, was established by intersecting the 100-year flood hazard zone under present climate conditions (from chapters 3 and 4) with country subdivisions known to have been affected. While the 100-year flood footprint is not an accurate representation of actual flood extent, it serves as a proxy for areas with the highest hazard during historical floods. This allowed me to analyse demographic and economic growth within the exposed area, as well as calculate reported losses relative to potential damages. Additionally, copula theory was used to analyse the dependence structure between four different variables: area inundated, fatalities, persons affected and financial losses. The simulated data pairs were used to fill in missing information in the database for historical flood events and provide a better estimate of trends in flood losses. Finally, the underreporting of smaller flood events in available sources is estimated and its impact on the results quantified.

6.2.2. DATABASE OF FLOOD EXPOSURE

The general methodology of the exposure database is based on the concepts used to build the HYDE database [153, 335]³. First, two detailed maps of population and land use are compiled for one point in time – “baseline maps”. Other time points in the past and in the future were calculated based on those baseline maps. Here, the maps refer to the year 2011/12, and have a spatial resolution of 100 m. For the years between 1870–2020 only the total population and land use at NUTS 3 regional level (1353 units) [336] is known. Hence, for each time step, the population and the different land use classes was redistributed inside each NUTS 3 region in order to match the regional totals.

Baseline land cover/use was taken from Corine Land Cover (CLC) 2012, version 18.5a [337] and population from GEOSTAT grid containing figures from 2011 population censuses [338]. The population grid was further refined to 100 m resolution using two disaggregation methodologies described by Batista e Silva *et al.* [339]. First, the 1 km population was redistributed into land use classes within each grid cell using an iterative “limiting variable” method (M1 in the aforementioned paper) and CLC 2012 map. Then,

³This section contains a very brief description of the methods; the full description can be found in Appendix G

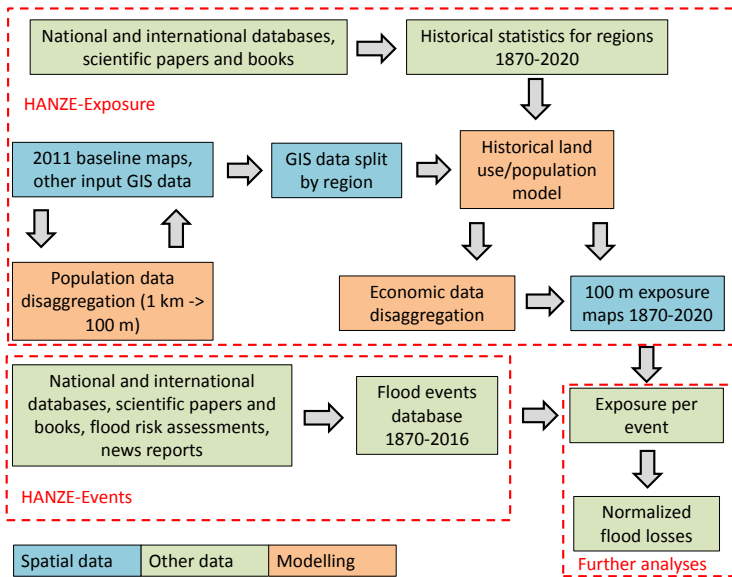


Figure 6.1: Workflow of the study.

population from land use classes was further distributed into 100 m cells proportional to soil sealing (method M3 in Batista e Silva *et al.* [339]) taken from the Imperviousness 2012 dataset [337].

A database of statistics covering years 1870–2020 at NUTS 3 level was compiled from multiple sources covering population number, percent living in urban areas, persons per households, percent of land covered by croplands and pasture, and area covered by transportation infrastructure. The land use and population distribution was modified starting from the baseline map as follows. Change in population per urban grid cell was firstly considered proportional to the mean number of persons per household. Surplus population and urban fabric from this procedure was removed starting with grid cells furthest away from urban centres until it reach the total urban population per region recorded in historical statistics. Then, area covered by industry was changed proportionately to GDP per capita in the industrial sector, in constant prices. Grid cells located furthest from the urban centres were removed first, starting with the baseline map and moving in time from it. Reservoirs were removed when the year of the map was earlier than the year of an reservoir's construction, taken from GRanD database [69]. Grid cells of road and rail infrastructure were redistributed to match historical statistics on their total length per region, with grid cells reallocated as in case of industry. Airports were removed from the map when the year of the map was earlier than the year of an airport's construction. Airport land use class in CLC 2012 was connected with actual airports mostly through OurAirports database [340] and year of construction was found in Internet resources. Construction sites were removed for maps before 2010, and burnt areas for before 2005, otherwise were kept unchanged. Croplands were redistributed to match their historical area per region. Grid cells with the lowest value of suitability index

for agriculture were removed first and grid cells not used economically with the highest suitability index were added first. Suitability index for agriculture is proportional to slope (from EU-DEM [338]) and FAO crop suitability index for high-input cereals [341]. Pastures were computed in the same way as croplands, only with replacing the FAO crop suitability index for cereals with index for high-input alfalfa. In cases where land has become unoccupied after the application of the aforementioned procedure, natural land cover typical in the nearest neighbourhood of a grid cell was assigned. If there was no natural land cover in the vicinity, forest land cover was assigned. Finally, the population of grid cells which transitioned from urban to non-urban during the calculation was reduced according to a value specific to each land use type. The non-urban population was changed proportionally to the evolution of mean number of persons per household. In case of further mismatch between output rural population and historical data per region, population was added/removed one person per grid cell at a time, starting with areas closest to urban centres. The remaining CLC 2012 classes (ports, dump sites, natural water bodies and courses, glaciers etc.) were assumed constant. Changes in urban population distribution was validated using a set of 42 population density cross-sections from 19 cities, spanning from 1871 to 1971. A reasonable match was achieved between reconstructed curves of population density-distance from city centre relationship and estimates published in literature. The validation of population maps and urban population density functions is presented in section G.5.

As a last step, GDP (compiled at NUTS 3 level with sectoral breakdown) and wealth (non-financial, produced, tangible fixed assets compiled as a percentage of national GDP with sectoral breakdown and then multiplied by GDP at NUTS 3 level) were disaggregated to a 100 m grid. 50 % of GDP and wealth generated by agriculture (without forestry) was distributed proportionally among the population living in areas considered agricultural. The remaining 50 % was uniformly distributed among agricultural CLC classes. Production and wealth in forestry sector was distributed as for agricultural, but using forest CLC cells instead of agricultural lands. 50 % of GDP and wealth in sectors of industry and services was distributed proportionally to the population of any land use class, and the other 50 % uniformly distributed to industry or services-related CLC grid cells. The value of dwellings was distributed proportionally to the population of any land use class. The value of infrastructure was uniformly distributed to certain land use classes: roads, railways, airports, ports and urban fabric.

6.2.3. DATABASE OF PAST DAMAGING FLOODS

HANZE-Events includes information on past damaging floods that occurred in the domain (37 countries and territories) between 1870 and 2016. Per each event, several variables were recorded. Full listing of variables and their description included in HANZE-Events is presented in Appendix Table G.3. The most important information gathered on damaging floods were:

- Country: which country was affected, which was necessary to convert all nominal financial losses to a single benchmark.
- Date: when did the event happen, especially which year, so that the exposure per given year could be assigned to an event.

- Regions affected: in which NUTS level 3 regions damages were recorded, so that the zone exposed to flooding could be assigned to an event.
- Impact: what were the consequences of the flood, in four categories: total area flooded, number of persons killed (fatalities) incl. missing presumed dead, number of persons affected, monetary value of losses).

Several rules were applied to determine whether a flood event indicated in sources should be included in the database, as follows:

- At least one of four statistics (area flooded, persons killed (fatalities), persons affected, losses) had to be available for a given event. However, if no persons were known to have been killed or missing in the flood, at least one of the other statistics had to be available.
- Insignificant floods, i.e. events which affected only a small part of one region, with no fatalities and less than 200 persons affected, were not included.
- Available information for a given event had to be sufficient in order to assign month, year, country, regions affected, type of flood, and general cause of the event. Flood source (river/lake/sea name), detailed information on the cause and day of the event were not required.
- Floods that were caused by insufficient drainage in urban areas not connected with any river system, floods caused entirely by dam failure unrelated with a severe meteorological event, or caused by geophysical phenomena (such as tsunamis or *jökulhlaup* events) were not included.
- Flood events that had impact on more than one country were split per country as long as data were available on per country basis. Otherwise they were presented as one flood event. Also, in the case of an event affecting several regions of a country, when the availability of statistics per region is uneven, the event was split accordingly.

Records of flood events were obtained from a large variety of sources (more than 300), including international and national databases, scientific publications, and news reports. The source of information is indicated per event in the HANZE-Events data set. In the majority of cases, entries taken from international databases were cross-checked with other EM sources and amended as necessary. Databases particularly worth mentioning are EM-DAT [326], Dartmouth Flood Observatory [89], NatCatService [5], European Environment Agency database of historical information submitted under Floods Directive [327], the national flood databases of France [333], Italy [331], Spain [283], and the United Kingdom [330, 332], and several national and regional preliminary flood risk assessments.

In order to convert reported losses from various currencies and reference years to a single benchmark, information on inflation and currencies was needed. Data on all currencies that were used in the study area between 1870 and present were compiled together with their conversion rates to euro. For countries not currently using the euro,

2011 exchange rates from Eurostat [334] were used. Further, country-level GDP deflators were collected to adjust nominal losses to real losses in 2011 prices. Detailed information on currency and deflator dataset, as well as example of converting nominal losses to 2011 euros is provided in section G.4.3.

6.2.4. METHODS FOR ANALYSING TRENDS IN FLOOD LOSSES

In this chapter, trends in flood losses were analysed in four variants. First, using losses as reported in the events database, with financial losses adjusted for price inflation to 2011 euros. Second, using normalized losses, i.e. adjusted for change in exposure. Further, using normalized and gap-filled losses, i.e. loss data amended with estimates of missing information per event. Finally, using loss data that were normalized, gap-filled and corrected for underreporting, i.e. with added estimates of losses caused by small floods that have occurred before loss data have begun to be systematically recorded.

NORMALIZING AND AMENDING FLOOD LOSS DATA

Recorded losses were taken directly from HANZE database, while further transformations of the data were carried out by combining exposure data over each flood event's "footprint". The flood footprint was obtained by intersecting a map of regions affected by an event with the flood map from the RAIN project [175, 202], available from an online repository for river [173] and coastal [342] floods. The flood maps are for a 100-year return period and historical scenario (1971–2000). The floodplain includes all river sections with a catchment area above 100 km². The map does not include flood defences and therefore constitutes all potentially inundated areas. While the 100-year flood footprint is not an accurate representation of actual flood extent, it serves as a proxy for areas in danger during historical floods. It should be noted that seven events were not included in the normalization and further analysis due to lack of flood extent data: four flash floods in Malta (where rivers were too small for inclusion in RAIN flood map) and three coastal floods in Sicily (where no flood hazard was indicated in RAIN map).

Normalization was carried out by multiplying reported losses by the relative change in population, GDP or wealth within each event's footprint. An example calculation for the 1953 North Swea flood in the Netherlands is presented in Table 6.1. In the affected regions' 100-year coastal flood zone, according to HANZE-Exposure, population increased by 60 % between 1953 and 2011, while GDP increased 5.6 times and wealth 7.4 times. It is therefore assumed that the vulnerability is constant within the timeframe of the study and all losses would have changed proportionally to local demographic and economic growth. It should be noted that because the exposure data are calculated in 5/10-year time steps, the exposure for events that occurred in between the time steps was linearly interpolated.

Missing information on losses for events recorded in HANZE database was filled based on correlation between the four variables describing flood damages. Normalized values relative to potential damages within a given flood footprint were used. The empirical distribution of each variable was converted to ranks and the joint distribution of each pair of variables was fitted to five types of copulas (Gaussian, Gumbel, Clayton, Frank and Plackett) [162]. The best-fitting copula for each case was chosen according to the "Blanket Test" described by Genest *et al.* [280], which uses the Cramèr–von Mises

Table 6.1: Reported losses, exposure in the potential flood zone of the event, relative and normalized losses for the 1953 coastal flood in the Netherlands.

Category	Reported losses (1953)	Exposure (1953)	Exposure (2011)	Relative losses (1953)	Normalized losses (2011)
Area flooded (km ²)	2000	3917	3917	51.1 %	2000
Persons killed	1835	1 245 000	1 988 000	0.15 %	2930
Persons affected	188 000	1 245 000	1 988 000	15.1 %	300 100
Losses in euro (2011 prices)	4.8 bln	13.6 bln*	75.8 bln*	35.5 %	26.9 bln
		46.5 bln	341.8 bln	10.4 %	35.5 bln

* upper figure – GDP, lower figure – wealth.

statistic (see A.7 and related description in Appendix A) For a given event and missing data, the available variable that was most highly correlated with the missing particular sample of the variable of interest was used. The conditional copula was sampled 10 000 times to generate samples of the conditional distribution of interest and mean of the conditional damage was used as the estimate of the missing values. The relative damage was the multiplied by total exposure within a given flood event's footprint. The graphs of dependency structures (transformed to standard normal space) are shown in Appendix Fig. H.1 with correlations and best-fitting copula types are included in Appendix Table H.1.

Underreporting of smaller flood events in the past was estimated by transforming normalized and gap-filled damage statistics (with financial losses normalized by wealth only) to ranks (highest to lowest) and dividing the events into quintiles based on their average rank. It was then assumed that the catalogue of events in the upper quintile (20 %), i.e. the most severe events, is complete over the entire dataset. For the other four quintiles, the catalogue is assumed to be complete only during the most recent period: 1990–2016. During this period, the ratio of events between four lower quintiles to the highest one was 1.60, 2.02, 2.42 and 2.29 (higher quintile to lower). For other 30-year time periods (1870–1899, 1900–1929, 1930–1959, 1960–1989) the ratio is lower, which was considered to be a function of underreporting of less severe floods (Appendix Fig. H.6). Hence, reported flood events were multiplied by factors necessary to achieve the same ratios between quintiles as in 1990–2016, where the highest quintile was not adjusted as it is assumed that the records of most severe floods are complete. The same factors were applied to multiply flood consequences for all variables.

CALCULATING TRENDS

Trends were analysed using Poisson regression, which is better suited for count data than linear regression [343, 344]. Statistical significance of the trends presented in the paper was analysed by Monte Carlo simulation. The trend calculated for a given variable (rate parameter of Poisson regression) was compared with 10 000 samples of randomised data series. Those randomised series were annual number of flood events or their consequences, where each flood event had a randomly assigned year from a uniformly distributed interval [1870,2016]. For each of the 10 000 randomised series the Poisson regression was calculated in order to obtain confidence intervals. The trend for

a given variable was considered significant if the rate parameter was higher than in 95 % of trends of randomised data series. As an additional check, the t test was applied to the calculated trends, yielding the same results at $\alpha = 0.05$ significance level.

As mentioned previously, the reported values of variables were normalized for further analysis. To test statistical significance in the normalized data series, the uncertainty distribution of past exposure was estimated first. It was assumed to be a log-normal distribution fitted to the empirical distribution of change in exposure between given time point and 2011 within all NUTS 3 regions. This log-normal exposure distribution was sampled to obtain a random value of exposure per given flood event. This sampling was repeated 10 000 times for each flood event to generate a set of randomised data series of annual normalized flood losses. This allowed to compute uncertainty ranges in normalized data series shown in Appendix H. Then, a randomised data series were further randomised by assigning a year from a uniformly distributed interval [1870,2016] to each flood event, as in previous paragraph. The trend was considered significant if it was higher than 95 % of randomly-generated trends.

For gap-filled data series, the uncertainty in the modelled data was further incorporated into significance testing. For each missing value of flood loss for a given event, 10 000 samples of marginal distribution of that variable obtained during the copula analysis. This allowed to compute uncertainty ranges in normalized data series shown in Appendix H. Like for normalization, the data series incorporating uncertainty of gap-filling were further randomised by assigning a year from a uniformly distributed interval [1870,2016] to each flood event, as in previous paragraph. The trend was considered significant if it was higher than 95 % of randomly-generated trends.

VALIDATION OF TRENDS

Comparison of exposure and flood losses trend was carried out using two Environment Agency (EA) maps. “Risk of Flooding from Rivers and Sea”, April 2017 version, contains highly-detailed flood hazard zones at several probabilities of occurrence (see section 4.3.4 for more information). “Recorded Flood Outlines”, May 2017 version, contains actual flood extents continuously recorded since 1946, with a limited number of events from earlier years as well [54]. The flood hazard zones were intersected with population and wealth maps for 1870–2020, and the recorded outlines since 1946 were intersected with the disaggregated baseline population map. Additionally, trends reported annual losses for Poland for 1947–2006 were compared with the trends based on HANZE-Events. Annual losses from Polish sources [13, 60, 61] were normalized using national GDP series.

Additional analysis was carried out comparing flood loss trends with precipitation trends. They were computed using NOAA-CIRES 20th Century Reanalysis, version 2c [345]. It is a global climate reanalysis for 1851–2014 with a 3-hour temporal resolution and 2° spatial resolution⁴. A total of 329 grid cells intersect with the study area, for which daily precipitation amounts were extracted for years 1870–2014. For every grid cell an empirical return period (from 10 to 100 years) of 3-, 6-, 12-hour and 1-, 2-, 3-, 5- and 7-day precipitation was calculated and then the number of events which exceeded this threshold was obtained. Finally, this number of extreme events was weighted by the size of 100-year river flood hazard zones within each grid cell. Trends were also analysed

separately for Mediterranean countries (Cyprus, Greece, Italy, Malta, Spain and Portugal) and remaining countries in the domain. However, comparison of trends in the 20th Century Reanalysis with daily gridded observations from E-OBS [138] since 1950 shows potential bias in the reanalysis. In E-OBS, trends are quite uniform across time and duration of rainfall, in contrast to much larger variability in the reanalysis.

6.3. RESULTS

When flood events are specified to be “small” or “major”, the distinction pertains to severity of floods, i.e. the amount of losses generated by those floods relative to the overall distribution of losses for all events where small floods are those in the lower percentiles of this distribution and major floods are those in the upper percentiles.

6.3.1. TRENDS IN EXPOSURE

Between 1870 and 2016, Europe experienced substantial growth in population (130 %), urban area (more than 1000 %), and wealth (more than 2000 % in constant prices). However, there has been large variability in patterns of development between regions. In 8 % of European regions (NUTS 3), the total population in 2016 was lower than in 1870. Rural population across the continent declined, and fixed assets in agriculture barely changed in contrast with large increases in wealth in the housing, industry and services sectors (Appendix Fig. H.2). Most important for this study are relative trends within and outside of flood-prone areas. Since 1870, the percentage of population, GDP and wealth exposed to the 100-year flood has decreased slightly for river floods, but increased for coastal floods (Fig. 6.2a). When analysed at the continental scale, those trends are partly caused by the aforementioned rates of demographic and economic growth between regions (Appendix Fig. H.3). As the map in Fig. 6.2b shows, while overall exposure to floods has declined in most countries, especially those in central and northern Europe, relative exposure has increased in several western and southern European states including France, Germany, Italy and the Netherlands. In general, changes in exposure of production (measured by GDP) and wealth are in line with trends in population, with some exceptions, e.g. in Italy and Hungary, where the percentage of wealth exposed has not changed since 1870 despite growth in the relative exposure of their national populations.

6.3.2. DISTRIBUTION OF FLOOD EVENTS IN EUROPE

The HANZE database includes records for 1,564 flood events (1870–2016), of which 879 (56 %) are flash floods, i.e. river floods lasting less than 24 hours, 606 (39 %) are river floods, 56 (4 %) are coastal floods and the remaining 23 (1.5 %) are compound events, i.e. floods caused by a co-occurrence of storm surge and high river flows (Fig. 6.3). For the purpose of this analysis, “flood events” (or simply “events”) refer only to damaging floods fulfilling criteria for inclusion in the HANZE database (see section 6.2.3). Flood events are very unevenly distributed, both during any given year and geographically (Fig. 6.4). In southern Europe, flash floods constituted the majority of flood events, and were most prevalent between September and November. In central and western Europe, river floods were more frequent than flash floods, with flood losses concentrated between

⁴Approximately 20 000 to 36 000 km² grid cells over Europe.

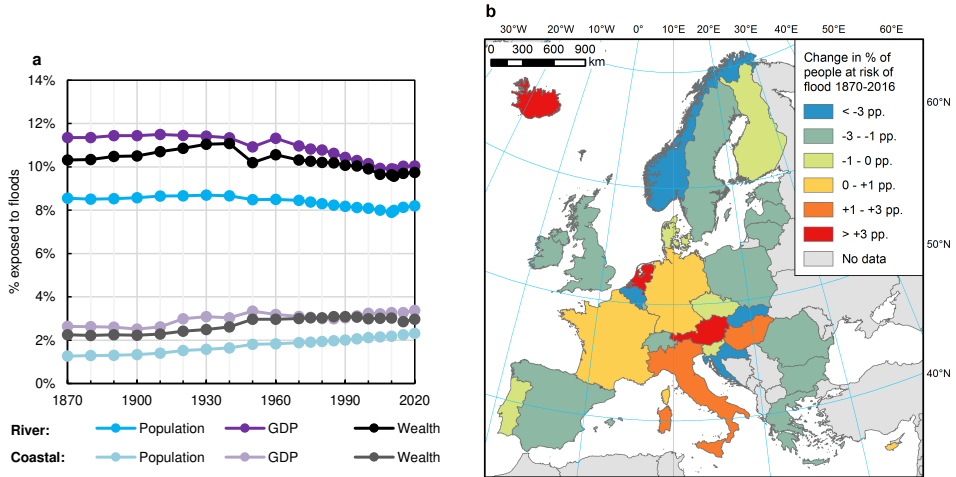


Figure 6.2: Trends in flood exposure. Percent of the population exposed to the 100-year river and coastal flood in Europe (a), including short-term projection to year 2020, and change in population exposed (b), in percentage points, to the 100-year flood (either river or coastal) in each country (1870–2016).

6

June and August. In northern Europe, floods were mostly caused by snowmelt and rarely resulted in significant losses. Coastal floods were mostly recorded in regions which border the North and Baltic seas.

In total, HANZE contains information on flood events that affected 1005 regions, or 74 % of all NUTS3 regions within the study area. The number of floods by region is presented in Fig. 6.5. On average, a flood event affected 2.8 NUTS 3 regions. The spatial distribution of floods contained in the database is heavily influenced by availability of historical records. More than half of the events in the database occurred in only three countries, namely Italy (36 %), Spain (15 %) and France (10 %), all of which have publicly-available and searchable databases of historical floods. Thus, the large number of recorded flood events in those countries is a result of better coverage of events with relatively small impact on population or assets. In contrast, total flood losses are more evenly spread out across Europe and less than a third of people affected by floods resided in the aforementioned three countries. This is partially a result of better coverage of major flood events across all countries, whereas flood events recorded in Italy, Spain and France were dominated by flash floods.

It should be noted that quantitative information on floods losses was not always obtainable. The most frequently available statistic was the number of fatalities, as they were recorded for 1,547 flood events (99 %), of which 372 events resulted in no deaths. For the remaining 17 events some fatalities were reported to have occurred, but the exact number of deaths was unknown. Information on the total flooded area was only available for 157 events (10 %), persons affected for 682 (44 %) and monetary losses for 560 (36 %).

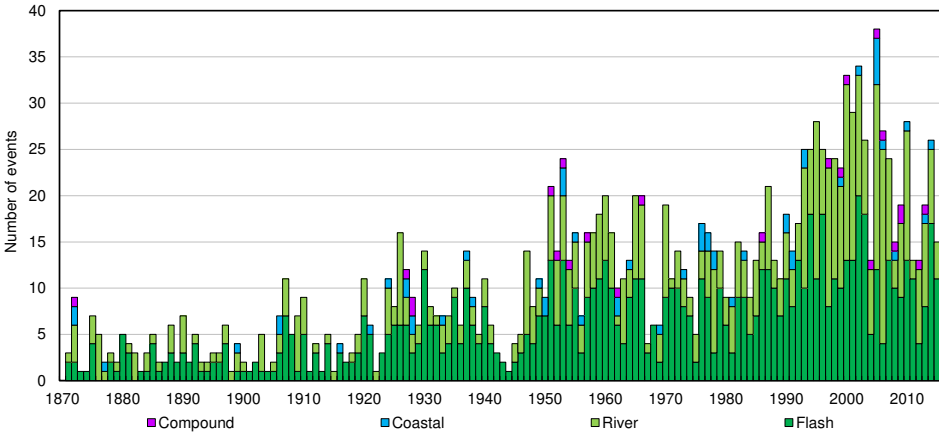


Figure 6.3: Distribution of flood events in HANZE by year and type (1870–2016).

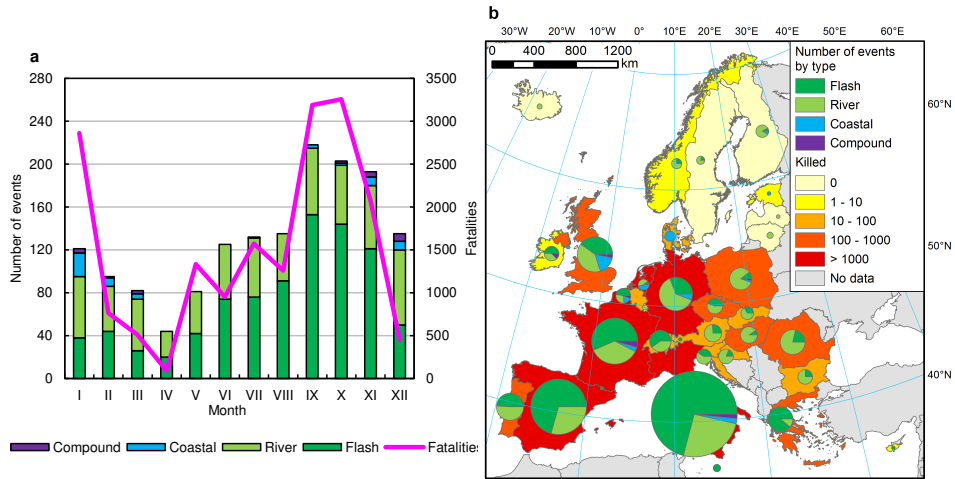


Figure 6.4: Flood occurrences and fatalities. Total number of flood events and fatalities (unadjusted, reported values) between 1870 and 2016, (a) by month and (b) by country.

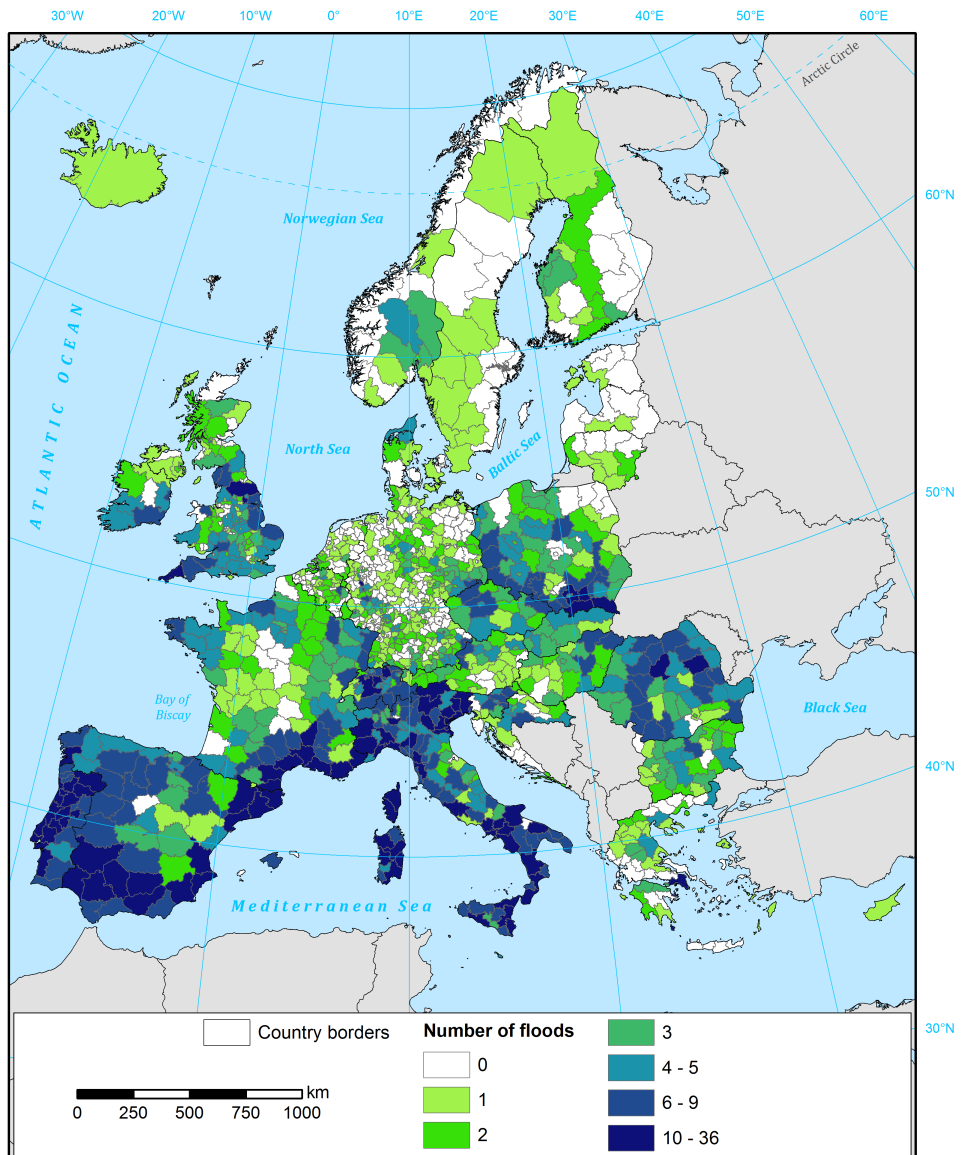


Figure 6.5: Total number of floods events recorded in HANZE database by NUTS3 region (1870–2016).

6.3.3. TRENDS IN REPORTED AND NORMALIZED FLOOD LOSSES

In Fig. 6.6, the records from the database are aggregated per year, and shown in two variants. In saturated colours, the original, unadjusted values of damages are shown as reported in historical records. Only the monetary value of losses was adjusted for price of inflation and converted to 2011 euros. In less intense colours, the normalized values, i.e. those adjusted for change in population, GDP or wealth within the individual floods' footprints, are presented between the year of the event and 2011. It is important to note that vulnerability to floods is assumed to be constant and that the reported losses are only multiplied by the change in number of persons, production or assets in a given footprint (see Methods section for details).

The resulting trends are reported in Table 6.2 for five periods: 1870–2016, 1900–2016, 1930–2016, 1950–2016 and 1970–2016. Most flood events recorded in the database occurred in recent decades, with relatively small numbers of events reported for the late 19th century. Over most of the period of record, the total area inundated increased significantly, however no significant trend is observed after 1930. Given that area flooded is known only for a tenth of all events in the database, confidence in this finding is low. In contrast, the number of fatalities is available for almost all flood events in the database and a negative trend of at least 1 % per year is observed, even though it is only statistically significant for the period between 1950 and 2016. Finally, for both the number of persons affected and monetary losses adjusted for inflation, a positive trend is observed over all periods of record. However, for 1950–2016 and 1970–2016 the trend is not significant.

Normalization has a considerable effect on the observed results. The downward trend in fatalities becomes much more pronounced, reaching -4.6 % per year (1950–2016). It also becomes statistically significant except for the period between 1970 and 2016; however, uncertainty regarding past exposure to floods renders the trends for this time period insignificant. Nonetheless, during the period from the 1980s to the present there have been fewer (normalized) deaths than almost any period prior. In contrast, the number of persons affected increases consistently throughout time, but the trend is less pronounced than before normalization (approximately 1 % per year compared to almost 2 % without adjustment). Still, the total number of flood victims peak around the year 2000. In terms of financial losses, the increase for 1870–2016 becomes smaller after normalization (1.4–1.5 % per year instead of 3 %), but still significant. However, when using the starting years 1900 and 1930 for the analysis, the trend in financial losses becomes statistically insignificant. The biggest shift in financial losses occurs for the period between 1950 and 2016 where the trend (-2.6 % per year) is statistically significant. This is similar to the finding before normalization, however the trend is now downward rather than upward. Correcting losses by changes in both GDP and wealth indicates that losses peaked in the 1950s rather than the 2000s. In general, flood losses have been declining in the entire post-1945 period despite some noticeable cycles of higher and lower loss-generating periods.

6.3.4. TRENDS IN FLOOD LOSSES CORRECTED FOR MISSING RECORDS

Historical records of flood events often do not contain all or even most of the statistics on the consequences of floods. Hence, in order to better assess trends in flood losses, gaps in the database were filled using estimates based on an analysis of the dependence

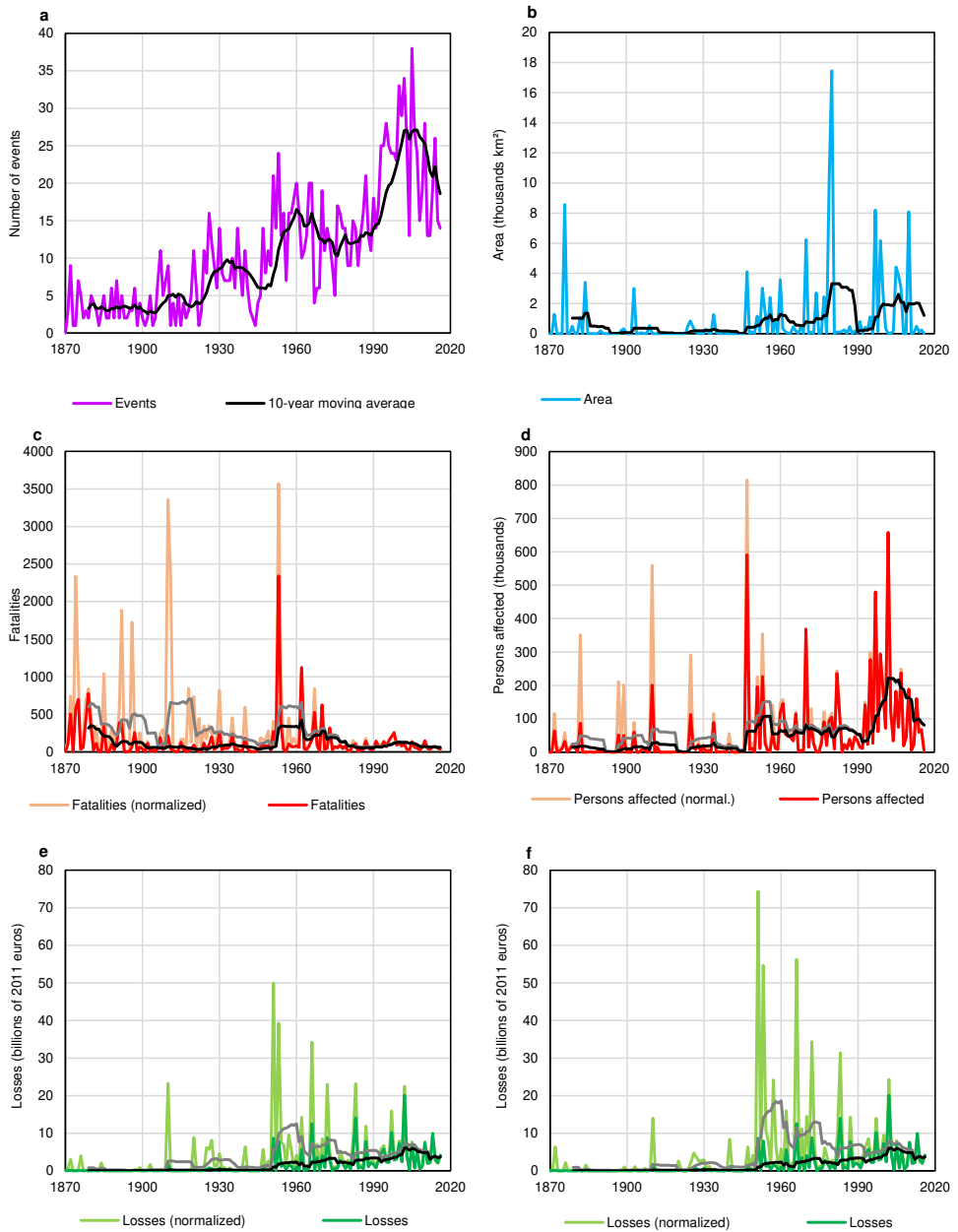


Figure 6.6: Trends in flood losses per year. Comparison of unadjusted, reported values (dark colours) and normalized values, i.e. adjusted to 2011 levels of exposure (lighter colours), for (a) number of events; (b) area inundated; (c) fatalities; (d) persons affected; (e) financial value of losses with normalization by GDP and (f) financial value of losses with normalization by wealth.

Table 6.2: Comparison of trends in annual flood losses. Values are in % per year and equal the rate parameter in Poisson regression. The time periods all end in 2016. For uncertainty ranges, see Appendix Figs. H.4 and H.5.

Start year	Reported					Normalized				Normalized and gap-filled				
	Events	Area	Fatalities	Affected	Losses	Fatalities	Affected	Losses (1)	Losses (2)	Area	Fatalities	Affected	Losses (1)	Losses (2)
1870	* 1.5	* 1.4	-0.3	* 2.0	* 3.0	* -1.1	* 1.1	* 1.5	* 1.4	* 1.6	* -1.2	* 0.7	0.2	-0.1
1900	* 1.5	* 2.0	0.2	* 2.0	* 2.8	* -1.4	* 1.2	1.0	0.9	* 1.8	* -1.3	0.6	0.2	0.3
1930	* 1.3	1.6	-0.9	* 1.7	* 2.4	* -1.8	1.1	-0.1	0.3	* 1.7	-1.8	0.4	-0.5	-0.0
1950	* 1.0	0.6	* -3.3	1.4	1.3	* -4.6	0.8	* -2.6	-1.8	* 1.3	* -4.7	-0.1	* -2.3	* -1.5
1970	* 1.4	-1.5	-1.7	1.2	1.3	-1.9	0.9	-1.6	-0.6	1.0	* -2.0	0.3	-1.2	-0.3

(1) normalized by wealth, (2) normalized by GDP, * significant at $\alpha = 0.05$.

structure between all pairs of variables using copulas. Gap-filled annual losses are presented in Fig. 6.7. The difference between the unadjusted and gap-filled data is clearly visible in the graphs; only in the case of the number of fatalities are the differences small. This is because there were few gaps in the historical record of the number of fatalities.

The addition of modelled data to the historical record affected many of the observed trends, both compared to reported and normalized losses (Table 6.2). The trend in inundated area for 1950–2016 becomes statistically significant after gap-filling (1.3 % per year), while an opposite trend is indicated for 1970–2016: an annual increase of 1 % (not significant) instead of an annual decrease of 1.5 %. However, for the entire period 1870–2016, there is little difference in the observed upward trend after gap-filling (1.6 % instead of 1.4 %). In terms of the number of deaths, there is almost no change in trends, as fatalities decline across the board, with the trend for 1950–2016 reaching -4.7 % per year. The number of persons affected before correcting for missing records shows an 0.8–1.2 % increase across all considered time periods, while after correction, the trend decreases to at most 0.7 %, annually, with a small decline during the period between 1950 and 2016. Only the 1870–2016 trend is statistically significant. Moreover, the normalized monetary value of losses after gap-filling no longer shows a significant trend for the whole period, and losses normalized by wealth increase by only 0.2 % per year, while normalized by GDP decline by 0.1 % per year. For all other time slices, the general trends are the same as before correcting for missing data.

6.3.5. VARIATION IN FLOOD LOSS TRENDS BY AREA AND TYPE OF FLOOD

Trends calculated for all events in Europe include variations within different groups of floods. Supplementary Table H.2 consists of five tables identical to Table 1, but presenting the results for two subdomains: the Mediterranean countries (Cyprus, Greece, Italy, Malta, Portugal and Spain) and all other countries. The results are also shown for the different types of flood events flash floods, river floods and river/coastal/compound floods together. The tables are synthesized in Appendix Fig. 6.8, in which normalized and gap-filled trends can be compared for different selections of flood events. There is a sharp contrast between the trends observed in the Mediterranean region (containing 57 % of events) and all other countries. Trends for the subdomains diverge substantially over time for all variables except fatalities. Especially for the period since 1950, there are significant downward trends in the Mediterranean countries in normalized and gap-filled fatalities, persons affected and monetary losses, whereas opposite or not statis-

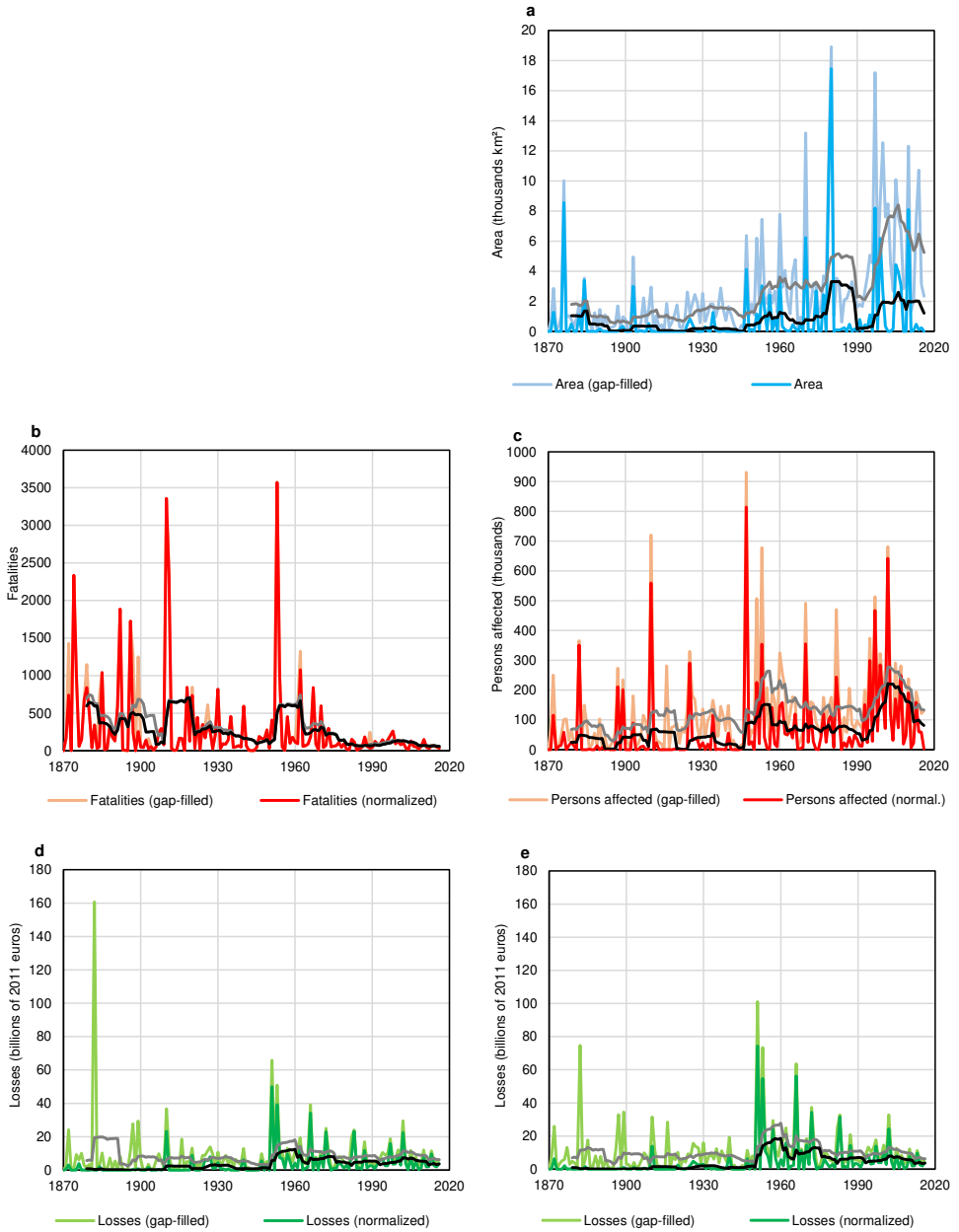


Figure 6.7: Trends in normalized flood losses per year. Comparison of losses with (lighter colours) and without gap-filling (dark colours) for (a) area inundated; (b) fatalities; (c) persons affected; (d) financial value of losses with normalization by GDP and (e) financial value of losses with normalization by wealth.

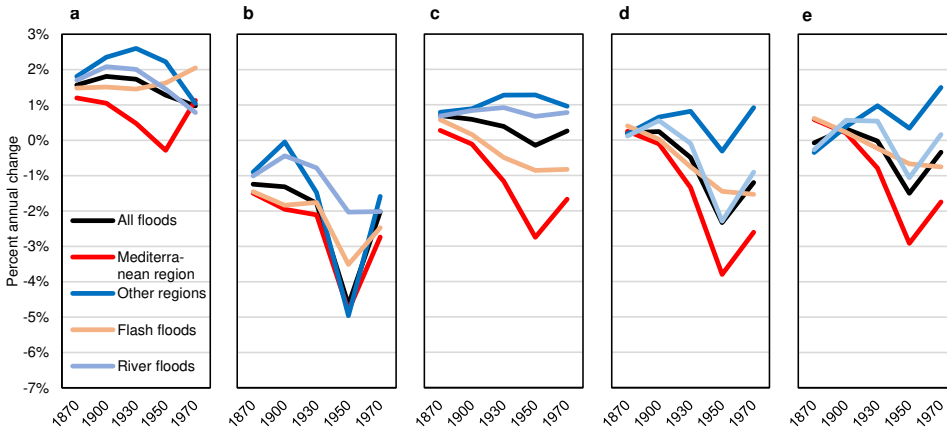


Figure 6.8: Trends in normalized and gap-filled losses for different starting years. Data for all flood events, two subdomains (Mediterranean regions and other parts of Europe) and two types of floods (river and flash), for (a) area inundated; (b) fatalities; (c) persons affected; (d) financial value of losses with normalization by GDP and (e) financial value of losses with normalization by wealth.

tically significant trends are observed in the other parts of Europe. This difference is partly because flash floods constitute a larger share of events in the Mediterranean region than in the northern European countries. However, when looking for trends in the consequences of flash flood (56 % of events) and river flood (39 %) events, the differences are smaller. The decline in fatalities and number of persons affected due to flash flood events are larger than those from river floods. For economic losses, they are broadly similar.

6.4. DISCUSSION

The findings presented here include several uncertainties. The quality of input data - flood events and exposure - is of crucial importance, but this is discussed in the HANZE database documentation in section G.5. This section concentrates on other influences on observed flood trends, particularly the completeness of data on flood damages and validation of the trends based on other sources of data.

6.4.1. ESTIMATION OF UNDERREPORTING OF FLOOD EVENTS

Completeness of the database of historical floods has a large impact of observed trends. In principle, per each major flood event in the record, there should also be multiple smaller ones. For the purposes of this analysis, flood events are considered as “small” or “major” in relation to their severity, i.e. the amount of losses generated by those floods relative to the overall distribution of losses for all events, where small floods are those in the lower percentiles of this distribution and major floods are those in the upper percentiles. There are relatively few small events recorded in HANZE before about 1950. If one divides the flood events by severity into quintiles (Fig. 6.9 and Appendix Fig. H.6), the smaller the flood, the steeper the observed trend in number of flood events. For

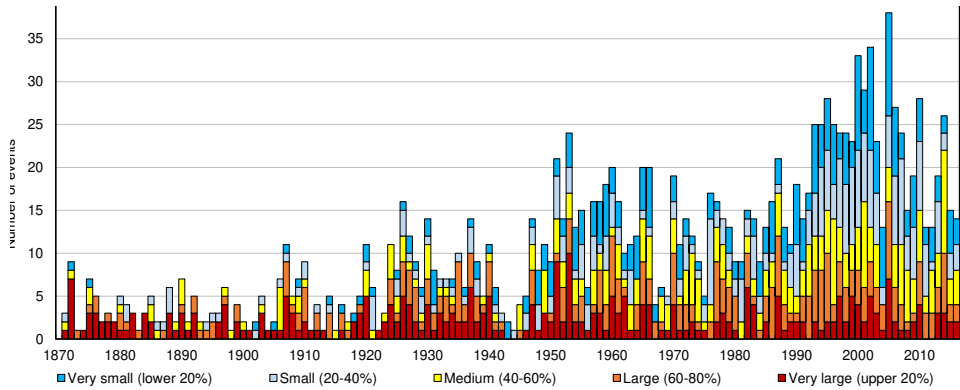


Figure 6.9: Severity of floods. Annual number of flood events classified by severity into quintiles. Classification is based on normalized and gap-filled values of losses.

example, the annual increase in number of flood events in the uppermost quintile (i.e. largest floods) is 0.3 % per year compared to 2 % per year for those in the lowest quintile. This finding is also the same when splitting flood events by decile (with less than 0.1 % increase per year in the upper 10 %). This points to substantial underreporting of smaller floods historically; they are simply not mentioned in contemporary publications referring to historical events. Yet, small floods remain important since they can have a large contribution to overall damages over longer periods of time [346]. In the present, better availability of news reports and government data improves coverage considerably.

To estimate the quantity of missing information, or underreporting, the number of events was adjusted (except those in the upper 20 %) before 1990 so that the ratio between number of events in each quintile is the same as after 1990. A summary of all adjustments to reported data is presented in Fig. 6.10. It was found that correcting for underreporting diminishes most of the upward trend observed in the number of flood events, whereas it only slightly reduces the growth in area inundated. Yet, given the very small number of recorded flood extents (even for the most recent events), there is considerable uncertainty in both gap-filling and the correction applied for underreporting. The decline in number of fatalities becomes more pronounced with every adjustment and the gap-filled data suggest that the number of people affected peaked in the mid-20th century, with no significant trend thereafter. After all corrections are applied, a downward trend in financial losses becomes apparent, although for losses normalized by wealth a mid-century peak is indicated. In total, it was estimated that flooding affected 0.03 % of European population per year on average between 1870 and 2016, and generated losses equal 0.08–0.09 % of GDP (depending on normalization variant).

6.4.2. VALIDATION OF FLOOD FOOTPRINTS

Another source of uncertainty is the delineation of flood “footprints”. 100-year flood hazard zones from pan-European modelling carried out in project RAIN (chapters 2 and 3), which correspond to the climate and physical geography of the 1971–2000 period, were used here. However, it is acknowledged that not every flood in the database is a 100-year

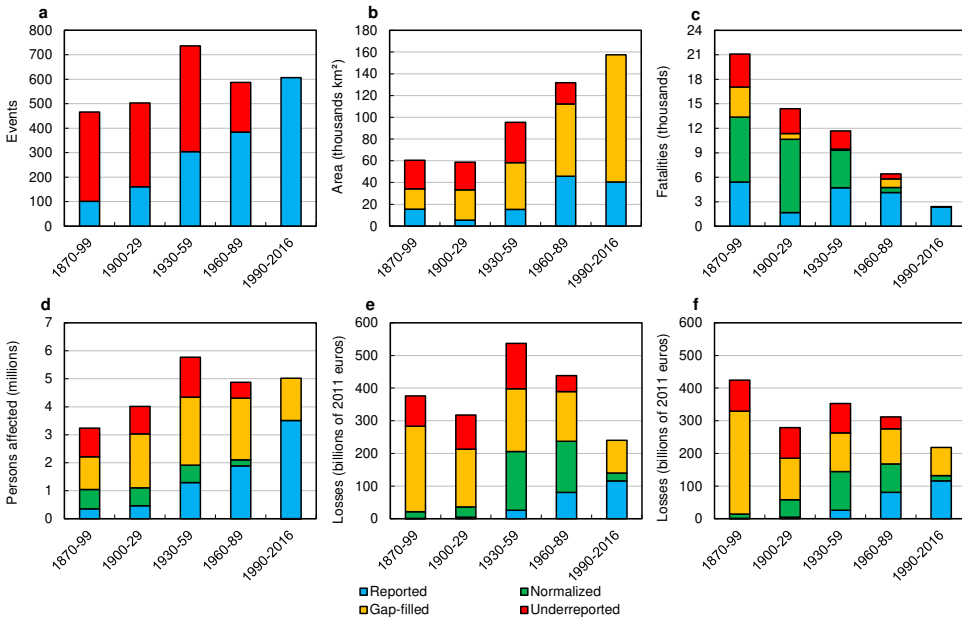


Figure 6.10: Flood losses in 30-year periods. Reported number of flood events and their consequences is summed per 30-year periods, with three types of adjustments: normalization, gap-filling of missing (normalized) loss data and estimation of underreporting of small flood events and normalized damages they caused, for (a) number of events; (b) area inundated; (c) fatalities; (d) persons affected; (e) financial value of losses with normalization by GDP and (f) financial value of losses with normalization by wealth.

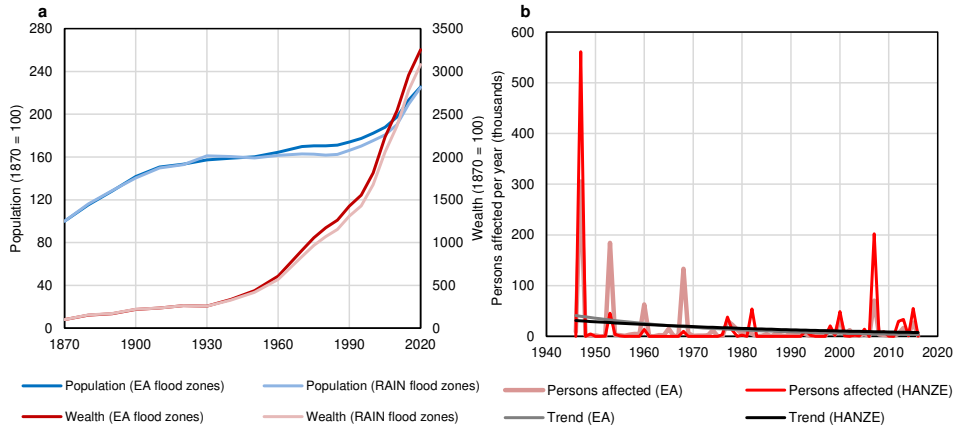


Figure 6.11: Validation of flood trends. (a) Trends in population and fixed assets living within 100-year flood hazard zone in England, using Environment Agency (EA) flood risk map and RAIN project map used in this analysis. (b) estimated persons affected (normalized) in England, compiled by intersecting EA historical flood outlines with HANZE-Exposure population grid, and compared with normalized reported persons affected from HANZE-Events.

6

event, and that the 100-year floodplain boundaries do not remain stationary over time, given, for example, changes in climate, river geometry, urban development, or construction of hydraulic structures [37, 62]. But, because detailed, local flood hazard maps and recorded outlines for historical floods are not readily available for all locations in Europe, the 100-year floodplain is used as a proxy for floodplain extent and as a delineation of areas subject to high flood hazards. To validate the assumption that the 100-year is a viable proxy, the results were recalculated for England using flood extents from a comprehensive study by the Environment Agency (EA) [54]. Trends in exposure inside and outside the flood hazard zones are very similar for both pan-European maps from RAIN project and more detailed maps from EA (Fig. 6.11). The normalized number of affected persons within actual flood outlines recorded by EA yields an annual downward trend for 1946–2016 of 3.5%, compared to a 2% decline using the HANZE flood footprints and reported number of persons affected. However, the records are dominated by just a few events, especially the 1947 Thames valley flood and 2007 country-wide summer flood, hence there is large uncertainty in this comparison. The total (normalized) number of people within EA flood outlines for 1946–2016 is 1.11 million, compared to normalized reported number of people affected in HANZE of 1.19 million.

I also analysed trends in reported annual losses for Poland between 1947 and 2006 based on national government statistics (Fig. 6.12). For inflation-adjusted, but not normalized, losses an annual upward trend of 3.9% per year was found compared to a 4.2% increase in HANZE. Correcting for national GDP growth, reported annual losses still increase by 1.9%. In contrast, normalized and gap-filled data for Poland in HANZE indicate a 2.8% increase per year.

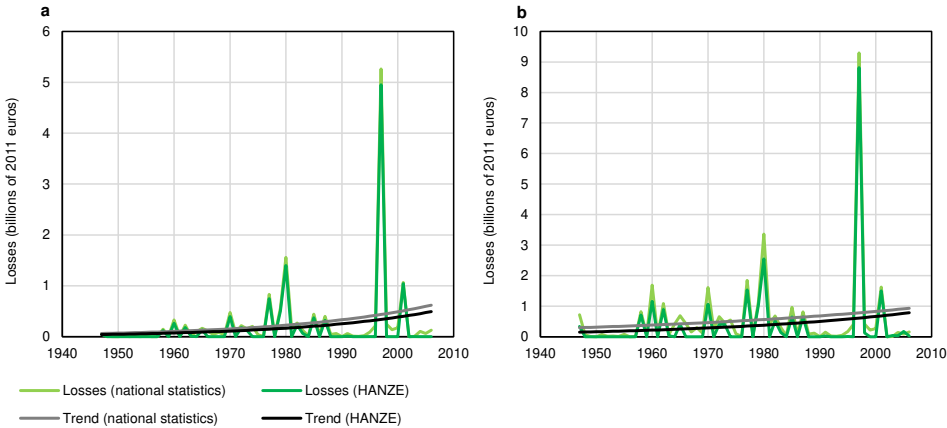


Figure 6.12: Annual financial losses to floods in Poland, 1947–2006, based on national statistics and HANZE database: (a) reported and (b) normalized and gap-filled.

6.4.3. OTHER UNCERTAINTIES IN FLOOD TRENDS

This analysis contains further sources of uncertainty which are less easily quantifiable. For instance, it is assumed that the flood hazard zones are constant over time. Climate change notwithstanding, many developments may alter local flood hazard, such as river regulation or construction of defences, bypass channels and reservoirs. In case of the latter, the erection of large reservoirs is included in the land use maps, but their effects on the size of flood hazard zones is not considered. Other uncertainties are related to the normalization and gap-filling of damage statistics, though the probable margins of error were included in statistical significance testing. Naturally, reported data could also contain many inaccuracies and inconsistencies. For example, there are many variations in the way that the number of people affected are reported across different sources, ranging from the number of evacuees to the number persons whose houses were either inundated or destroyed. Often, only the number of houses affected (flooded, damaged or destroyed) was provided for a given event. In this case, 4 persons per household were assumed, as some other national/international databases also used this assumption. In other cases, there might also be incomplete coverage of financial loss data, in the sense they do not always include all categories of assets. Information on area inundated more often than not refers only to agricultural land flooded rather than complete extent of events.

Nevertheless, the findings presented here are consistent with previous studies. No significant trend was reported for financial losses normalized using country-level statistical data for major European floods (1970–2006) [292], major European windstorms (1970–2008) [318], or Spanish floods (insured losses, 1971–2008) [318]. For those time periods, insignificant downward trends were observed in the HANZE gap-filled financial losses normalized by wealth (-0.4 to -0.7 % per year). In the United States, an insignificant annual decline of 0.49 % was found in flood losses normalized by change in tangible wealth (1932–1997) [347]. This is similar to a 0.12 % decline recorded in HANZE

during those years for Europe. In Australia, no trend was found in insured losses from weather-related hazards for years 1967–2006, when the losses were corrected for increase in dwelling value [348]; however, in HANZE, an insignificant upward trend of 0.2 % per year was observed.

Given the one-and-half century timespan of the study, a very important question is raised as to whether the results indicate an influence of climate change. In the aforementioned study for the US, trends in precipitation were found to be similar to trends in flood losses per capita. For Europe, the 20th Century Reanalysis [345] was used to obtain trends in the number of episodes of extreme precipitation above given return periods with a duration from 1 to 7 days, weighted by the size of flood zones within each grid cell of the reanalysis. An annual increase varied from 0.7–1.4 % for a 10-year return period up to 0.8–2.4 % for a 100-year return period. This is in between the value of increase both in the (unadjusted) number of flood events and (gap-filled) area inundated, which is contained in 1.4–1.7 % range (for all floods, flash floods and river floods alike). In the Mediterranean region, there is a smaller increase, or even decrease in more recent decades, of extreme precipitation than in other parts of Europe which is also consistent with trends in number of events in the two sub-domains. The overall upward trend and the contrast between northern and southern Europe is consistent with other studies, both for extreme precipitation [294, 349, 350] and large flood occurrences [36, 42]. However, the number of events and flooded area must have had less pronounced trends for the continent as a whole, since the records of past floods have grown more complete over time, as shown in Fig. 6.10. This might indicate that, on average, flood hazard in Europe increased due to climate change. Consequently, if the amount of losses mostly declined given constant exposure, vulnerability of population and assets decreased. On the other hand, given the significant deficiencies in the available data on flooded area, uncertainty in the underreporting of smaller flood events and potential bias in reanalysis data, this relation could be coincidental. The average for Europe also masks large spatial diversity of meteorological and hydrological trends, let alone differences in adaption to flood risk. Also, this study did not consider localized pluvial floods, i.e. flash floods which occur in urban areas disconnected from riverine or coastal floodplains. Growing soil sealing by artificial surfaces connected with the aforementioned increase in frequency of severe (short and intense) rainfall events must have had an impact on the number of observed urban floods.

In future studies, research could focus on the influence of social, political and technical factors on changes in flood vulnerability and risk. In this study, the most significant trend observed was a decline in flood-related fatalities of 1.4 % per year since 1870 and 4.3 % since 1950. Many technological factors could explain this decrease, such as vast improvements in communication and transportation, which allowed more effective evacuation, rescue and relief operations, and the establishment of meteorological and hydrological agencies, which allowed for continuous observation and forecasting of rainfall and river discharges, improved early warning and disaster preparedness. Moreover, flood prevention, emergency management and disaster relief have largely become permanent government services, in contrast to ad-hoc local arrangements of the past. However, in contrast to fatalities and the monetary value of losses, the area inundated and the number of persons affected shows an increase, which suggests that structural

Table 6.3: Flood footprint characteristics and relative losses. The table shows rank correlation between relative losses (reported versus potential) for the 310 major floods in the uppermost quintile as shown in Appendix Fig. H.6.

Flood footprint characteristic		Relative losses				
		Area inundated	Fatalities	Persons affected	Losses per GDP	Losses per wealth
GDP per capita		-0.18	-0.29	-0.23	-0.41	-0.41
Population density		0.07	-0.26	-0.40	-0.30	-0.33
Land use	urban fabric	0.11	-0.34	-0.30	-0.31	-0.34
	other artificial	0.07	-0.12	-0.20	-0.24	-0.24
structure (% share)	agricultural	-0.06	0.10	0.07	0.19	0.19
	natural	0.06	-0.02	0.03	-0.07	-0.08
Wealth structure (% share)	agriculture	0.01	0.30	0.29	0.38	0.38
	industry	0.10	0.12	0.12	0.18	0.16
	services	0.16	-0.14	-0.06	-0.03	-0.01
	housing	-0.08	-0.23	-0.17	-0.26	-0.28
	infrastructure	-0.22	-0.23	-0.31	-0.28	-0.28

flood protection didn't have as much effect as the decline in vulnerability of the population and assets. In general, vulnerability has declined compared to GDP per capita, as evidenced in Table 6.3. It shows rank correlations between relative losses (reported, but not gap-filled versus potential) for 310 major floods (the uppermost quintile in Fig. 6.9) and GDP per capita, finding all variables negatively correlated. The strongest correlation was between GDP per capita and monetary value of losses, and the weakest with area inundated. This is somewhat similar to global-scale findings for modern countries [329], but here those effects can be traced over the same sample of countries over almost one and half centuries.

Changes to the landscape could also have had an effect on vulnerability. Areas affected by floods urbanised to a higher degree than Europe in general (Appendix Fig. H.7), while croplands have been phased out faster. Dwellings, especially urban, have become sturdier as brick and concrete is more often used as construction material than timber or adobe. The percentage of flood footprints under urban fabric has stronger negative correlation with relative fatalities and people affected than GDP per capita for the 310 major floods mentioned in the previous paragraph (Table 6.3). At the same time, there is a positive correlation between agriculture share of land and relative fatalities, persons affected and monetary losses. Analysing the structure of wealth, the only types of wealth more strongly correlated with relative losses than GDP per capita is the share of infrastructure (for inundated area and persons affected) and agriculture (for fatalities and persons affected) in total wealth. This indicates that areas with high concentration of urban fabric and infrastructure are better protected than less important urban zones, let alone rural areas. This is an intuitive conclusion, but supported by evidence from events spanning almost 150 years. Further analysis may help to understand changes in flood protection standards and land use-damage functions. Still, more data collection is needed, especially to gain a better understanding of local hydrological trends. Only when the climate signal is fully removed from the data, can the trend in flood vulnerability be computed with confidence and the effectiveness of adaptation assessed.

6.5. CONCLUSIONS

The HANZE-Exposure database was made to provide data allowing me to normalize historical flood losses. It enabled me to analyse demographic and economic growth within the areas exposed to flood, as well as calculate reported losses relative to potential damages. Additionally, copula theory was used to analyse the dependence structure between four different variables: area inundated, fatalities, persons affected and financial losses. The simulated data pairs were used to fill in missing information in the database for historical flood events and provide a better estimate of trends in flood losses. Finally, the underreporting of smaller flood events in available sources was estimated, and its impact on the results quantified. Combined with HANZE-Events, a compilation of flood loss data since 1870, the analysis resulted in a pan-European study of long-term changes in flood risk in Europe. The results obtained using the HANZE database indicate an increase in inundated area contrasted by a consistent decline in flood fatalities for the period 1870-2016, with no significant trend in the number of persons affected or financial losses. However, for the period after 1950, a considerable decline in fatalities and monetary losses was observed. Moreover, it was shown that the majority of quantitative information regarding historical flood losses is underreported by modern sources and that this has a profound impact on calculated trends. The results indicate that when correcting for underreporting, the annual number of flood events and persons affected have increased much less than calculated using uncorrected series (and possibly declined since the mid-20th century), and that financial losses have declined over time. Numerous applications of the HANZE database for further studies is foreseen, including an analysis of trends for other hazards, an assessment of the potential impacts of climate change on historical losses, and studies of individual events and their impact on flood management.



ATTENZIONE PERICOLO 

POSSIBILITÀ DI ONDE DI PIENA IMPROVISE
ANCHE PER MANOVRE SU OPERE IDRAULICHE

DANGER 

POSSIBILITY OF SUDDEN FLOOD WAVES ALSO
BECAUSE OF MANOEUVRES ON HYDRAULIC PLANTS

 **ATTENTION DANGER** 

POSSIBILITÉ DE CRUES SOUDAINES À LA SUITE
AUSSI DE MANOEUVRES SUR OUVRAGES HYDRAULIQUES

 **ACHTUNG GEFAHR** 

MÖGLICHKEIT PLÖTZLICHER FLUTWELLEN AUCH
ZUFOLGE VON BETÄTIGUNG DER STAUDAMMSCHÜTZE

Previous page: A flash flood warning sign in Alta Valle Antrona in the Italian Alps.

7

CONCLUSIONS AND RECOMMENDATIONS

7.1. CONCLUSIONS

THIS thesis explored multiple aspects of pan-European flood risk. Investigations of river, coastal and compound floods, as well as flood losses and exposure were carried out to address six research problems. Each of the five main chapters covered a selection of three or four of the six research problems.

I. Accuracy Chapters 2–4 dealt with the issue of accuracy in river and coastal flood modelling. In chapter 2, a Bayesian Network-based model was built to estimate extreme river discharges. It achieved similar accuracy as previous pan-European studies that used physics-based rainfall-runoff models, and shown better performance than an alternative statistical method called regional frequency analysis (R^2 of 0.89 compared to 0.70 between simulated and observed 100-year discharge). Those results were then applied as boundary conditions for modelling, with a 1-D hydrodynamic SOBEK model and planar approach to inundation estimation (chapter 3). Despite the simplifications, the Pan-European river flood maps have shown slightly better alignment with high-resolution, locally-produced maps than European map based on LISFLOOD model, though not for all case studies. Modelling storm surges in chapter 4 also yielded good results, showing better alignment between modelled and observed storm surges relative to a previous European study, and extreme sea levels relative to results from a global model. Finally, the comparison of pan-European coastal flood maps between three different studies that used static inundation method has shown that correcting the underlying digital elevation model improves the accuracy of the maps.

II. Efficiency Both chapter 2 and 3 achieved the goal of simplifying the methodology in order to reduce the computational time while retaining the accuracy of the outcomes. In fact, the simulation time consumption was reduced significantly, dispensing with the need of using a computational cluster, therefore showing that pan-European river flood analyses could be carried out more efficiently. Bayesian Network-based model allowed

computation of river discharge scenarios under present and future for rivers of all sizes on a desktop PC. Similarly, the modelling of river flood hazard zones was conducted without the use of a computer cluster, whereas the LISFLOOD-based map required a 60-processor unit, even for a much smaller number of river sections than this study.

III. Spatial coverage and resolution The problem of improving spatial coverage and resolution was addressed in all chapters. In chapter 2, thanks to its high efficiency, the Bayesian Network-based model provided estimates of extreme river discharges at given return periods for rivers with a total length of almost 2 million km. This is approximately four times more than estimates from the pan-European LISFLOOD model. Chapter 3 has the same resolution and similar extent to the LISFLOOD-based map, but lowers the minimum catchment size of rivers, resulting in 2.5 times higher coverage (almost 500 000 km of rivers). The estimates of extreme sea levels in chapter 4 are available in finer resolution than previously, while also for the first time with utilizing a high-resolution regional climate model instead of a coarser general circulation model. Estimates of joint probability of occurrence of surges, waves, precipitation and river discharges (chapter 5) utilize for the first time the potential of high-resolution observations and models. In the final part of the thesis (chapter 6), exposure data are provided for the first time in 100 m resolution, while the database of past damaging floods uses a subnational scale of analysis and combination with flood hazard zones for the first time. In combination with the pan-European flood maps, this lead to the first analysis of flood loss trends normalized with local-scale exposure data.

IV. Joint probabilities in floods Chapter 5 investigated compound flood potential; it is the first pan-European assessment on this topic. The analysis presented a composite index that identified areas where compound floods are most likely to occur: southern Europe for coastal-flash flood combination and north-western Europe for coastal-river flood variant. The joint probabilities calculated from both models and observations were compared extensively. Overall, models recreate the dependency between storm surges and precipitations fairly well, but achieved much poorer performance when modelling the storm surge-river discharge joint occurrence. The chapter also analysed past occurrences of compound floods in Europe, 24 of which were identified between 1870 and 2016, based on data compiled in chapter 6.

V. Historical trends in flood risk components The analysis of long-term trends in flood losses, exposure and vulnerability in Europe (chapter 6) is more comprehensive than any previous study. The work generated a large database, HANZE, containing gridded exposure estimates and data on 1564 damaging floods going back to 1870. Such a long timespan, despite large uncertainty related to the underlying data, enabled a truly long-term analysis of occurrence of damaging floods and their consequences. The analysis shows the dominant role of exposure in driving flood losses, which have not increased relative to the size of the economy or asset value since 1870. A large decline in flood-related fatalities was also observed. The study also innovatively attempted to quantify missing data on flood losses, a majority of which were unreported, according to estimates presented herein.

VI. Data availability and reusability All chapters resulted in large amounts of data that are of potential interest for other researchers. Therefore, all relevant outputs were made publicly available, mostly in GIS format or other formats specific for particular

groups of users. Data from chapters 2–4 and 6 are available from 4TU.Centre for Research Data, while those from chapter 5 are provided online by the European Commission – Joint Research Centre data repository (see Appendix I for links to data).

7.2. RECOMMENDATIONS

This thesis provided many detailed methods and output datasets that could help both researchers and practitioners improve their assessments of flood hazard and risk in Europe. Yet, some broader recommendations based on the work presented here can also be formulated.

1. The Bayesian Network-based model of extreme river discharges was inspired by a more than a century-long engineering practice of applying empirical equations to obtain estimates of discharges in places where no gauge records are available. A Bayesian approach vastly improved calculation of extreme discharges at given return periods, showing potential for further applications. One possibility would be operational flood forecasting, as the computational efficiency of the method could allow more frequent updating of forecasts and improve uncertainty estimation.
2. Both river and coastal flood hazard estimates were found to be very sensitive to assumptions regarding existing flood protection levels. Yet, there is very little direct information available on reliability of dikes, barriers or coastal protection measures in Europe, even if one considers only the overtopping failure mechanism, and even if only the nominal protection standards (as opposed to the actual reliability) are taken into account. Hence, more effort should be put on gathering information from local water authorities concerning flood defences. Further, data on past flood occurrences (such as collected in HANZE database) should be utilized for that purpose, combined with a river discharge/storm surge reanalysis and a set of social, economic and policy variables. In this respect, a Bayesian-network approach would be helpful to process the information.
3. The European Union's Floods Directive was a milestone in European flood mapping, but it largely neglected the problem of disseminating and sharing flood risk data. The availability of flood maps in a format that is reusable by researchers is still very low, as is exemplified by how few case studies were used to compare local flood maps with the pan-European hazard maps. Flood modelling on European scale will be difficult to advance without means to extensively validate the results. Researchers should put more pressure on the relevant authorities to release the flood maps as reusable datasets in public domain, as well as sharing the data that were obtained through individual requests to the authorities whenever possible.
4. Analysis of long-term trends in flood exposure has shown that exposure is the main driver of flood losses. More attention should be given to this subject, especially as many countries try to limit flood risk by spatial planning. Migrations of populations and changes in economic structure cause significant changes to exposure and vulnerability. Even at present, despite slow economic and demographic growth, urban areas are expanding very fast. It is not surprising then that urban

floods, caused by lack of drainage in build-up areas, is a growing concern, if the area covered by artificial surfaces has increased tenfold since 1870. Thus, even if heavy precipitation is stable over time, large increases in urban flooding may be observed. Further, the effect of changes in structural flood protection on exposure should be quantified.

5. This study has only slightly touched the topic of trends in flood vulnerability of societies and economies. Yet the study met the question, having accounted for the effect of changes in exposure, what is the source of the observed trends in flood losses: change in hazard or change in vulnerability? The question could not be conclusively answered due to the lack of long-term data on changes in flood hazard in Europe. There is currently no climate reanalysis with both sufficient resolution and timespan to reconstruct changes in extreme discharge and flood hazard in a long-term perspective, though work on such models is in progress (e.g. ERA5 reanalysis [351]). Another problem are the changes in river and coastal hydrography due to flood protection works, dredging, sedimentation, meandering, erosion etc. Archival maps and data from water authorities should be collected to reconstruct past hydrography, which could have significant impact on flood hazard estimates. Altogether, the hydrological and climatological research covering a long timespan would result in pan-European data on changes in flood vulnerability and allow a multivariate analysis of factors influencing vulnerability over time. Such work would also enable better modelling of vulnerability in studies on future flood risk.
6. Pan-European flood research is often too inaccurate for local-scale application in flood management, due to relatively low resolution of input data and the lack of accurate information on reliability of flood defences at European level. Yet, they still have practical value at such scale. Some processes cannot be captured when analysing flood hazard or risk at a local authority area. Most importantly, future developments in climate require European or global-scale modelling, which then need to be transformed into changes in river discharge or storm surge occurrence, requiring modelling on catchment/basin scale. The future demographic, economic or political outlook are also difficult to model on local level as mostly driven by developments at national and international levels. Further, new adaptation strategies, flood management concepts, operational systems or other computer models are possible thanks to large European datasets covering diverse environmental conditions. It is therefore recommended to investigate the applicability of large flood assessment before carrying out local-scale analysis.
7. Compound floods were only studied here in terms of the co-occurrence of extreme precipitation, river discharges and storm surges. However, it is clear from the results and historical cases of compound floods that the phenomena need to be analysed further in local scale studies. At European level, it would not be possible to recreate the effect of river and coastal water levels exacerbating each other and intensifying the resulting flood. That depends very much on e.g. river channel geometry, exposition of the coast, tidal amplitude and presence of flood defences. The effort would be nonetheless beneficial in improving flood risk estimates in

many coastal and estuarine areas of Europe. The priority areas for this research could be identified using the composite index presented in this thesis.

As a final remark, it can be added that the work presented here will eventually be rendered obsolete by the development of new models, datasets and methods. But, until then, this thesis will be a useful reference on the topic of European flood risk and contribute to the field's advancement. The work may be safely left with the comment of an 18th century researcher upon his estimates of the population of France:

" [The results] are not to be viewed with much confidence but they are a first step towards the truth. The proper way to criticize them is to displace them by more accurate figures. They are like old maps of unexplored parts of the world, useful or even necessary until rectified by new discoveries."

M. Moheau, *Recherches et considérations sur la population de la France* (1778), as quoted by Willcox [352].



APPENDICES



A

DIAGNOSIS OF UNDERLYING ASSUMPTIONS REGARDING THE NON-PARAMETRIC BAYESIAN NETWORKS

A.1. INTRODUCTION

This appendix provides additional details related to the methodology of Non-Parametric Bayesian Networks (NPBN) described in section 2.2.4. Firstly, a diagnosis of the copula models for our BN is presented in order to justify the use of the Gaussian copula in the NPBN. Secondly, the procedure and results of the validation of the graphical structure of the BN is described. Additionally, more examples of conditionalization of the model mentioned in section 2.2.5 are provided.

A.2. COPULAS

A copula is, loosely, a joint distribution on the unit hypercube with uniform $[0, 1]$ margins. Copulas are very useful models of dependence. In fact, every continuous joint distribution can be uniquely represented by a copula. In the bivariate case, random variables X and Y are converted into uniform $[0, 1]$ variates through their margins. The transformed variates, usually denoted as u and v , are then fitted to one of many copula models. Representing probabilistic dependence through a bivariate copulas requires selecting one of the many copula types. A detailed review is presented by [162]. Here, three of the most popular copula types are investigated in order to determine which one is best in representing the joint distribution of variables included in the BN model of

This appendix has been included as a supplement to the paper published in *Hydrology and Earth System Sciences* **21**, 2615–2636 (2017) [114].

discharges. First, the Gaussian copula, which has the following cumulative distribution function:

$$C(u, v; \rho) = \Phi_\rho(\Phi^{-1}(u), \Phi^{-1}(v)), \rho \in [-1, 1] \tag{A.1}$$

where Φ is the bivariate Gaussian cumulative distribution and ρ is the (conditional) product moment correlation between the two marginal probability distributions u and v in the interval $[0, 1]$. Second, the Gumbel copula, parameterized by δ :

$$C(u, v; \delta) = \exp(-([\log(u)]^\delta + [\log(v)]^\delta)^{1/\delta}), \delta \geq 1 \tag{A.2}$$

Third, the Clayton copula, parameterized by α :

$$C(u, v; \alpha) = (u^{-\alpha} + v^{-\alpha} - 1)^{-\alpha}, \alpha \in [-1, \infty) \tag{A.3}$$

In contrast to many other types of copulas, these copulas require one parameter. These copulas model an important aspect of joint distributions known as tail dependence. The upper tail dependence coefficient λ_U for two random variables X and Y is:

$$\lambda_U = \lim_{u \rightarrow 1} P(X > F_X^{-1}(u) | Y > F_Y^{-1}(u)) = \lim_{u \rightarrow 1} P(U > u | V > u) \tag{A.4}$$

Roughly, a value of $\lambda_U > 0$ indicates that it is likely (more than normal) to observe values of U greater than u given that V is greater than u for u arbitrarily close to 1. Lower tail dependence would be defined similarly as eq. A.4, but then for the lower quadrant of the joint distribution. The Gaussian copula presents no tail dependence $\lambda_U = 0$, while Clayton presents lower tail dependence $\lambda_L = 2^{-\frac{1}{\alpha}}$ and the Gumbel copula presents upper tail dependence $\lambda_U = 2 - 2^{\frac{1}{\delta}}$. The investigation of these copulas covers a range of dependence structures that are usually observed in data.

Apart from a visual inspection, two measures are applied in order to advise on the copula best representing a particular bivariate distribution. Firstly, semi-correlations are computed, an approach suggested by Joe [162]. The semi-correlations are the Pearson's product moment correlation coefficients computed in the upper and lower quadrants of the normal transforms of the original variables. For positive correlation, semi-correlations in the upper right (*NE*) and lower left (*SW*) quadrants are:

$$\rho_{ne} = \rho(Z_1, Z_2 | Z_1 > 0, Z_2 > 0) \tag{A.5}$$

$$\rho_{sw} = \rho(Z_1, Z_2 | Z_1 < 0, Z_2 < 0) \tag{A.6}$$

where (Z_1, Z_2) are the standard normal transforms of (X, Y) . For negative correlation, semi-correlations in the upper left (*NW*) and lower right (*SE*) quadrants are ρ_{nw} and ρ_{se} are defined similarly [162]. In general, larger absolute values of the semi-correlations than the "overall" correlation indicate tail dependence.

The second diagnostic tool is one of the test statistics in the "Blanket Test" class discussed by Genest *et al.* [280], which is the Cramèr-von Mises statistic (M). The test statistic of interest for a sample of length n is computed as follows:

$$M_n(\mathbf{u}) = n \sum_{|\mathbf{u}|} (C_{\hat{\theta}_n}(\mathbf{u}) - B(\mathbf{u}))^2, \mathbf{u} \in [0, 1]^2 \tag{A.7}$$

where $B(\mathbf{u}) = \frac{1}{n} \sum_{i=1}^n \mathbf{1}(U_i \leq \mathbf{u})$ is the empirical copula and $C_{\hat{\theta}_n}(\mathbf{u})$ is a parametric copula with parameter $\hat{\theta}_n$ estimated from the sample. Notice that the statistic is the sum of squared differences between the empirical copula and the parametric estimate. If the correlation is negative, the M statistic for Gumbel and Clayton was computed with the rotated copula. The results of the two measures applied to the variables of our Bayesian Network are presented in Table A.1, while graphs for a few selected cases are shown in Fig. A.1.

Table A.1: Semi-correlations (ρ) and “Blanket Test” (M) statistic for all pairs of variables used in the Bayesian Network for extreme river discharges. M_ρ is the statistic for the Gumbel copula, M_δ for the Gaussian copula, and M_α for the Clayton copula. Lowest M values per pair of variables are bolded.

<i>X</i>	<i>Y</i>	ρ	ρ_{ne}	ρ_{sw}	ρ_{nw}	ρ_{se}	M_ρ	M_δ	M_α
Area	MaxDischarge	0.82	0.78	0.52	0.30	0.07	0.011	0.026	0.535
Area	Steepness	-0.59	-0.28	0.01	-0.46	-0.22	0.213	0.089	0.190
Buildup	Lakes	-0.14	-0.25	0.25	-0.16	0.05	1.746	1.543	1.614
Buildup	Marshes	-0.16	-0.28	0.17	-0.19	0.06	3.688	3.164	3.704
Buildup	MaxDischarge	0.16	0.24	0.17	0.26	-0.19	0.283	0.280	0.293
Buildup	RunoffCoef	-0.33	-0.17	-0.04	-0.28	-0.03	0.528	0.211	0.158
Buildup	Steepness	-0.38	-0.18	-0.11	-0.26	0.11	0.372	0.061	0.241
Lakes	Marshes	0.57	0.33	0.41	-0.30	-0.15	4.852	4.617	3.550
Lakes	MaxDischarge	0.29	-0.16	0.14	0.38	-0.05	1.865	1.527	1.282
Lakes	RunoffCoef	0.27	0.18	0.00	-0.18	0.14	0.691	0.727	0.947
Lakes	Steepness	-0.37	-0.05	-0.09	-0.33	-0.01	1.586	0.397	1.029
Marshes	MaxDischarge	0.31	-0.21	0.10	0.43	-0.05	3.644	3.127	2.734
Marshes	RunoffCoef	0.34	0.25	0.08	-0.16	0.04	1.791	1.724	1.872
MaxDischarge	MaxEvent	0.14	-0.20	0.16	0.03	0.21	0.159	0.083	0.045
MaxDischarge	RunoffCoef	0.15	-0.22	0.19	0.00	0.19	0.190	0.072	0.027
MaxDischarge	Steepness	-0.28	-0.33	-0.06	-0.09	-0.10	0.158	0.135	0.203
MaxEvent	Steepness	0.61	0.30	0.15	0.07	0.25	0.136	0.115	0.777
RunoffCoef	Steepness	0.30	0.13	-0.03	0.16	0.18	0.032	0.017	0.156

Analysis of the results indicates that the Gaussian copula is a good representation for most bivariate pairs of variables. This is indicated by relatively small differences in semi-correlations and low values of M statistic for the Gaussian copula. The difference between the empirical and parametric copulas is the smallest if Gaussian copula is used for 12 out of 18 pairs of variables included in the BN (examples: Fig. A.1b and A.1d). The M statistic indicates the Clayton copula as the best one for 5 pairs (e. g. Fig. A.1c), and only for one pair – *Area* & *MaxDischarge* – the Gumbel copula gave the best result (Fig. A.1a). In case of 3 of 5 pairs for which the M statistic indicated the Clayton copula as best-fitting (*MaxDischarge* & *RunoffCoef*, *MaxDischarge* & *Steepness*, *Lakes* & *Marshes*), the difference is small with respect to the same value for the Gaussian copula. Also, the difference in semi-correlations indicates only slight tail dependence, hence Gaussian copula is still a valid assumption. In summation, the results point towards the Gaussian copula as a suitable assumption for most of the bivariate distributions in the Bayesian Network for extreme river discharges. In our data, the variables most clearly displaying tail dependence (upper) is the *Area* & *MaxDischarge* pair.

A.3. VALIDATION OF THE BAYESIAN NETWORK

The Bayesian Network is constructed and validated in terms of accuracy of the results it produces in chapter 2. I, however, also verify to what extent the assumption of joint normal copula is valid. For that purpose, the determinant of the rank correlation matrix can be used. A rank correlation matrix is created by calculating the rank correlation between every possible pair of variables. The determinant is equal to 1 if all variables are independent, and equal to 0 if there is linear dependence between variables that have

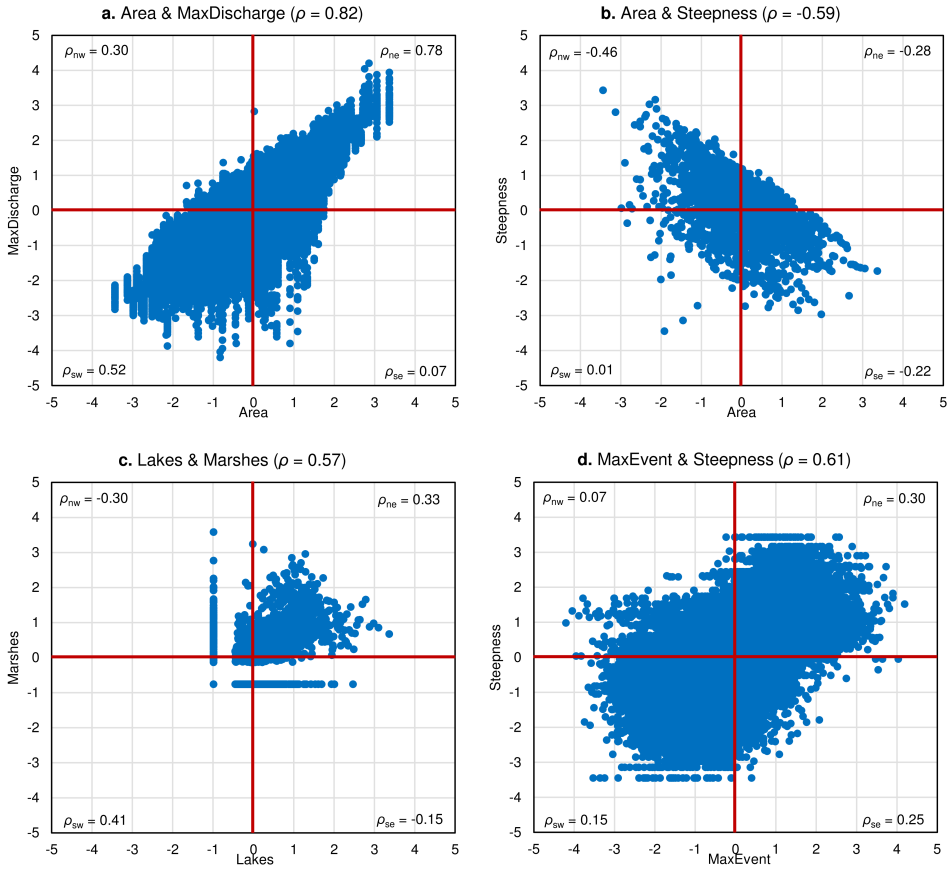


Figure A.1: Graphs of selected pairs of variables of the Bayesian Network. The values of variables were transformed to standard normal, with correlation indicated for the whole sample and for each quadrant.

been transformed to standard normals.

The determinants can be utilized in two ways. Firstly, the determinants of the empirical rank correlation matrix (DER) and empirical normal rank correlation matrix (DNR) were calculated. The former is obtained by transforming the marginals to uniforms and then calculating the product moment correlation of the transformed variables, while the latter is obtained by transforming the marginals to standard normal and then transforming the product moment correlations to rank correlations according to the following formula:

$$r(X, Y) = \frac{6}{\pi} \arcsin\left(\frac{\rho(X, Y)}{2}\right) \tag{A.8}$$

Those determinants will, in general, be different because the empirical copula will typically be different from the normal copula. Therefore, it can be analysed whether the determinant of DER is within the 90 % confidence bound of the determinant of DNR. If it does, that shows that a joint normal copula is a reasonable assumption. Secondly, the same comparison could be done between DNR and the determinant of a rank correlation matrix for a non-parametric Bayesian Network using normal copula (DBN). For details on this methodology the reader is referred to Hanea *et al.* [161].

In case of our BN, DER remained within the 90 % bound of DNR if no more than ca. 310 samples were drawn in the procedure. DNR was within the 90 % bound of DBN for up to ca. 400 samples. Those are a relatively small values, indicating that the joint normal copula may not be the best assumption. However, Hanea *et al.* [161] notice that the test is severe for large datasets, and the BN for extreme discharges contains 75 000 samples of each variable.

The rank correlation matrices can also be analysed not only in terms of determinants, but also through calculation of the so called d-calibration score [353]:

$$d(\Sigma_1, \Sigma_2) = 1 - \sqrt{1 - \eta(\Sigma_1, \Sigma_2)} \tag{A.9}$$

$$\eta(\Sigma_1, \Sigma_2) = \frac{|\Sigma_1|^{\frac{1}{4}}, |\Sigma_2|^{\frac{1}{4}}}{|\frac{1}{2}\Sigma_1 + \frac{1}{2}\Sigma_2|^{\frac{1}{2}}} \tag{A.10}$$

where Σ_1, Σ_2 are the correlation matrices of interest. This score is a measure of “closeness” between two correlation matrices. The score is 1 if the matrices are equal and 0 if one matrix contains a pair of variables perfectly correlated, and the other one does not, and the score will be “small” as the matrices differ from each other elementwise. The distance between the empirical and empirical normal rank correlation matrices is within the uncertainty bounds if more than 800 samples are drawn. In case of the distance between the empirical normal and normal rank correlation matrices, it is within the uncertainty bounds if less than 250 samples are drawn. This confirms the results of the test based on the determinants.

A.4. CONDITIONALIZING THE BAYESIAN NETWORK

To provide additional visualisation of the BN’s conditionalization described in section 2.2.5, three different states of the BN are presented here. The example is the same as

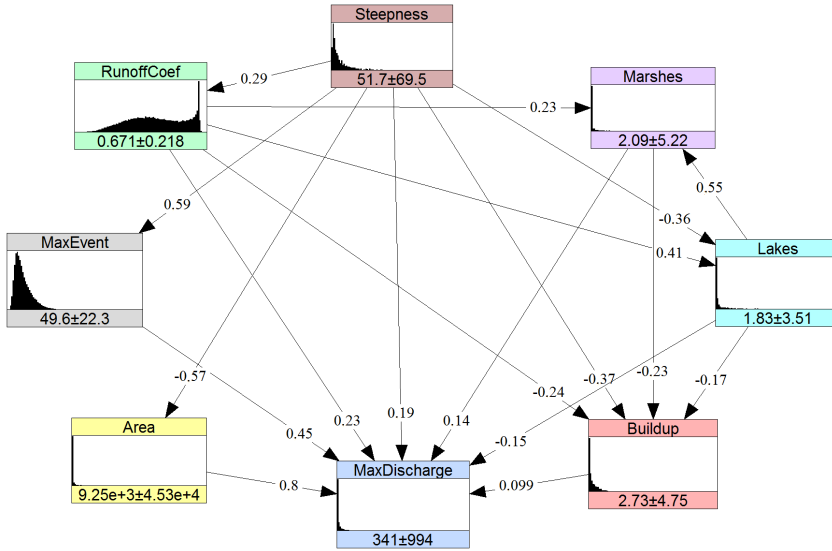


Figure A.2: Unconditional Bayesian Network.

in Fig. 2.4 of chapter 2, i.e. river Rhine at Basel station in Switzerland in year 2005. In Fig. A.2 the Bayesian Network is unconditional. In Fig. A.3 it is conditionalized on two variables (area and steepness); it can be seen how the distributions of all variables have changed. In Fig. A.4 seven nodes were used to conditionalize the network, providing a better estimate of discharges.

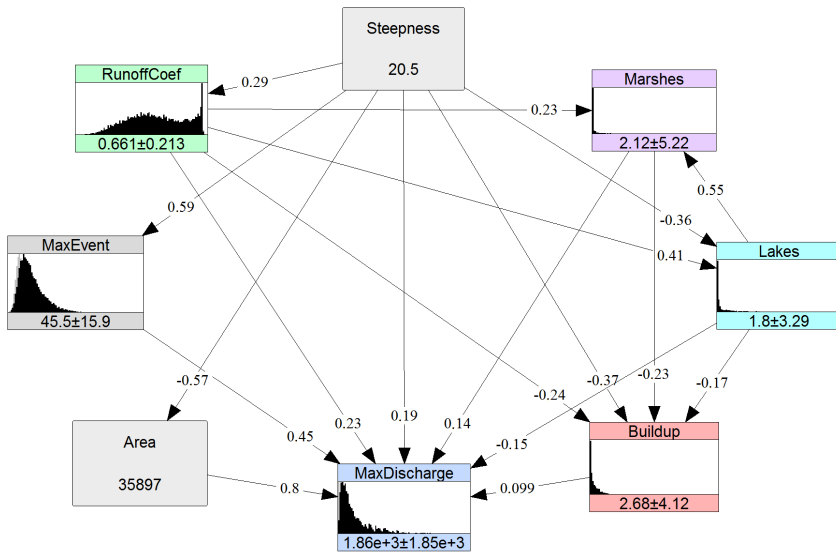


Figure A.3: Bayesian Network conditionalized on two variables.

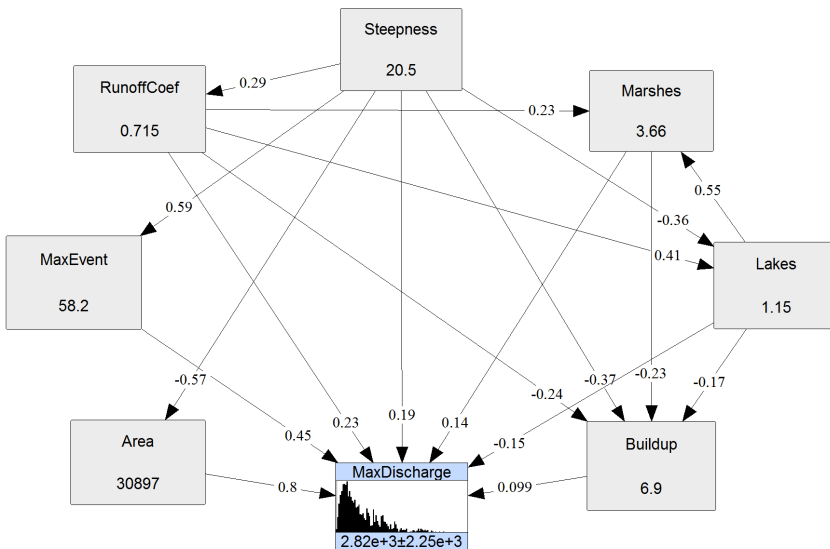


Figure A.4: Bayesian Network conditionalized on seven variables.

B

EXTREME RIVER DISCHARGES UNDER ALTERNATE CLIMATE MODELS

This appendix presents the validation of the Bayesian network (BN) model for extreme river discharges using two additional climate models, different than those used in chapter 2. The first model is one of the EURO-CORDEX climate simulations, combining global circulation model HadGEM2-ES from Met Office Hadley Centre [354] with KNMI's regional climate model RACMO22E [355], realisation r1i1p1 and downscaling realisation v2. The other model is the ERA-Interim climate reanalysis [139]. In this case, the BN model was quantified based on data from 1979–2013.

Two sets of graphs equivalent to Figs. 2.5 and 2.6 in section 2.3.1 are presented here. Figs. B.1 and B.2 compare simulated and observed discharge based on HadGEM2-ES-RACMO22E model, while Figs. B.3 and B.4 are based in ERA-Interim reanalysis. Further, a summarized comparison of the different model variants is given in Table B.1, including the regional frequency analysis based methodology from Smith *et al.* [123]. Finally, Fig. B.5 is the equivalent to Fig. 2.10 from section 2.3.2 and shows the climate change predictions based on the HadGEM2-ES-RACMO22E model.

The comparison of the models show that the BN had the best performance in estimating extreme river discharge with the climate model EC-EARTH-COSMO_4.8_clm17, which was used in chapter 2. However, when considering specific discharge, slightly better results were achieved with the alternative EURO-CORDEX model, HadGEM2-ES-RACMO22E. The performance of the model using ERA-Interim is the worst among the three models analysed. This is likely due to the coarse resolution of the model (0.75° compared to 0.11° in EURO-CORDEX). Yet, all models were better according to the measures of model performance than a regional frequency analysis.

This appendix has been included as a supplement to the paper published in *Hydrology and Earth System Sciences* **21**, 2615–2636 (2017) [114].

B

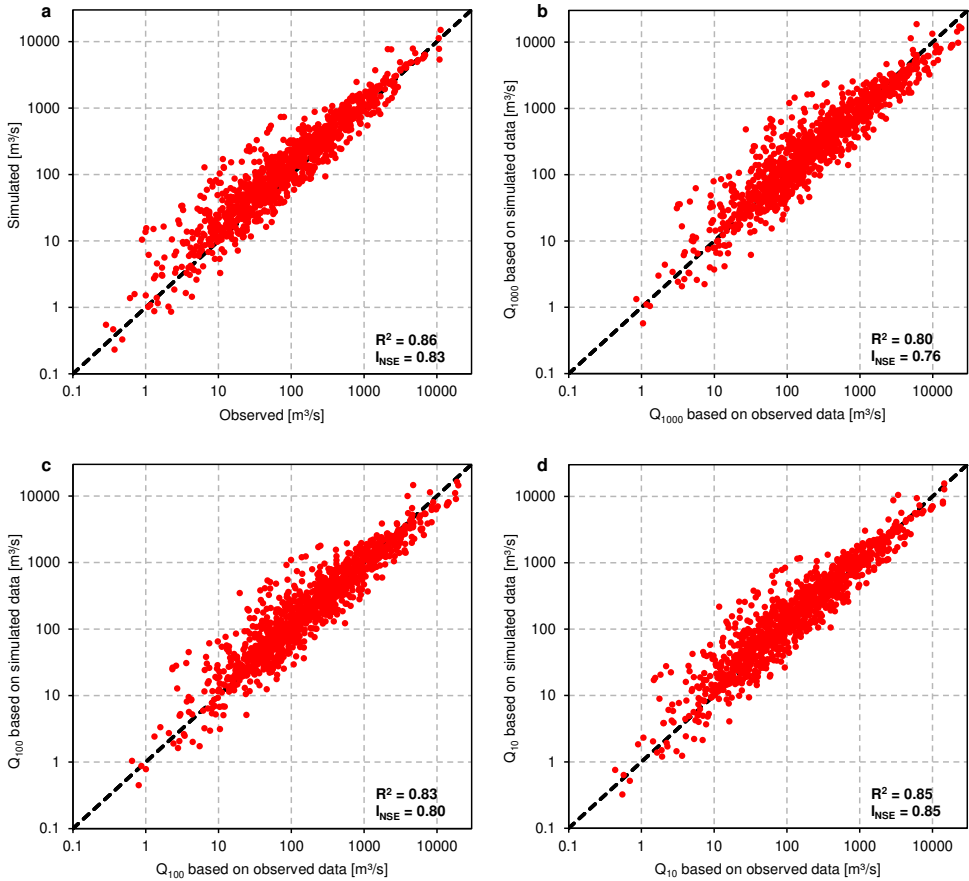


Figure B.1: Simulated and observed average annual maxima of daily river discharges (a) and annual maxima fitted to Gumbel distribution to calculate 1000-, 100- and 10-year return periods (b–d), for 1125 stations. 30-year periods of annual maxima were used (the most recent available out of 1971–2000, 1961–90 or 1951–80). Data based on the HadGEM2-ES-RACMO22E climate model.

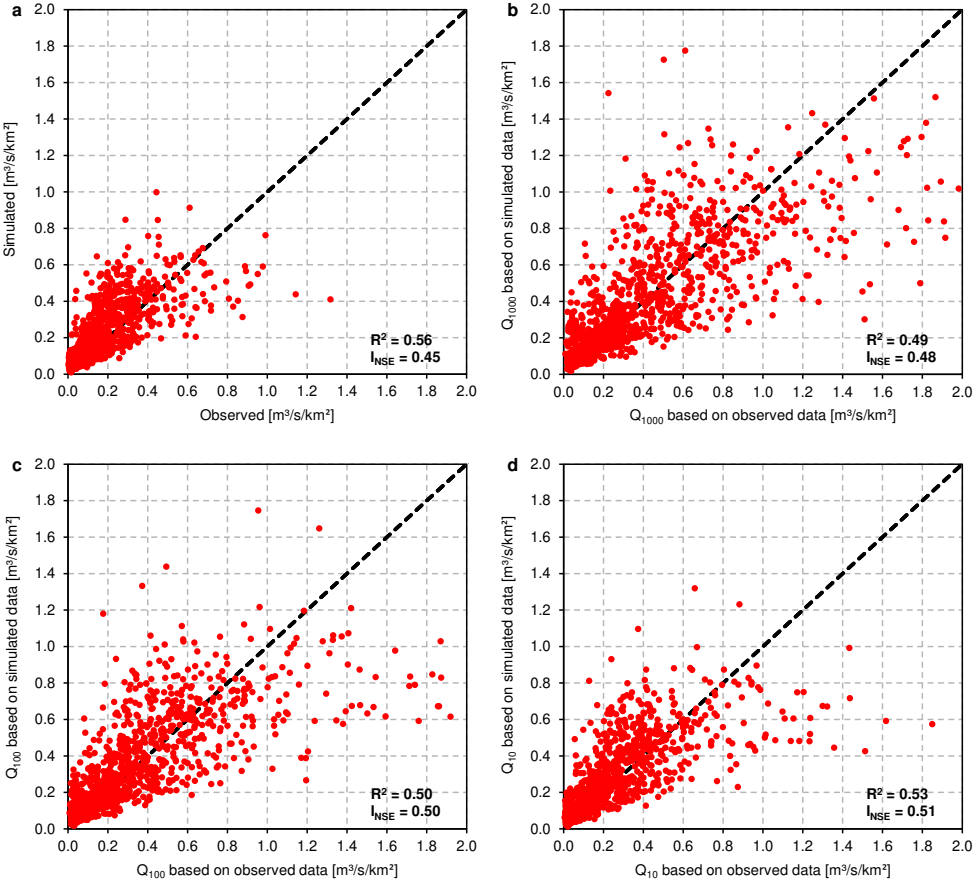


Figure B.2: The same as Fig. B.1, but for specific discharge, i.e. divided by catchment area.

B

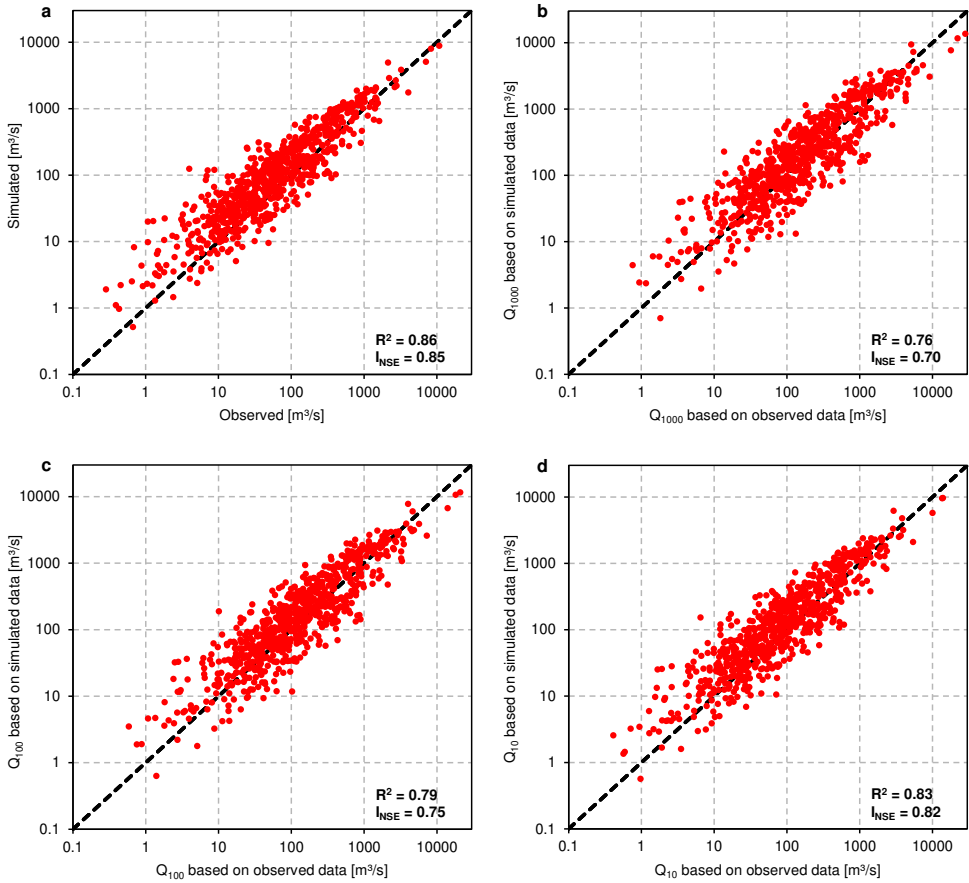


Figure B.3: Simulated and observed average annual maxima of daily river discharges (a) and annual maxima fitted to Gumbel distribution to calculate 1000-, 100- and 10-year return periods (b-d), for 764 stations (1981–2010). Data based on the ERA-Interim climate model.

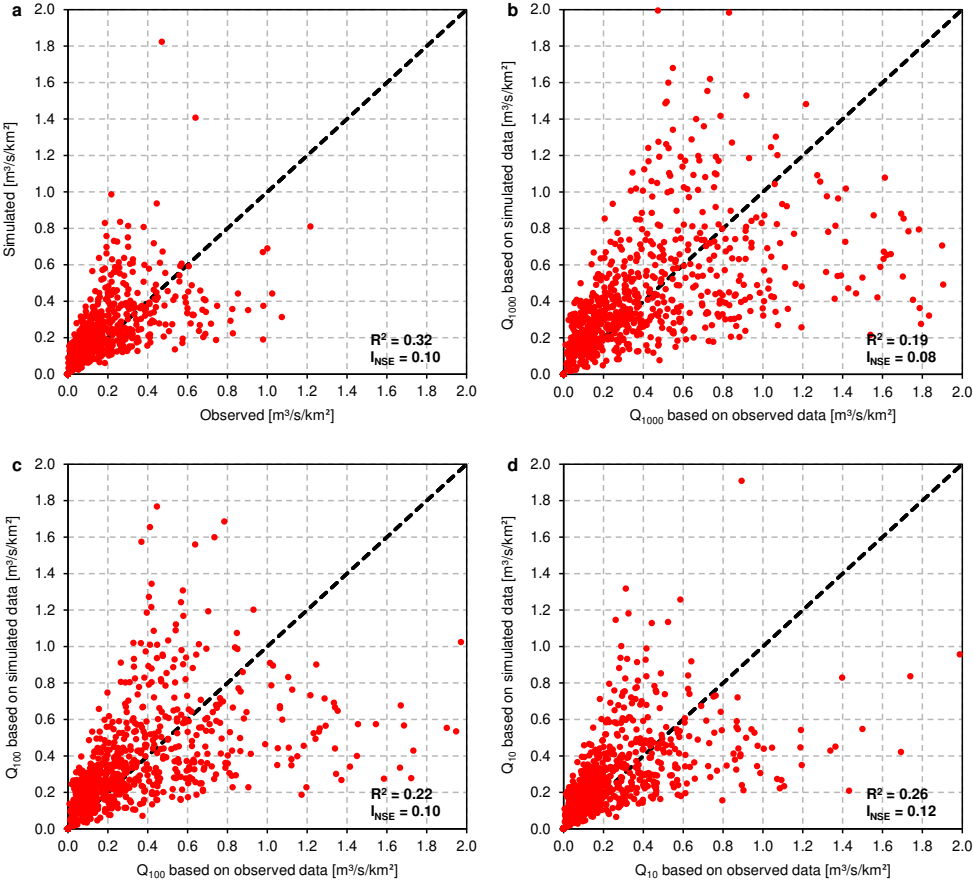


Figure B.4: The same as Fig. B.3, but for specific discharge, i.e. divided by catchment area.

B

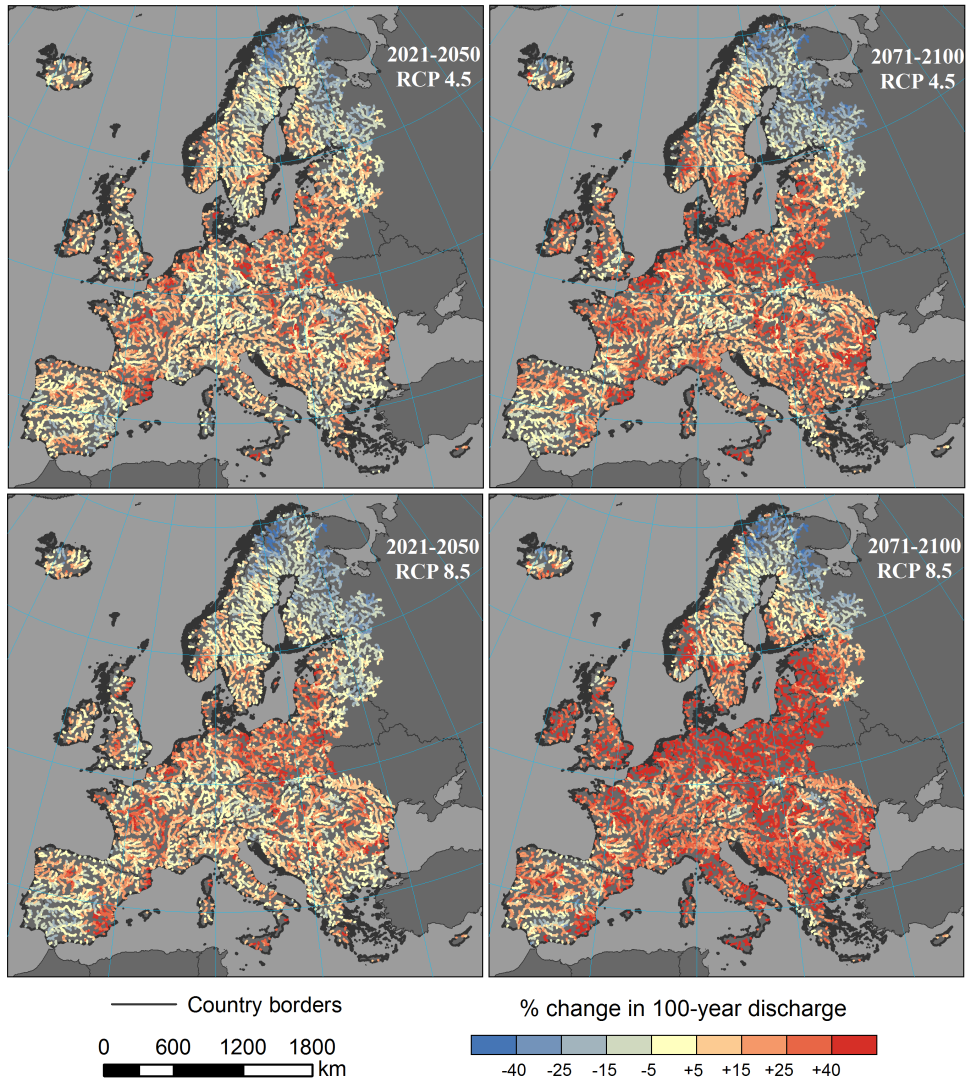


Figure B.5: Predicted trends in daily river discharge with a 100-year return period (Gumbel distribution) under climate-change scenarios RCP 4.5 and RCP 8.5 (rivers with catchment area above 500 km² only). Predictions based on EC- HadGEM2-ES-RACMO22E climate model run.

Table B.1: Comparison of results for 3 climate models in the quantification of the BN for extreme river discharges, together with regional frequency analysis (RFA).

Model		EC-EARTH-COSMO_4.8 _clm17		HadGEM2-ES- RACMO22E		ERA-Interim		RFA	
		R ²	NSE	R ²	NSE	R ²	NSE	R ²	NSE
Discharge	Q _{MAMX}	0.92	0.92	0.86	0.83	0.86	0.85	0.78	0.71
	Q ₁₀₀₀	0.87	0.74	0.80	0.76	0.76	0.70	0.65	0.27
	Q ₁₀₀	0.89	0.80	0.83	0.80	0.79	0.75	0.70	0.44
	Q ₁₀	0.91	0.88	0.85	0.85	0.83	0.82	0.75	0.58
Specific discharge	Q _{MAMX}	0.52	0.41	0.56	0.45	0.32	0.10	0.28	-0.02
	Q ₁₀₀₀	0.43	0.41	0.49	0.48	0.19	0.08	0.15	-2.94
	Q ₁₀₀	0.44	0.43	0.50	0.50	0.22	0.10	0.17	-1.35
	Q ₁₀	0.48	0.43	0.53	0.51	0.26	0.12	0.22	-0.45



C

MAPS OF EXTREME RIVER DISCHARGES IN EUROPE

This appendix presents estimated extreme daily river discharge with a 100-year return period for all rivers, supporting the analysis in section 2.3.2. The maps cover historical (1971–2000) and future (2021–2050 and 2071–2100) scenarios.

This appendix has been included as a supplement to the paper published in *Hydrology and Earth System Sciences* **21**, 2615–2636 (2017) [114].

ESTIMATED EXTREME DAILY RIVER DISCHARGE 1971-2000, 100-year return period

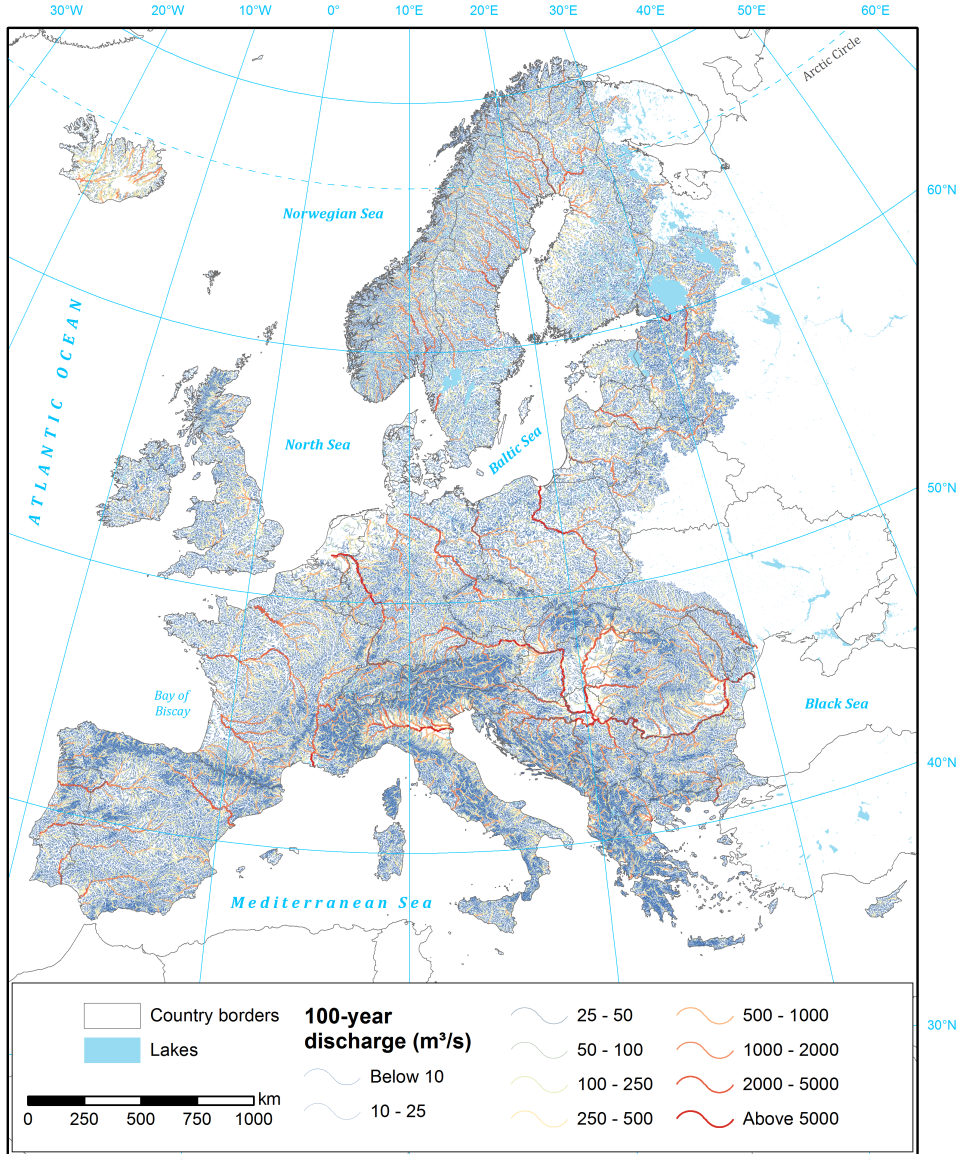
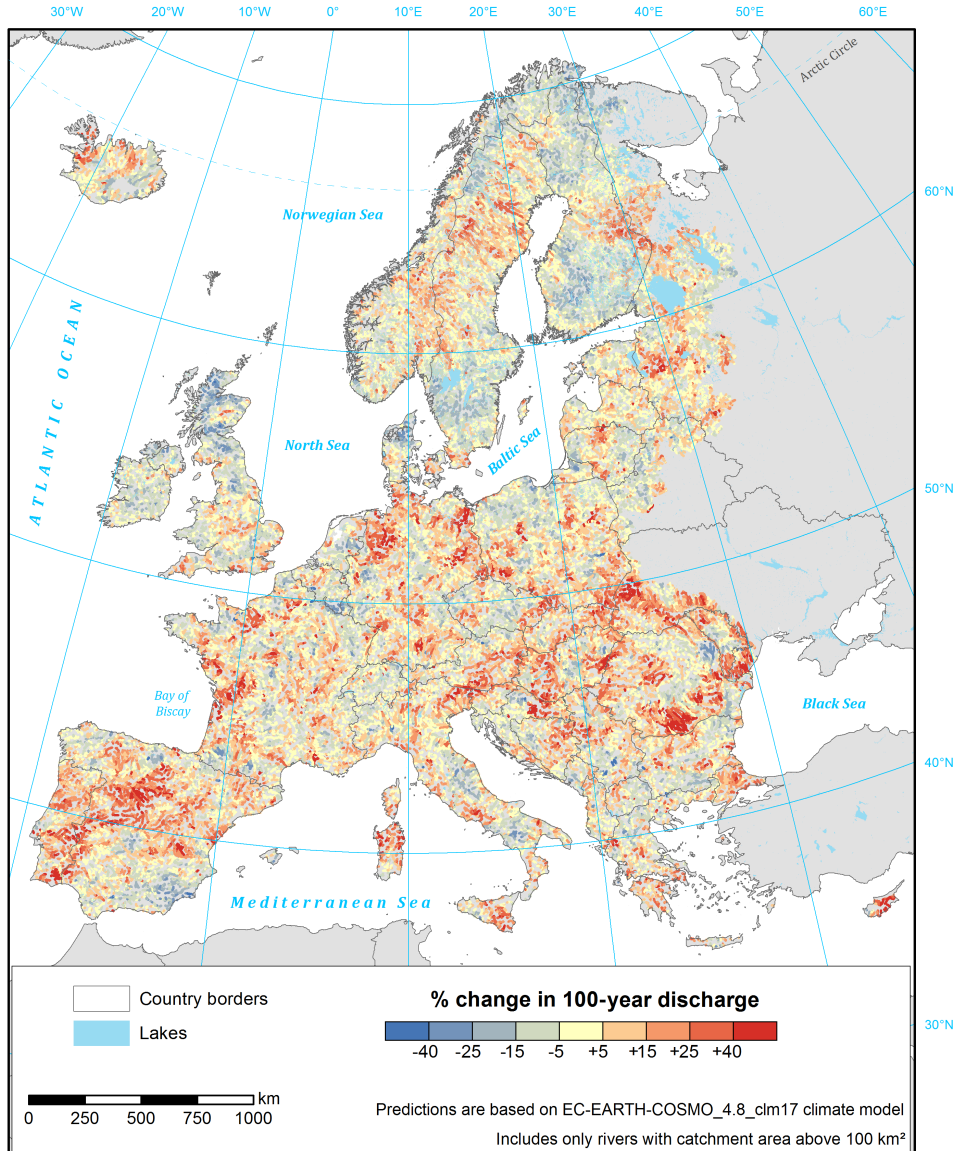


Figure C.1: Extreme daily river discharge with a 100-year return period (Gumbel distribution) for years 1971–2000. Estimates based on EC-EARTH-COSMO_4.8_clm17 climate model run.

PROJECTED CHANGE IN EXTREME DAILY RIVER DISCHARGE 2021-2050 to 1971-2000, 100-year return period, RCP 4.5 scenario



C

Figure C.2: Projected change in 100-year river discharge (Q_{100}) in 2021–2050 relative to 1971–2000 for emission scenario RCP 4.5. Predictions based on EC-EARTH-COSMO_4.8_clm17 climate model run.

PROJECTED CHANGE IN EXTREME DAILY RIVER DISCHARGE 2071-2100 to 1971-2000, 100-year return period, RCP 4.5 scenario

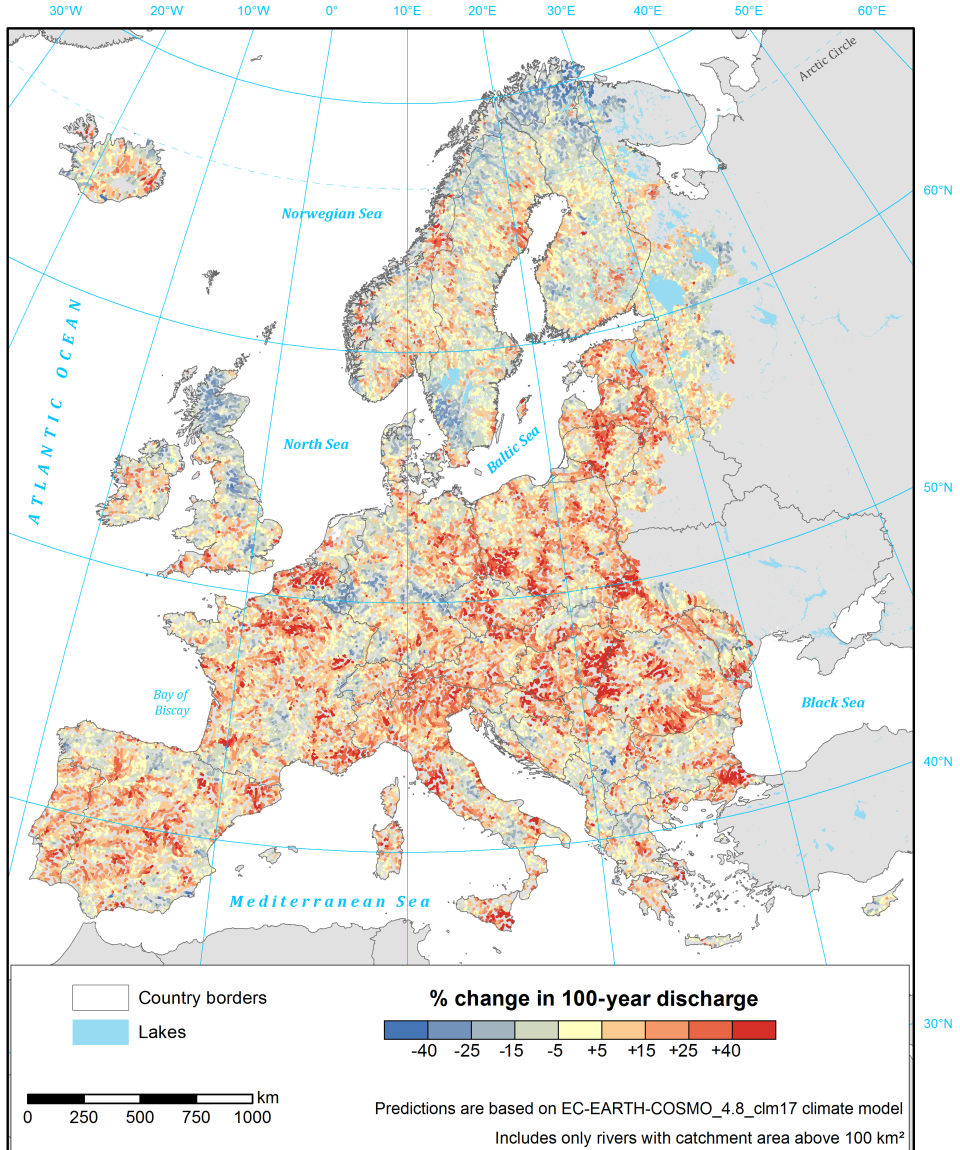
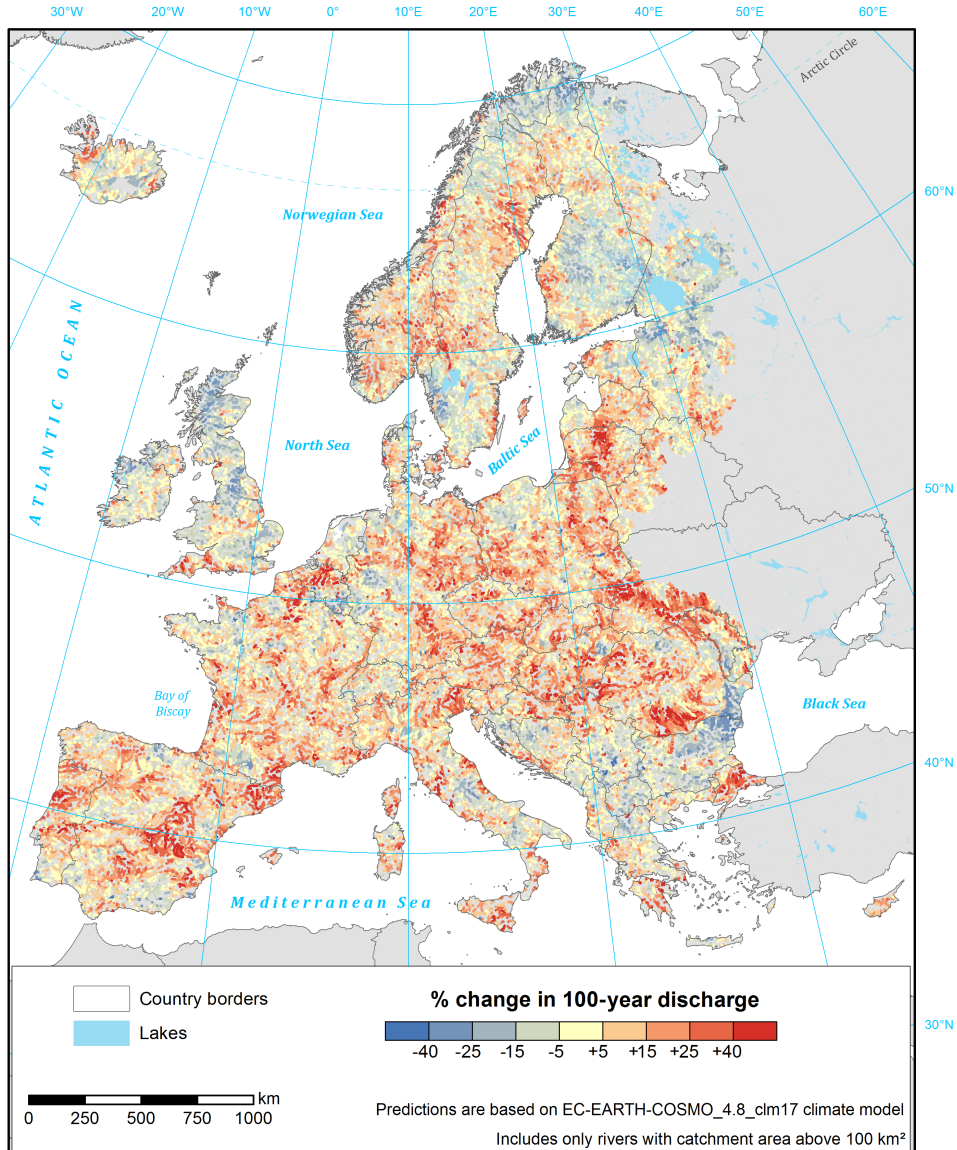


Figure C.3: Projected change in 100-year river discharge (Q_{100}) in 2071–2100 relative to 1971–2000 for emission scenario RCP 4.5. Predictions based on EC-EARTH-COSMO_4.8_clm17 climate model run.

PROJECTED CHANGE IN EXTREME DAILY RIVER DISCHARGE 2021-2050 to 1971-2000, 100-year return period, RCP 8.5 scenario



C

Figure C.4: Projected change in 100-year river discharge (Q_{100}) in 2021–2050 relative to 1971–2000 for emission scenario RCP 8.5. Predictions based on EC-EARTH-COSMO_4.8_clm17 climate model run.

PROJECTED CHANGE IN EXTREME DAILY RIVER DISCHARGE 2071-2100 to 1971-2000, 100-year return period, RCP 8.5 scenario

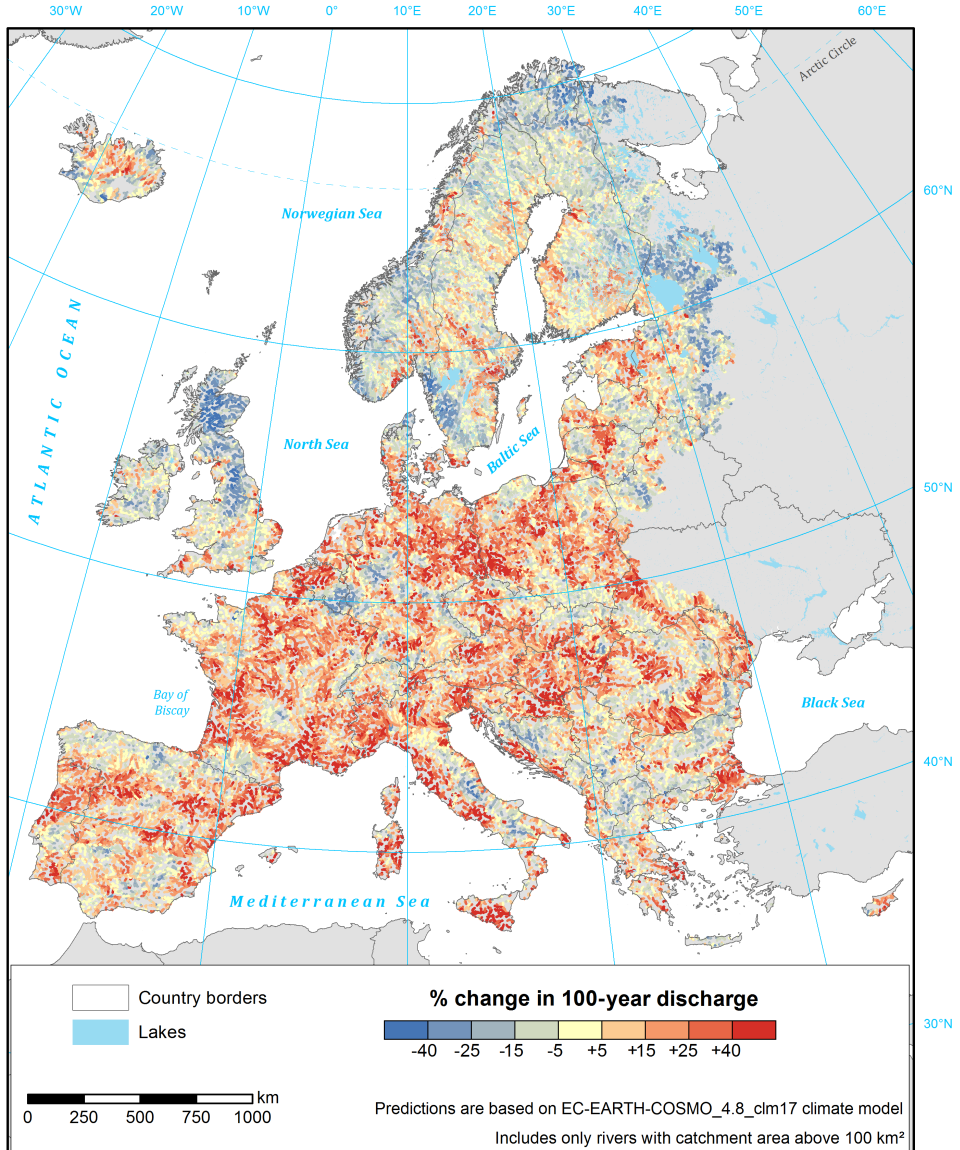


Figure C.5: Projected change in 100-year river discharge (Q_{100}) in 2071–2100 relative to 1971–2000 for emission scenario RCP 8.5. Predictions based on EC-EARTH-COSMO_4.8_clm17 climate model run.

D

MAPS OF RIVER FLOOD HAZARD IN EUROPE

This appendix presents the river flood hazard zones at different return periods for the whole European domain, supporting the analysis in chapter 3. The maps cover historical (1971–2000) scenario in two variants, with or without flood protection. Estimated flood protection standards are presented in Fig. D.3.

Contents of this appendix has been published either as a supplement to the paper published in *Natural Hazards and Earth System Sciences* **17**, 1267–1283 (2017) [175] or in RAIN project report D2.5 [33].

RIVER FLOOD HAZARD ZONES 1971-2000, 10- to 1000-year return period - no flood protection

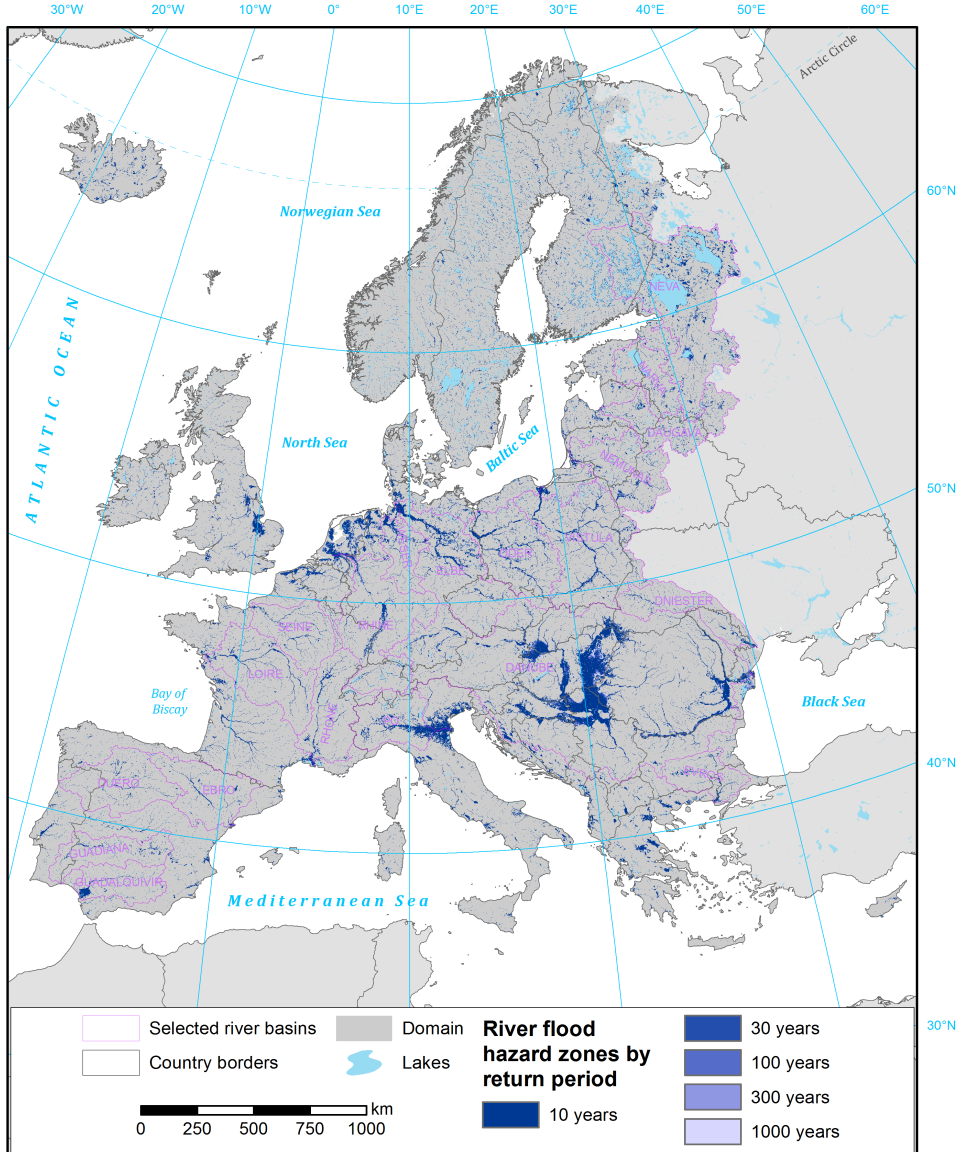
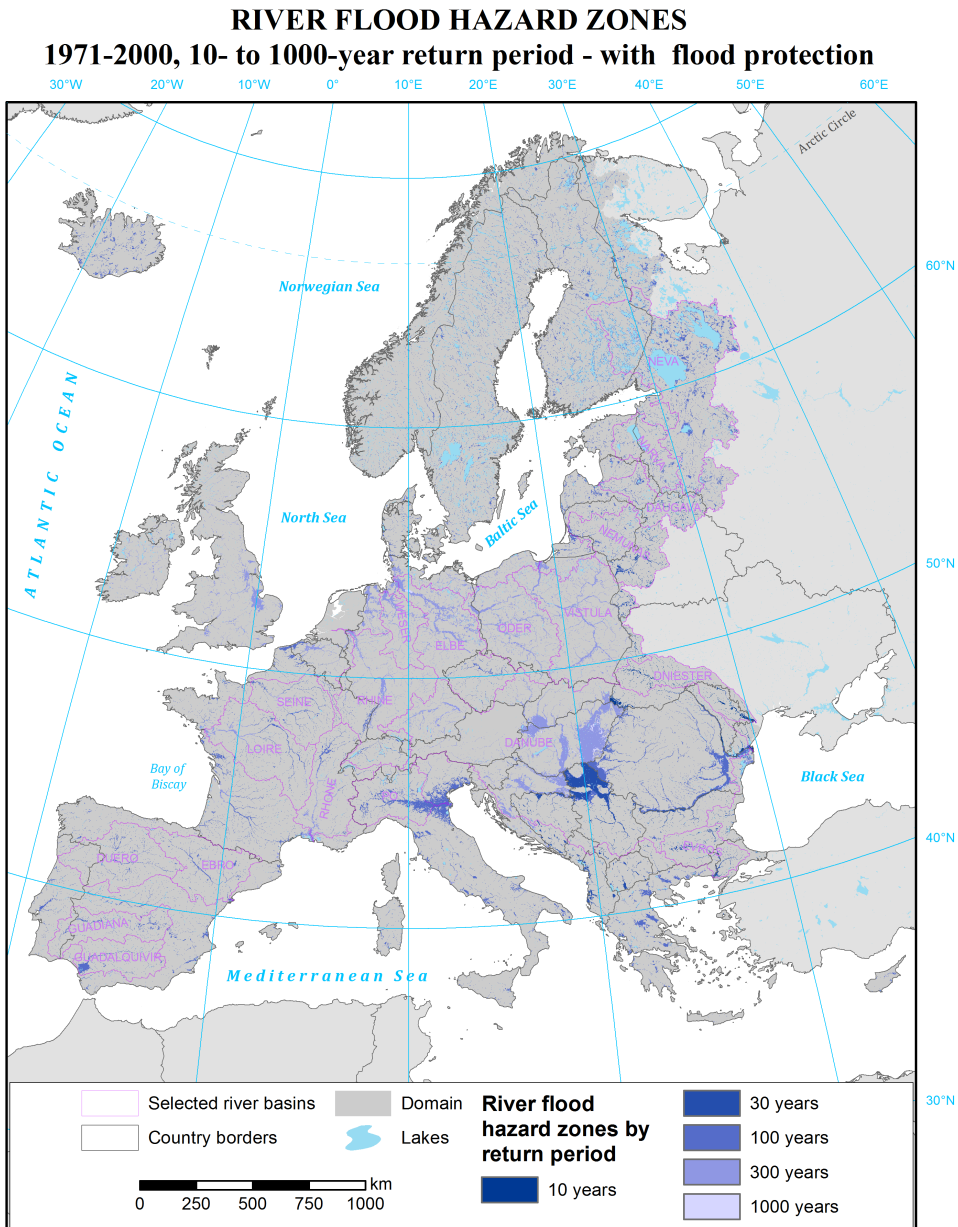


Figure D.1: River flood hazard zones at different return periods (Gumbel distribution) for years 1971–2000, **without** flood protection. Estimates based on EC-EARTH-COSMO_4.8_clm17 climate model run.



D

Figure D.2: River flood hazard zones at different return periods (Gumbel distribution) for years 1971–2000, **with** (estimated) flood protection. Estimates based on EC-EARTH-COSMO_4.8_clm17 climate model run.

D

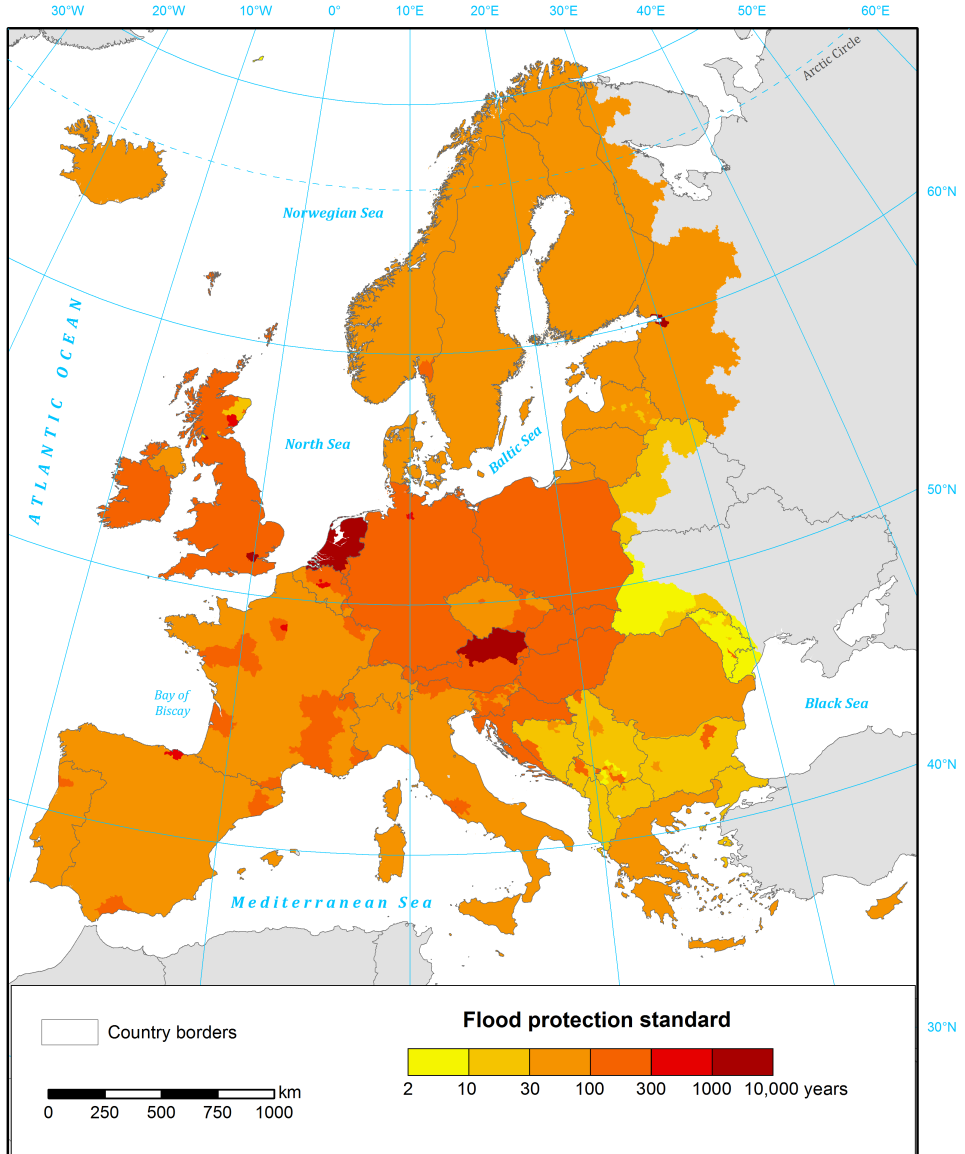


Figure D.3: Estimated flood protection standards, according to Scussolini *et al.* [66]

E

MAPS OF COASTAL FLOOD HAZARD IN EUROPE

This appendix presents the coastal flood hazard zones at different return periods for the whole European domain, supporting the analysis in chapter 4. The maps cover historical (1971–2000) scenario in two variants, with or without flood protection. Estimated flood protection standards are presented in Fig. D.3 in Appendix D.

COASTAL FLOOD HAZARD ZONES 1971-2000, 100-year return period - no flood protection

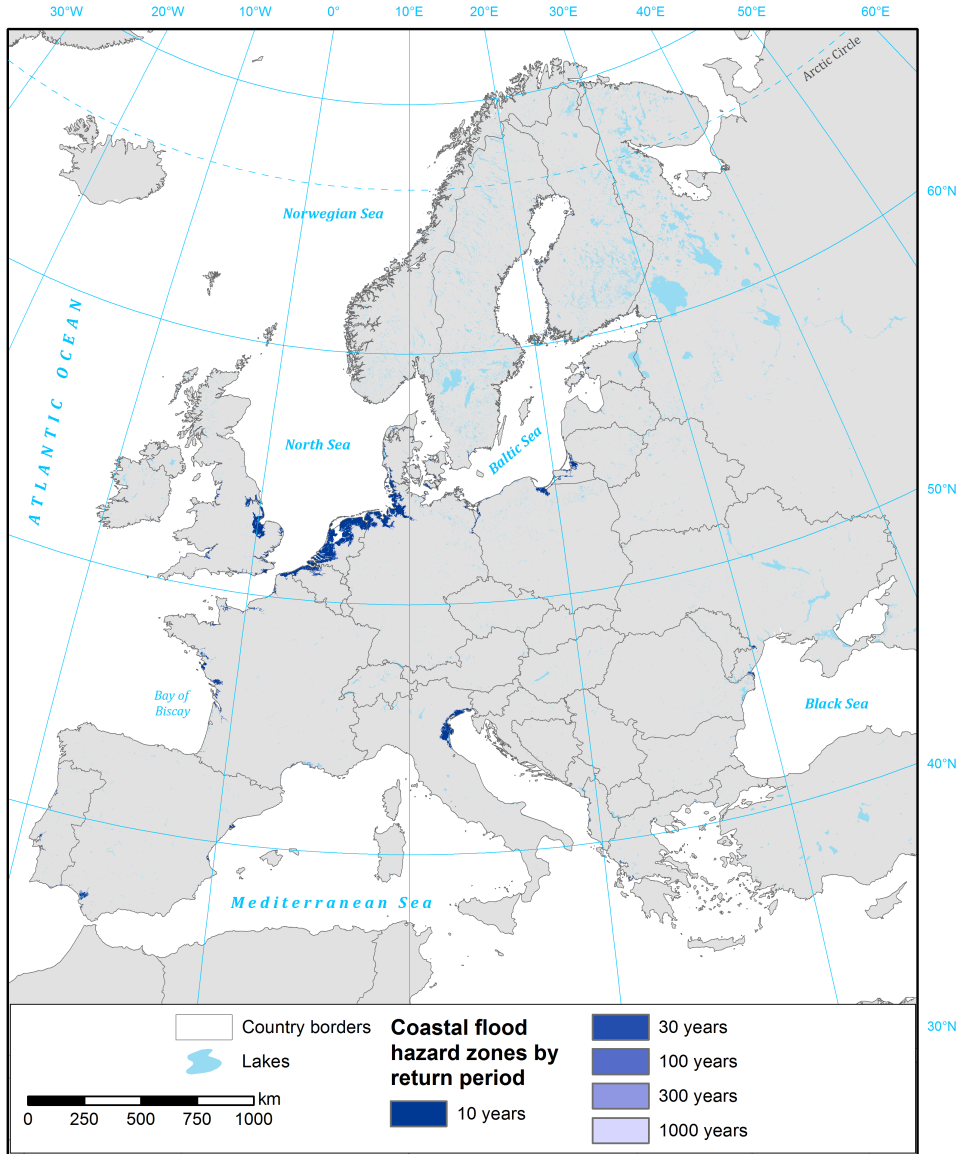
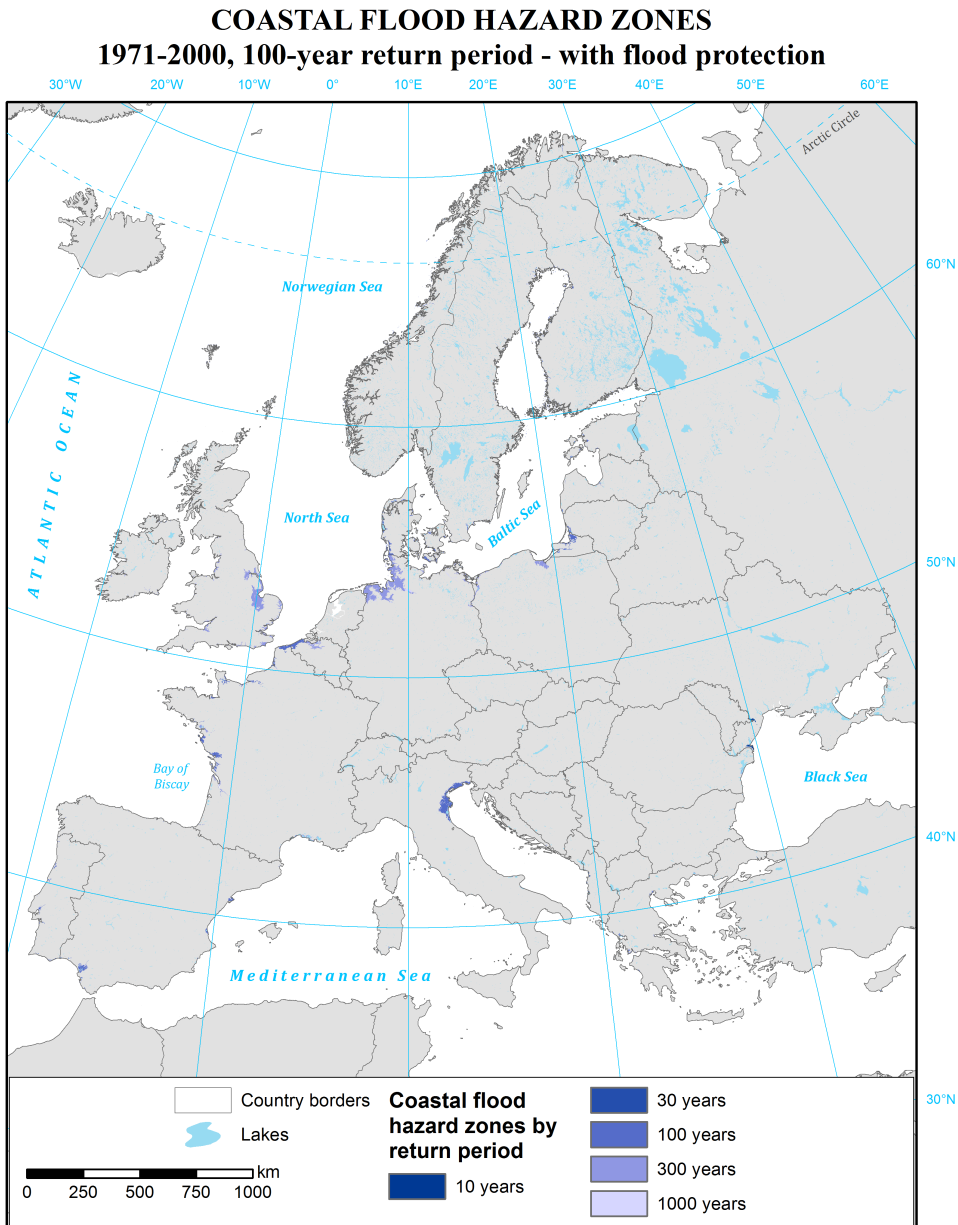


Figure E.1: Coastal flood hazard zones at different return periods (Gumbel distribution) for years 1971–2000, **without** flood protection. Estimates based on EC-EARTH-RCA4 climate model run.



E

Figure E.2: River flood hazard zones at different return periods (Gumbel distribution) for years 1971–2000, **with** (estimated) flood protection. Estimates based on EC-EARTH-RCA4 climate model run.



F

SUPPLEMENTARY INFORMATION ON COMPOUND FLOOD POTENTIAL

This appendix contains additional maps and graphs related to compound flood potential, supporting the analysis in chapter 5.

This appendix has been included as a supplement to the paper submitted to Hydrology and Earth System Sciences [264].

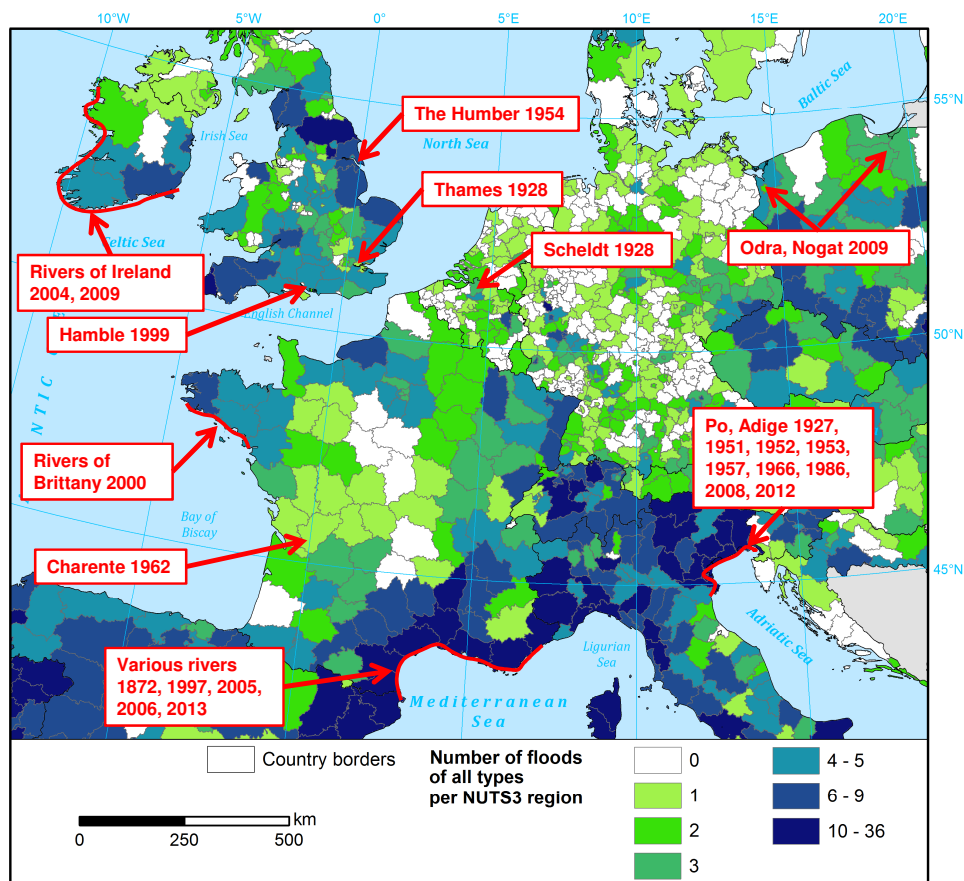


Figure F1: Occurrences of compound floods in Europe, 1870–2016, according to HANZE database (chapter 6), with the total number of floods of any type shown in the background. [section 5.1]

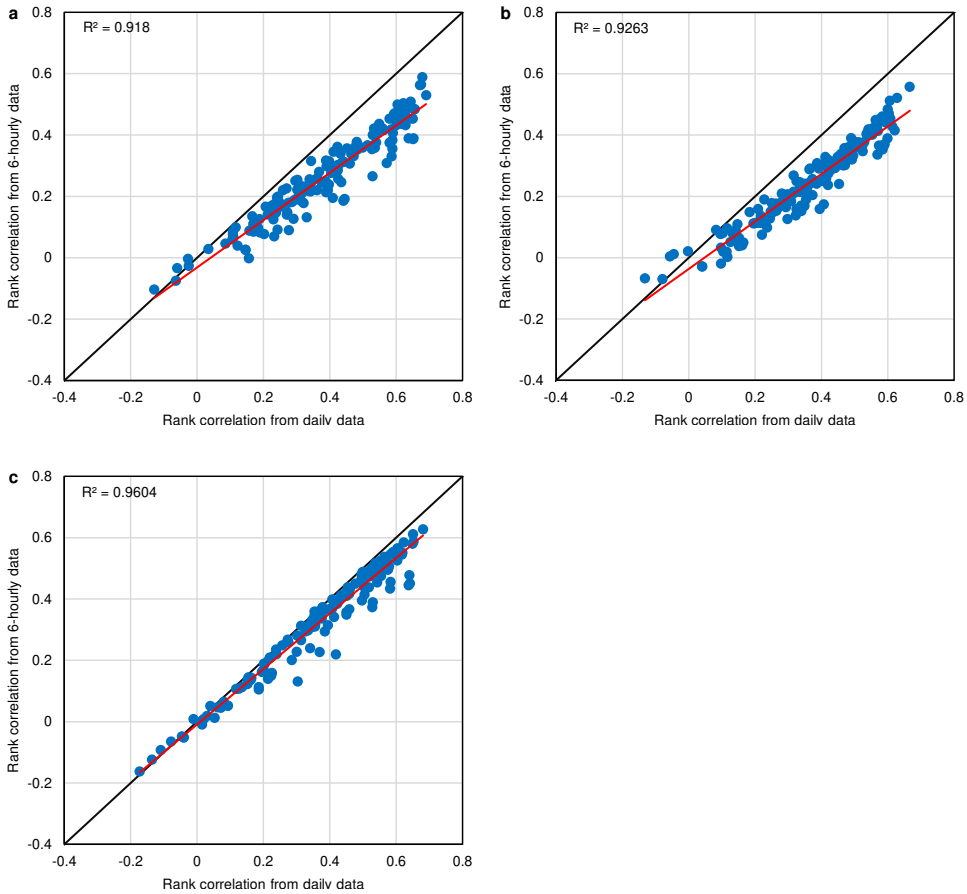


Figure F2: Comparison of rank correlations for daily and 6-hourly data series, for (a) storm surge heights and precipitation (Delft3D/ERA-Interim + ERA-Interim), (b) storm surge heights and precipitation (Delft3D/CORDEX + CORDEX) and (c) storm surge heights and significant wave height (Delft3D/ERA-Interim + WaveWatch III/ERA-Interim). [section 5.3]

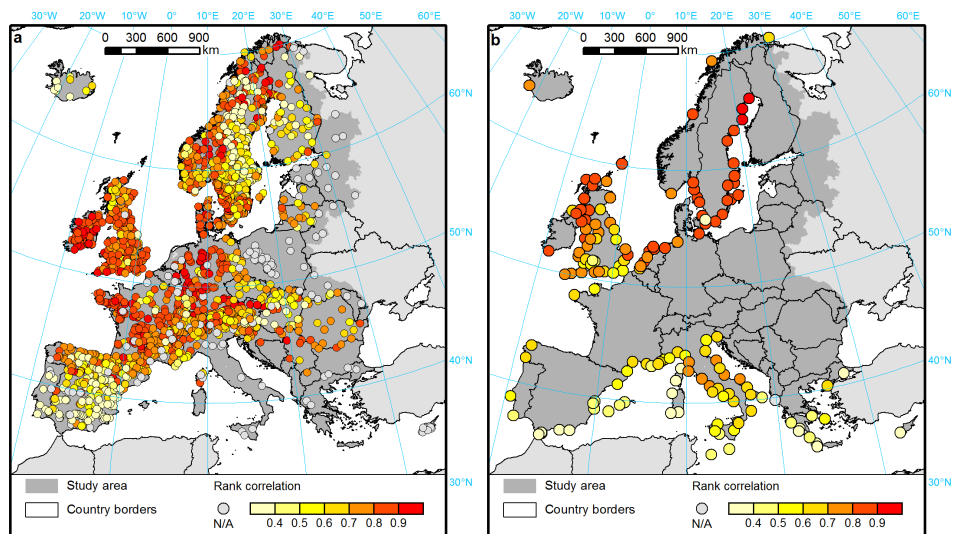


Figure E3: Rank correlation between modelled and observed (a) daily river discharges and (b) storm surge heights. Modelled discharge from EFAS, storm surge from Delft3D/ERA-Interim, observations from tide and river gauges. [section 5.3.2]

F

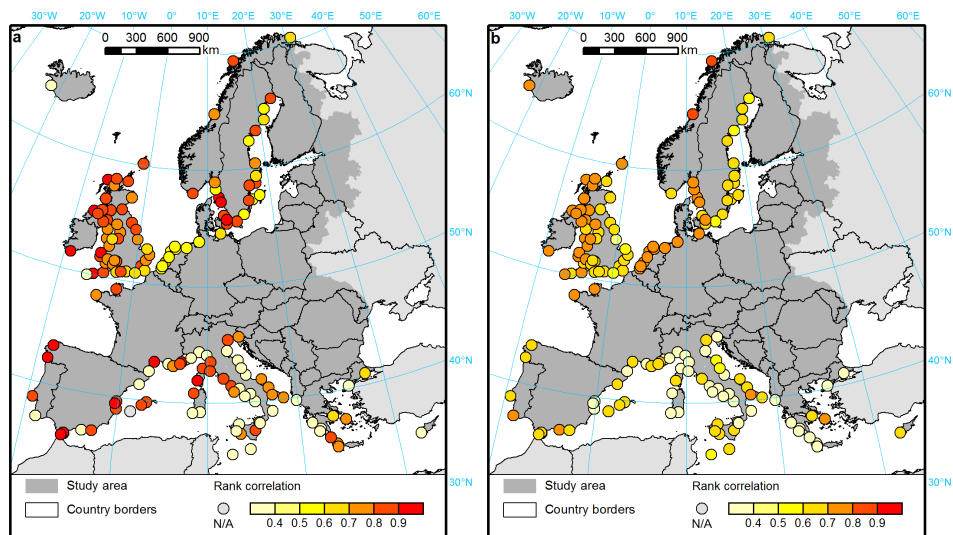
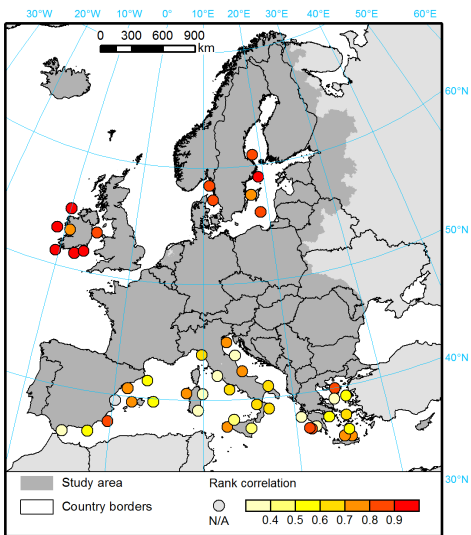


Figure F4: (a) rank correlation between EFAS-Meteo and E-OBS precipitation. (b) rank correlation between modelled precipitation from ERA-Interim and observed precipitation from E-OBS. [section 5.3.2]



F

Figure E5: Rank correlation between modelled (WW3/ERA-Interim) and observed significant wave height. [section 5.3.2]

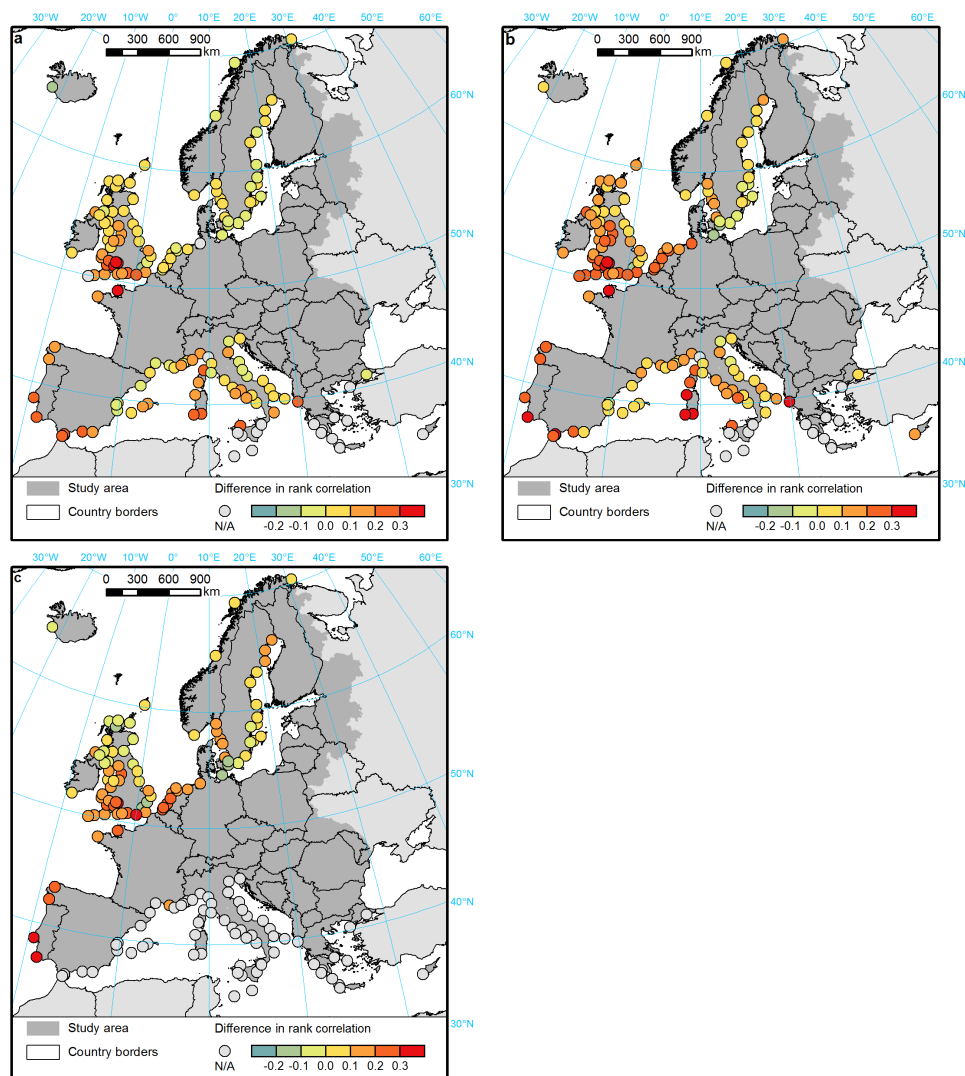


Figure F6: Difference in rank correlation between modelled and observed dependency for daily storm surge and precipitation: (a) Delft3D/ERA-Interim + EFAS-Meteo, (b) Delft3D/ERA-Interim + ERA-Interim and (c) Delft3D/CORDEX + CORDEX. [section 5.3.2]

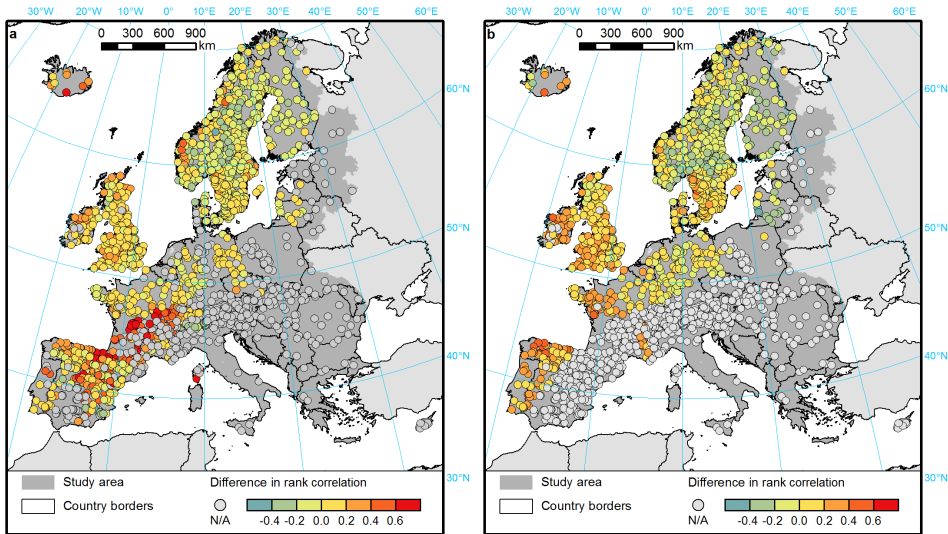


Figure F7: Difference in rank correlation between modelled and observed dependency for daily storm surge and river discharge: (a) Delft3D/ERA-Interim + EFAS/EFAS-Meteo and (b) Delft3D/CORDEX + EFAS/CORDEX. [section 5.3.2]

F

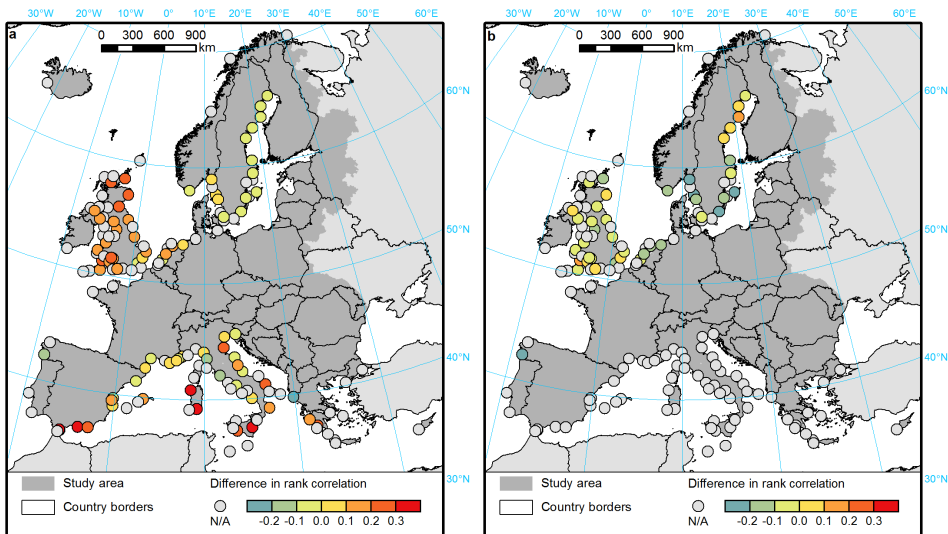


Figure F8: Difference in rank correlation between modelled and “observed” (tide gauges + EFAS/EFAS-Meteo) daily storm surge and river discharge for closest river with catchment area of at least 500 km²: (a) Delft3D/ERA-Interim + EFAS/EFAS-Meteo and (b) Delft3D/CORDEX + EFAS/CORDEX. [section 5.3.2]

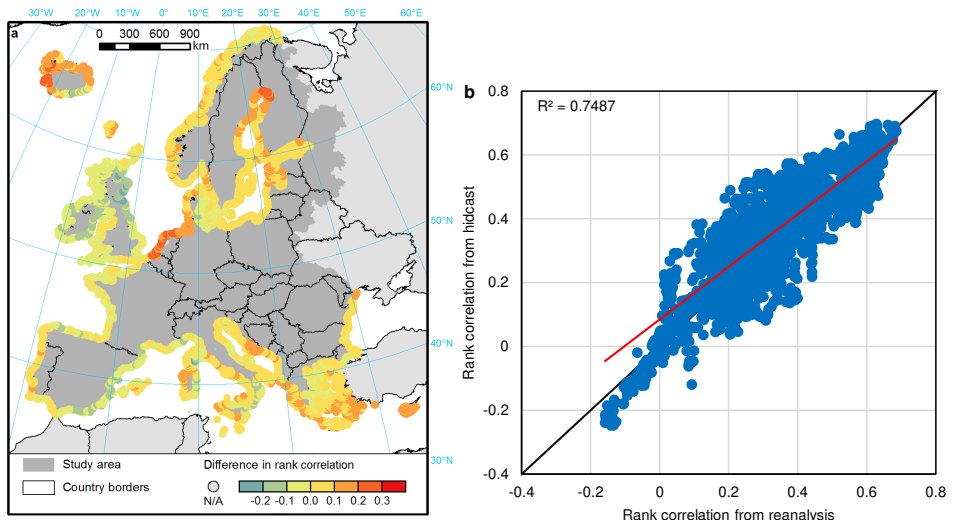


Figure E9: Difference in rank correlation between hindcast (Delft3D/CORDEX + CORDEX) and reanalysis (Delft3D/ERA-Interim + EFAS/EFAS-Meteo) daily storm surge and precipitation, for (a) individual coastal segments and (b) altogether. [section 5.3.3]

F

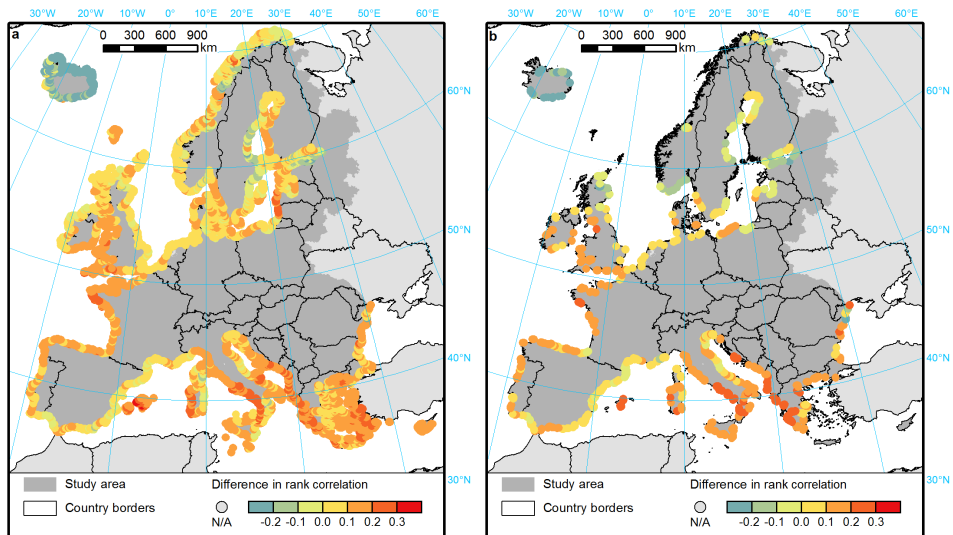


Figure E10: Difference in rank correlation between hindcast (Delft3D/CORDEX + CORDEX) and reanalysis (Delft3D/ERA-Interim + EFAS/EFAS-Meteo) daily storm surge and river discharge for (a) any closest river and (b) for closest river with catchment area of at least 500 km². [section 5.3.3]

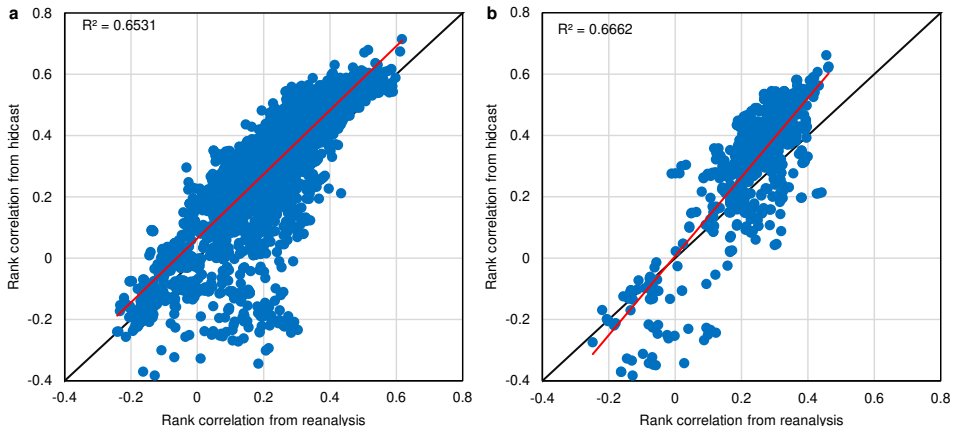


Figure F.11: Comparison of rank correlations between hindcast (Delft3D/CORDEX + EFAS/CORDEX) and reanalysis (Delft3D/ERA-Interim + EFAS/EFAS-Meteo) daily storm surge and river discharge for (a) any closest river and (b) for closest river with catchment area of at least 500 km². [section 5.3.3]

F

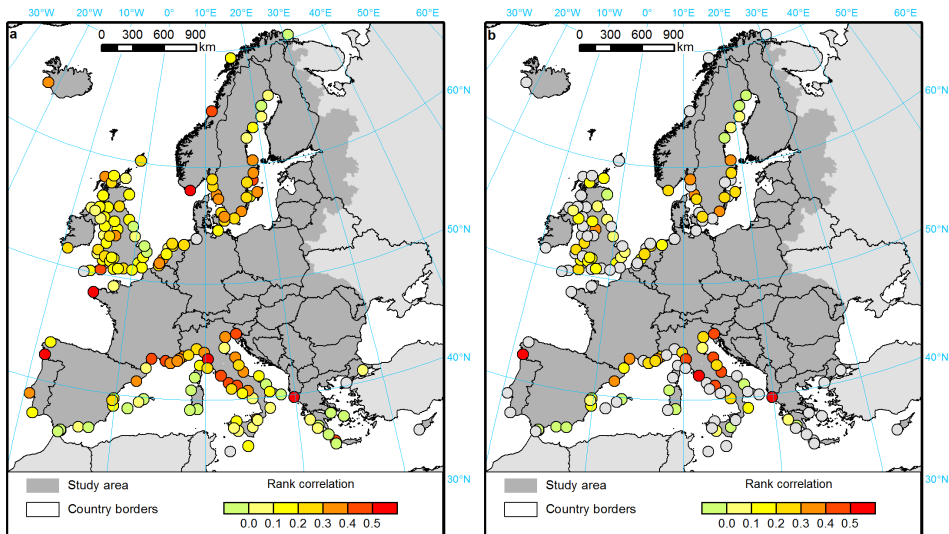


Figure F.12: Rank correlation between daily observed storm surge and EFAS river discharge, for (a) any closest river and (b) for closest river with catchment area of at least 500 km². [section 5.3.3]

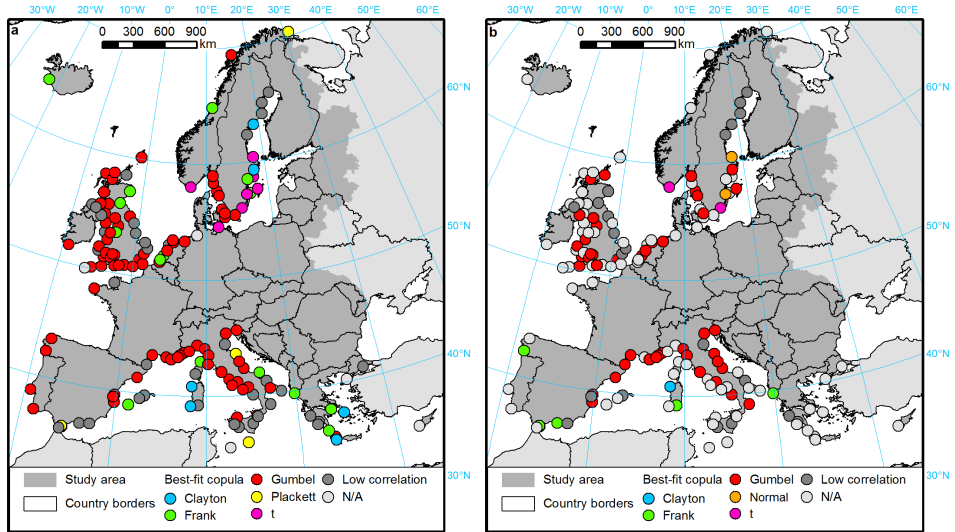


Figure F.13: Best-fitting copula for dependency between daily observed storm surge and EFAS river discharge, for (a) any closest river and (b) for closest river with catchment area of at least 500 km². [section 5.3.3]

F

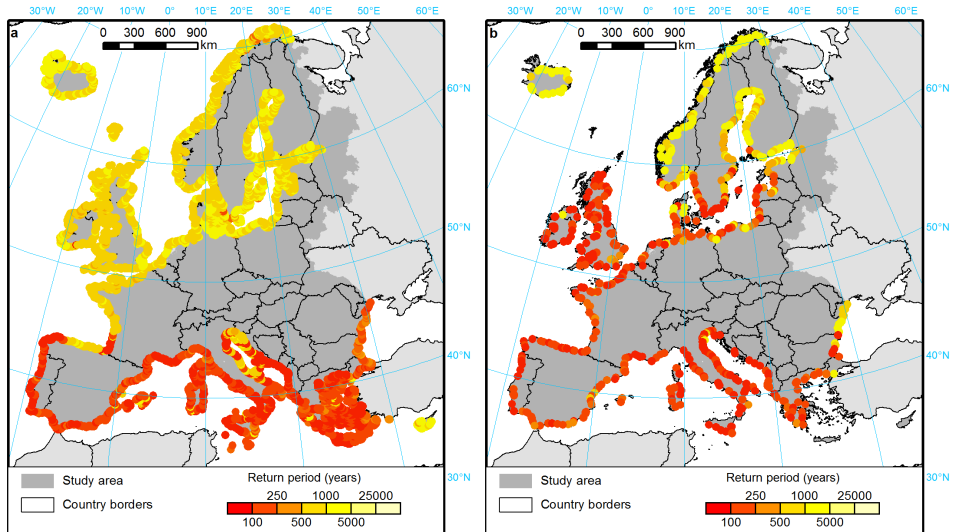
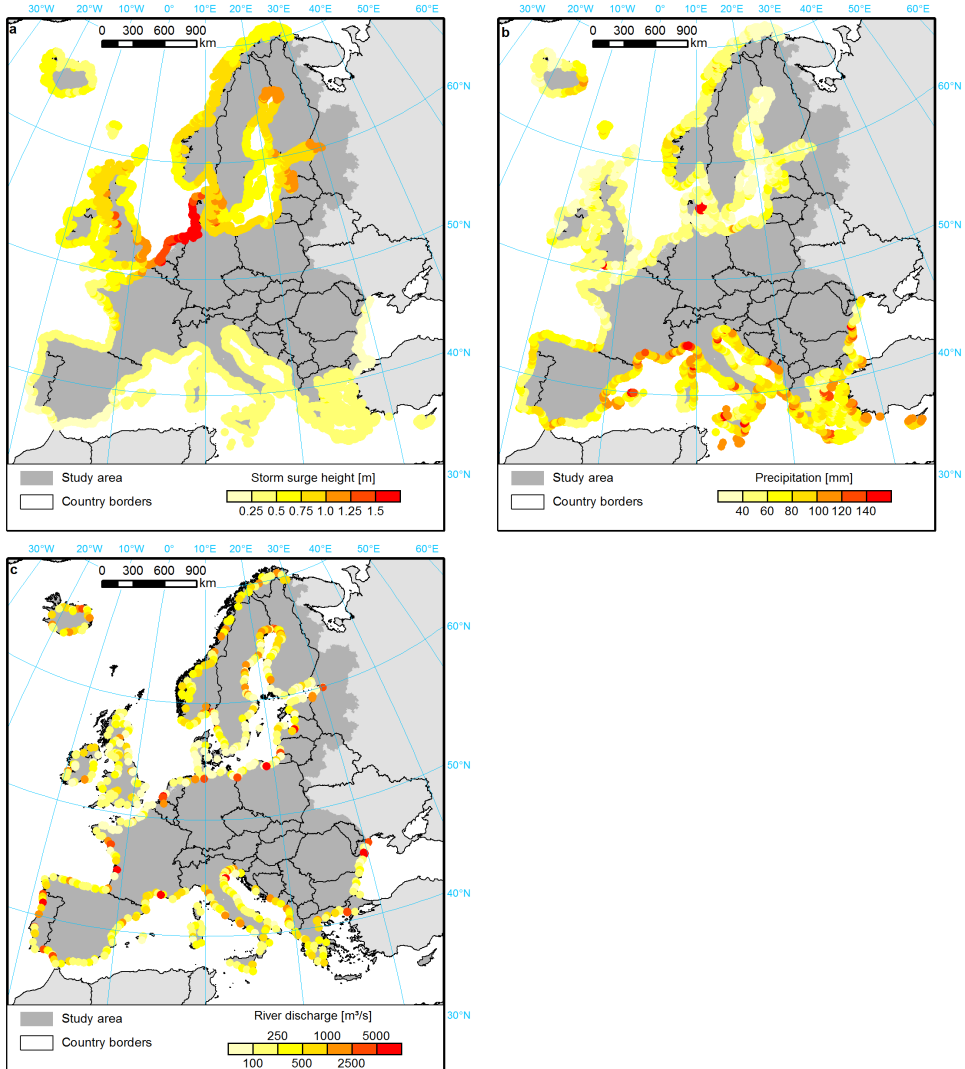


Figure F.14: Return period (in years) of (a) a 10-year precipitation event, or (b) 10-year extreme high river discharge, occurring on the same day as a 10-year storm surge. [section 5.3.4]



F

Figure F.15: Intensities of (a) 10-year daily average storm surge, (b) 10-year daily precipitation, and (c) 10-year river discharge. [section 5.3.4]

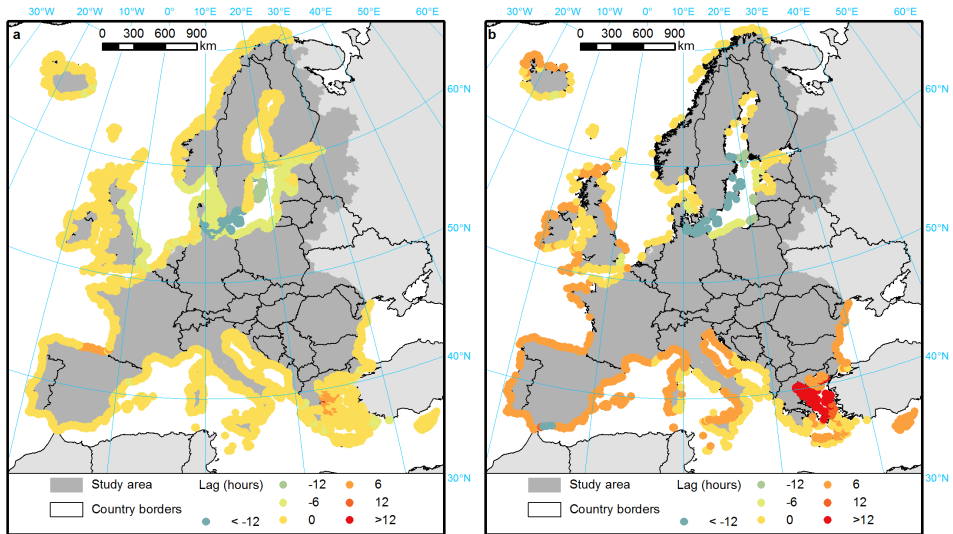


Figure E16: Lag between storm surge height (Delft3D/ERA-Interim) and (a) 6-hourly precipitation from ERA-Interim or (b) 6-hourly significant wave height from WaveWatch III/ERA-Interim, that has the highest correlation with storm surge height series. [section 5.4.2]

F

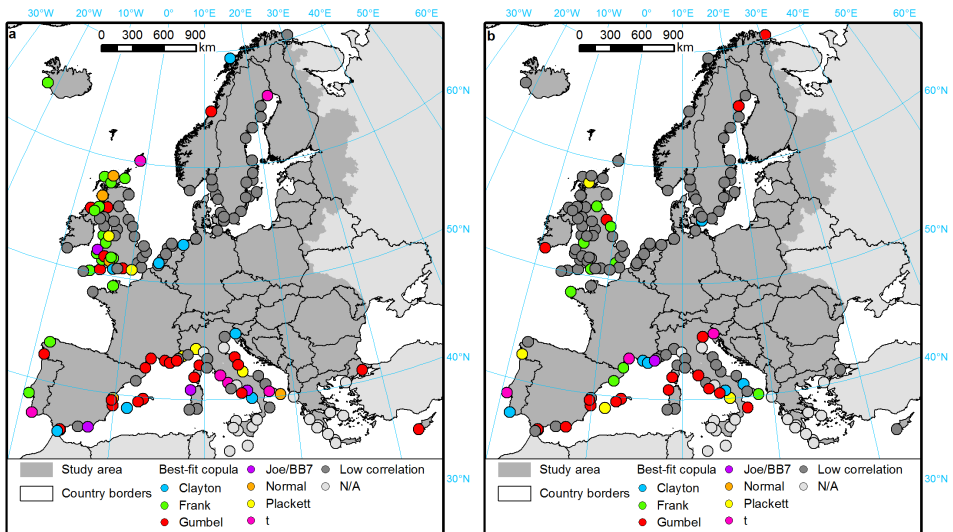


Figure E17: Best-fitting copula type for dependency between observed daily storm surge and precipitation, using (a) only the upper 95th percentile of storm surge or (b) only the upper 95th percentile of precipitation. [section 5.4.3]

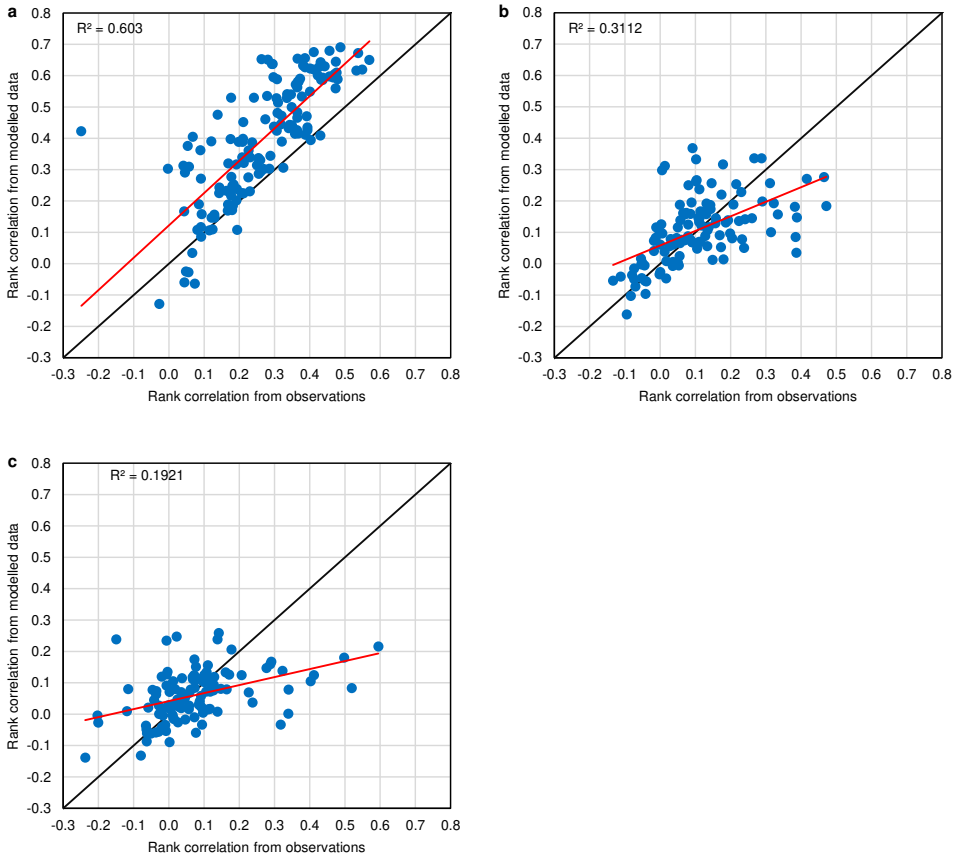


Figure F18: Comparison of rank correlations between modelled (Delft3D/ERA-Interim + ERA-Interim) and observed (tide gauges + E-OBS) daily storm surge height and precipitation, using (a) all available data, (b) 95th percentile of storm surge heights and corresponding precipitation and (c) 95th percentile of precipitation and corresponding storm surge heights. [section 5.4.3]

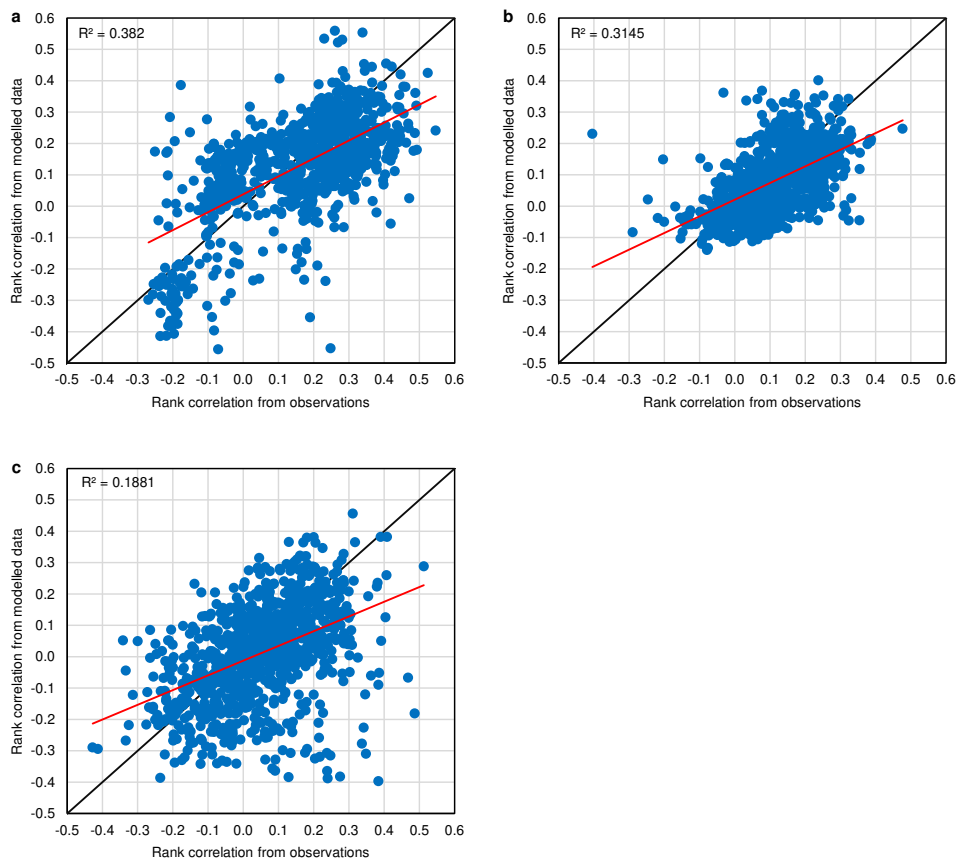


Figure F.19: Comparison of rank correlations between modelled (Delft3D/ERA-Interim + EFAS) and observed (tide gauges + river gauges) daily storm surge height and river discharges, using (a) all available data, (b) 95th percentile of storm surge heights and corresponding river discharges and (c) 95th percentile of river discharges and corresponding storm surge heights. Graph (a) is for the same set of river gauges as (b) and (c). [section 5.4.3]

G

DOCUMENTATION OF HANZE DATABASE

G.1. INTRODUCTION

This appendix contains the full methodological details on the HANZE database (6). The domain was described in section 6.2.1, but the full map of the domain is presented here. HANZE-Events was described in section 6.2.3, but the data structure of this database is shown below. HANZE-Exposure is covered here in entirety (synthetically described in section 6.2.2), together with a quality assessment.

G.2. DOMAIN

HANZE domain, covering 37 countries and territories, as described in section 6.2.1, is presented in Fig. G.1.

G.3. CONTENTS OF THE DATABASE

HANZE is available as several data files in an online repository [357]. The complete list of files of HANZE and their contents is shown in Table G.1. Exposure maps in 100 m resolution are provided as GeoTIFF rasters in ETRS89/LAEA projection, consistent with INSPIRE European grid. The baseline maps of land use and population (100 m resolution) are also included. For the benefit of climate research groups in particular, the data sets are provided also in aggregated, lower-resolution versions. Two files in netCDF format are included: 5 arc minute grid in geographical coordinates (WGS84) and finally 0.11° rotated-pole grid as used in EURO-CORDEX climate modelling framework [140].

Input historical statistics and the HANZE-Events database of past damaging floods are provided as Excel files. A list of variables included in those files is detailed in Table G.2. Apart from the statistical information, the two files (one with demographic and

This appendix was edited from the paper published in *Earth System Science Data* **10**, 565–581 (2018) [282], the paper's supplement and online documentation of HANZE database [356].

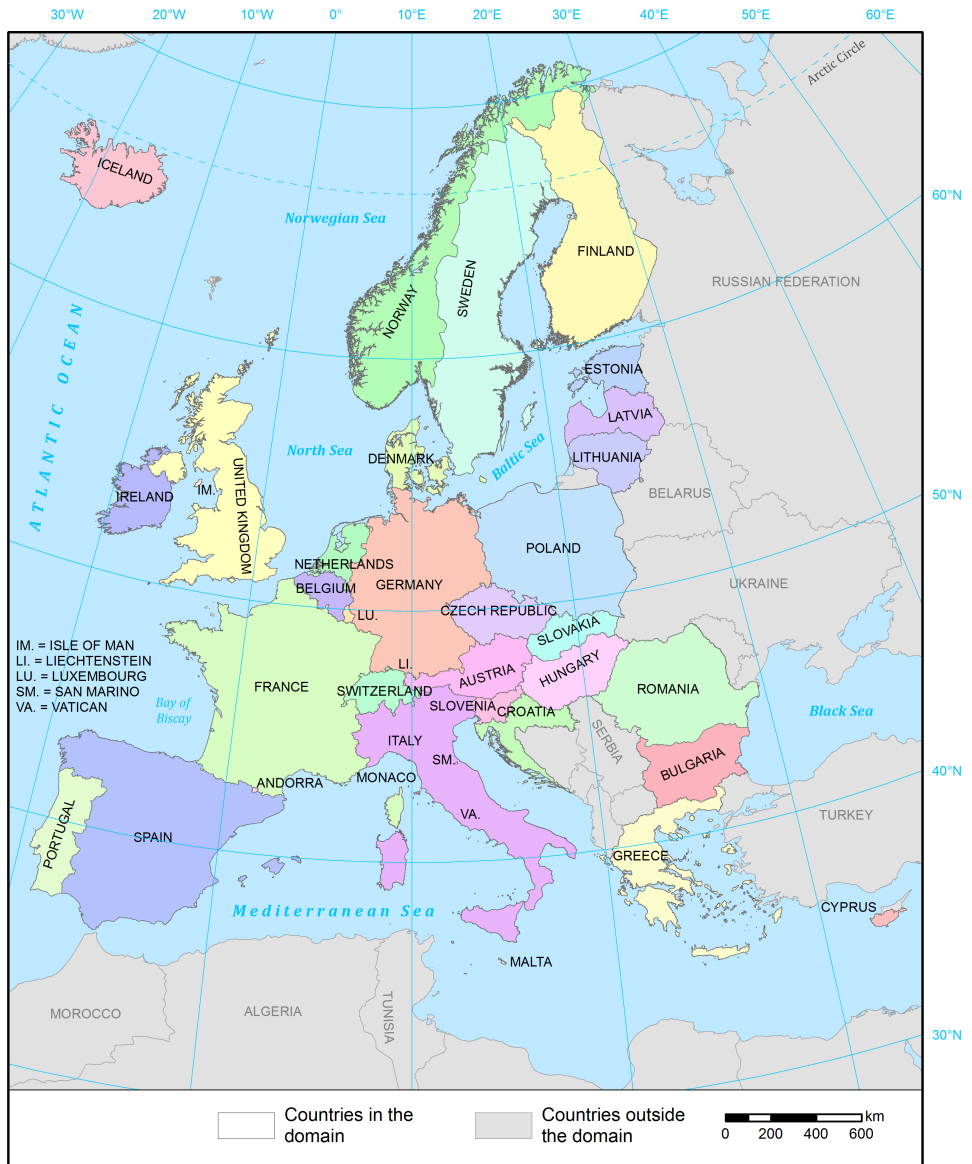


Figure G.1: Countries covered by the HANZE database [section 6.2.1].

Table G.1: List of files of HANZE database. XXXX represents the value indicating the year to which data set pertains.

Type	File	Format	Variables/contents
Output	CLC_XXXX	8 bit TIFF	land cover/use type, 44 classes according to CORINE Land Cover
Output	Pop_XXXX	16 bit TIFF	total population per grid cell (in persons)
Output	GDP_XXXX	16 bit TIFF	gross domestic product (GDP) per grid cell per year (\times EUR 10 000 in constant 2011 prices)
Output	FA_XXXX	16 bit TIFF	wealth per grid cell (\times EUR 100 000 in constant 2011 prices)
Output	Exposure_5min	netCDF	land use (fraction of urban areas, croplands, pastures, forests, water), total population, GDP, and wealth per grid cell aggregated to 5 arcmin resolution
Output	Exposure_cordex_0.11	netCDF	as above, but aggregated to EURO-CORDEX rotated-pole grid, 0.11° resolution
Output	Events_floods	Excel	list of past damaging floods (list of variables in Table G.3)
Input	Expo_input_CLC_Pop	Excel	historical land use/cover and population statistics
Input	Expo_input Econ	Excel	historical economic and currency statistics
Input	CLC_base	8 bit TIFF	baseline land cover/use type, 44 classes according to CORINE Land Cover
Input	Pop_base	16 bit TIFF	total baseline (disaggregated) population per 100 m grid cell (in persons)

Table G.2: Variables included in the input data files.

Variable	Unit
Population	Thousands of persons
Urban fraction	Urban population as % of total population
Persons per household	Mean number of persons
Croplands	% of total area
Pastures	% of total area
Infrastructure	Area covered by road and rail infrastructure in ha
Census information	Additional information on the 2011 censuses
Airports	Airports identified in the CLC data
Reservoirs	Reservoirs identified in the CLC data
GDP	Million euro in constant 2011 prices
GDP from agriculture	% of total GDP
GDP from industry	% of total GDP
Wealth in housing	% of total GDP
Wealth in agriculture	% of GDP from agriculture
Wealth in industry	% of GDP from industry
Wealth in services	% of GDP from services
Wealth in infrastructure	% of total GDP
Forestry index	% of GDP from agriculture
Deflator	Index, 2011 = 100 (for defunct countries, 1990 = 100)
Currencies	List of all currencies used in the domain since 1870
Currency conversion	Conversion factors to euro (euro = 1). For countries not currently using euro, 2011 exchange rates were used.

G

environmental data and one with economic data) each includes a table with all sources and transformations made to the data per country, per variable, and per year, as well as a list of references. The contents of the HANZE-Events database with explanations of all data recorded per event is shown in Table G.3.

G.4. METHODOLOGICAL ASPECTS OF HANZE-EXPOSURE

G.4.1. OVERVIEW

The general concept of the methodology is based on HYDE database from the Netherlands Environmental Assessment Agency [153, 319, 335]. Firstly, two detailed maps of population and land use is compiled for one time point. Complete surveys of those variables with a high spatial resolution are very few, and datasets constructed with a certain methodology rarely extend beyond a single time point. Therefore, once the two maps are collected—call them “baseline maps”—other time points in the past and in the future could be calculated based on the baseline maps. In this study, the baseline maps refer to the year 2011/12, and have a spatial resolution of 100 m. For the years between 1870–2020 only know the total population and land use at NUTS 3 regional level is known. Hence, for each time step, the population and the different land use classes had to be redistributed inside each NUTS 3 region in order to match the regional totals. Several methodologies were used in order to provide the best approximation of spatial distribution of each land use class and population. Efforts were concentrated on estimating past

Table G.3: Information included in HANZE-Events database [section 6.2.3].

Variable	Description
No.	Event number
Country code	NUTS0 country code
Year	Year of the event (assigned from starting date)
Country name	Country in which the event occurred, using political divisions of the time of the event. In the case of the historical countries of Czechoslovakia, East Germany, USSR, and Yugoslavia, the appropriate successor states were used instead of the original country.
Start date	Date on which the flood event started and ended; the exact daily dates are not always known, or are imprecise, but an event was included in the database as long as the starting month could be identified.
End date	Date on which the flood event ended
Type	Type of flood event, which can be River, Coastal, River/Coastal, or Flash. The events were assigned to River/Coastal type if both factors contributed to the flooding (they are referred to in the analysis as "Compound" floods). Flash flood type was assigned if the event was caused by rainfall lasting less than a day. However, often the information on meteorological conditions was missing and hence division of events into River and Flash floods was made based on dates of the event, location, season, and impacts.
Flood source	Name of the river, lake, or sea from which the flood originated, if available. The list of names is usually not comprehensive.
Regions affected	Regions where flood damages were reported, using the NUTS3 delimitation of regions, 2010 edition.
Area flooded	Area inundated by the flood in km ² . This statistic more often than not relates only to agricultural land.
Persons killed	Number of deaths due to the flood, including missing persons.
Persons affected	Number of people whose houses were flooded. However, the reported numbers of persons affected often only show the number of evacuees or persons rendered homeless by the event. If no other number was available, these were used. If only the number of houses flooded was reported, the number persons affected was estimated by multiplying the number of houses by 4.
Losses (nominal value)	Damages in monetary terms, in the currency and prices of the year of the flood event.
Losses (millions of EUR, 2011)	Damages in monetary terms converted to euro, correcting for price inflation relative to 2011.
Cause	The meteorological causes of the event, including precipitation values, surge heights, etc., if available.
Notes	Other relevant information, including co-occurrence of related events such as landslides or dam breaks, information on large discrepancies in the sources, estimated return periods, and other relevant statistics.
Sources	List of publications and databases from which the information was obtained.

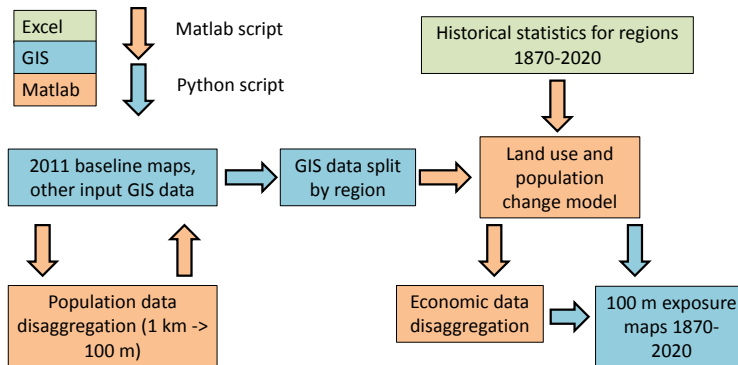


Figure G.2: Workflow of HANZE-Exposure.

and future residential urban areas (where most population is settled) and lands used by agriculture and infrastructure.

The procedure is summarized in Fig. G.2, outlining preparation of baseline maps (section G.4.2), compiling a database of regional-level statistical data (section G.4.3), modelling of changes in land use and population distribution (section G.4.4), disaggregation of economic variables (section G.4.5) and production of final exposure maps with a 100 m resolution.

G.4.2. STEP 1: BASELINE MAPS

There are very few high-resolution population and land cover/land use maps, and data sets constructed with a certain methodology rarely extend beyond a single time point. Therefore, two maps (one each for population and land cover) for a single year (2011 or 2012) were collected as baseline for the study. All other time points between 1870 and 2020 are calculated from those baseline maps using historical statistics with substantially lower resolution.

The baseline land cover/use is based on CORINE Land Cover (CLC) 2012, version 18.5a [337]. CLC is a project supervised by the European Environment Agency. It has so far produced four pan-European land use maps for 1990, 2000, 2006 and 2012. The maps are prepared mostly by manual classification of land cover patches from satellite imagery with a resolution of 25 m or better. For the latest edition, images collected during 2011–2012 were used. The inventory consists of 44 classes (Fig. G.3). The minimum size of areal features is 25 ha. For linear objects such as roads, railways, and rivers, a minimum width of 100 m is used. CLC 2012 is first displayed as a vector map, and can then be transformed into a raster with 100 m resolution. CLC 2012 covers the entire domain with the exception of Andorra. For this particular country, the land cover/use map was constructed with overlaying data from four different sources, top to bottom:

1. CLC 2012 v18.5a, which covers a small strip around the border;
2. CLC 2000 v18.5, an earlier edition which covers a larger strip around the border [337];

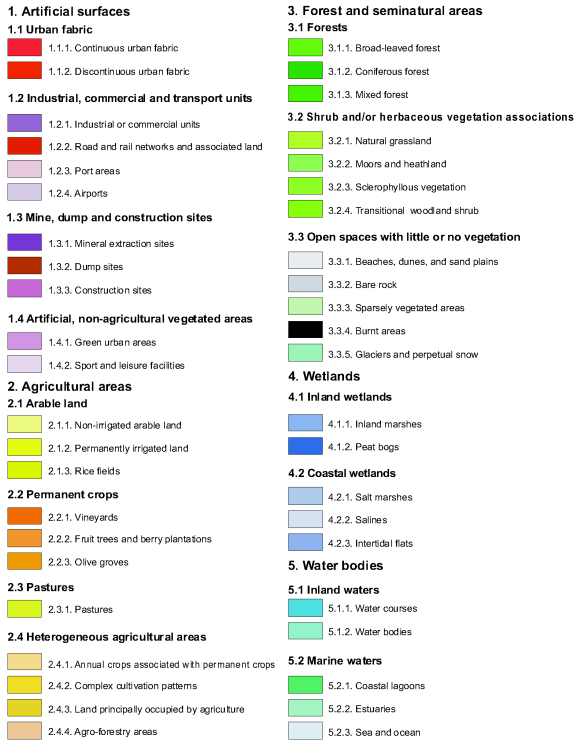


Figure G.3: Corine Land Cover classes. Source: European Environment Agency [360].

G

3. OpenStreetMap, accurate as of mid-2016 [358];

4. Global Land Cover 2000 [359].

The final map for the full domain of 37 countries and territories is presented in Fig. G.4.

The baseline population map is based on the GEOSTAT 2011 population grid, version 2.0.1 [338]. This data set has 1 km resolution and for most countries it represents the actual population enumerated and georeferenced during the 2011 round of population censuses, complemented by estimates by the European Commission's Joint Research Centre. This data set is presented in Fig. G.5. For this study, the 1 km grid had to be further disaggregated to 100 m resolution. Several methods have been proposed for this procedure and tested for Europe [361, 362]. Here, methods M1 and M3 described in Batista e Silva *et al.* [339] are combined. M1 denotes the "limiting variable method" used in cartography for creating dasymetric maps of population density. The procedure is an iterative algorithm applied separately for each 1 km grid cell. The steps are as follows:

1. First, uniform population density is assigned for each land use class in a 1 km grid cell:

$$Y_{LG}^0 = Y_G = \frac{X_G}{S_G}, \quad (\text{G.1})$$

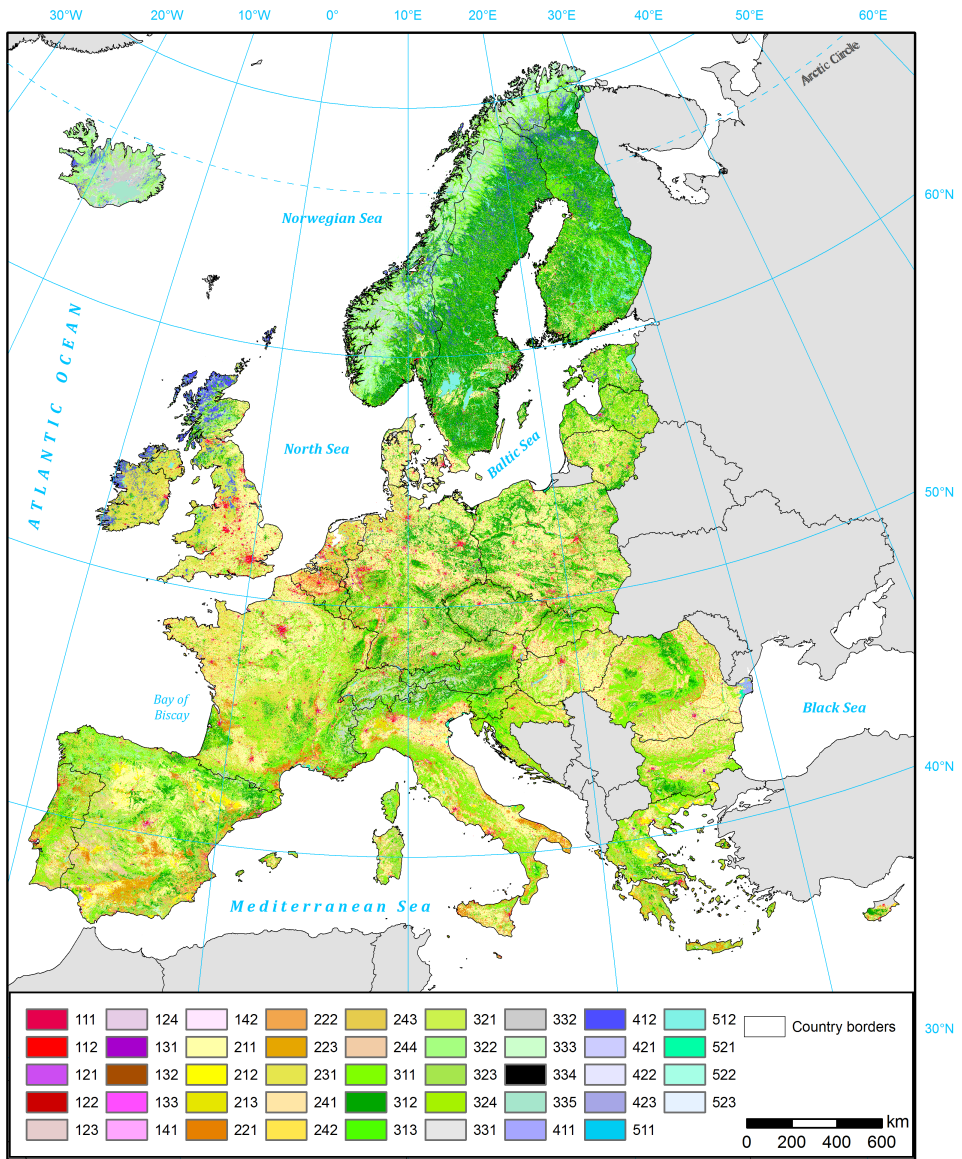


Figure G.4: Baseline land cover/use from Corine Land Cover 2012 by Copernicus Land Management Service, except for Andorra. For explanation of CLC classes, see Fig. G.3.

where Y_{LG}^0 is the population density for land use $L \in \{1, \dots, n\}$ in grid cell G at step 0, Y_G is the population density in the grid cell, i.e. population number X_G divided by area S_G .

2. A population density threshold T_L is defined for each one of n land use classes.
3. Land use classes are ranked and the subindex L is renumbered from lowest to highest population density; i.e. $L = 1$ denotes the least densely populated land use class in the grid cell.
4. Proceeding in order starting with $L = 1$, in step L the density attributed to class L in the previous step is modified if it is above the threshold, i.e. if $Y_{LG}^{L-1} > T_L$. That creates a surplus population U_{LG}^L :

$$U_{LG}^L = S_{LG} \cdot (Y_{LG}^{L-1} - T_L) \quad (\text{G.2})$$

5. Surplus is then redistributed among the remaining land use classes M ; hence

$$Y_{LG}^L = T_L, \quad (\text{G.3})$$

$$Y_{MG}^L = Y_{MG}^{L-1} + \frac{U_{LG}^L}{\sum S_{MG}}, M > L \quad (\text{G.4})$$

6. If after completing all iterations there is still surplus population, i.e. if $X_G > \sum T_L S_{LG}$, it is redistributed proportionally to the threshold:

$$Y_{LG} = \frac{T_L X_G}{\sum T_L S_{LG}} \quad (\text{G.5})$$

The crucial aspect of this method is defining the threshold T_L . Here, I use thresholds suggested by Eicher and Brewer [363]; i.e. the 70th percentile of the population density of grid cells for which only one land use class was reported in the baseline land use map. Such “pure” cells constituted around 5 % of all population grid cells. The final thresholds T_L are shown in Table G.4. For artificial surfaces other than urban fabric, the CLC classes were merged for the threshold calculation, as very few, if any, pure cells could be found for each of those classes. Also, for all areas covered by wetlands, water, sand, glaciers, bare rocks or burnt vegetation the threshold was set at 0, as those terrains are in principle uninhabitable. It should be noted that land use classes with $T_L = 0$ are still included in the algorithm described above.

The result of the calculation, however, is only the population per land use in each 1 km grid cell. Hence, the population had to be disaggregated further. For this, an approach similar to method M3 was used. This method redistributes the population proportionally to the level of soil sealing, or imperviousness of the ground. This variable has a range from 0 %, which indicates completely natural surface, to 100 %, which indicates land completely sealed by an artificial surface. This information could not be used directly to redistribute the population as large soil sealing may be caused both by residential and non-residential buildings as well as infrastructure. However, large elements

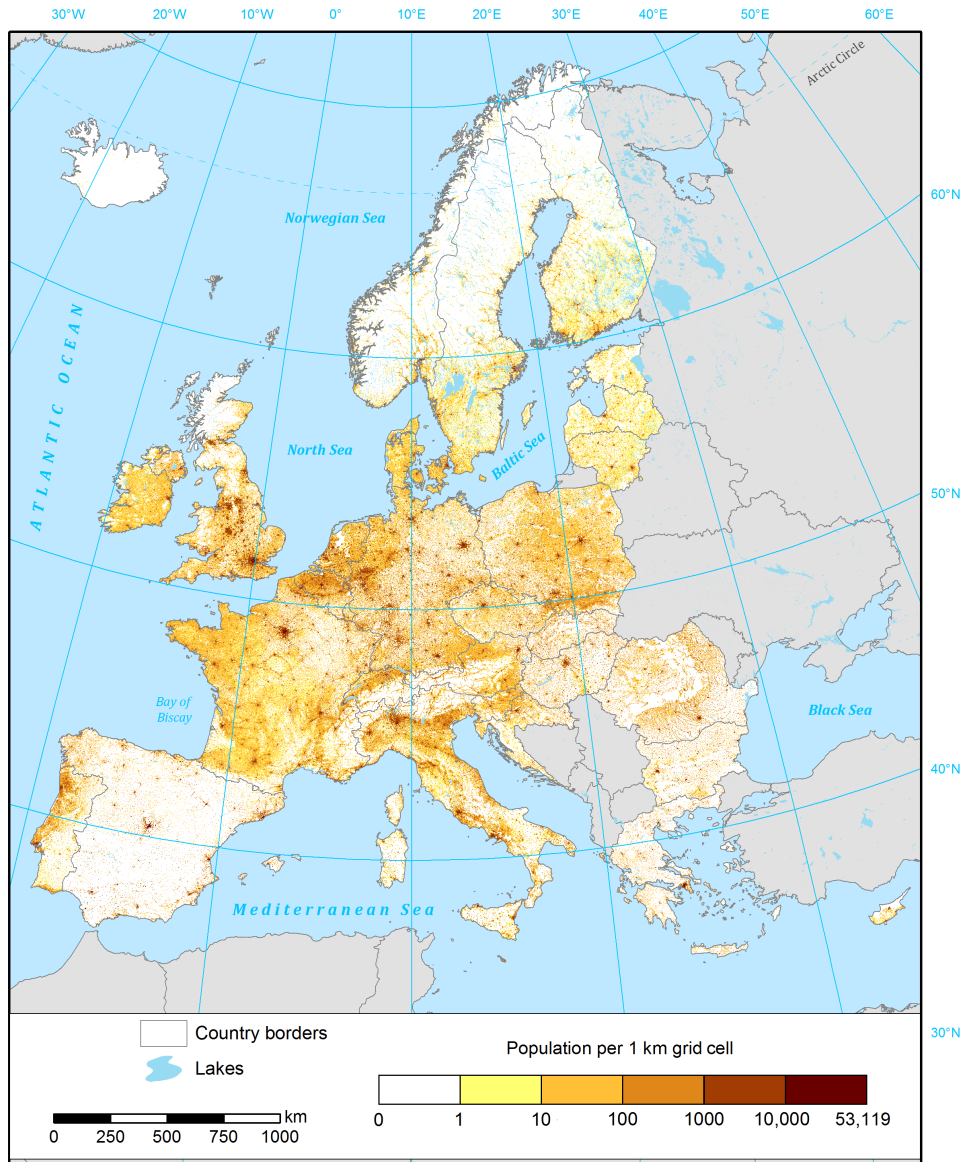


Figure G.5: GEOSTAT population grid from 2011 censuses, 1 km resolution, by Eurostat.

Table G.4: Thresholds for population disaggregation algorithm T_L

CLC class name and code	Threshold (persons per km ²)	CLC class name and code	Threshold (persons per km ²)
Continuous urban fabric (111)	22 666	<i>Land principally occupied by agriculture</i> (243)	40
Discontinuous urban fabric (112)	6452	Agro-forestry areas (244)	10
Other artificial (121–142)	59	Broad-leaved forest (311)	9
Non-irrigated arable land (211)	32	Coniferous forest (312)	6
Permanently irrigated land (212)	64	Mixed forest (313)	9
Rice fields (213)	9	Natural grasslands (321)	18
Vineyards (221)	50	Moors and heathland (322)	18
Fruit trees and berry plantations (222)	44	Sclerophyllous vegetation (323)	10
Olive groves (223)	60	Transitional woodland-shrub (324)	11
Pastures (231)	40	Sparsely vegetated areas (333)	40
Annual crops associated with permanent crops (241)	71	<i>Uninhabitable natural areas</i> (331–332, 334–523)	0
Complex cultivation patterns (242)	82		

of infrastructure or industry were already taken into account using the limiting variable method.

Data on soil sealing were obtained from the Imperviousness 2012 data set [337]. It was created based on high-resolution satellite photos taken during 2011–2012 in visible and infrared spectrum. This data set has 100 m resolution, which was resampled to a 1 km grid, so that average population density in grid cells with given imperviousness could be calculated. The resulting relationship can be approximated as a power law function, based on cell imperviousness ranging from 1 to 96 % (Fig. G.6). Cells with 0 % imperviousness should, in principle, not be inhabited. Additionally, a power law function converges at 0 %. At the opposite on scale, almost no 1 km cells have values above 96 %. Hence, the population X_g in 100 m grid cell g is equal to

$$X_g = \left[\frac{Z_g}{\sum Z_g} Y_{LG} S_{LG} \right] \quad (\text{G.6})$$

where Z_g is the population of grid cell g obtained from the power function divided by the maximum population (at 96 % imperviousness):

$$Z_g = \frac{19.479 V_g^{1.3195}}{8031} \quad (\text{G.7})$$

where V_g is the imperviousness in grid cell g . The population X_g is rounded to the closest integer, as population numbers need to be integers. However, rounding can cause difference between the population X_{LG} before and after disaggregation through soil sealing. In such a case, the population is increased or reduced randomly (with equal probability) within the land use class, one person at a time, until the population X_{LG} matches the value before the second stage of disaggregation. This completes the process, an example of which is shown in Fig. G.7.

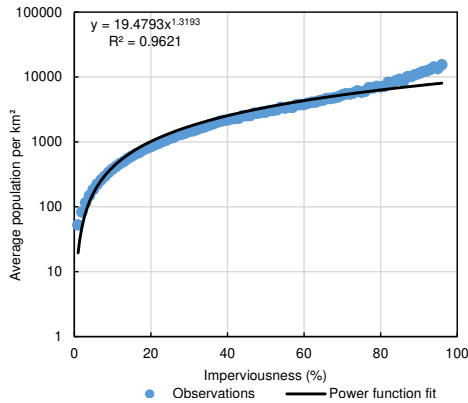


Figure G.6: Relationship between average population density per imperviousness (soil sealing) class.

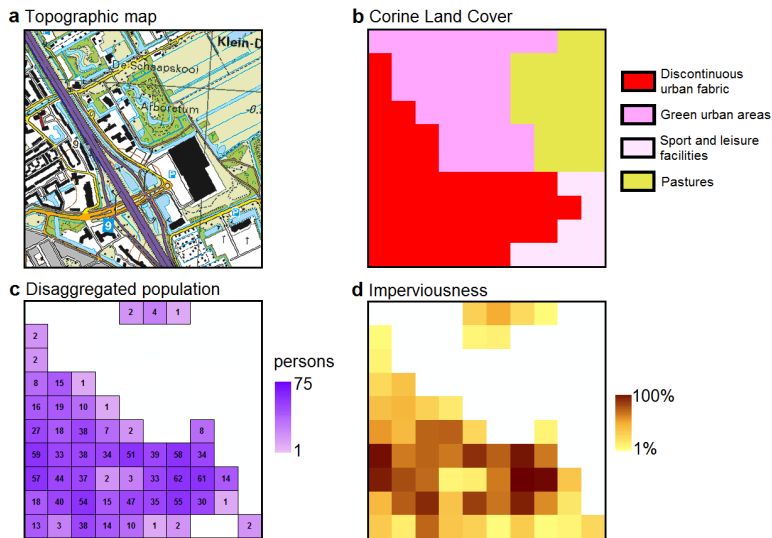


Figure G.7: Disaggregation result and source data for a fragment of the city of Delft in the Netherlands. The area shown corresponds to a 1 km grid in the GEOSTAT population data set. In this grid cell, the population at the time of the 2011 census was 1218. Panel (a) was extracted from a Dutch 1 : 25000 topographic map for reference. Panel (b) shows the land use structure according to CORINE Land Cover 2012, and panel (d) shows soil sealing according to Imperviousness 2012 data set. The final disaggregated 100 m population grid is presented in panel (c).

G.4.3. STEP 2: HISTORICAL STATISTICS

Reconstruction of exposure for years other than the baseline maps requires historical statistics for several variables. Most of those statistics have been collected at regional level. The Nomenclature of Territorial Units for Statistics (NUTS), 2010 edition [336], was used here to define the region. This classification has four levels (0, 1, 2, 3), where 0 is the national level and 3 is the finest regional division. Level 3 was chosen for this study, resulting in 1353 regions in the study area (Fig. G.8). A vector map of regions was obtained from ESRI (2016) with amendments based on Eurostat [338] map in order to fully match NUTS 2010 classification. Coastlines in the vector map were further adjusted using the aforementioned CLC 2012 map. NUTS favours administrative divisions in defining the regions, though often statistical (analytical) regions are used instead, created by amalgamation of smaller administrative units. For example, the regions in the Netherlands are defined as follows:

- NUTS 1: 4 statistical regions (*Landsdelen*);
- NUTS 2: 12 provinces (*Provincies*);
- NUTS 3: 40 statistical regions (*COROP-gebieden*).

It can be noticed that only at NUTS 2 level the actual administrative divisions of the Netherlands are used, while the NUTS 1 and 3 regions are groups of provinces and municipalities, respectively. A NUTS 3 region in the study area has an average area of 3580 km² and an average total population of 379 000 as of 2011 census. Almost a third of all regions are located in Germany (412), since they are typically smaller than in most other countries (average population is only 195 000). It should be noted that NUTS 2010 classification was used instead of newer editions (2013 or 2016) because 2011 census data, matching the baseline population map, were disseminated using this classification of regions.

TOTAL POPULATION

Total population refers to the overall number of persons living in a region. Population can be defined as *de facto* population, i.e. the number of persons physically present in an area at a given moment of time, or *de jure*, i.e. the number of persons usually resident in an area, excluding short-term movements or migrations of population [364]. Countries typically have their own, specific rules what counts into their population figures, deviating to a various degree from the *de facto* and *de jure* concepts. Such differences are mostly not relevant relative to countries' overall population size. The prime sources of population figures are censuses, held typically every decade, supplement by annual balances of births, deaths and migrations. Starting with the 1970s, many European countries gradually replaced censuses with population registers, providing continuous information on population size.

For this database, statistics were generally compiled from country-specific sources, though for 1960–2010 data from [334] were mostly used, which included recalculation of historical census data to modern administrative divisions by Gløersen and Lürer [365], and annual population estimates starting with 1990. Population projections up to 2020

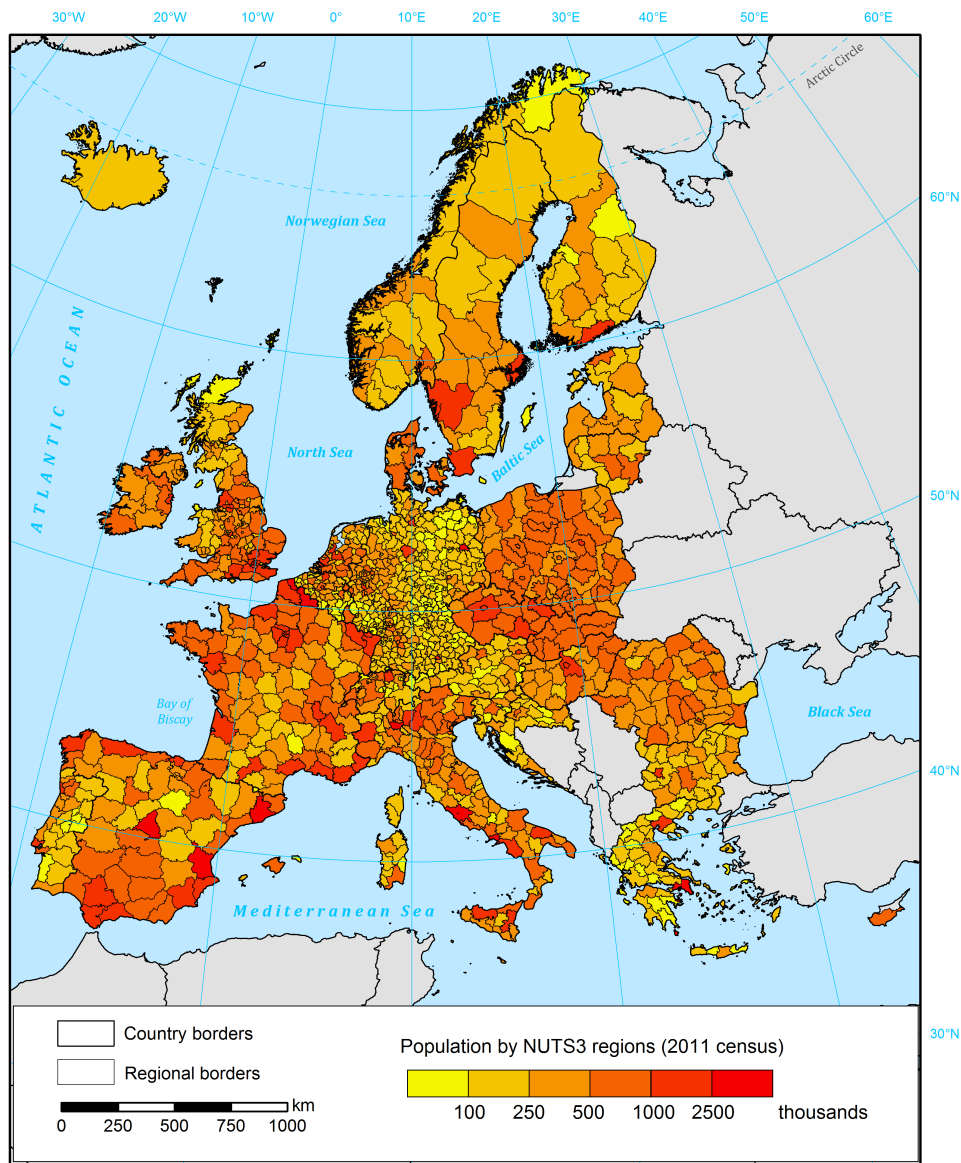


Figure G.8: NUTS 3 regions (2010 version) in the study area and their population, Region boundaries based on ESRI map with modifications (see text for explanations).

were generally obtained from EUROPOP2013 projections by Eurostat, except for countries with no subdivision into regions, which were obtained from newer EUROPOP2015 projections or United Nations *World Population Prospects: 2015 Revision* [366].

However, data at current administrative divisions were not always available. In several cases, historical divisions were recalculated using one of two methods: the “population method” and the “territorial method”. The population method recalculates the population of “old” administrative divisions to “new” ones by shifting overlapping proportions of population between the territorial units. More formally, the population X_A^t in each post-reform (“new”) administrative unit A in year t is a sum of fractions F_{AB} multiplied by the population X_B^t of pre-reform units B :

$$X_A^t = \sum F_{AB} X_B^t \quad (\text{G.8})$$

The fractions F_{AB} could only be determined if both populations X_A^t and X_B^t are known for the same year; in other words, F_{AB} is the percentage of B 's population living within the boundaries of A . Yet, the extent of administrative changes may not allow to calculate the fractions. The territorial method, on the other hand, requires a digital map of both pre- and post-reform administrative divisions. The fraction F_{AB} is then the percentage of B 's territory also belonging to A . This assumes equal population density within A and B , therefore this information could only be used to determine population growth rates X_A^t / X_A^{t-1} . Those growth rates were used to extrapolate the population from the earliest year for which data for A are known. It should be noted that both methods could be used for different time periods for the same country, also multiple times, in order to achieve population estimates for the 2010 version of NUTS 3 regions. The two methods were used depending on the availability of data.

URBAN FRACTION

The fraction of the overall number of persons living in a region that reside in areas defined as urban. The definitions of urban areas vary from country to country [26]; the criterion could be administrative (legally designated cities or towns), demographic (all settlements or communes with more inhabitants than a given threshold) or statistical, based on multiple criteria (population number or density, percent of non-agricultural employment, distance between buildings etc.). For the purpose of this study, the urban population is defined as the population disaggregated into CLC classes 111 and 112 (urban fabric); the remainder of the population is therefore considered rural.

However, the disaggregation procedure (see main paper) was only done for the 2011 baseline map. Therefore, national definitions of urban populations were used to determine growth rates of urban and rural populations, which were used to extrapolate the urban fraction from the baseline map. For some countries, different definitions were used in different time periods. They could all be used, however, as the various time series overlapped, allowing them to be linked to the 2011 map. The data was mostly collected from national sources, supplemented by United Nations *World Urbanization Prospects* [26] and other international yearbooks.

MEAN NUMBER OF PERSONS PER HOUSEHOLD

The total population divided by the total number of households in a region. Typically, a household is defined as one or more people who occupy a single housing unit [367].

Households consists both of private households and collective households, i.e. institutions such as prisons, nursing homes, dormitories, homeless shelters, army barracks etc. [368]. However, the statistics on the latter were not always available, though this has minor effect on the accuracy of the estimates, as population in institutions typically do not exceed 1 % of total population, according to data published in United Nations yearbooks [364]. Additionally, data on the number of dwellings was sometimes used if the number of private households was not available. Usually the difference between the two statistics is negligible (some dwellings may not be occupied, while some might contain more than one household). The data was mostly collected from national sources, supplemented by several international compendia.

LAND USE STRUCTURE

The region's area, or its percentage, covered by different land use classes. The definitions vary between countries; for the purpose of this study, the 2012 statistics were obtained directly from the baseline land use map. The following land use classes were calculated:

- Croplands: CLC classes 211-213 "Arable land", 221-223 "Permanent crops" and 241-244 "Heterogeneous agricultural areas";
- Pastures: CLC class 231 "Pastures";
- Infrastructure: CLC class 122 "Road and rail networks and associated land".

For years 2000–2012, the data were obtained or interpolated from Corine Land Cover datasets, and the trend in land use change was extrapolated to 2020. For 1870–1995, are covered by croplands, pastures and forests was extrapolated using different data series following various definitions. For more recent years, regional data from Eurostat were largely used, otherwise national statistics, FAO [369] or HYDE 3.2 [319] provided the necessary data. Area covered by road and rail infrastructure was extrapolated using statistics on motorway and railway length, mostly from national statistics, Eurostat and Mitchell [370].

GDP AND ITS COMPOSITION

GDP is the gross domestic product, i.e. value of an economy's total output of goods and services, less intermediate consumption, plus net taxes on products and imports, in a specified period [334]. Here, estimates of GDP at constant prices were included, adjusted to 2011 price levels, with average currency exchange rates in 2011 used to convert GDP value to euro. The starting point for all countries, except for the microstates, are Eurostat's GDP data at regional level calculated using the 2010 European System of National and Regional Accounts, or ESA 2010 [371]. GDP was calculated in the past with a variety of methodologies, while for the early 20th and late 19th centuries GDP estimates are often based on proxies. Therefore, the different time series of data were linked to current Eurostat estimates.

Data on GDP by sector were also collected. Strictly, they represent the percentage composition of gross value added (GVA), a subcomponent of GDP (GDP minus net taxes), as data on net taxes are not collected by sector. Nevertheless, the GVA composition was applied to GDP. The following sectors were distinguished, based on NACE Rev. 2 [371]:

- Agriculture: Agriculture, forestry and fishing (A);
- Industry: Mining and quarrying (B), Manufacturing (C), Electricity, gas, steam and air conditioning supply (D), Water supply; sewerage, waste management and remediation activities (E);
- Services: construction (F) and all remaining sectors (G–U).

As can be noticed, the difference between traditional three-sector split is the inclusion of construction in services rather than in industry. The data sources, apart from Eurostat and some international compilations, were mostly country-specific. For years 2017–2020, the GDP data were extrapolated using April 2017 projections by the International Monetary Fund [372].

WEALTH AND ITS COMPOSITION

“Wealth” is considered here in a narrow sense, and relates to assets that could be destroyed during a natural hazard and conceivably contribute to reported losses. Therefore, “wealth” is comprised of tangible fixed assets. Fixed assets are produced non-financial assets that are used repeatedly or continuously in production processes for more than one year. They consist of dwellings, other (non-residential) buildings and structures, machinery and equipment, and cultivated biological resources. Therefore, the following items are excluded: all financial assets, intangible assets (e.g. patents and software), inventories of produced goods, valuables, natural resources (incl. land, sub-soil assets and non-cultivated biological resources) and consumer durables [371]. Potential inclusion of inventories, consumer durables and non-cultivated biological resources (mainly forests) was reviewed. Those categories are destructible, and of considerable monetary value. However, very little data is available for those. An analysis of inventories and consumer durables data from OECD [373], Goldsmith [374], Piketty and Zucman [375] and some other country-specific sources has shown that those assets are rather stable relative to GDP. Therefore, the omission of the assets shouldn’t affect the analysis of trends in vulnerability to natural hazards.

Statistics on tangible fixed assets according to ESA 2010 methodology are available from Eurostat for most, though not all, countries. However, the Eurostat series mostly start in 1995, and were amended with OECD, Goldsmith (1985) and several other compilations and country-specific sources. Historical series were linked to Eurostat’s ESA 2010 estimates, where available. The value of assets is measured in current replacement costs, i.e. the market or basic cost of replacing an asset in the year, for which the statistic was calculated. The assets were grouped into five categories for the purposes of this study:

- Dwellings (residential buildings);
- Infrastructure, i.e. non-residential buildings and structures in ‘transportation and storage’ category (NACE sector H), which is intended to represent the value of roads, railways, airports, harbours and the like;
- Agricultural assets, i.e. non-residential buildings and structures, and machinery and equipment related to production in agriculture, forestry or fishery (NACE sector A), and cultivated biological resources;

Table G.5: Currency database format.

Column	Description
Code	NUTS0 two-letter country code
Name	Country/territory name
Currency	Currency name*
Code1	Three-letter currency code*
Code2	ISO 4217 numeric currency code
Start date	Date or year when currency first entered circulation
End date	Date or year when currency was withdrawn from circulation
Conversion	Conversion factor between new and old currency
Note	Information relevant for correctly applying the information on currencies

Notes: * the currency name/code equals ISO 4217 currency name/code if the field "Code2" is filled; otherwise the name/code is assigned solely for the purposes of disambiguation of different currencies in this database.

- Industrial assets, i.e. non-residential buildings and structures, and machinery and equipment related to mining, manufacturing and utilities (NACE sectors B–E);
- Services assets, i.e. non-residential buildings and structures, and machinery and equipment related to other economic activity (NACE sectors F–U), and weapons systems, except assets under "infrastructure" category.

Value of dwellings and infrastructure was calculated and inserted into the database as a relative value, in % of GDP. For the remaining three categories, their value was calculated relative to GDP generated by corresponding categories of production – agriculture (NACE sector A), industry (sectors B–E), and services (sectors F–U).

G

CURRENCY AND DEFLATORS

In order to convert reported losses from various currencies and reference years to a single benchmark, information on inflation and currencies were collected. Two tables were prepared and are included with other HANZE input data. The first one includes all currencies that were used in the study area between 1870 and present, with their names, ISO 4217 codes, starting and ending dates of validity as well as conversion factors to euro (Table G.5). For countries not currently using the euro, 2011 exchange rates from Eurostat [334] were used. Information on currencies and conversion factors was mostly gathered from ISO 4217 [376] and GHOC databases [377], supplemented by various Internet resources.

The second table contains deflators used to adjust nominal losses to real losses in 2011 prices. The GDP deflator was generally used, as it allowed us to make the loss adjustments consistent with GDP values. Alternative price indices were used only if the GDP was not available, but they were always "anchored" to the GDP deflator series. These other series included indices of consumer, wholesale, retail, or cost-of-living prices. The source of the data was usually the same as those for the GDP data; they are listed in detail in the data files themselves. Some natural hazards databases, such as EM-DAT, report losses in US dollars, therefore exchange rates were obtained at ad hoc basis to convert those values to national currencies, usually by utilizing the same sources as for

GDP or deflator series. It should be noted that the currency conversions and deflators used here omit four cases of hyperinflation: Germany 1923, Poland 1923, Greece 1944 and Hungary 1946. Inclusion of those cases would cause large distortions to the data series. Hyperinflation periods and resulting currency changes were marked in the data set. The data set also includes deflator series for three former countries – Czechoslovakia, the Soviet Union and Yugoslavia – as many countries were their constituents in the past.

An example calculation is shown below for the sake of illustration. It shows the conversion of an estimate of losses due to the 1934 flood in southern Poland:

1. Losses in 1934 currency and prices: 74 600 000 “pre-war” Zlotys (PLO);
2. “Pre-war” Zloty (PLO) was converted to “post-war” Zloty (PLL) at par (1:1) in 1944, then denominated to “heavy” Zloty (PLZ) at 100:3 in 1950, and again to “new” Zloty (PLN) in 1995 at 10 000:1. Additionally, the exchange rate to euro (EUR) in 2011 was 4.1206, hence

$$74600000 / \frac{1}{1} / \frac{100}{3} / \frac{10000}{1} / 4.1206 = 54.3125 \quad (\text{G.9})$$

3. Therefore, the uninflated value of losses equals 54.3125 EUR. From the GDP deflator series, the price index can be extracted for 1934, which is approx. 0.0000712, where year 2011 equals 100. Therefore:

$$54.3125 \times \frac{100}{0.0000712} = 76281571 \quad (\text{G.10})$$

4. Hence, the losses from the 1934 flood were approximately 76 300 000 EUR in 2011 prices.

G.4.4. STEP 3: LAND USE AND POPULATION CHANGE MODELLING

After the baseline maps and a database of historical statistics were completed, changes in land use and population over time were modelled. This was carried out for each of the 1353 NUTS 3 regions separately in specified order. A summary of the procedure is included in Table G.6 and the most important details of the methodology are described below.

URBAN POPULATION

Redistribution of population within urban areas and growth of cities were modelled based on two factors: change in urban population size and change in number of persons per households. Increasing population combined with smaller families in each dwelling have caused a substantial increase in the demand for housing. Between 1870 and 2011, the number of urban households in Europe increased eight-fold. Those extra dwellings were typically constructed outside the urban centres, as existing houses were rarely replaced by bigger ones. Many studies have shown a functional relationship between population density and distance from the city centre [378–380]. Clark [381] showed that over time the sharp decline in population density with distance has become much less pronounced. This is largely caused by the aforementioned social change: in existing households, families have become smaller, and thus the population declines closer to

Table G.6: Summary of historical land use and population modelling approaches, by CORINE Land Cover classes (see Fig. G.3). The number in first column indicates the order in which the modification of land use and population was done.

Order	Land use and population type	Modelling approach
1	urban fabric (CLC 111 and 112) and urban population redistribution	Population per urban grid cell is modified according to changes in mean number of persons per household. Surplus population (the difference between urban population in a region after this modification and the value reported in the historical statistics database) and urban fabric are removed starting with grid cells furthest away from urban centers (see text for details).
2	industrial or commercial units (CLC 121)	Area of CLC 121 in a region changes proportionately to industrial production per capita in constant prices. "Industrial" grid cells located furthest from the urban centres are removed first when going back in time.
3	reservoirs (part of CLC 512)	Reservoirs are removed completely using the information on year of construction. 1069 objects and their construction year were identified using GRanD database [69].
4	road and rail networks and associated land (CLC 122)	Area of CLC 122 in a region changes as defined in the historical statistics database. "Infrastructure" grid cells located furthest from the urban centres are removed first when going back in time.
5	airports (CLC 124)	Airports are removed completely using the information on year of construction. 1548 objects were identified using mostly OurAirports [340] database and year of construction was mostly obtained from various language editions of Wikipedia.
6	construction sites (CLC 133)	All construction removed from the land use map for years 1870–2005, otherwise as in the baseline map.
7	croplands (CLC 211–223 and 241–244)	The area covered by croplands in a region is adjusted to match the value in the historical statistics, so that the grid cells least suitable for agriculture are removed first, while unutilized grid cells with the highest suitability are added first. Suitability is proportional to slope and crop suitability index for high-input cereals by FAO [341]. Grid cells ranked the same are disambiguated with distance from urban centres (see text for details).
8	pastures (CLC 231)	As for croplands, but with crop suitability index for high-input alfalfa used instead of cereals (see text for details).
9	burnt areas (CLC 334)	All burnt areas removed from the land use map for years 1870–2000, otherwise as in the baseline map.
10	natural areas other than water (CLC 311–333 and 335–422)	If after application of previous steps some land becomes unoccupied, it is assumed that this land was covered by the same natural land cover typical to its nearest neighbourhood (the most frequently occurring type within 200 m from the outline of the grid cell in question). If no natural land cover was located in the vicinity, the unoccupied land was assumed to be covered by forest (CLC 311).
11	rural population redistribution	Population of grid cells which were changed from urban to non-urban is modified, then non-urban population is modified according changes in mean number of persons per household. If needed, rural population increased/reduced based on distance from urban centres to match historical statistics for a region (see text for details).
12	remaining land use classes	Assumed constant, as in the baseline map.

the centre and the surplus population is accommodated further from the centre in less-developed areas.

In light of the above, the modelling procedure is as follows:

1. In every urban fabric grid cell g in region r the population P in time step t is modified relative to $t - 1$ (2011 baseline is step 0) to account for change in household size:

$$P_{t,r,g} = P_{t-1,r,g} \frac{H_{t,r}}{H_{t-1,r}} \quad (\text{G.11})$$

where $H_{t,r}$ is the average number of persons per household in each region.

2. All grid cells in a NUTS 3 region are ranked by distance from urban centres, where the highest ranked cells are the closest to any urban centre.
3. Surplus population S_t is calculated as

$$S_{t,r} = (U_{t-1,r} - U_{t,r}) H_{t,r} - U_{t,r} \quad (\text{G.12})$$

where $U_{t,r}$ is the urban population in the region according to the historical statistics database.

4. If S_t is positive, it means that the urban area in time step t was smaller relative to $t - 1$. Urban grid cells are removed starting with the lowest ranked, and their population is removed as well until the urban population in the region matches the desired value of $U_{t,r}$.
5. If S_t is negative, it means that the urban area in time step t was larger relative to $t - 1$. Land use in non-urban grid cells are replaced by CLC 112 class starting with the highest ranked. In each such grid cell, the population is increased to the threshold value of 64 persons (as defined in Table G.4, unless it is already higher than that. Urban areas are not allowed to sprawl into uninhabitable areas (Table G.4).

The important aspect influencing the result of this process is the “distance from urban centre”. Urban networks have several levels of hierarchy, with large agglomerations influencing population distributions far outside their borders. Therefore, the distance from urban centre is a weighted sum of three Euclidean distances from the following:

- Centres of large agglomerations, as presented in a shapefile data set from United Nations [26], which shows the arbitrary centres of cities with a population larger than 300 000.
- Centroids of population clusters. These clusters were calculated by Eurostat [338] from the 1 km population grid. The centroids were weighted, based on the population in each grid cell.
- Centroids of patches of urban fabric. The patches were taken from CORINE Land Cover 2012, and centroids were based on the geometry of those patches.

Equal weighting of the three layers was found to be optimal by analysing the accuracy of the chosen approach (see section G.5.2).

LAND USE CHANGES

fter urban fabric and population are redistributed, changes in area covered by other types of artificial surfaces, as well as reservoirs, are accounted for (see Table G.6). Then, evolution in cropland area is modelled using an approach similar to one utilized in HYDE database of historical land use and population [153]. It involves changing the allocation of croplands over time according to the land's suitability for agriculture. Therefore, if in time step t the cropland area was smaller than in time step $t - 1$, "cropland" grid cells are removed according to their ranking of suitability, starting with the lowest ranked cell (least suitable for croplands), until the value of cropland area in the historical statistics database is achieved. Conversely, if in time step t the cropland area was larger than in time step $t - 1$, "non-cropland" grid cells are changed to CLC class 211 (non-irrigated agricultural land) starting with the highest ranked cell.

The suitability is a sum of two indicators, which were also used in the HYDE database. The first indicator is the slope of the terrain, which is a serious limiter on agricultural activity, and which was calculated from EU-DEM data set at 100 m resolution [338]. A close exponential-type relationship between percentage of area used for croplands and slope was found. The second indicator is the crop suitability index for high-input cereals as calculated by FAO in the Global Agro-Ecological Zones (GAEZ) database [341, 382]. The resolution of this data set is 5 arc minutes¹. The index combines data on climate (1961–1990), soil, and terrain to estimate potential yield of various crops. Out of several crops tested, high-input cereals have highest (second-order polynomial) correlation with cropland fraction.

For the slope indicator, the upper bound was set at 0 % slope, while for the crop suitability index the upper bound was set at the polynomial function's maximum (approx. 1500). The suitability indicator for croplands I_c in a given grid cell is thus

$$I_c = \frac{0.5299e^{-0.063S}}{0.5299} + \frac{-1.6 \times 10^{-7}C^2 + 5.6 \times 10^{-4}C + 0.143}{0.6327} \quad (\text{G.13})$$

where S is the slope and C is the crop suitability index.

The main drawback of the method is that due to the relatively coarse resolution of the GAEZ data set, there are often many cells with the same rank, and the total area of croplands from the model does not exactly match the data in the historical statistics database. Therefore, when too many cells have the same rank, they are further ranked by the centroid distance (as for urban population), so that agricultural land with a given suitability class is the first added closest to urban areas, and is the first removed furthest away from urban areas.

Modelling the changes in pastures follows the same methodology as croplands, except that the crop suitability index for cereals was replaced by the same index for high-input alfalfa (also known as lucerne), a common crop growing in meadows and pastures. The suitability indicator for pastures I_p in a given grid cell is thus

$$I_p = \frac{0.1272e^{-0.047S}}{0.1272} + \frac{-6.9 \times 10^{-8}C^2 + 1.7 \times 10^{-4}C + 0.0293}{0.1356} \quad (\text{G.14})$$

¹Approximately 40 to 60 km² grid cells over Europe.

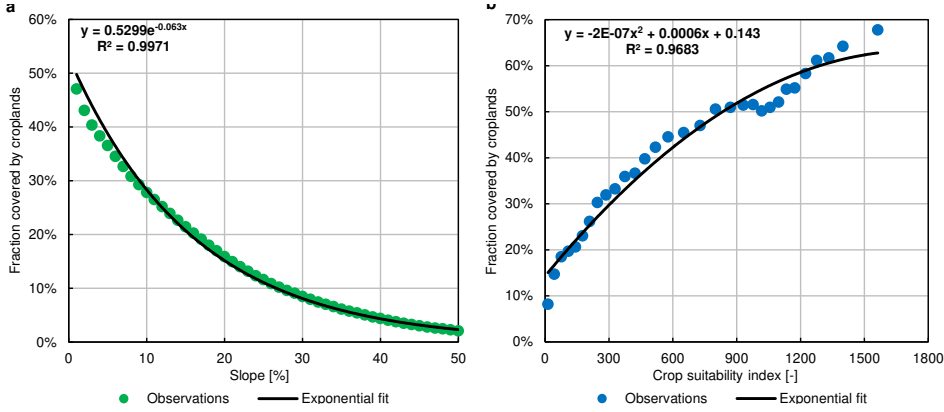


Figure G.9: Fraction covered by croplands compared with (a) slope and (b) crop suitability index for high-input cereals. Average fractions were calculated for slope divided into classes by rounding slopes to full percentages, and for crop suitability divided into 32 bins.

The functional relationships used for analysing agricultural land use changes are presented in Figs. G.9 and G.10. After modelling croplands and pastures, burnt areas are removed where necessary (see Table G.6) and unoccupied land is replaced by natural vegetation.

RURAL POPULATION

The final step is the redistribution of rural population. The procedure, similar to one employed for urban population, is as follows:

1. For a given time step t and region r , the difference between rural population $R_{t,r}$ in non-urban grid cells (after application of all previous procedures in a given time step) and the rural population according to the NUTS 3 database $N_{t,r}$ was calculated as

$$W_{t,r} = R_{t,r} - N_{t,r} \quad (\text{G.15})$$

2. If $W_{t,r} > 0$, the population of formerly urban grid cells u , which transitioned from urban to non-urban during the time step, was modified. Otherwise, this step was omitted. If the population of former urban grid cells was higher than the surplus, i.e. $\sum R_{t,r,u} > W_{t,r}$, the population number in all those cells was reduced by the same proportion, so that the rural population in the region would match the NUTS3 database:

$$R_{t,r,u} = R_{t,r,u} \frac{W_{t,r}}{\sum R_{t,r,u}} \quad (\text{G.16})$$

3. If $W_{t,r} < 0$, the population number in all those cells was reduced to zero, i.e. $R_{t,r,u} = 0$.
4. Then, the population in all non-urban grid cells was modified according to the

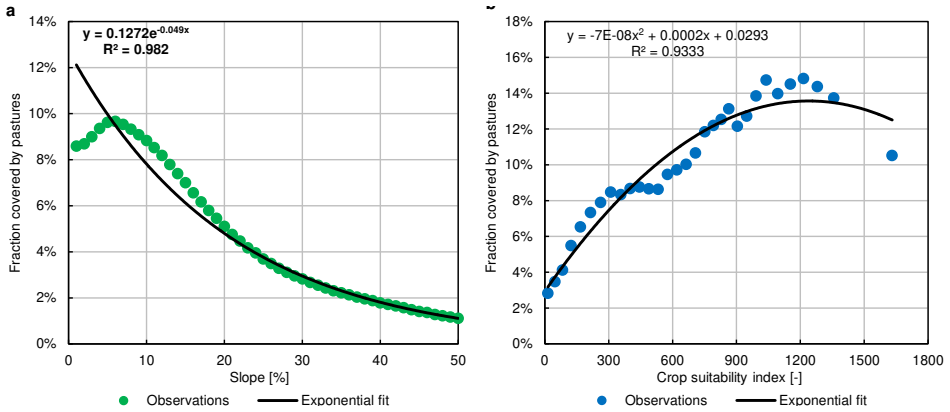


Figure G.10: Fraction covered by pastures compared with (a) slope and (b) crop suitability index for high-input alfalfa. Average fractions were calculated for slope divided into classes by rounding slopes to full percentages, and for crop suitability divided into 32 bins.

change in average household size, i.e.

$$R_{t,r} = R_{t-1,r} \frac{H_{t,r}}{H_{t-1,r}} \quad (\text{G.17})$$

where $R_{t,r}$ is the rural population in region r in time step t , and $H_{t,r}$ is the average household size.

5. In the case that the realized $R_{t,r}$ and expected $N_{t,r}$ numbers of rural population are still different, population is increased or reduced iteratively, one person at a time to/from an inhabitable, non-urban grid cell (CLC classes 211 to 324; see Table G.4), starting with those closest to the urban centre, until $R_{t,r} = N_{t,r}$.

G.4.5. STEP 4: DISAGGREGATED ECONOMIC DATA

Disaggregation of economic data provides estimates of GDP and wealth per grid cell, just like the population and land use data. It was carried out after historical gridded population and land use were obtained. The methodology presented here extends the approach proposed in the European Union's ESPON 2013 Programme [383] and some other studies, such as G-Econ project [322], in which the GDP is disaggregated proportionally to the population. This approach works well with a relatively coarse resolution of the output grid; however at 100 m resolution the economic variables are much less connected with the place of residence of the population. On the other hand, all economic activities still require labour input. Using the observation that employee's compensation constitutes approximately half of GDP in European countries [334], the GDP and wealth are disaggregated in equal proportion using population and land use.

Table G.7 provides a summary of the assumptions behind the disaggregation. Additional assumptions had to be made for the agricultural sector, which is the most dispersed, as almost three-quarters of the study area are covered by agricultural land use or forests. At the same time, farmland and pastures are more productive and contain

Table G.7: Disaggregation of economic variables by population and land use classes (CLC: CORINE Land Cover).

Variable	Category	Disaggregated according to the distribution of...	
		population	land use
GDP	agriculture excl. forestry	population in CLC211–244	CLC211–244
GDP	forestry	population in CLC311–313	CLC311–313
GDP	industry	total population	CLC121
GDP	services	total population	CLC111–121/133/141/142
Wealth	housing	total population	–
Wealth	agriculture excl. forestry	population in CLC211–244	CLC211–244
Wealth	forestry	population in CLC311–313	CLC311–313
Wealth	industry	total population	CLC121
Wealth	services	total population	CLC111–121/133/141/142
Wealth	infrastructure	–	CLC111/112/122–124

more assets than forests, especially since trees do not count as fixed assets. However, a breakdown of GDP by agriculture and forestry is not available at regional level, and very limited historical data exist with such detail on national level. Hence, agricultural GDP and wealth at the regional level were broken down to forestry (including logging) and remaining agriculture (including fishing and aquaculture) using the sectoral split at national level in 2011 from Eurostat [334]. The share of forestry in the agricultural sector varies from zero in Malta to 73 % in Sweden.

Half of the GDP generated by agriculture (excluding forestry), as well as half of the wealth in this sector is distributed proportionally to the population living in agricultural areas. The other half was distributed equally among CLC classes 211–244 (“agricultural areas”). GDP and wealth in forestry was distributed the same way, but by using CLC classes 311–313 (“forests”). Half of the GDP and half of the wealth in industry and services were distributed proportionally to the population in all grid cells, while the other halves were distributed equally among specific land use classes where a given production is concentrated, as in Table G.7.

For the remaining two classes of wealth, the approach was slightly different. The entire wealth in housing (dwellings) was distributed proportionally to the population in all grid cells. The entire value of infrastructure, on the other hand, was distributed equally over selected land use classes: urban fabric, airports, ports, roads, and railway sites (CLC 111, 112 and 122–124).

G.5. QUALITY ASSESSMENT OF HANZE

The accuracy of the data involved in HANZE database is influenced by three elements: (1) quality of baseline maps and historical statistics; (2) robustness of the methodologies used for disaggregation of data and modelling change in population and land use; and (3) completeness and reliability of the records of past damaging floods.

G.5.1. ACCURACY OF BASELINE MAPS

The baseline land cover/use map, CORINE Land Cover 2012, was employed for this analysis before final validation was made, but subsequently the map was found to have the-

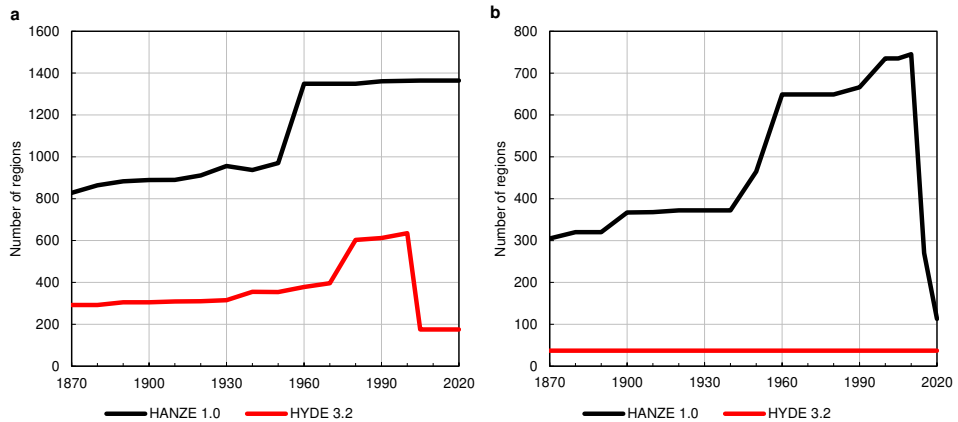


Figure G.11: Comparison of the number of regional-level population estimates used in HANZE and HYDE 3.2 [384] databases, for (a) total population and (b) urban fraction.

matic accuracy of around 90 % [337]. Still, the use of thresholds of minimum size (25 ha) and width (100 m) of objects necessary for inclusion in the map result in many small objects with large effects on population distribution to be omitted, e.g. small bodies of water or smaller pieces of infrastructure and villages. It should also be noted that mapping was done by country independently, and therefore the classification of land use is not always fully consistent between countries, and the thematic accuracy varied from 82 to 97 % between countries. Validation reports are also available for imperviousness layers and elevation models from Copernicus Land Monitoring Service [337].

The baseline GEOSTAT population grid's accuracy is described in reports available from the data provider [338]. Though for most countries the quality of the 1 km grid is very high, with 98–100 % of the national populations georeferenced, there are exceptions. In Bulgaria, for example, only 57 % of the population was georeferenced and the remainder was disaggregated from settlements or local administrative units. In Italy the entire data set was calculated from enumeration areas, albeit their average size was below 1 km². For some smaller countries, the population distribution was calculated by the European Commission – Joint Research Centre using land use data. Basic information on GEOSTAT accuracy per country has been included in the HANZE database.

Historical statistics were compiled from a large variety of sources. Total population figures were mostly available at regional level, while the remaining statistics were usually available only at national level beyond the most recent 2–3 decades. Inevitably, there are inaccuracies from applying national trends at the regional level. Also, economic data series before approx. 1950 for western Europe and 1990 for central Europe are more often than not reconstructions based on ancillary or proxy data. Notwithstanding those limitations, the HANZE database represents an improvement in resolution and thematic coverage over the HYDE database for the study area. A comparison in the number of regional estimates of total and urban population included in both databases is shown in Fig. G.11.

G.5.2. VALIDATION OF LAND USE AND POPULATION GRIDS

In this study, the population distribution was disaggregated from 1 km to 100 m using two methods validated previously in literature [339]. Lack of comparative data at such resolution prevents us from further analysing the quality of the disaggregation. Still, the original resolution is very fine and the refining narrows the distribution of population by eliminating areas that are uninhabitable or very unlikely to be inhabited. There is no comparative information for economic variables downscaled from regional level to gridded data.

Lack of comparable data for validation is also evident for historical land use changes. Some reconstructions of past land cover/use were made from old maps [324, 325], but there is limited consistency in classification or minimal mapping units to allow for an accurate comparison. CORINE Land Cover is available for 2000 and 2006, but often indicated changes in land use are only reclassifications rather than actual developments. Hence, changes in historical croplands and pasture distribution were not validated directly. The general methodology used here, i.e. reallocating croplands and pastures based on land suitability for agriculture, has been extensively utilized in many studies before [385–389]. A more detailed uncertainty and sensitivity analysis of the input data and methods would be possible using structured expert judgment [390, 391].

Some analysis, however, could be made on the historical distribution on urban population. Estimates with the Clark [392] model of urban population density are available for 19 cities, which consider population distribution in urban areas as an exponential function:

$$y = Ae^{-bx} \quad (\text{G.18})$$

where y is the population density (in persons per km²), x is the distance from the city centre (in kilometres), and A and b are exponential function coefficients. A total of 42 estimates of this equation spanning a whole century, from 1871 to 1971 were collected, of which a complete list can be found in Table G.8. In the population map constructed herein, the population density was calculated for 500 m wide zones around (arbitrarily chosen) city centres, interpolated to match the time points from literature, and then fitted to an exponential function.

A comparison of function parameters is presented in Fig. G.12. Overall, a good fit was achieved for the b parameter, but only a relatively poor one for the parameter A . For cities where more than 1 year of data was available, a decline of both parameters over time was observed, as in the literature case studies. A better match of modelled and observed estimates of eq. G.18 parameters would be difficult, since the exponential curve fits are very sensitive to the sample size (distance from the city centre) and the source material: literature studies used census wards of different sizes instead of a disaggregated population grid used here.

Further validation of historical population grid was done by using Eurostat-produced estimates of population at local administrative unit (LAU). This data set [365]) is provided at LAU level 2, except Denmark, Lithuania, Portugal, and Slovenia, where coarser LAU level 1 data are available; data for microstates, except Liechtenstein, are missing. Population is provided at census dates or interpolated/extrapolated to six reference dates (1 January every decade from 1961 to 2011). Data at census dates were extensively used in HANZE database by aggregating them to NUTS3 regions. Here, LAUs in the Eurostat

Table G.8: Estimates of urban population density. A , b – exponential function parameters. D – maximum distance from the city centre [km], for which population data were used to calculate exponential function parameters (values marked with an asterisk * are estimates, as the source does not specify the distance).

Name	Region	Year	A	b	D	Source
Aarhus	DK042	1950	279	0.96	*8	Clark [381]
Berlin	DE300	1885	1120	0.68	8	Clark [381, 392]
Berlin	DE300	1900	1580	0.59	10	Clark [381, 392]
Birmingham	UKG31	1921	401	0.50	*10	Clark [381]
Birmingham	UKG31	1938	201	0.29	*12	Clark [381]
Budapest	HU101	1935	1080	0.56	5	Clark [381, 392]
Copenhagen	DK011	1940	231	0.37	*10	Clark [381]
Cork	IE025	1926	199	1.02	3	Hourihan [393]
Cork	IE025	1936	177	0.88	3	Hourihan [393]
Cork	IE025	1951	176	0.91	4	Hourihan [393]
Cork	IE025	1961	114	0.70	4	Hourihan [393]
Cork	IE025	1971	158	0.62	4	Hourihan [393]
Dublin	IE021	1901	391	0.68	4	Hourihan [393]
Dublin	IE021	1911	379	0.65	4	Hourihan [393]
Dublin	IE021	1926	352	0.59	4	Hourihan [393]
Dublin	IE021	1951	106	0.25	8	Hourihan [393]
Dublin	IE021	1961	105	0.21	8	Hourihan [393]
Dublin	IE021	1971	113	0.17	8	Hourihan [393]
Dublin	IE021	1936	270	0.53	6	Clark [381, 392]
Frankfurt am Main	DE712	1890	550	1.16	*5	Clark [381]
Frankfurt am Main	DE712	1933	340	0.57	*7	Clark [381]
Leeds	UKE42	1951	116	0.31	*10	Clark [381]
Limerick	IE023	1961	136	1.09	3	Hourihan [393]
Limerick	IE023	1971	126	0.88	3	Hourihan [393]
Liverpool	UKD72	1921	1275	0.50	9	Clark [381, 392]
London	UKI11	1871	865	0.38	17	Clark [381]
London	UKI11	1901	660	0.23	20	Clark [381]
London	UKI11	1921	443	0.17	25	Clark [381]
London	UKI11	1931	475	0.17	*26	Clark [381]
London	UKI11	1939	320	0.14	*28	Clark [381]
London	UKI11	1951	240	0.12	29	Clark [381]
London	UKI11	1961	205	0.09	33	Clark [381]
Manchester	UKD31	1931	155	0.16	18	Clark [392]
Manchester	UKD31	1939	143	0.18	*20	Clark [381]
Oslo	NO011	1938	308	0.50	4	Clark [381, 392]
Paris	FR101	1896	1430	0.50	12	Clark [381, 392]
Paris	FR101	1931	1820	0.47	14	Clark [381, 392]
Paris	FR101	1946	695	0.21	*16	Clark [381]
Stockholm	SE110	1880	610	1.30	*5	Clark [381]
Stockholm	SE110	1940	425	0.48	*8	Clark [381]
Vienna	AT130	1890	660	0.50	7	Clark [381, 392]
Zurich	CH040	1936	328	0.29	*10	Clark [381]

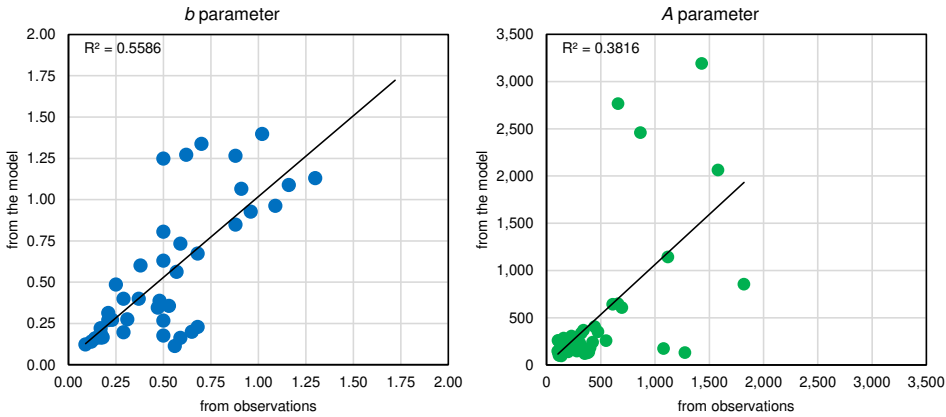


Figure G.12: Estimates of A and b parameters (eq. G.18) from modelled and observed population data.

dataset were connected with a vector map from Eurostat [338]. For Greece, only LAU level 1 map was available; therefore population estimates were aggregated accordingly. Administrative changes were accounted for to synchronize the population data set and the map, though a small number of LAUs for Ireland and the United Kingdom could not be matched between the data sets (as a result validation was not possible for region UKK14). The final map has 109 177 units, which was then intersected with population grids for 1960, 1970, 1980, 1990, 2000, and 2010. Then, for each LAU two measures commonly used for flood map validation (as in chapters 3 and 4) were employed. Test for “correctness” (or “hit rate” I_{cor}) indicates what percentage of the reference unit population is recreated in the HANZE map:

$$I_{\text{cor}} = \frac{P_{\text{HM}} \cap P_{\text{RM}}}{P_{\text{RM}}} \cdot 100 \quad (\text{G.19})$$

where P_{HM} is the population in the HANZE map and P_{RM} is the population estimate in the reference map. However, this test does not penalize overestimation; therefore another measure for “fit” (or “critical success index” I_{fit}) is applied:

$$I_{\text{fit}} = \frac{P_{\text{HM}} \cap P_{\text{RM}}}{P_{\text{HM}} \cup P_{\text{RM}}} \cdot 100 \quad (\text{G.20})$$

The scores for each NUTS3 region (simple average of LAUs in a given region) can be found online in the Supplementary File 2 of the paper describing HANZE database [282]. A simple average of scores for all LAUs is shown in Table G.9. The results for 2010 map, which is almost identical to the baseline map, are not 100 % due to relatively low geometrical accuracy of LAU map, use of interpolation in Eurostat data set as opposed to data for the exact year used to produce the population grid, and some missing data at LAU level. Scores for both measures decline over time, and they also vary greatly among countries. It should be noted that population dynamics at the LAU level is significant, as an average LAU changed its population by 91 % between 1960 and 2010 (median change was 36 %), with a decline recorded in 48 % of LAUs

Table G.9: Scores in two measures of accuracy of gridded population estimates (simple average for all LAUs).

Measure	1960	1970	1980	1990	2000	2010
Correctness	88 %	88 %	88 %	90 %	93 %	97 %
Fit	43 %	49 %	57 %	66 %	76 %	93 %

G.5.3. QUALITY OF FLOOD EVENT DATA

The quality of records of past floods depends on two main factors: (1) completeness (what share of past floods could be traced) and (2) the reliability of information on the location and quantitative data on losses. Completeness varies substantially between countries, few of which maintain publicly available databases of flood losses. Historical information contained in mandatory preliminary flood risk assessments was sometimes very extensive, but often little or no quantitative information on losses was included. International databases of events have short timespan: EM-DAT nominally starts with year 1900, but very few floods are included before 1970. NatCatService and EEA's compilation of Floods Directive data have coverage from 1980 and Dartmouth Flood Observatory from 1985. Due to the development of Internet, availability of news reports on floods increased substantially starting with mid-1990s, though an increasing number of old newspaper articles are digitized and provide a valuable resource. Under-reporting for central European countries before 1990 is also evident, due to communist-era censorship.

The reliability of past flood loss data remains an open question. Efforts were made to gather multiple sources for past events, especially large ones. In the vast majority of cases, records of floods from international databases can be corroborated by other sources or at least by other international databases. Some records were found to be either dubious or were not primarily flood events, but rather landslides, as uncovered by a detailed study for Portugal by Zêzere *et al.* [394]. The most extreme case is a record in EM-DAT, according to which a flood along the Danube in Romania in 1926 caused 1000 deaths. However, the Romanian preliminary flood risk assessment indicates that national literature sources do not contain any mention of flood fatalities in that year [395]. A calamity of such magnitude, which would have been the deadliest European flood in the past 150 years, must have left a trace in several sources. Therefore, this event was not included in HANZE. Also, there are some cases of floods occurring with other hazards (windstorms, hail, landslides), where it was not possible to disentangle flood losses from those from other causes. Therefore some flood records include or might include those other losses, which are marked in the database under "Notes" category. On the other hand, some flash floods were not included if the majority of losses were not caused by floodwater.

H

SUPPLEMENTARY INFORMATION ON TRENDS IN FLOOD EXPOSURE AND LOSSES

This appendix contains additional maps, graphs and tables related to historical trends in flood exposure and losses, supporting the analysis in chapter 6.

This appendix has been included as a supplement to the paper published in *Nature Communications* 9, 1985 (2018) [281].

Table H.1: Reported losses, exposure in the potential flood zone of the event, relative and normalized losses for the 1953 coastal flood in the Netherlands. [section 6.2.4]

Pair of variables	Spearman's rank correlation	Best-fitting copula type
Area inundated & Fatalities	0.352	Frank
Area inundated & Persons affected	0.527	Clayton
Area inundated & Losses (norm. by GDP)	0.431	Clayton
Area inundated & Losses (norm. by wealth)	0.376	Clayton
Fatalities & Persons affected	0.272	Normal
Fatalities & Losses (norm. by GDP)	0.469	Gumbel
Fatalities & Losses (norm. by wealth)	0.473	Gumbel
Persons affected & Losses (norm. by GDP)	0.667	Frank
Persons affected & Losses (norm. by wealth)	0.677	Frank

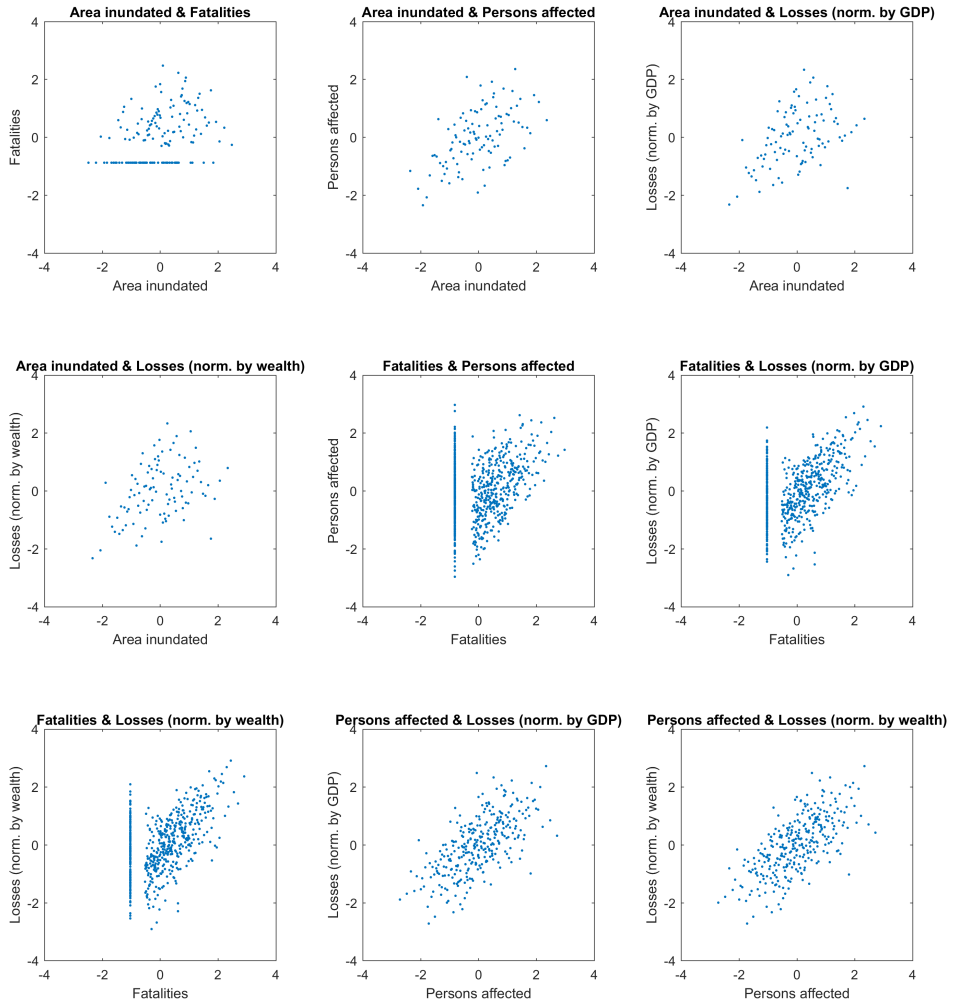


Figure H.1: Dependency between pairs of variables (normalized damage statistics relative to potential exposure per flood footprint) transformed to standard normal. [section 6.2.4]

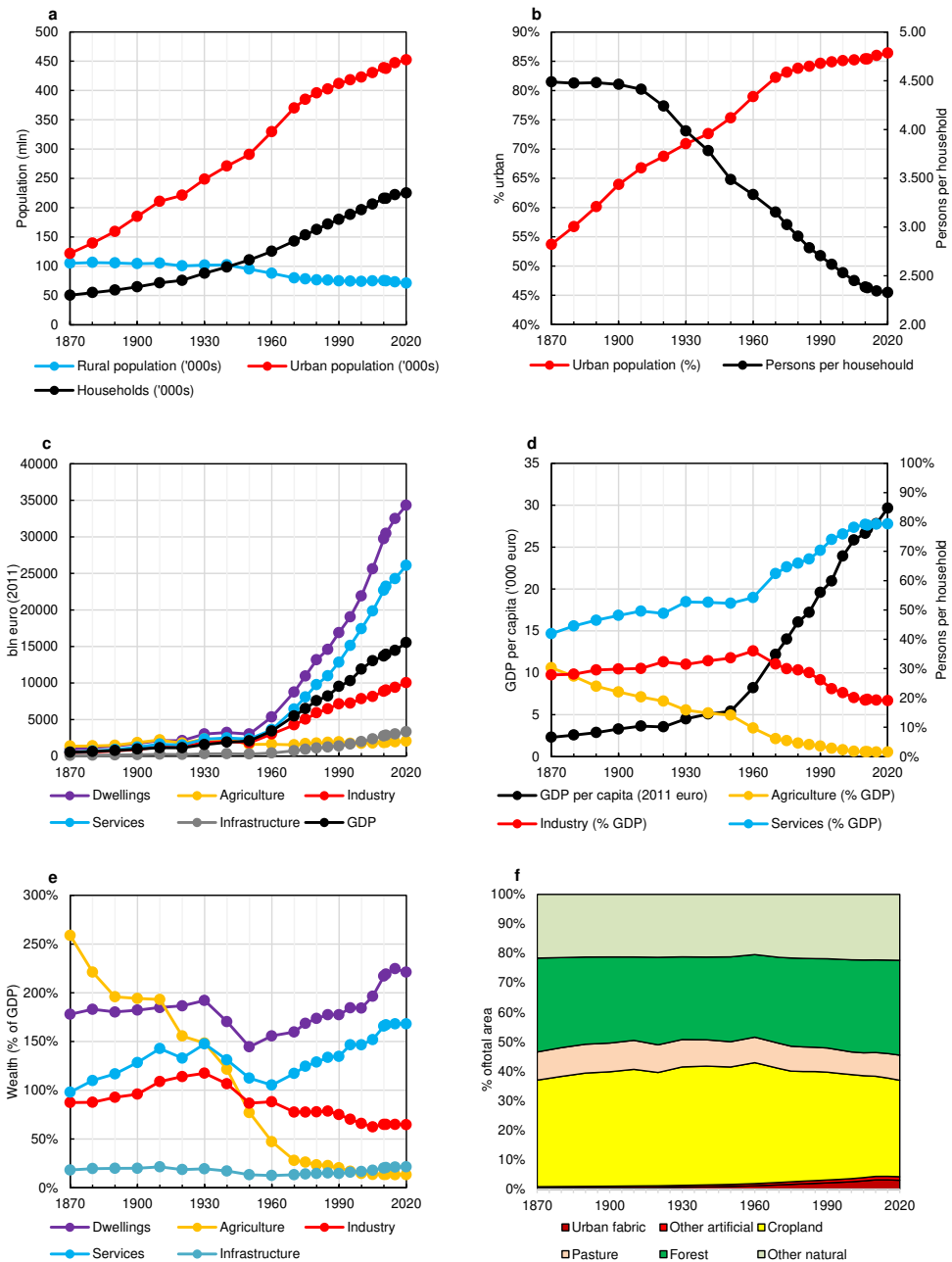


Figure H.2: Temporal trends for selected socio-economic variables, 1870–2020: (a-b) population and households; (c) wealth by sector and GDP; (d) GDP structure; (e) wealth by sector relative to GDP; (f) Land use. Graphs include short-term projections through 2020. Aggregated for 37 European countries and territories. [section 6.3.1]

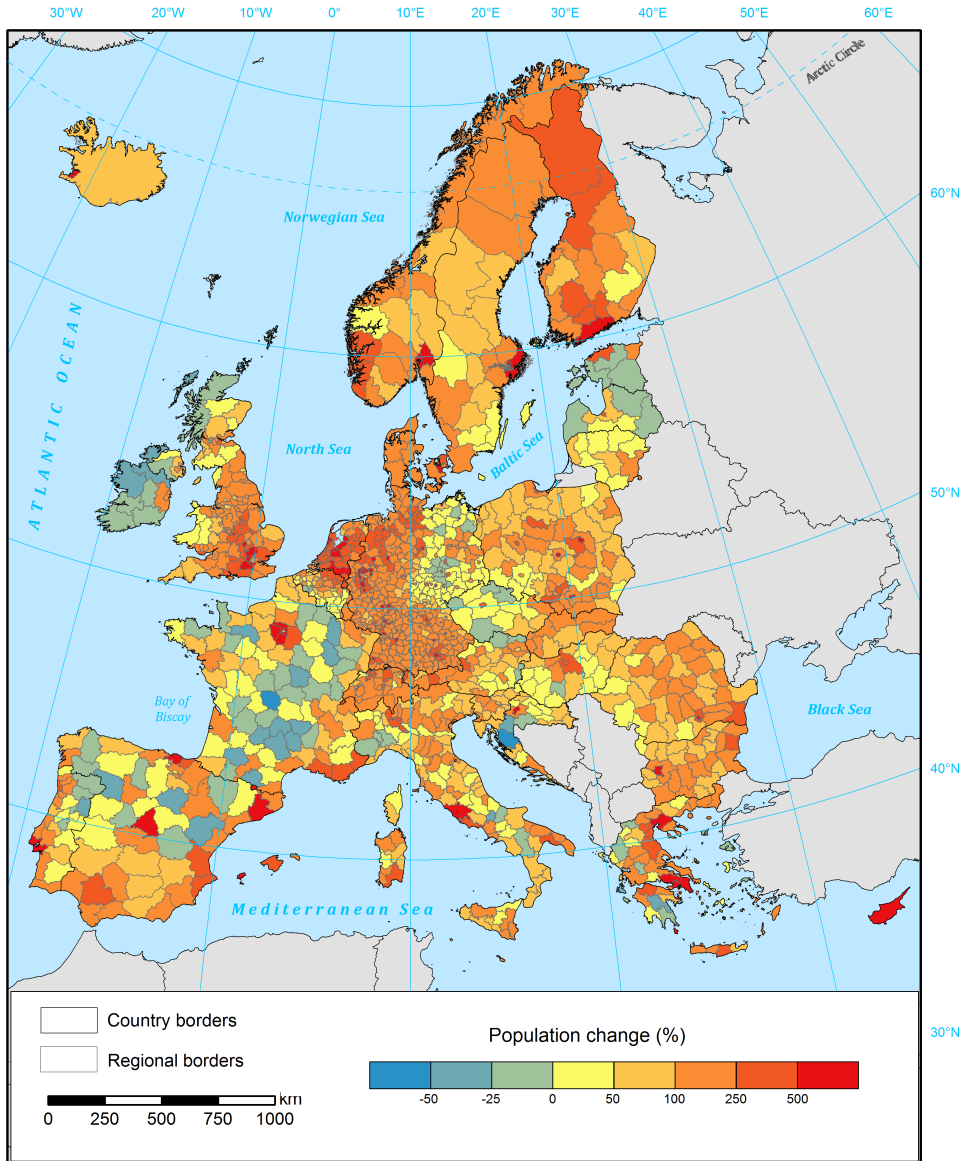


Figure H.3: Population change (%) by NUTS 3 regions from 1870 to 2015. [section 6.3.1]

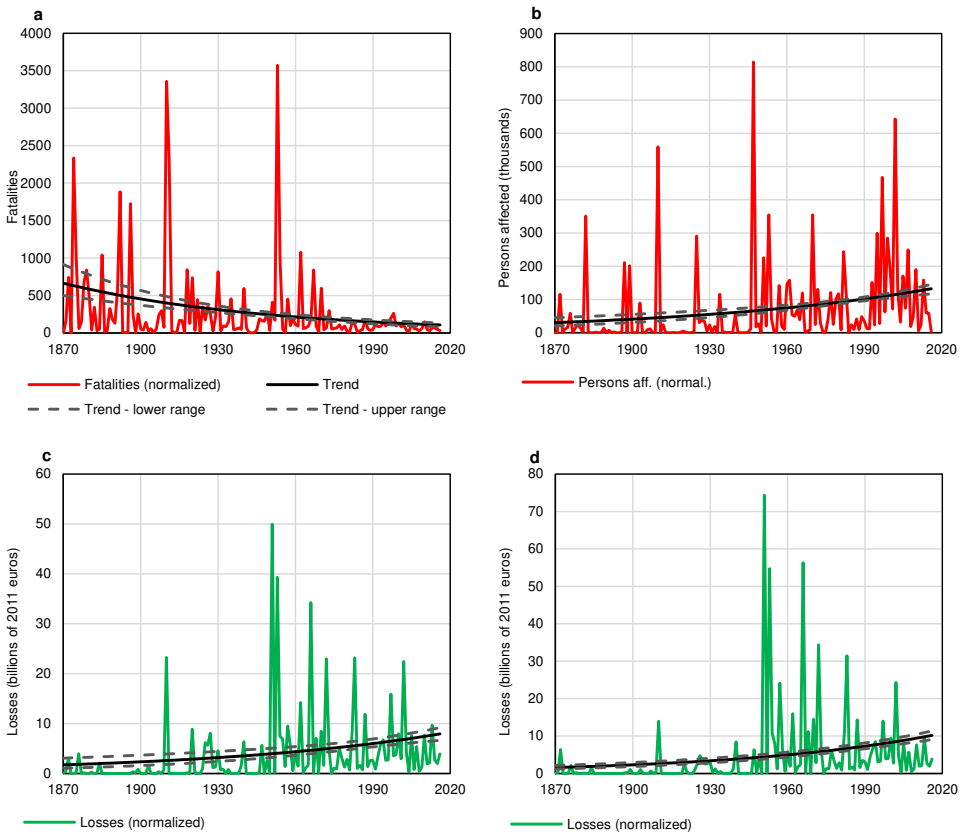


Figure H.4: Trends in normalized flood losses with 95% confidence intervals, for (a) fatalities; (b) persons affected; (c) financial value of losses with normalization by GDP and (d) financial value of losses with normalization by wealth. [section 6.3.3]

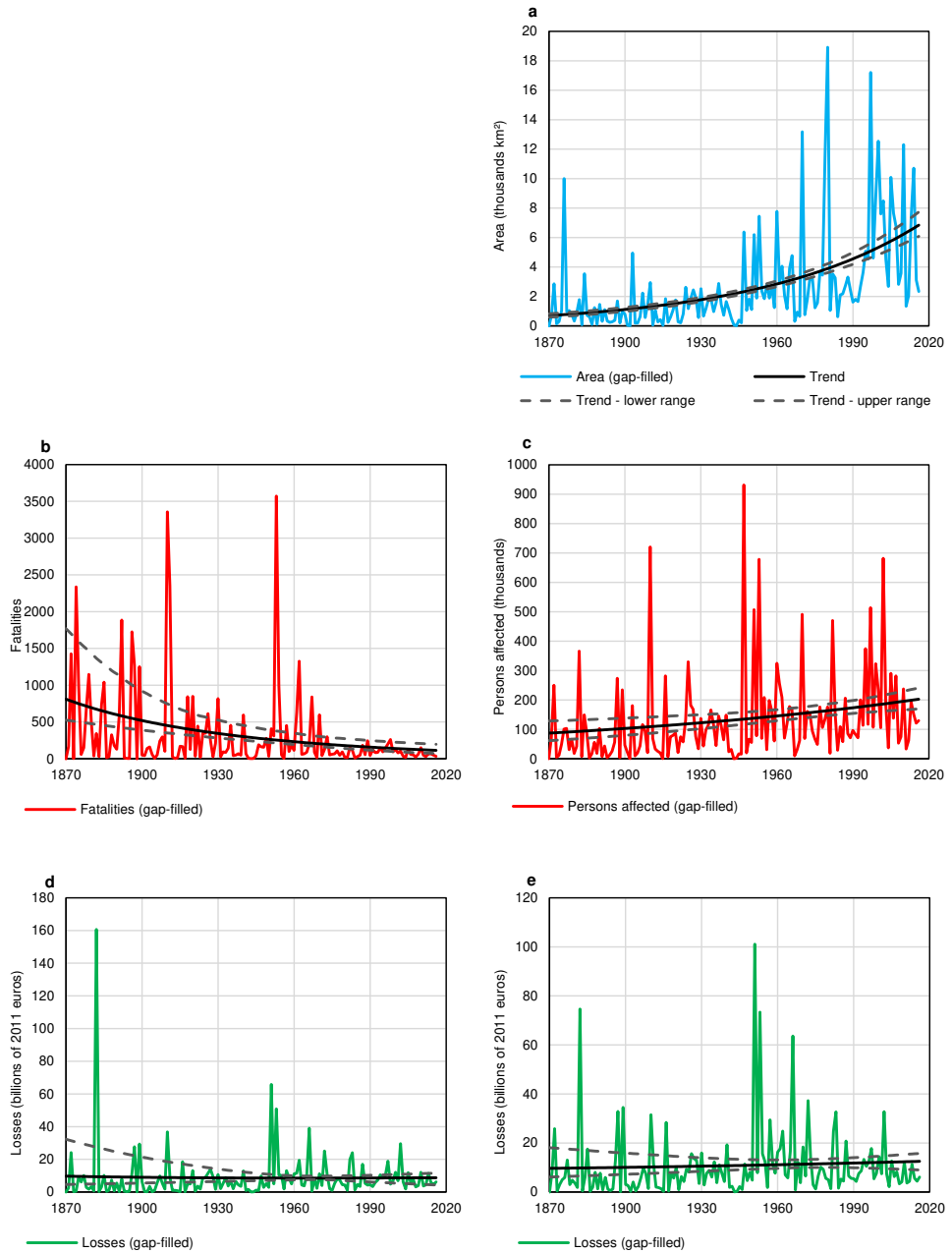


Figure H.5: Trends in normalized and gap-filled flood losses with 95% confidence intervals, for (a) area inundated; (b) fatalities; (c) persons affected; (d) financial value of losses with normalization by GDP and (e) financial value of losses with normalization by wealth. [section 6.3.3]

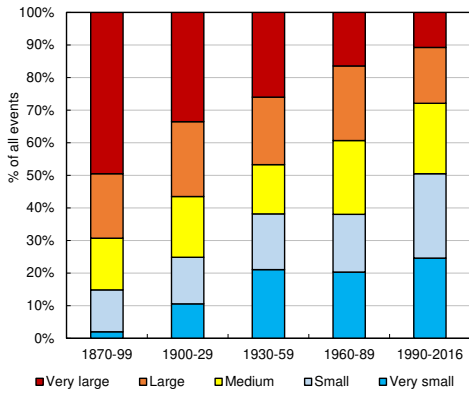


Figure H.6: Flood events classified by severity per time period. [section 6.2.4]

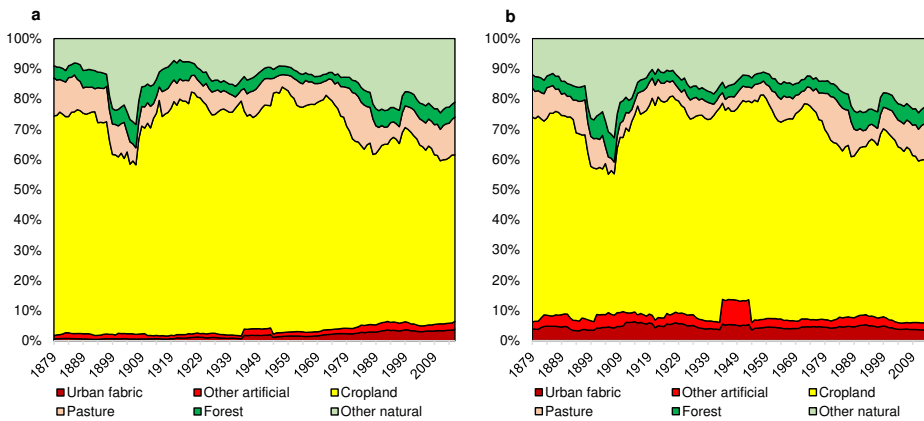


Figure H.7: Annual land use structure of flood footprints. Graphs are for 10-year moving average (ending on the year indicated), (a) with reconstructed land use at the time of flood events and (b) using 2011 land use.

Table H.2: Trends in losses in different aggregations. Data are for reported, normalized and gap-filled annual losses during five periods in the historical record. [section 6.3.5]

(a) Mediterranean countries (Cyprus, Greece, Italy, Malta, Portugal, Spain)

Start year	Reported					Normalized				Normalized and gap-filled				
	Events	Area	Fata-lities	Affe-cted	Losses	Fata-lities	Affe-cted	Losses (1)	Losses (2)	Area	Fata-lities	Affe-cted	Losses (1)	Losses (2)
1870	*1.2	*1.6	-0.5	*1.6	*2.3	*-1.5	*1.2	1.1	1.2	*1.2	*-1.5	0.3	0.3	0.6
1900	*0.8	*2.6	-0.1	*1.6	*1.9	*-2.2	*1.3	0.7	0.8	*1.0	*-2.0	-0.1	-0.1	0.2
1930	0.2	1.9	-1.0	0.6	0.9	-2.3	0.1	-1.0	-0.8	0.5	*-2.1	-1.2	*-1.3	-0.8
1950	*-0.6	1.4	*-3.1	-1.5	-1.1	*-4.5	-2.2	*-4.7	-4.3	-0.3	*-4.7	*-2.7	*-3.8	*-2.9
1970	0.3	6.8	-2.2	-1.7	-3.1	-2.4	-2.5	-6.0	-5.3	1.1	-2.7	-1.7	-2.6	-1.7

(1) normalized by wealth, (2) normalized by GDP; * significant at $\alpha = 0.05$.**(b) Non-Mediterranean countries (other than above)**

Start year	Reported					Normalized				Normalized and gap-filled				
	Events	Area	Fata-lities	Affe-cted	Losses	Fata-lities	Affe-cted	Losses (1)	Losses (2)	Area	Fata-lities	Affe-cted	Losses (1)	Losses (2)
1870	*2.1	*1.4	-0.2	*2.1	*3.7	-0.7	*1.0	*1.5	0.9	*1.8	-0.9	*0.8	0.2	-0.3
1900	*2.5	*2.0	0.6	*2.1	*3.6	0.1	1.1	*1.2	0.4	*2.3	0.0	*0.9	0.6	0.4
1930	*3.0	1.6	-0.8	*2.1	*3.7	-1.5	1.4	0.9	0.8	*2.6	-1.5	*1.3	0.8	1.0
1950	*3.0	0.5	*-3.5	*2.6	*3.2	*-5.0	2.1	-0.5	-0.1	*2.2	-5.0	1.3	-0.3	0.3
1970	*2.5	-2.0	-1.4	2.0	*4.0	-1.6	1.8	1.7	2.3	1.0	-1.6	1.0	0.9	1.5

(1) normalized by wealth, (2) normalized by GDP; * significant at $\alpha = 0.05$.**(c) Flash floods**

Start year	Reported					Normalized				Normalized and gap-filled				
	Events	Area	Fata-lities	Affe-cted	Losses	Fata-lities	Affe-cted	Losses (1)	Losses (2)	Area	Fata-lities	Affe-cted	Losses (1)	Losses (2)
1870	*1.4	*2.9	-0.7	*2.2	*3.1	*-1.6	*1.7	1.5	1.5	*1.5	*-1.5	0.6	0.4	*0.6
1900	*1.3	2.7	0.2	*2.5	*2.9	*-2.1	*2.0	1.3	1.1	*1.5	*-1.8	0.2	0.0	0.2
1930	*0.9	2.3	-0.5	1.8	*2.3	-1.9	1.2	0.2	0.3	*1.4	-1.8	-0.5	-0.8	-0.2
1950	*0.6	2.2	-2.2	0.6	1.2	-3.2	0.2	-1.3	-0.9	*1.6	*-3.5	-0.9	-1.4	-0.7
1970	*0.9	2.8	-1.7	-0.8	-0.8	-2.1	-1.3	-3.0	-2.3	*2.0	-2.5	-0.8	-1.5	-0.8

(1) normalized by wealth, (2) normalized by GDP; * significant at $\alpha = 0.05$.**(d) River floods**

Start year	Reported					Normalized				Normalized and gap-filled				
	Events	Area	Fata-lities	Affe-cted	Losses	Fata-lities	Affe-cted	Losses (1)	Losses (2)	Area	Fata-lities	Affe-cted	Losses (1)	Losses (2)
1870	*1.7	*1.4	0.0	*2.0	*3.5	-0.8	*0.9	*1.3	0.9	*1.7	-1.0	*0.7	0.1	-0.3
1900	*1.9	*2.1	0.7	*2.1	*3.4	-0.3	1.1	1.0	0.5	*2.1	-0.4	0.8	0.6	0.6
1930	*1.9	1.7	0.1	*2.0	*3.4	-0.8	1.3	0.2	0.5	*2.0	-0.8	0.9	-0.1	0.5
1950	*1.6	0.8	-0.4	2.2	*2.7	-1.9	1.7	-2.0	-1.2	*1.5	-2.0	0.7	-2.3	*-1.1
1970	*2.1	-1.7	-2.1	1.7	2.3	-2.0	1.4	-1.1	0.0	0.8	-2.0	0.8	-0.9	0.2

(1) normalized by wealth, (2) normalized by GDP; * significant at $\alpha = 0.05$.**(e) River, coastal and compound floods**

Start year	Reported					Normalized				Normalized and gap-filled				
	Events	Area	Fata-lities	Affe-cted	Losses	Fata-lities	Affe-cted	Losses (1)	Losses (2)	Area	Fata-lities	Affe-cted	Losses (1)	Losses (2)
1870	*1.7	*1.4	0.1	*1.9	*3.0	-0.5	*0.9	*1.2	0.9	*1.6	-0.7	0.6	0.1	-0.2
1900	*1.8	2.0	0.3	*1.9	2.8	-0.4	1.0	0.8	0.4	*1.9	-0.4	0.6	0.3	0.3
1930	*1.8	1.6	-1.2	*1.7	2.4	-1.9	1.0	-0.4	-0.1	*1.8	-1.9	0.7	-0.5	0.0
1950	*1.4	0.6	*-4.5	1.6	1.3	*-6.4	0.9	-3.3	-2.6	1.2	*-6.4	0.0	*-3.3	*-2.2
1970	*2.1	-1.6	-1.8	1.6	2.4	-1.7	1.3	-1.0	0.1	0.7	-1.7	0.7	-1.0	0.0

(1) normalized by wealth, (2) normalized by GDP; * significant at $\alpha = 0.05$.**(f) Flash floods (under assumption of flood footprints equalling whole area of affected regions)**

Start year	Normalized			
	Fata-lities	Affe-cted	Losses (1)	Losses (2)
1870	*-1.9	*1.3	1.4	1.5
1900	-0.3	*2.0	1.4	1.2
1930	-1.0	1.3	0.3	0.3
1950	-3.0	0.0	-1.4	-1.1
1970	-2.5	-1.5	-3.5	-2.8

(1) normalized by wealth, (2) normalized by GDP; * significant at $\alpha = 0.05$.

Table H.3: Largest flood events in Europe, 1870–2016, according to HANZE database, in chronological order. The events are those which were among top 10 in any of the five variables (normalized losses except area inundated). Losses in mln euros in 2011 prices, inundated area in km². Notes: (1) normalized by GDP, (2) normalized by wealth.

Year	Country name	Type	Flood source	Cause	Reported losses			Normalized losses		
					Area inundated	Fatalities	Persons affected	Losses	Fatalities	Persons affected
1874	Spain	Flash River	Ondara, Sio, Corb Szamos, Tisza, Danube	Extreme rainfall	575	2800	2336	11 373		
1876	Hungary	Flash	Guadalentin, Mundo, Segura	Snowmelt	7667	29 000	68	42 50 744	906	1839
1879	Spain	Flash		Extreme rainfall up to 600 mm in 1 h	777	23 000	839	24 829		
1882	Germany	River	Rhein, Neckar, Mosel, Main	Heavy rainfall and snowmelt	1100	48 70 000	219	319 633		
1885	Italy	River	Po, Tanaro	Heavy rainfall	306		864			
1892	Italy	Flash	Mannu, Flumineddu	Extreme rainfall	203		1367			
1896	Greece	Flash	Kifissos, Ilissos, Kyklovorou	Extreme rainfall	62		1706			
1903	Poland	River	Wisla, Skawa, Kamienna, Sola, Skawa, Raba, Dunajec	Heavy rainfall 7-11 July up to 128 mm/day	3000	60 000	36	0	89 299	816 535
1910	France	River	Seine	Heavy rainfall and snowmelt, several waves	16	200 000	1462	45	558 935	20 425 11 806
1910	Italy	Flash		Extreme rainfall	200		3302			
1911	Italy	Flash		Extreme rainfall	40		2345			
1918	Italy	Flash		Extreme rainfall	13		841			
1920	Germany	River	Danube, Salzach	Heavy rainfall	740	112 000	396	289 719	6181	8750 2504
1925	Germany	River	Rhine, Mosel	Heavy rainfall and snowmelt			415			2595
1947	United Kingdom	River	Thames, Trent, Severn, Ouse	Snowmelt	2760	400 000	419	0	561 142	1924 2984
1951	Italy	River	Po, Adige	Heavy rainfall throughout the month	1080	123 170 000	7857	139	192 255	41 914 64 681
1953	Netherlands	Coastal	North Sea	Storm surge up to 3 m	2000	188 000	4824	2930	300 145	26 886 35 488
1954	Italy	Flash	Bonea, Cavatola	Extreme rainfall up to 320 mm in 6 h	322	5750	802	928	16 571	5549 9176
1957	Spain	River	Turia	Heavy rainfall up to 400 mm in 48 h	86	23 200	1110	417	112 525	8019 21 793
1960	Poland	River	Wisla, Sola, Dunajec, Wisloka, San, Odra	Heavy rainfall up to 203 mm in 9 days	3527	5 108 000	263	6	132 457	1155 1392

Table H.4: Largest flood events in Europe (continued).

Year	Country name	Type	Flood source	Cause	Reported losses			Normalized losses				
					Area inundated	Fatalities	Persons affected	Fatalities affected	Persons affected	Losses (1)	Losses (2)	
1962	Germany	Coastal	North Sea	Storm surge	120	315	20 000	4932	271	17 201	11 369	11 686
1966	Italy	Compound	Arno, Stave, Adige, Adriatic Sea	Extreme rainfall up to 344.5 mm in 24 h; Acqua alta (194 cm) in Venice	118	78 000	11 863	135	89 251	31 953	52 785	
1968	Italy	Flash	Cervo, Elvo, Strona di Mosso, Tanaro, Gromolo	Extreme rainfall up to 395 mm in 24 h	484	76	4000	3422	79	4176	6856	10990
1970	Romania	River	Mures, Tisza, Somes, Siret	Extreme snowmelt	2,445	300	238 755	1472	272	216 304	4116	7236
1972	Italy	River		Heavy rainfall up to 1500 mm in 2 weeks		20	64 000	8169	35	113 018	21 902	33 129
1974	Croatia	River	Sava, Kupa, Krapiha, Una	Heavy rainfall	2700	0			0			
1979	Poland	River	Narew, Bug, Wisla, Noteć, Ina, Rega, Warta	Snowmelt and ice jam	10 000	3	71 000	501	3	77 284	1024	1026
1980	Poland	River	San, Wisłok, Odra, Wisła, Noteć, Wieprz, Bóbr	Heavy rainfall spread over June and July	17 450	1	104 000	1398	1	116 664	2553	2536
1983	Spain	Flash	Nervión	Extreme rainfall up to 503 mm in 24 h		45	106 000	11 521	43	101 893	19 119	26 608
1995	Netherlands	River	Meuse, Rhine	Heavy rainfall and snowmelt	153	1	200 000	103	1	223 381	136	137
1997	Poland	River	Odra, Nysa Kłodzka	Heavy rainfall (2 events), up to more than 500 mm in a month	6,658	56	224 500	4951	59	237 046	8813	7025
1999	Hungary	River	Tisza	Heavy rainfall and snowmelt	3,600	2	90 700	261	2	84 280	289	267
2002	Czech Rep.	River	Vltava, Blanice, Mabe, Uhlava, Labě, Sazava	Heavy rainfall (2 waves), daily precipitation up to 160 mm	17	17	225 000	3377	17	231 365	4210	4062
2002	Germany	River	Elbe, Danube, Mulde	Heavy rainfall (2 waves), daily precipitation up to 160 mm	27	27	330 000	9952	25	309 130	10 809	11 626
2010	Poland	River	Wisła	Heavy rainfall	5540	25	100 000	2330	25	101 044	2439	2415



DATA AVAILABILITY

The datasets that were produced during the research described in this thesis were made, to the extent feasible, publicly available through online repositories. Majority of the data are in GIS format and compliant with basic aspects of the INSPIRE Directive [111], such as the use of a standard 100 m grid in all raster datasets and ETRS89/LAEA projection in all datasets. Exposure data was additionally provided in netCDF format that is commonly used in climate research. The available datasets are listed below:

- Data on extreme river discharges and river flood hazard zones (chapters 2 and 3) are available from 4TU Centre for Research Data, “Pan-European data sets of river flood probability of occurrence under present and future climate”, <https://doi.org/10.4121/uuid:968098ce-afe1-4b21-a509-dedaf9bf4bd5>.
- Data on storm surge heights, extreme sea levels and coastal flood hazard zones (chapter 4) are available from 4TU Centre for Research Data, “Pan-European data sets of coastal flood probability of occurrence under present and future climate”, <https://doi.org/10.4121/uuid:e06ca666-90e2-4a2c-a1d0-4c39f815b04d>.
- Data on compound flood potential (chapter 5) are available from the Joint Research Centre Data Catalogue, “Compound flood potential in Europe”, <http://data.jrc.ec.europa.eu/dataset/jrc-liscoast-10010>.
- The HANZE database of exposure to natural hazards and past damaging floods (chapter 6) is available from 4TU Centre for Research Data, “HANZE: Historical Analysis of Natural Hazards in Europe”, <https://doi.org/10.4121/collection:HANZE>.

Maps of chapters 2 and 3 were further used to as indicators of flood hazard in two applications made for BRIGAIID project:

- River and coastal flood hazard indicators available as an online map from ESRI ArcGIS, “BRIGAIID indicators of loading conditions at national, regional and local

level”,

<http://www.arcgis.com/home/item.html?id=312d18a14b524d6db594641342925a53>.

- River and coastal flood hazard maps for the historical scenario (1971–2000) were used by HKV Consultants to create a mobile application “My Flood Risk?”, <https://climateinnovationwindow.eu/innovations/my-flood-risk>.

BIBLIOGRAPHY

- [1] H. H. Lamb, *Climate: Present Past and Future. Vol. 2: Climatic History and the Future*. (Methuen, London, 1977).
- [2] Aristotle, *Meteorologica. Translated by Webster, W. E. in The Works of Aristotle*, edited by W. D. Ross (Oxford University Press, Oxford, 1931).
- [3] G. S. Aldrete, *Floods of the Tiber in Ancient Rome* (Johns Hopkins University Press, Baltimore, 2007).
- [4] J. Neumann, *Climatic change as a topic in the classical Greek and Roman literature*, *Climatic Change* 7, 441 (1985).
- [5] Munich Re, *NatCatService*, (2018).
- [6] E. A. Pechenick, C. M. Danforth, and P. S. Dodds, *Characterizing the Google Books corpus: Strong limits to inferences of socio-cultural and linguistic evolution*, *PLoS ONE* 10, e0137041 (2015).
- [7] Google, *Google Books Ngram Viewer*, (2013).
- [8] European Union, *Directive 2007/60/EC of the European Parliament and of the Council of 23 October 2007 on the assessment and management of flood risks*, *Official Journal L* 13/4, 3 (2007).
- [9] E. Gumbel, *Statistics of Extremes* (Columbia University Press, New York, 1958).
- [10] R. A. Pielke, *Flood impacts on society: damaging floods as a framework for assessment*, in *Floods, Volume 1*, Routledge Hazards and Disasters Series, edited by D. J. Parker (Routledge, London, 2000) pp. 133–155.
- [11] United Nations, *2009 UNISDR terminology on disaster risk reduction*, Geneva, Switzerland (2009).
- [12] B. Merz, J. Hall, M. Disse, and A. Schumann, *Fluvial flood risk management in a changing world*, *Natural Hazards and Earth System Sciences* 10, 509 (2010).
- [13] Z. Mikulski, *Gospodarka wodna* (Wydawnictwo Naukowe PWN, Warsaw, Poland, 1998).
- [14] E. Bajkiewicz-Grabowska and Z. Mikulski, *Hydrologia ogólna* (Wydawnictwo Naukowe PWN, Warsaw, Poland, 2011).

- [15] V. Nilsen, J. A. Lier, J. T. Bjerkholt, and O. G. Lindholm, *Analysing urban floods and combined sewer overflows in a changing climate*, *Journal of Water and Climate Change* **2**, 260 (2011).
- [16] S. van Baars and I. M. van Kempen, *The causes and mechanisms of historical dike failures in the Netherlands*, *E-Water* **2009**, 1 (2009).
- [17] T. Dunne and L. B. Leopold, *Water in Environmental Planning* (Freeman, San Francisco, 1978).
- [18] R. Horton, *Frequency of recurrence of Hudson River floods*, *U.S. Weather Bureau Bulletin* **2**, 109 (1913).
- [19] B. Bobée, G. Cavadias, F. Ashkar, J. Bernier, and P. Rasmussen, *Towards a systematic approach to comparing distributions used in flood frequency analysis*, *Journal of Hydrology* **142**, 121 (1993).
- [20] E. J. Gumbel, *The return period of flood flows*, *The Annals of Mathematical Statistics* **12**, 163 (1941).
- [21] G. J. van Oldenborgh, K. van der Wiel, A. Sebastian, R. Singh, J. Arrighi, F. Otto, K. Haustein, S. Li, G. Vecchi, and H. Cullen, *Attribution of extreme rainfall from Hurricane Harvey, August 2017*, *Environmental Research Letters* **12**, 24009 (2017).
- [22] J. Majewski, *Geografia fizyczna świata* (Wydawnictwo Naukowe PWN, Warsaw, Poland, 2006).
- [23] A. L. de Jager and J. V. Vogt, *Development and demonstration of a structured hydrological feature coding system for Europe*, *Hydrological Sciences Journal* **55**, 661 (2010).
- [24] PBL Netherlands Environmental Assessment Agency, *HYDE*, (2015).
- [25] Viewfinder Panoramas, *Digital elevation data*, (2014).
- [26] United Nations, *World Urbanization Prospects*, (2014).
- [27] M. Kottek, J. Grieser, C. Beck, B. Rudolf, and F. Rubel, *World map of the Köppen-Geiger climate classification updated*, *Meteorologische Zeitschrift* **15**, 259 (2006).
- [28] S. E. Fick and R. J. Hijmans, *WorldClim 2: new 1-km spatial resolution climate surfaces for global land areas*, *International Journal of Climatology* **37**, 4302 (2017).
- [29] A. Haines, B. Finlayson, and T. McMahon, *A global classification of river regimes*, *Applied Geography* **8**, 255 (1988).
- [30] C. Schneider, C. L. R. Laizé, M. C. Acreman, and M. Flörke, *How will climate change modify river flow regimes in Europe?* *Hydrology and Earth System Sciences* **17**, 325 (2013).

- [31] A. M. G. Klein Tank, J. B. Wijngaard, G. P. Können, R. Böhm, G. Demarée, A. Gocheva, M. Mileta, S. Pashiardis, L. Hejkrlik, C. Kern-Hansen, R. Heino, P. Bessemoulin, G. Müller-Westermeier, M. Tzanakou, S. Szalai, T. Pálsdóttir, D. Fitzgerald, S. Rubin, M. Capaldo, M. Maugeri, A. Leitass, A. Bukantis, R. Aberfeld, A. F. V. van Engelen, E. Forland, M. Miletus, F. Coelho, C. Mares, V. Razuvaev, E. Nieplova, T. Cegnar, J. Antonio López, B. Dahlström, A. Moberg, W. Kirchhofer, A. Ceylan, O. Pachaliuk, L. V. Alexander, and P. Petrovic, *Daily dataset of 20th-century surface air temperature and precipitation series for the European Climate Assessment*, *International Journal of Climatology* **22**, 1441 (2002).
- [32] H. H. Lamb, *Historic Storms of the North Sea, British Isles and Northwest Europe* (Cambridge University Press, Cambridge, 1991).
- [33] P. Groenemeijer, A. Vajda, I. Lehtonen, M. Kämäräinen, A. Venäläinen, H. Gregow, N. Becker, K. Nissen, U. Ulbrich, D. Paprotny, O. Morales Nápoles, and T. Púčik, *Present and future probability of meteorological and hydrological hazards in Europe*, Research Report D2.5 (RAIN project, 2016).
- [34] G. D. Egbert, A. F. Bennett, and M. G. G. Foreman, *TOPEX/POSEIDON tides estimated using a global inverse model*, *Journal of Geophysical Research: Oceans* **99**, 24821 (1994).
- [35] M. Barriendos, J. L. Ruiz-Bellet, J. Tuset, J. Mazón, J. C. Balasch, D. Pino, and J. L. Ayala, *The "Prediflood" database of historical floods in Catalonia (NE Iberian Peninsula) AD 1035–2013, and its potential applications in flood analysis*, *Hydrology and Earth System Sciences* **18**, 4807 (2014).
- [36] G. Benito, R. Brázdil, J. Herget, and M. J. Machado, *Quantitative historical hydrology in Europe*, *Hydrology and Earth System Sciences* **19**, 3517 (2015).
- [37] P. H. Nienhuis, *Environmental History of the Rhine-Meuse Delta* (Springer Netherlands, 2008).
- [38] J. Herget and H. Meurs, *Reconstructing peak discharges for historic flood levels in the city of Cologne, Germany*, *Global and Planetary Change* **70**, 108 (2010).
- [39] G. Rothlisberger, *Chronik der Unwetterschaden in der Schweiz*, *Berichte der Eidgenössischen Forschungsanstalt für Wald, Schnee und Landschaft*, Vol. 330 (Eidgenössische Forschungsanstalt für Wald, Schnee und Landschaft, Birmensdorf, Switzerland, 1991).
- [40] RZGW w Krakowie, *Powodzie w polsce i małopolsce*, (2016).
- [41] R. Glaser, D. Riemann, J. Schönbein, M. Barriendos, R. Brázdil, C. Bertolin, D. Camuffo, M. Deutsch, P. Dobrovolný, A. van Engelen, S. Enzi, M. Halíčková, S. J. Koenig, O. Kotyza, D. Limanówka, J. Macková, M. Sghedoni, B. Martin, and I. Himmelsbach, *The variability of European floods since AD 1500*, *Climatic Change* **101**, 235 (2010).

- [42] J. Hall, B. Arheimer, M. Borga, R. Brázdil, P. Claps, A. Kiss, T. R. Kjeldsen, J. Kriaučiūnienė, Z. W. Kundzewicz, M. Lang, M. C. Llasat, N. Macdonald, N. McIntyre, L. Mediero, B. Merz, R. Merz, P. Molnar, A. Montanari, C. Neuhold, J. Parajka, R. A. P. Perdigão, L. Plavcová, M. Rogger, J. L. Salinas, E. Sauquet, C. Schär, J. Szolgay, A. Viglione, and G. Blöschl, *Understanding flood regime changes in Europe: a state-of-the-art assessment*, *Hydrology and Earth System Sciences* **18**, 2735 (2014).
- [43] J. Herget, A. Kapala, M. Krell, E. Rustemeier, C. Simmer, and A. Wyss, *The millennium flood of July 1342 revisited*, *CATENA* **130**, 82 (2015).
- [44] C. Rohr, *The Danube floods and their human response and perception (14th to 17th C)*, *History of Meteorology* **2**, 71 (2005).
- [45] A. M. J. de Kraker, *Flood events in the southwestern Netherlands and coastal Belgium, 1400–1953*, *Hydrological Sciences Journal* **51**, 913 (2006).
- [46] R. Brázdil, G. R. Demarée, M. Deutsch, E. Garnier, A. Kiss, J. Luterbacher, N. Macdonald, C. Rohr, P. Dobrovolný, P. Kolář, and K. Chromá, *European floods during the winter 1783/1784: scenarios of an extreme event during the 'Little Ice Age'*, *Theoretical and Applied Climatology* **100**, 163 (2010).
- [47] V. Thorndycraft, M. Barriendos, G. Benito, M. Rico, and A. Casas, *The catastrophic floods of AD 1617 in Catalonia (northeast Spain) and their climatic context*, *Hydrological Sciences Journal* **51**, 899 (2006).
- [48] Meteo France, *Pluies extrêmes en France métropolitaine*, (2017), last accessed 13 January 2018.
- [49] D. Duband, *La genèse des crues dans le bassin de la Loire*, *La Houille Blanche* **6/7**, 54 (1996).
- [50] Z. W. Kundzewicz, K. Szamałek, and P. Kowalczak, *The Great Flood of 1997 in Poland*, *Hydrological Sciences Journal* **44**, 855 (1999).
- [51] D. Zanchettin, P. Traverso, and M. Tomasino, *Po river discharges: a preliminary analysis of a 200-year time series*, *Climatic Change* **89**, 411 (2008).
- [52] T. J. Marsh, B. J. Greenfield, and J. A. Hannaford, *The 1894 Thames flood—a reappraisal*, *Proceedings of the Institution of Civil Engineers - Water Management* **158**, 103 (2005).
- [53] N. Macdonald and H. Sangster, *High-magnitude flooding across Britain since AD 1750*, *Hydrology and Earth System Sciences* **21**, 1631 (2017).
- [54] Environment Agency, *Recorded Flood Outlines*, (2017).
- [55] B. Wiśniewski and T. Wolski, *Katalogi wezbrań i obniżeń sztormowych poziomów morza oraz ekstremalne poziomy wód na polskim wybrzeżu* (Maritime University of Szczecin, Szczecin, Poland, 2009).

- [56] J. I. Barredo, *Major flood disasters in Europe: 1950–2005*, *Natural Hazards* **42**, 125 (2007).
- [57] Delta Works Online, *Disasters*, (2004).
- [58] S. N. Jonkman, M. Bočkarjova, M. Kok, and P. Bernardini, *Integrated hydrodynamic and economic modelling of flood damage in the Netherlands*, *Ecological Economics* **66**, 77 (2008).
- [59] Rijkswaterstaat Department of Communication, *Lessons learned from flood defence in the Netherlands*, *Irrigation and Drainage* **55**, S121 (2006).
- [60] Główny Komitet Przeciwpowodziowy, *Zarys monografii powodzi w Polsce w 40-lecie działalności Głównego Komitetu Powodziowego* (Ministerstwo Ochrony Środowiska i Zasobów Naturalnych, Warsaw, Poland, 1988).
- [61] Central Statistical Office, *Central statistical office*, (2018).
- [62] A. Kryżanowski, M. Brilly, S. Rusjan, and S. Schnabl, *Structural flood-protection measures referring to several European case studies*, *Natural Hazards and Earth System Sciences* **14**, 135 (2014).
- [63] D. van Dantzig, *Economic decision problems for flood prevention*, *Econometrica* **24**, 276 (1956).
- [64] R. Vergouwe, *The National Flood Risk Analysis for the Netherlands*, Technical Report (Rijkswaterstaat VNK Project Office, 2015).
- [65] R. Jorissen, E. Kraaij, and E. Tromp, *Dutch flood protection policy and measures based on risk assessment*, *E3S Web of Conferences* **7**, 20016 (2016).
- [66] P. Scussolini, J. C. J. H. Aerts, B. Jongman, L. M. Bouwer, H. C. Winsemius, H. de Moel, and P. J. Ward, *FLOPROS: an evolving global database of flood protection standards*, *Natural Hazards and Earth System Sciences* **16**, 1049 (2016).
- [67] D. Paprotny, *Analiza zagrożenia powodziowego w Dolinie Dolnej Regi i rejonie jeziora Resko Przymorskie z wykorzystaniem modelowania hydraulicznego*, *mathesis*, University of Szczecin, Szczecin, Poland (2012).
- [68] L. F. Mooyaart and S. N. Jonkman, *Overview and design considerations of storm surge barriers*, *Journal of Waterway, Port, Coastal, and Ocean Engineering* **143**, 06017001 (2017).
- [69] B. Lehner, C. R. Liermann, C. Revenga, C. Vörösmarty, B. Fekete, P. Crouzet, P. Döll, M. Endejan, K. Frenken, J. Magome, C. Nilsson, J. C. Robertson, R. Rödel, N. Sinding, and D. Wisser, *High-resolution mapping of the world's reservoirs and dams for sustainable river-flow management*, *Frontiers in Ecology and the Environment* **9**, 494 (2011).
- [70] W. Silva, F. Klijn, and J. Dijkman, *Room for the Rhine Branches in The Netherlands*, Technical Report R3294 (WL | Delft Hydraulics, 2001).

- [71] Government of Ireland, *Planning System and Flood Risk Management - Guidelines for Planning Authorities*, Technical Report (Ministry for the Environment, Heritage and Local Government, and Office of Public Works, 2009).
- [72] Bundesamt für Umwelt, *Gefahrenkarten, Intensitätskarten und Gefahrenhinweiskarten*, (2016).
- [73] Department for Communities & Local Government, *Technical Guidance to the National Planning Policy Framework*, Technical Report (Crown copyright, London, 2012).
- [74] B. Kolen, R. Slomp, and S. N. Jonkman, *The impacts of storm Xynthia February 27-28, 2010 in France: lessons for flood risk management*, *Journal of Flood Risk Management* **6**, 261 (2013).
- [75] H. Kreibich and A. H. Thielen, *Coping with floods in the city of Dresden, Germany*, *Natural Hazards* **51**, 423 (2009).
- [76] K. T. Lendering, S. N. Jonkman, and M. Kok, *Effectiveness of emergency measures for flood prevention*, *Journal of Flood Risk Management* **9**, 320 (2016).
- [77] B. Kolen, B. Maaskant, S. N. Jonkman, and J. T. Needham, *Comparison of evacuation methods used in the Netherlands and the USACE dam and levee safety programs for the Natomas Basin (CA)*, *E3S Web of Conferences* **7**, 19007 (2016).
- [78] S. Priestley, *Flood risk management and funding*, Technical Report Briefing Paper CBP07514 (House of Commons Library, London, 2017).
- [79] P. B. Sayers, M. Horritt, E. Penning-Rowsell, and A. McKenzie, *Climate Change Risk Assessment 2017: Projections of future flood risk in the UK*, Technical Report (Committee on Climate Change, London, 2015).
- [80] Delta Programme Commissioner, *Delta Programme 2018*, Technical Report (Ministry of Infrastructure and the Environment & Ministry of Economic Affairs, 2017).
- [81] Ministry of Finance, *Ministry of Finance*, (2018).
- [82] Z. Mikulski, *Zbiorniki retencyjne*, in *Geografia fizyczna Polski*, edited by A. Richling and K. Ostaszewska (Wydawnictwo Naukowe PWN, Warsaw, Poland, 2005).
- [83] A. Cieślak, *Contemporary coastal transformation – the coastal management and protection aspect*, *Journal of Coastal Research* **SI 22**, 63 (1995).
- [84] K. Dębski, *Roczne maksima odpływu, ich objętość i częstotliwość*, *Gospodarka Wodna* **2**, 191 (1936).
- [85] PIHM, *Przepływy charakterystyczne rzek polskich w latach 1951–1960* (Wydawnictwo Komunikacji i Łączności, Warsaw, Poland, 1967).
- [86] Z. Kaczmarek, *Metody statystyczne w hydrologii i meteorologii* (Wydawnictwo Komunikacji i Łączności, Warsaw, Poland, 1970).

- [87] Head Office of Geodesy & Cartography, *Geoportal*, (2018).
- [88] KZGW, *Mapy zagrożenia powodziowego - isok*, (2015).
- [89] G. R. Brakenridge, *Global active archive of large flood events*, (2017), Dartmouth Flood Observatory, University of Colorado.
- [90] US Geological Survey, *The National Atlas of the United States of America* (US Department of the Interior, Washington D.C., 1970).
- [91] H. Apel, G. T. Aronica, H. Kreibich, and A. H. Thielen, *Flood risk analyses—how detailed do we need to be?* *Natural Hazards* **49**, 79 (2009).
- [92] J. M. Cain and M. T. Beatty, *The use of soil maps in the delineation of flood plains*, *Water Resources Research* **4**, 173 (1968).
- [93] A. J. C. Barré de Saint-Venant, *Théorie du mouvement non permanent des eaux, avec application aux crues des rivières et à l'introduction de marées dans leurs lits*, *Comptes rendus hebdomadaires des séances de l'Académie des sciences* **73**, 147 (1871).
- [94] P. D. Bates and A. P. J. De Roo, *A simple raster-based model for flood inundation simulation*, *Journal of Hydrology* **236**, 54 (2000).
- [95] H. de Moel, J. van Alphen, and J. C. J. H. Aerts, *Flood maps in Europe – methods, availability and use*, *Natural Hazards and Earth System Sciences* **9**, 289 (2009).
- [96] Amt der NÖ Landesregierung, *Karten & Geoinformationen*, (2016).
- [97] T. G. Masaryk Water Research Institute, *Flood risk mapping in the Czech Republic*, (2011).
- [98] Government of Italy, *Decreto legislativo 23 febbraio 2010, n. 49 "attuazione della direttiva 2007/60/ce relativa alla valutazione e alla gestione dei rischi di alluvioni"*, *Gazzetta Ufficiale*, Parta Prima, Serie Generale **77**, 1 (2010).
- [99] K. Rotnicki and R. K. Borówka, *Impact of a future sea level rise in the Polish Baltic Coastal Zone*, in *Changing Climate and the Coast Volume 2*, edited by J. G. Titus (Environmental Protection Agency, Washington D.C., 1990) pp. 247–264.
- [100] D. Paprotny and P. Terefenko, *New estimates of potential impacts of sea level rise and coastal floods in Poland*, *Natural Hazards* **85**, 1249 (2017).
- [101] A. de Roo, J. Barredo, C. Lavallo, K. Bodis, and R. Bonk, *Potential Flood Hazard and Risk Mapping at Pan-European Scale*, in *Digital Terrain Modelling Development and Applications in a Policy Support Environment*, edited by R. J. Peckham and G. Jordan (Springer, 2007).
- [102] N. Luger, Z. W. Kundzewicz, E. Genovese, S. Hochrainer, and M. Radziejewski, *River flood risk and adaptation in Europe—assessment of the present status*, *Mitigation and Adaptation Strategies for Global Change* **15**, 621 (2010).

- [103] J. H. Christensen and O. B. Christensen, *Severe summertime flooding in Europe*, *Nature* **421**, 805 (2003).
- [104] B. Lehner, P. Döll, J. Alcamo, T. Henrichs, and F. Kaspar, *Estimating the impact of global change on flood and drought risks in Europe: A continental, integrated analysis*, *Climatic Change* **75**, 273 (2006).
- [105] R. Dankers and L. Feyen, *Climate change impact on flood hazard in Europe: An assessment based on high-resolution climate simulations*, *Journal of Geophysical Research: Atmospheres* **113**, D19105 (2008).
- [106] L. Alfieri, L. Feyen, F. Dottori, and A. Bianchi, *Ensemble flood risk assessment in Europe under high end climate scenarios*, *Global Environmental Change* **35**, 199 (2015).
- [107] L. McFadden, R. J. Nicholls, A. Vafeidis, and R. S. J. Tol, *A methodology for modeling coastal space for global assessment*, *Journal of Coastal Research* **234**, 911 (2007).
- [108] A. T. Vafeidis, R. J. Nicholls, L. McFadden, R. S. J. Tol, J. Hinkel, T. Spencer, P. S. Grashoff, G. Boot, and R. J. T. Klein, *A new global coastal database for impact and vulnerability analysis to sea-level rise*, *Journal of Coastal Research* **24**, 917 (2008).
- [109] M. I. Vousdoukas, E. Voukouvalas, L. Mentaschi, F. Dottori, A. Giardino, D. Bouziotas, A. Bianchi, P. Salamon, and L. Feyen, *Developments in large-scale coastal flood hazard mapping*, *Natural Hazards and Earth System Sciences* **16**, 1841 (2016).
- [110] J. Thielen, J. Bartholmes, M.-H. Ramos, and A. de Roo, *The European Flood Alert System – Part 1: Concept and development*, *Hydrology and Earth System Sciences* **13**, 125 (2009).
- [111] INSPIRE Thematic Working Group Natural Risk Zones, *INSPIRE Data Specification on Natural Risk Zones - Technical Guidelines*, Technical Report D2.8.III.12 (European Commission Joint Research Centre, 2013).
- [112] W. Kron, *Flood risk = hazard • values • vulnerability*, *Water International* **30**, 58 (2005).
- [113] International Organization for Standardization, *ISO Guide 73:2009 - Risk management - Vocabulary*, ISO, Geneva, Switzerland (2009).
- [114] D. Paprotny and O. Morales Nápoles, *Estimating extreme river discharges in Europe through a Bayesian network*, *Hydrology and Earth System Sciences* **21**, 2615 (2017).
- [115] P. H. Whitfield, *Floods in future climates: a review*, *Journal of Flood Risk Management* **5**, 336 (2012).
- [116] L. Feyen, R. Dankers, K. Bódis, P. Salamon, and J. I. Barredo, *Fluvial flood risk in Europe in present and future climates*, *Climatic Change* **112**, 47 (2012).

- [117] R. Rojas, L. Feyen, A. Bianchi, and A. Dosio, *Assessment of future flood hazard in Europe using a large ensemble of bias-corrected regional climate simulations*, *Journal of Geophysical Research: Atmospheres* **117**, D17109 (2012).
- [118] L. Alfieri, P. Salamon, A. Bianchi, J. Neal, P. Bates, and L. Feyen, *Advances in pan-European flood hazard mapping*, *Hydrological Processes* **28**, 4067 (2014).
- [119] P. J. Ward, B. Jongman, F. Sperna Weiland, A. Bouwman, R. van Beek, M. F. P. Bierkens, W. Ligtoet, and H. C. Winsemius, *Assessing flood risk at the global scale: model setup, results, and sensitivity*, *Environmental Research Letters* **8**, 044019 (2013).
- [120] H. C. Winsemius, L. P. H. van Beek, B. Jongman, P. J. Ward, and A. Bouwman, *A framework for global river flood risk assessments*, *Hydrology and Earth System Sciences* **17**, 1871 (2013).
- [121] J. R. Meigh, F. A. K. Farquharson, and J. V. Sutcliffe, *A worldwide comparison of regional flood estimation methods and climate*, *Hydrological Sciences Journal* **42**, 225 (1997).
- [122] J. L. Salinas, G. Laaha, M. Rogger, J. Parajka, A. Viglione, M. Sivapalan, and G. Blöschl, *Comparative assessment of predictions in ungauged basins – part 2: Flood and low flow studies*, *Hydrology and Earth System Sciences* **17**, 2637 (2013).
- [123] A. Smith, C. Sampson, and P. Bates, *Regional flood frequency analysis at the global scale*, *Water Resources Research* **51**, 539 (2015).
- [124] C. C. Sampson, A. M. Smith, P. D. Bates, J. C. Neal, L. Alfieri, and J. E. Freer, *A high-resolution global flood hazard model*, *Water Resources Research* **51**, 7358 (2015).
- [125] V. T. Chow, *Applied hydrology* (McGraw-Hill, New York, 1988).
- [126] S. K. Sando, *Techniques for Estimating Peak-Flow Magnitude and Frequency Relations for South Dakota Streams*, *Water-Resources Investigations Report 98-4055* (U.S. Geological Survey, Denver, Colorado, USA, 1998).
- [127] J. Stachý and B. Fal, *Zasady obliczania maksymalnych przepływów prawdopodobnych*, *Prace Instytutu Badawczego Dróg i Mostów* **3-4**, 91 (1986).
- [128] I. O. Peereboom, O. S. Waagø, and M. Myhre, *Preliminary Flood Risk Assessment in Norway – An example of a methodology based on a GIS-approach*, *Technical Report No. 7/2011* (Norwegian Water Resources and Energy Directorate, Oslo, Norway, 2011).
- [129] P. T. Padi, G. Di Baldassarre, and A. Castellarin, *Floodplain management in Africa: Large scale analysis of flood data*, *Physics and Chemistry of the Earth, Parts A/B/C* **36**, 292 (2011).
- [130] C. Herold and F. Mouton, *Global flood hazard mapping using statistical peak flow estimates*, *Hydrology and Earth System Sciences Discussions* **8**, 305 (2011).

- [131] D. Paprotny and O. Morales Nápoles, *A Bayesian Network for extreme river discharges in Europe*, in *Safety and Reliability of Complex Engineered Systems*, edited by L. Podofillini, B. Sudret, B. Stojadinović, E. Zio, and W. Kröger (CRC Press/Balkema, Leiden, the Netherlands, 2015) pp. 4303–4311.
- [132] Global Runoff Data Centre, *BfG – The GRDC*, (2016).
- [133] Norwegian Water Resources & Energy Directorate, *Historiske vannføringsdata til produksjonsplanlegging*, (2015).
- [134] Swedish Meteorological & Hydrological Institute, *Vattenweb Mätningar*, (2016).
- [135] Centro de Estudios Hidrográficos, *Anuario de aforos 2011–2012*, (2012).
- [136] B. Fal, *Przepływy charakterystyczne głównych rzek polskich w latach 1951–1995*, Materiały Badawcze – Instytut Meteorologii i Gospodarki Wodnej. Hydrologia i Oceanologia No. 26 (IMGW, Warsaw, Poland, 2000).
- [137] J. V. Vogt, P. Soille, A. de Jager, E. Rimaviciute, W. Mehl, S. Foisneau, K. Bodis, J. Dusart, M. L. Paracchini, P. Haastrup, and C. Bamps, *A pan-European River and Catchment Database*, Technical Report EUR 22920 EN (European Commission-Joint Research Centre, Luxembourg, 2007).
- [138] M. R. Haylock, N. Hofstra, A. M. G. Klein Tank, E. J. Klok, P. D. Jones, and M. New, *A European daily high-resolution gridded data set of surface temperature and precipitation for 1950–2006*, *Journal of Geophysical Research: Atmospheres* **113**, D20119 (2008).
- [139] D. P. Dee, S. M. Uppala, A. J. Simmons, P. Berrisford, P. Poli, S. Kobayashi, U. Andrae, M. A. Balmaseda, G. Balsamo, P. Bauer, P. Bechtold, A. C. M. Beljaars, L. van de Berg, J. Bidlot, N. Bormann, C. Delsol, R. Dragani, M. Fuentes, A. J. Geer, L. Haimberger, S. B. Healy, H. Hersbach, E. V. Hólm, L. Isaksen, P. Kallberg, M. Köhler, M. Matricardi, A. P. McNally, B. M. Monge-Sanz, J.-J. Morcrette, B.-K. Park, C. Peubey, P. de Rosnay, C. Tavalato, J.-N. Thépaut, and F. Vitart, *The ERA-Interim reanalysis: configuration and performance of the data assimilation system*, *Quarterly Journal of the Royal Meteorological Society* **137**, 553 (2011).
- [140] D. Jacob, J. Petersen, B. Eggert, A. Alias, O. B. Christensen, L. M. Bouwer, A. Braun, A. Colette, M. Déqué, G. Georgievski, E. Georgopoulou, A. Gobiet, L. Menut, G. Nikulin, A. Haensler, N. Hempelmann, C. Jones, K. Keuler, S. Kovats, N. Kröner, S. Kotlarski, A. Kriegsmann, E. Martin, E. van Meijgaard, C. Moseley, S. Pfeifer, S. Preuschmann, C. Radermacher, K. Radtke, D. Rehid, M. Rounsevell, P. Samuelsson, S. Somot, J.-F. Soussana, C. Teichmann, R. Valentini, R. Vautard, B. Weber, and P. Yiou, *EURO-CORDEX: new high-resolution climate change projections for European impact research*, *Regional Environmental Change* **14**, 563 (2014).
- [141] B. Rockel, A. Will, and A. Hense, *The Regional Climate Model COSMO-CLM (CCLM)*, *Meteorologische Zeitschrift* **17**, 347 (2008).

- [142] S. Kotlarski, K. Keuler, O. B. Christensen, A. Colette, M. Déqué, A. Gobiet, K. Gørgen, D. Jacob, D. Lüthi, E. van Meijgaard, G. Nikulin, C. Schär, C. Teichmann, R. Vautard, K. Warrach-Sagi, and V. Wulfmeyer, *Regional climate modeling on European scales: a joint standard evaluation of the EURO-CORDEX RCM ensemble*, *Geoscientific Model Development* **7**, 1297 (2014).
- [143] R. Rojas, L. Feyen, A. Dosio, and D. Bavera, *Improving pan-European hydrological simulation of extreme events through statistical bias correction of RCM-driven climate simulations*, *Hydrology and Earth System Sciences* **15**, 2599 (2011).
- [144] DHI GRAS, *EU-DEM Statistical Validation Report*, Technical Report (European Environment Agency, Copenhagen, Denmark, 2014).
- [145] T. G. Farr, P. A. Rosen, E. Caro, R. Crippen, R. Duren, S. Hensley, M. Kobrick, M. Paller, E. Rodriguez, L. Roth, D. Seal, S. Shaffer, J. Shimada, J. Umland, M. Werner, M. Oskin, D. Burbank, and D. Alsdorf, *The Shuttle Radar Topography Mission*, *Reviews of Geophysics* **45**, RG2004 (2007).
- [146] O. J. Gericke and J. C. Smithers, *Review of methods used to estimate catchment response time for the purpose of peak discharge estimation*, *Hydrological Sciences Journal* **59**, 1935 (2014).
- [147] H. H. G. Savenije, *HESS Opinions: "Topography driven conceptual modelling (FLEX-Topo)"*, *Hydrology and Earth System Sciences* **14**, 2681 (2010).
- [148] S. Gharari, M. Hrachowitz, F. Fenicia, and H. H. G. Savenije, *Hydrological landscape classification: investigating the performance of HAND based landscape classifications in a central European meso-scale catchment*, *Hydrology and Earth System Sciences* **15**, 3275 (2011).
- [149] H. Gao, M. Hrachowitz, F. Fenicia, S. Gharari, and H. H. G. Savenije, *Testing the realism of a topography-driven model (FLEX-Topo) in the nested catchments of the Upper Heihe, China*, *Hydrology and Earth System Sciences* **18**, 1895 (2014).
- [150] European Environment Agency, *Corine Land Cover 2000 raster data*, (2014).
- [151] European Environment Agency, *CLC2006 technical guidelines*, Technical Report No. 17/2017 (European Environment Agency, Copenhagen, Denmark, 2007).
- [152] S. A. Bartalev, A. S. Belward, D. V. Erchov, and A. S. Isaev, *A new SPOT4-VEGETATION derived land cover map of Northern Eurasia*, *International Journal of Remote Sensing* **24**, 1977 (2003).
- [153] K. Klein Goldewijk, A. Beusen, G. van Drecht, and M. de Vos, *The HYDE 3.1 spatially explicit database of human-induced global land-use change over the past 12,000 years*, *Global Ecology and Biogeography* **20**, 73 (2011).
- [154] P. Panagos, M. V. Liedekerke, A. Jones, and L. Montanarella, *European Soil Data Centre: response to European policy support and public data requirements*, *Land Use Policy* **29**, 329 (2012).

- [155] FAO, IIASA, ISRIC, ISS-CAS, and JRC, *Harmonized World Soil Database (version 1.2)*, Technical Report (FAO and IIASA, Rome, Italy and Laxenburg, Austria, 2012).
- [156] European Environment Agency, *EEA Fast Track Service Precursor on Land Monitoring - Degree of soil sealing*, (2014).
- [157] T. Hengl, J. M. de Jesus, R. A. MacMillan, N. H. Batjes, G. B. M. Heuvelink, E. Ribeiro, A. Samuel-Rosa, B. Kempen, J. G. B. Leenaars, M. G. Walsh, and M. R. Gonzalez, *SoilGrids1km — global soil information based on automated mapping*, PLoS ONE **9**, e105992 (2014).
- [158] J. Pearl, *Probabilistic Reasoning in Intelligent Systems: Networks of Plausible Inference* (Morgan Kaufmann, San Mateo, California, USA, 1988).
- [159] D. Kurowicka and R. Cooke, *Uncertainty analysis with high dimensional dependence modelling* (John Wiley & Sons Ltd, Chichester, UK, 2006).
- [160] O. Morales Nápoles and R. D. J. M. Steenbergen, *Large-Scale Hybrid Bayesian Network for Traffic Load Modeling from Weigh-in-Motion System Data*, Journal of Bridge Engineering **20**, 04014059 (2015).
- [161] A. Hanea, O. Morales Nápoles, and D. Dan Ababei, *Non-parametric Bayesian networks: Improving theory and reviewing applications*, Reliability Engineering & System Safety **144**, 265 (2015).
- [162] H. Joe, *Dependence Modeling with Copulas* (Chapman & Hall/CRC, London, 2014).
- [163] A. M. Hanea, D. Kurowicka, and R. M. Cooke, *Hybrid method for quantifying and analyzing Bayesian Belief Nets*, Quality and Reliability Engineering International **22**, 709 (2006).
- [164] O. Morales Nápoles, D. Worm, P. van den Haak, A. Hanea, W. Courage, and S. Miraglia, *Reader for course: Introduction to Bayesian Networks*, Technical Report TNO-060-DTM-2013-01115 (TNO, Delft, the Netherlands, 2013).
- [165] R. H. Moss, J. A. Edmonds, K. A. Hibbard, M. R. Manning, S. K. Rose, D. P. van Vuuren, T. R. Carter, S. Emori, M. Kainuma, T. Kram, G. A. Meehl, J. F. B. Mitchell, N. Nakicenovic, K. Riahi, S. J. Smith, R. J. Stouffer, A. M. Thomson, J. P. Weyant, and T. J. Wilbanks, *The next generation of scenarios for climate change research and assessment*, Nature **463**, 747 (2010).
- [166] F. M. Mutua, *The use of the Akaike Information Criterion in the identification of an optimum flood frequency model*, Hydrological Sciences Journal **39**, 235 (1994).
- [167] Y. Hirabayashi, R. Mahendran, S. Koirala, L. Konoshima, D. Yamazaki, S. Watanabe, H. Kim, and S. Kanae, *Global flood risk under climate change*, Nature Climate Change **3**, 816 (2013).

- [168] R. W. Katz, M. B. Parlange, and P. Naveau, *Statistics of extremes in hydrology*, Advances in Water Resources **25**, 1287 (2002).
- [169] A. Gelman, J. B. Carlin, H. S. Stern, D. B. Dunson, A. Vehtari, and D. B. Rubin, *Bayesian data analysis*, 3rd ed. (Chapman & Hall/CRC, London, 2013).
- [170] D. Moriasi, J. Arnold, M. van Liew, R. Binger, R. Harmel, and T. Veith, *Model evaluation guidelines for systematic quantification of accuracy in watershed simulations*, Transactions of the ASABE **50**, 885 (2007).
- [171] S. Wrede, J. Seibert, and S. Uhlenbrook, *Distributed conceptual modelling in a Swedish lowland catchment: a multi-criteria model assessment*, Hydrology Research **44**, 318 (2013).
- [172] R. Dankers and L. Feyen, *Flood hazard in Europe in an ensemble of regional climate scenarios*, Journal of Geophysical Research: Atmospheres **114**, D16108 (2009).
- [173] D. Paprotny and O. Morales Nápoles, *Pan-European data sets of river flood probability of occurrence under present and future climate*, Dataset (TU Delft, 2016).
- [174] A. A. O. Couasnon, *Characterizing flood hazard at two spatial scales with the use of stochastic models: An application to the contiguous United States of America and the Houston Ship Channel*, Master's thesis, TU Delft (2017).
- [175] D. Paprotny, O. Morales Nápoles, and S. N. Jonkman, *Efficient pan-European river flood hazard modelling through a combination of statistical and physical models*, Natural Hazards and Earth System Sciences **17**, 1267 (2017).
- [176] Environment Agency, *Risk of Flooding from Rivers and Sea*, (2016).
- [177] R. Rojas, L. Feyen, and P. Watkiss, *Climate change and river floods in the european union: Socio-economic consequences and the costs and benefits of adaptation*, Global Environmental Change **23**, 1737 (2013).
- [178] L. Alfieri, P. Burek, L. Feyen, and G. Forzieri, *Global warming increases the frequency of river floods in Europe*, Hydrology and Earth System Sciences **19**, 2247 (2015).
- [179] J. M. van der Knijff, J. Younis, and A. P. J. de Roo, *LISFLOOD: a GIS-based distributed model for river basin scale water balance and flood simulation*, International Journal of Geographical Information Science **24**, 189 (2010).
- [180] F. Dottori, P. Salamon, A. Bianchi, L. Alfieri, F. A. Hirpa, and L. Feyen, *Development and evaluation of a framework for global flood hazard mapping*, Advances in Water Resources **94**, 87 (2016).
- [181] F. Pappenberger, E. Dutra, F. Wetterhall, and H. L. Cloke, *Deriving global flood hazard maps of fluvial floods through a physical model cascade*, Hydrology and Earth System Sciences **16**, 4143 (2012).

- [182] H. C. Winsemius, J. C. J. H. Aerts, L. P. H. van Beek, M. F. P. Bierkens, A. Bouwman, B. Jongman, J. C. J. Kwadijk, W. Ligtoet, P. L. Lucas, D. P. van Vuuren, and P. J. Ward, *Global drivers of future river flood risk*, *Nature Climate Change* **6**, 381 (2016).
- [183] S. N. Jonkman, *Advanced flood risk analysis required*, *Nature Climate Change* **3**, 1004 (2013).
- [184] P. J. Ward, B. Jongman, P. Salamon, A. Simpson, P. Bates, T. D. Groeve, S. Muis, E. C. de Perez, R. Rudari, M. A. Trigg, and H. C. Winsemius, *Usefulness and limitations of global flood risk models*, *Nature Climate Change* **5**, 712 (2015).
- [185] M. Mokrech, A. S. Kebede, R. J. Nicholls, F. Wimmer, and L. Feyen, *An integrated approach for assessing flood impacts due to future climate and socio-economic conditions and the scope of adaptation in Europe*, *Climatic Change* **128**, 245 (2015).
- [186] Deltares, *SOBEK Hydrodynamics, Rainfall Runoff and Real Time Control User Manual* (2016).
- [187] Joint Research Centre, *Pan European Flood Hazard Map for a 100 year return period event*, Dataset (Joint Research Centre, 2014).
- [188] Sächsisches Landesamt für Umwelt, Landwirtschaft und Geologie, *Geodaten-download des Fachbereichs Wasser*, (2016).
- [189] Landesbetrieb für Hochwasserschutz und Wasserwirtschaft Sachsen-Anhalt, *Hochwassergefahrenkarten - Geodaten der Überschwemmungsflächen herunterladen*, (2016).
- [190] Kanton Bern, *Geoportal des Kantons Bern*, (2016).
- [191] Eurostat, *Regions in the European Union: Nomenclature of territorial units for statistics - NUTS 2013/EU-28*, Luxembourg (2015).
- [192] J. Chatterton, C. Viavattene, J. Morris, E. Penning-Rowsell, and S. Tapsell, *The costs of the summer 2007 floods in England*, Technical Report (Environment Agency, Bristol, United Kingdom, 2010).
- [193] A. H. te Linde, P. Bubeck, J. E. C. Dekkers, H. de Moel, and J. C. J. H. Aerts, *Future flood risk estimates along the river Rhine*, *Natural Hazards and Earth System Sciences* **11**, 459 (2011).
- [194] D. Yamazaki, F. O'Loughlin, M. A. Trigg, Z. F. Miller, T. M. Pavelsky, and P. D. Bates, *Development of the global width database for large rivers*, *Water Resources Research* **50**, 3467 (2014).
- [195] J. K. Vrijling, *Probabilistic design of water defense systems in the Netherlands*, *Reliability Engineering & System Safety* **74**, 337 (2001).
- [196] L. Marchi, M. Borga, E. Preciso, and E. Gaume, *Characterisation of selected extreme flash floods in Europe and implications for flood risk management*, *Journal of Hydrology* **394**, 118 (2010).

- [197] N. Nirupama and S. P. Simonovic, *Increase of flood risk due to urbanisation: A Canadian example*, *Natural Hazards* **40**, 25 (2007).
- [198] C. Svensson and D. A. Jones, *Dependence between sea surge, river flow and precipitation in south and west Britain*, *Hydrology and Earth System Sciences* **8**, 973 (2004).
- [199] F. Prettenhaler, P. Amrusch, and C. Habsburg-Lothringen, *Estimation of an absolute flood damage curve based on an Austrian case study under a dam breach scenario*, *Natural Hazards and Earth System Sciences* **10**, 881 (2010).
- [200] J. Rajczak, P. Pall, and C. Schär, *Projections of extreme precipitation events in regional climate simulations for Europe and the Alpine Region*, *Journal of Geophysical Research: Atmospheres* **118**, 3610 (2013).
- [201] D. Paprotny, O. Morales Nápoles, and G. Nikulin, *Extreme sea levels under present and future climate: a pan-European database*, *E3S Web of Conferences* **7**, 02001 (2016).
- [202] D. Paprotny, O. Morales Nápoles, M. I. Vousdoukas, S. N. Jonkman, and G. Nikulin, *Accuracy of pan-European coastal flood mapping*, *Journal of Flood Risk Management*, e12459 (2018).
- [203] D. M. Lumbroso and F. Vinet, *A comparison of the causes, effects and aftermaths of the coastal flooding of England in 1953 and France in 2010*, *Natural Hazards and Earth System Sciences* **11**, 2321 (2011).
- [204] J. A. Church, P. U. Clark, A. Cazenave, J. M. Gregory, S. Jevrejeva, A. Levermann, M. A. Merrifield, G. A. Milne, R. S. Nerem, P. D. Nunn, A. J. Payne, W. T. Pfeffer, D. Stammer, and A. S. Unnikrishnan, *Sea Level Change*, in *Climate Change 2013: The Physical Science Basis Contribution of Working Group I to the Fifth Assessment Report of the Intergovernmental Panel on Climate Change*, edited by T. F. Stocker, D. Qin, G.-K. Plattner, M. Tignor, S. K. Allen, J. Boschung, A. Nauels, Y. Xia, V. Bex, and P. M. Midgley (Cambridge University Press, Cambridge, United Kingdom and New York, USA, 2013).
- [205] A. Sterl, H. van den Brink, H. de Vries, R. Haarsma, and E. van Meijgaard, *An ensemble study of extreme storm surge related water levels in the North Sea in a changing climate*, *Ocean Science* **5**, 369 (2009).
- [206] J. Hunter, *Estimating sea-level extremes under conditions of uncertain sea-level rise*, *Climatic Change* **99**, 331 (2010).
- [207] A. Wróblewski, *Analysis and forecast of long-term sea level changes along the Polish Baltic Sea coast. Part II. Annual mean sea levels –forecast to the year 2100*, *Oceanologia* **36**, 107 (1994).
- [208] S. Xu and W. Huang, *Frequency analysis for predicting 1% annual maximum water levels along Florida coast, US*, *Hydrological Processes* **22**, 4507 (2008).

- [209] G. Forzieri, L. Feyen, S. Russo, M. Voudoukas, L. Alfieri, S. Outten, M. Migliavacca, A. Bianchi, R. Rojas, and A. Cid, *Multi-hazard assessment in europe under climate change*, *Climatic Change* **137**, 105 (2016).
- [210] J. A. Church and N. J. White, *Sea-level rise from the late 19th to the early 21st century*, *Surveys in Geophysics* **32**, 585 (2011).
- [211] NOAA, *Laboratory for Satellite Altimetry / Sea Level Rise*, (2015).
- [212] W. R. Peltier, *Global glacial isostatic adjustment and modern instrumental records of relative sea level history*, in *International Geophysics* (Elsevier, 2001) pp. 65–95.
- [213] W. R. Peltier, D. F. Argus, and R. Drummond, *Space geodesy constrains ice age terminal deglaciation: The global ICE-6G_C (VM5a) model*, *Journal of Geophysical Research: Solid Earth* **120**, 450 (2015).
- [214] A. B. A. Slangen, R. S. W. van de Wal, Y. Wada, and L. L. A. Vermeersen, *Comparing tide gauge observations to regional patterns of sea-level change (1961–2003)*, *Earth System Dynamics* **5**, 243 (2014).
- [215] T. Wolski, B. Wiśniewski, A. Giza, H. Kowalewska-Kalkowska, H. Boman, S. Grabbi-Kaiv, T. Hammarklint, J. Holfort, and Ž. Lydeikaitė, *Extreme sea levels at selected stations on the Baltic Sea coast*, *Oceanologia* **56**, 259 (2014).
- [216] SHOM, *Statistiques des niveaux marins extrêmes des côtes de France (Manche et Atlantique)*, (2015).
- [217] J. R. M. Hosking and J. R. Wallis, *Regional Frequency Analysis* (Cambridge University Press, 1997).
- [218] L. Bardet, C.-M. Duluc, V. Rebour, and J. L'Her, *Regional frequency analysis of extreme storm surges along the French coast*, *Natural Hazards and Earth System Science* **11**, 1627 (2011).
- [219] P. Bernardara, M. Andreewsky, and M. Benoit, *Application of regional frequency analysis to the estimation of extreme storm surges*, *Journal of Geophysical Research: Oceans* **116**, C02008 (2011).
- [220] P. H. A. J. M. van Gelder and C. V. Mai, *Distribution functions of extreme sea waves and river discharges*, *Journal of Hydraulic Research* **46**, 280 (2008).
- [221] P. Sebastião, C. Guedes Soares, and E. Alvarez, *44 years hindcast of sea level in the Atlantic Coast of Europe*, *Coastal Engineering* **55**, 843 (2008).
- [222] C. Batstone, M. Lawless, J. Tawn, K. Horsburgh, D. Blackman, A. McMillan, D. Worth, S. Laeger, and T. Hunt, *A UK best-practice approach for extreme sea-level analysis along complex topographic coastlines*, *Ocean Engineering* **71**, 28 (2013).
- [223] A. Arns, T. Wahl, I. D. Haigh, and J. Jensen, *Determining return water levels at ungauged coastal sites: a case study for northern Germany*, *Ocean Dynamics* **65**, 539 (2015).

- [224] J. Hinkel, R. J. Nicholls, A. T. Vafeidis, R. S. J. Tol, and T. Avagianou, *Assessing risk of and adaptation to sea-level rise in the European Union: an application of DIVA*, Mitigation and Adaptation Strategies for Global Change **15**, 703 (2010).
- [225] J. Hinkel, D. Lincke, A. T. Vafeidis, M. Perrette, R. J. Nicholls, R. S. J. Tol, B. Marzeion, X. Fettweis, C. Ionescu, and A. Levermann, *Coastal flood damage and adaptation costs under 21st century sea-level rise*, Proceedings of the National Academy of Sciences **111**, 3292 (2014).
- [226] S. Muis, M. Verlaan, H. Winsemius, J. C. J. H. Aerts, and P. J. Ward, *The first global-scale hindcast of extreme sea levels*, in *E-proceedings of the 36th IAHR World Congress* (The Hague, the Netherlands, 2015).
- [227] S. Muis, M. Verlaan, H. C. Winsemius, J. C. J. H. Aerts, and P. J. Ward, *A global reanalysis of storm surges and extreme sea levels*, Nature Communications **7**, 11969 (2016).
- [228] S. Muis, M. Verlaan, R. J. Nicholls, S. Brown, J. Hinkel, D. Lincke, A. T. Vafeidis, P. Scussolini, H. C. Winsemius, and P. J. Ward, *A comparison of two global datasets of extreme sea levels and resulting flood exposure*, Earth's Future **5**, 379 (2017).
- [229] M. I. Vousdoukas, E. Voukouvalas, A. Annunziato, A. Giardino, and L. Feyen, *Projections of extreme storm surge levels along Europe*, Climate Dynamics **47**, 3171 (2016).
- [230] M. I. Vousdoukas, L. Mentaschi, E. Voukouvalas, M. Verlaan, and L. Feyen, *Extreme sea levels on the rise along Europe's coasts*, Earth's Future **5**, 304 (2017).
- [231] G. Strandberg, L. Barring, U. Hansson, C. Jansson, C. Jones, E. Kjellström, M. Kolax, M. Kupiainen, G. Nikulin, P. Samuelsson, A. Ullerstig, and S. Wang, *CORDEX scenarios for Europe from the Rossby Centre regional climate model RCA4*, Technical Report (SMHI, Norrköping, Sweden, 2015).
- [232] Deltares, *Delft3D-FLOW User Manual* (2014).
- [233] EMODnet, *Portal for Bathymetry*, (2016).
- [234] H. Charnock, *Wind stress on a water surface*, Quarterly Journal of the Royal Meteorological Society **81**, 639 (1955).
- [235] D. Fourcy and O. Lorvelec, *A new digital map of limits of oceans and seas consistent with high-resolution global shorelines*, Journal of Coastal Research **287**, 471 (2013).
- [236] University of Hawaii Sea Level Center, *Data Portal - Research Quality*, (2016).
- [237] British Oceanographic Data Centre, *International sea level*, (2015).
- [238] SMHI, *SMHI Öppna data*, (2015).
- [239] Rijkswaterstaat, *Waterbase*, (2015).

- [240] A. McMillan, C. Batstone, D. Worth, J. Tawn, K. Horsburgh, and M. Lawless, *Coastal flood boundary conditions for UK mainland and islands*, Technical Report (Environment Agency, Bristol, United Kingdom, 2011).
- [241] A. Grinsted, *Tidal fitting toolbox*, (2014).
- [242] A. Arns, T. Wahl, I. D. Haigh, J. Jensen, and C. Pattiaratchi, *Estimating extreme water level probabilities: A comparison of the direct methods and recommendations for best practise*, *Coastal Engineering* **81**, 51 (2013).
- [243] I. D. Haigh, R. Nicholls, and N. Wells, *A comparison of the main methods for estimating probabilities of extreme still water levels*, *Coastal Engineering* **57**, 838 (2010).
- [244] D. Stammer, R. D. Ray, O. B. Andersen, B. K. Arbic, W. Bosch, L. Carrère, Y. Cheng, D. S. Chinn, B. D. Dushaw, G. D. Egbert, S. Y. Erofeeva, H. S. Fok, J. A. M. Green, S. Griffiths, M. A. King, V. Lapin, F. G. Lemoine, S. B. Luthcke, F. Lyard, J. Morison, M. Müller, L. Padman, J. G. Richman, J. F. Shriver, C. K. Shum, E. Taguchi, and Y. Yi, *Accuracy assessment of global barotropic ocean tide models*, *Reviews of Geophysics* **52**, 243 (2014).
- [245] M. D. Pickering, N. C. Wells, K. J. Horsburgh, and J. A. M. Green, *The impact of future sea-level rise on the European Shelf tides*, *Continental Shelf Research* **35**, 1 (2012).
- [246] Aviso, *Combined mean dynamic topography*, (2015).
- [247] M.-H. Rio, S. Mulet, and N. Picot, *Beyond GOCE for the ocean circulation estimate: Synergetic use of altimetry, gravimetry, and in situ data provides new insight into geostrophic and Ekman currents*, *Geophysical Research Letters* **41**, 8918 (2014).
- [248] A. Voldoire, E. Sanchez-Gomez, D. S. y Méliá, B. Decharme, C. Cassou, S. Sénési, S. Valcke, I. Beau, A. Alias, M. Chevallier, M. Déqué, J. Deshayes, H. Douville, E. Fernandez, G. Madec, E. Maisonnave, M.-P. Moine, S. Planton, D. Saint-Martin, S. Szopa, S. Tyteca, R. Alkama, S. Belamari, A. Braun, L. Coquart, and F. Chauvin, *The CNRM-CM5.1 global climate model: description and basic evaluation*, *Climate Dynamics* **40**, 2091 (2013).
- [249] A. B. A. Slangen, M. Carson, C. A. Katsman, R. S. W. van de Wal, A. Köhl, L. L. A. Vermeersen, and D. Stammer, *Projecting twenty-first century regional sea-level changes*, *Climatic Change* **124**, 317 (2014).
- [250] M. Carson, A. Köhl, D. Stammer, A. B. A. Slangen, C. A. Katsman, R. S. W. van de Wal, J. Church, and N. White, *Coastal sea level changes, observed and projected during the 20th and 21st century*, *Climatic Change* **134**, 269 (2016).
- [251] M. Lilje, *Changing the geodetic infrastructure*, FIG Working Week 2004, Athens, Greece, May 22-27, 2004 (2004).

- [252] B. Poulter and P. N. Halpin, *Raster modelling of coastal flooding from sea-level rise*, International Journal of Geographical Information Science **22**, 167 (2008).
- [253] AHN, *Actueel Hoogtebestand Nederland*, (2017).
- [254] CODGiK, *NMT 100*, (2015).
- [255] Ordnance Survey, *OS Terrain 50 DTM*, Dataset (Data.gov.uk, 2016).
- [256] W. Augath and J. Ihde, *Definition and realization of vertical reference systems –the European solution EVRS/EVRF 2000*, FIG XXII International Congress, Washington D.C., USA, April 19-26, 2002 (2002).
- [257] B. Rabus, M. Eineder, A. Roth, and R. Bamler, *The shuttle radar topography mission—a new class of digital elevation models acquired by spaceborne radar*, ISPRS Journal of Photogrammetry and Remote Sensing **57**, 241 (2003).
- [258] R. B. Jongejan and B. Maaskant, *Quantifying flood risks in the Netherlands*, Risk Analysis **35**, 252 (2015).
- [259] H. van der Most and M. Wehrung, *Dealing with uncertainty in flood risk assessment of dike rings in the Netherlands*, Natural Hazards **36**, 191 (2005).
- [260] L. Pineau-Guillou, C. Lathuiliere, R. Magne, S. Louazel, D. Corman, and C. Perherin, *Sea levels analysis and surge modelling during storm Xynthia*, European Journal of Environmental and Civil Engineering **16**, 943 (2012).
- [261] J. F. Breilh, E. Chaumillon, X. Bertin, and M. Gravelle, *Assessment of static flood modeling techniques: application to contrasting marshes flooded during xynthia (western france)*, Natural Hazards and Earth System Sciences **13**, 1595 (2013).
- [262] D. Idier, F. Paris, G. Le Cozannet, F. Boulahya, and F. Dumas, *Sea-level rise impacts on the tides of the European Shelf*, Continental Shelf Research **137**, 56 (2017).
- [263] J. A. Ramirez, M. Lichter, T. J. Coulthard, and C. Skinner, *Hyper-resolution mapping of regional storm surge and tide flooding: comparison of static and dynamic models*, Natural Hazards **82**, 571 (2016).
- [264] D. Paprotny, M. I. Vousdoukas, O. Morales-Nápoles, S. N. Jonkman, and L. Feyen, *Compound flood potential in Europe*, Hydrology and Earth System Sciences Discussions, in review (2018).
- [265] M. Leonard, S. Westra, A. Phatak, M. Lambert, B. van den Hurk, K. McInnes, J. Risbey, S. Schuster, D. Jakob, and M. Stafford-Smith, *A compound event framework for understanding extreme impacts*, Wiley Interdisciplinary Reviews: Climate Change **5**, 113 (2014).
- [266] T. Wahl, S. Jain, J. Bender, S. D. Meyers, and M. E. Luther, *Increasing risk of compound flooding from storm surge and rainfall for major US cities*, Nature Climate Change **5**, 1093 (2015).

- [267] H. R. Moftakhari, G. Salvadori, A. AghaKouchak, B. F. Sanders, and R. A. Matthew, *Compounding effects of sea level rise and fluvial flooding*, Proceedings of the National Academy of Sciences **114**, 9785 (2017).
- [268] I. Lehtonen, K. Ruosteenoja, and K. Jylhä, *Projected changes in European extreme precipitation indices on the basis of global and regional climate model ensembles*, International Journal of Climatology **34**, 1208 (2014).
- [269] E. Bevacqua, D. Maraun, I. Hobæk Haff, M. Widmann, and M. Vrac, *Multivariate statistical modelling of compound events via pair-copula constructions: analysis of floods in ravenna (italy)*, Hydrology and Earth System Sciences **21**, 2701 (2017).
- [270] S. F. Kew, F. M. Selten, G. Lenderink, and W. Hazeleger, *The simultaneous occurrence of surge and discharge extremes for the Rhine delta*, Natural Hazards and Earth System Sciences **13**, 2017 (2013).
- [271] L. Bengtsson, *Probability of combined high sea levels and large rains in Malmö, Sweden, southern Öresund*, Hydrological Processes **30**, 3172 (2016).
- [272] C. Svensson and D. A. Jones, *Dependence between extreme sea surge, river flow and precipitation in eastern Britain*, International Journal of Climatology **22**, 1149 (2002).
- [273] V. N. Ntegeka, P. Salamon, G. Gomes, H. Sint, V. Lorini, J. Thielen del Pozo, and H. Zambrano, *EFAS-Meteo: A European daily high-resolution gridded meteorological data set for 1990–2011*, Technical Report EUR 26408 EN (Joint Research Centre, 2013).
- [274] L. Alfieri, L. Feyen, P. Salamon, J. Thielen, A. Bianchi, F. Dottori, and P. Burek, *Modelling the socio-economic impact of river floods in Europe*, Natural Hazards and Earth System Sciences **16**, 1401 (2016).
- [275] H. L. Tolman, *User manual and system documentation of WAVEWATCH-III version 2.22* (2002).
- [276] L. Mentaschi, M. I. Vousdoukas, E. Voukouvalas, A. Dosio, and L. Feyen, *Global changes of extreme coastal wave energy fluxes triggered by intensified teleconnection patterns*, Geophysical Research Letters **44**, 2416 (2017).
- [277] G. Salvadori and C. D. Michele, *On the use of copulas in hydrology: Theory and practice*, Journal of Hydrologic Engineering **12**, 369 (2007).
- [278] C. Schölzel and P. Friederichs, *Multivariate non-normally distributed random variables in climate research - introduction to the copula approach*, Nonlinear Processes in Geophysics **15**, 761 (2008).
- [279] O. Morales Nápoles, D. Paprotny, D. Worm, L. Abspöel-Bukman, and W. Courage, *Characterization of precipitation through copulas and expert judgement for risk assessment of infrastructure*, ASCE-ASME Journal of Risk and Uncertainty in Engineering Systems, Part A: Civil Engineering **3**, 04017012 (2017).

- [280] C. Genest, B. Remillard, and D. Beaudoin, *Goodness-of-fit tests for copulas: A review and a power study*, Insurance: Mathematics and Economics **44**, 199 (2009).
- [281] D. Paprotny, A. Sebastian, O. Morales Nápoles, and S. N. Jonkman, *Trends in flood losses in Europe over the past 150 years*, Nature Communications **9**, 1985 (2018).
- [282] D. Paprotny, O. Morales Nápoles, and S. N. Jonkman, *HANZE: a pan-European database of exposure to natural hazards and damaging historical floods since 1870*, Earth System Science Data **10**, 565 (2018).
- [283] Dirección General de Protección Civil, *Catálogo Nacional de Inundaciones Históricas*, (2015), last accessed 13 January 2018.
- [284] H. Zhong, P.-J. van Overloop, P. van Gelder, and T. Rijcken, *Influence of a storm surge barrier's operation on the flood frequency in the Rhine Delta area*, Water **4**, 474 (2012).
- [285] F. M. Calafat, E. Avgoustoglou, G. Jorda, H. Flocas, G. Zodiatis, M. N. Tsimplis, and J. Kouroutzoglou, *The ability of a barotropic model to simulate sea level extremes of meteorological origin in the Mediterranean Sea, including those caused by explosive cyclones*, Journal of Geophysical Research: Oceans **119**, 7840 (2014).
- [286] J. L. Rego and C. Li, *Nonlinear terms in storm surge predictions: Effect of tide and shelf geometry with case study from Hurricane Rita*, Journal of Geophysical Research: Oceans **115**, C06020 (2010).
- [287] L. Alfieri, F. Dottori, R. Betts, P. Salamon, and L. Feyen, *Multi-model projections of river flood risk in Europe under global warming*, Climate **6**, 6 (2018).
- [288] B. Jongman, S. Hochrainer-Stigler, L. Feyen, J. C. J. H. Aerts, R. Mechler, W. J. W. Botzen, L. M. Bouwer, G. Pflug, R. Rojas, and P. J. Ward, *Increasing stress on disaster-risk finance due to large floods*, Nature Climate Change **4**, 264 (2014).
- [289] Z. W. Kundzewicz, D. Graczyk, T. Maurer, I. Pińskwar, M. Radziejewski, C. Svensson, and M. Szwed, *Trend detection in river flow series: 1. annual maximum flow*, Hydrological Sciences Journal **50** (2005), 10.1623/hysj.2005.50.5.797.
- [290] M. Mudelsee, M. Börngen, G. Tetzlaff, and U. Grünewald, *No upward trends in the occurrence of extreme floods in central Europe*, Nature **425**, 166 (2003).
- [291] M. Rummukainen, *Changes in climate and weather extremes in the 21st century*, Wiley Interdisciplinary Reviews: Climate Change **3**, 115 (2012).
- [292] J. I. Barredo, *Normalised flood losses in Europe: 1970–2006*, Natural Hazards and Earth System Sciences **9**, 97 (2009).
- [293] M. R. Haylock and C. M. Goodess, *Interannual variability of European extreme winter rainfall and links with mean large-scale circulation*, International Journal of Climatology **24**, 759 (2004).

- [294] A. Moberg, P. D. Jones, D. Lister, A. Walther, M. Brunet, J. Jacobeit, L. V. Alexander, P. M. Della-Marta, J. Luterbacher, P. Yiou, D. Chen, A. M. G. Klein Tank, O. Saladié, J. Sigró, E. Aguilar, H. Alexandersson, C. Almarza, I. Auer, M. Barriendos, M. Begert, H. Bergström, R. Böhm, C. J. Butler, J. Caesar, A. Drebs, D. Founda, F.-W. Gerstengarbe, G. Micela, M. Maugeri, H. Österle, K. Pandzic, M. Petrakis, L. Srnec, R. Tolasz, H. Tuomenvirta, P. C. Werner, H. Linderholm, A. Philipp, H. Wanner, and E. Xoplaki, *Indices for daily temperature and precipitation extremes in Europe analyzed for the period 1901–2000*, *Journal of Geophysical Research: Atmospheres* **111**, D22106 (2006).
- [295] C. Matulla, W. Schöner, H. Alexandersson, H. von Storch, and X. L. Wang, *European storminess: late nineteenth century to present*, *Climate Dynamics* **31**, 125 (2008).
- [296] F. Feser, M. Barcikowska, O. Krueger, F. Schenk, R. Weisse, and L. Xia, *Storminess over the North Atlantic and northwestern Europe—A review*, *Quarterly Journal of the Royal Meteorological Society* **141**, 350 (2015).
- [297] B. Jongman, P. J. Ward, and J. C. J. H. Aerts, *Global exposure to river and coastal flooding: Long term trends and changes*, *Global Environmental Change* **22**, 823 (2012).
- [298] M. Kummu, H. de Moel, G. Salvucci, D. Viviroli, P. J. Ward, and O. Varis, *Over the hills and further away from coast: global geospatial patterns of human and environment over the 20th–21st centuries*, *Environmental Research Letters* **11**, 034010 (2016).
- [299] I. Schumacher and E. Strobl, *Economic development and losses due to natural disasters: The role of hazard exposure*, *Ecological Economics* **72**, 97 (2011).
- [300] L. M. Bouwer, *Have disaster losses increased due to anthropogenic climate change?* *Bulletin of the American Meteorological Society* **92**, 39 (2011).
- [301] L. M. Bouwer, R. P. Crompton, E. Faust, P. Hoppe, and R. A. Pielke Jr., *Confronting disaster losses*, *Science* **318**, 753 (2007).
- [302] J. E. Daniell, B. Khazai, F. Wenzel, and A. Vervaeck, *The CATDAT damaging earthquakes database*, *Natural Hazards and Earth System Sciences* **11**, 2235 (2011).
- [303] Munich Re, *Innovative new ways of analysing historical loss events*, (2016).
- [304] Q. Schiermeier, *Insurers' disaster files suggest climate is culprit*, *Nature* **441**, 674 (2006).
- [305] M. Mirza, *Climate change and extreme weather events: can developing countries adapt?* *Climate Policy* **3**, 233 (2003).
- [306] E. Neumayer and F. Barthel, *Normalizing economic loss from natural disasters: A global analysis*, *Global Environmental Change* **21**, 13 (2011).

- [307] Munich Re, *Topics Geo –natural catastrophes 2016 –analyses, assessments, positions*, (2017).
- [308] A. J. Stevens, D. Clarke, and R. J. Nicholls, *Trends in reported flooding in the UK: 1884–2013*, *Hydrological Sciences Journal* **61**, 50 (2016).
- [309] S. Fuchs, M. Keiler, and A. Zischg, *A spatiotemporal multi-hazard exposure assessment based on property data*, *Natural Hazards and Earth System Sciences* **15**, 2127 (2015).
- [310] A. Domeneghetti, F. Carisi, A. Castellarin, and A. Brath, *Evolution of flood risk over large areas: Quantitative assessment for the Po river*, *Journal of Hydrology* **527**, 809 (2015).
- [311] B. Jongman, E. E. Koks, T. G. Husby, and P. J. Ward, *Increasing flood exposure in the Netherlands: implications for risk financing*, *Natural Hazards and Earth System Sciences* **14**, 1245 (2014).
- [312] J. I. Barredo, D. Saurí, and M. C. Llasat, *Assessing trends in insured losses from floods in Spain 1971–2008*, *Natural Hazards and Earth System Sciences* **12**, 1723 (2012).
- [313] V. Röthlisberger, A. Zischg, and M. Keiler, *Spatiotemporal aspects of flood exposure in Switzerland*, *E3S Web of Conferences* **7**, 08008 (2016).
- [314] A. J. Stevens, D. Clarke, R. J. Nicholls, and M. P. Wadey, *Estimating the long-term historic evolution of exposure to flooding of coastal populations*, *Natural Hazards and Earth System Sciences* **15**, 1215 (2015).
- [315] M. Boudou, B. Danière, and M. Lang, *Assessing changes in urban flood vulnerability through mapping land use from historical information*, *Hydrology and Earth System Sciences* **20**, 161 (2016).
- [316] G. Sofia, G. Roder, G. Dalla Fontana, and P. Tarolli, *Flood dynamics in urbanised landscapes: 100 years of climate and humans' interaction*, *Scientific Reports* **7**, 40527 (2017).
- [317] D. Changnon and S. A. Changnon, *Evaluation of weather catastrophe data for use in climate change investigations*, *Climatic Change* **38**, 435 (1998).
- [318] J. I. Barredo, *No upward trend in normalised windstorm losses in Europe: 1970–2008*, *Natural Hazards and Earth System Sciences* **10**, 97 (2010).
- [319] K. Klein Goldewijk, A. Beusen, J. Doelman, and E. Stehfest, *Anthropogenic land use estimates for the Holocene – HYDE 3.2*, *Earth System Science Data* **9**, 927 (2017).
- [320] Center For International Earth Science Information Network, *Gridded population of the world, version 4 (gpwv4): Population count*, (2016).

- [321] M. Pesaresi, D. Ehrlich, S. Ferri, A. J. Florczyk, S. Freire, S. Halkia, A. Julea, T. Kemper, P. Soille, and V. Syrris, *Operating procedure for the production of the Global Human Settlement Layer from Landsat data of the epochs 1975, 1990, 2000, and 2014*, Technical Report EUR 27741 EN (Joint Research Centre, 2016).
- [322] W. Nordhaus and C. Xi, *Geographically based Economic data (G-Econ)*, (2011).
- [323] D. Murakami and Y. Yamagata, *Estimation of gridded population and gdp scenarios with spatially explicit statistical downscaling*, arXiv , 1610.09041 (2017).
- [324] R. Fuchs, P. H. Verburg, J. G. Clevers, and M. Herold, *The potential of old maps and encyclopaedias for reconstructing historic European land cover/use change*, Applied Geography **59**, 43 (2015).
- [325] R. Fuchs, M. Herold, P. H. Verburg, and J. G. P. W. Clevers, *A high-resolution and harmonized model approach for reconstructing and analysing historic land changes in Europe*, Biogeosciences **10**, 1543 (2013).
- [326] D. Guha-Sapir, R. Below, and P. Hoyois, *Em-dat: The cred/ofda international disaster database*, (2017), Université Catholique de Louvain, Brussels, Belgium.
- [327] European Environment Agency, *Flood phenomena*, (2015).
- [328] B. Jongman, H. C. Winsemius, J. C. J. H. Aerts, E. Coughlan de Perez, M. K. van Aalst, W. Kron, and P. J. Ward, *Declining vulnerability to river floods and the global benefits of adaptation*, Proceedings of the National Academy of Sciences **112**, E2271 (2015).
- [329] H. Visser, A. C. Petersen, and W. Ligtoet, *On the relation between weather-related disaster impacts, vulnerability and climate change*, Climatic Change **125**, 461 (2014).
- [330] A. R. Black and F. M. Law, *Development and utilization of a national web-based chronology of hydrological events*, Hydrological Sciences Journal **49**, 237 (2004).
- [331] F. Guzzetti and G. Tonelli, *Information system on hydrological and geomorphological catastrophes in Italy (SICI): a tool for managing landslide and flood hazards*, Natural Hazards and Earth System Sciences **4**, 213 (2004).
- [332] I. D. Haigh, M. P. Wadey, S. L. Gallop, H. Loehr, R. J. Nicholls, K. Horsburgh, J. M. Brown, and E. Bradshaw, *A user-friendly database of coastal flooding in the United Kingdom from 1915–2014*, Scientific Data **2**, 150021 (2015).
- [333] M. Lang, D. Coeur, A. Audouard, M. Villanova-Oliver, and J.-P. Pène, *BDHI: a French national database on historical floods*, E3S Web of Conferences **7**, 04010 (2016).
- [334] Eurostat, *Database*, (2018).

- [335] K. Klein Goldewijk, A. Beusen, and P. Janssen, *Long-term dynamic modeling of global population and built-up area in a spatially explicit way: HYDE 3.1*, *The Holocene* **20**, 565 (2010).
- [336] European Union, *Commission Regulation (EU) No 31/2011 of 17 January 2011 amending annexes to Regulation (EC) No 1059/2003 of the European Parliament and of the Council on the establishment of a common classification of territorial units for statistics (NUTS)*, *Official Journal L* **288**, 27 (2011).
- [337] Copernicus Land Monitoring Service, *Pan-European*, (2017).
- [338] Eurostat, *GISCO: geographical information and maps*, (2017).
- [339] F. Batista e Silva, J. Gallego, and C. Lavallo, *A high-resolution population grid map for Europe*, *Journal of Maps* **9**, 16 (2013).
- [340] OurAirports, *Open data downloads*, (2017).
- [341] FAO, *Global Agro-Ecological Zones*, (2016).
- [342] D. Paprotny and O. Morales Nápoles, *Pan-European data sets of coastal flood probability of occurrence under present and future climate*, Dataset (TU Delft, 2016).
- [343] A. J. Dobson, *An Introduction to Generalized Linear Models* (Chapman & Hall/CRC, 2002).
- [344] P. McCullagh and J. A. Nelder, *Generalized Linear Models* (Chapman and Hall, 1990).
- [345] G. P. Compo, J. S. Whitaker, P. D. Sardeshmukh, N. Matsui, R. J. Allan, X. Yin, B. E. Gleason, R. S. Vose, G. Rutledge, P. Bessemoulin, S. Brönnimann, M. Brunet, R. I. Crouthamel, A. N. Grant, P. Y. Groisman, P. D. Jones, M. C. Kruk, A. C. Kruger, G. J. Marshall, M. Maugeri, H. Y. Mok, Ø. Nordli, T. F. Ross, R. M. Trigo, X. L. Wang, S. D. Woodruff, and S. J. Worley, *The Twentieth Century Reanalysis Project*, *Quarterly Journal of the Royal Meteorological Society* **137**, 1 (2011).
- [346] H. R. Moftakhari, A. AghaKouchak, B. F. Sanders, and R. A. Matthew, *Cumulative hazard: The case of nuisance flooding*, *Earth's Future* **5**, 214 (2017).
- [347] R. A. Pielke and M. W. Downton, *Precipitation and damaging floods: Trends in the United States, 1932–97*, *Journal of Climate* **13**, 3625 (2000).
- [348] R. P. Crompton and K. J. McAneney, *Normalised Australian insured losses from meteorological hazards: 1967–2006*, *Environmental Science & Policy* **11**, 371 (2008).
- [349] A. M. G. Klein Tank and G. P. Können, *Trends in indices of daily temperature and precipitation extremes in Europe, 1946–99*, *Journal of Climate* **16**, 3665 (2003).
- [350] H. Madsen, D. Lawrence, M. Lang, M. Martinkova, and T. R. Kjeldsen, *Review of trend analysis and climate change projections of extreme precipitation and floods in Europe*, *Journal of Hydrology* **519**, 3634 (2014).

- [351] H. Hersbach and D. Dee, *ERA5 reanalysis is in production*, (2016).
- [352] W. F. Willcox, *Increase in the Population of the Earth and Its Continents since 1650*, in *International Migrations, Volume II: Interpretations*, edited by W. F. Willcox (National Bureau of Economic Research, 1931) pp. 33–82.
- [353] O. Morales Nápoles, A. M. Hanea, and D. T. H. Worm, *Experimental results about the assessments of conditional rank correlations by experts: Example with air pollution estimates*, in *Safety, Reliability and Risk Analysis: Beyond the Horizon*, edited by R. D. J. M. Steenbergen, P. H. A. J. M. van Gelder, S. Miraglia, and A. C. W. M. Vrouwenvelder (CRC Press/Balkema, Leiden, the Netherlands, 2013) pp. 1359–1366.
- [354] C. D. Jones, J. K. Hughes, N. Bellouin, S. C. Hardiman, G. S. Jones, J. Knight, S. Liddicoat, F. M. O'Connor, R. J. Andres, C. Bell, K.-O. Boo, A. Bozzo, N. Butchart, P. Cadule, K. D. Corbin, M. Doutriaux-Boucher, P. Friedlingstein, J. Gornall, L. Gray, P. R. Halloran, G. Hurtt, W. J. Ingram, J.-F. Lamarque, R. M. Law, M. Meinshausen, S. Osprey, E. J. Palin, L. Parsons Chini, T. Raddatz, M. G. Sanderson, A. A. Sellar, A. Schurer, P. Valdes, N. Wood, S. Woodward, M. Yoshioka, and M. Zerroukat, *The HadGEM2-ES implementation of CMIP5 centennial simulations*, *Geoscientific Model Development* 4, 543 (2011).
- [355] E. van Meijgaard, L. H. van Ulft, W. J. van de Berg, F. C. Bosveld, B. van den Hurk, G. Lenderink, and A. P. Siebesma, *The KNMI regional atmospheric climate model RACMO version 2.1*, Technical Report 302 (Royal Netherlands Meteorological Institute, De Bilt, the Netherlands, 2008).
- [356] D. Paprotny, O. Morales Nápoles, and S. N. Jonkman, *HANZE: Historical Analysis of Natural Hazards in Europe - database documentation*, (2018).
- [357] D. Paprotny, O. Morales Nápoles, and S. N. Jonkman, *HANZE: Historical Analysis of Natural Hazards in Europe, Dataset* (TU Delft, Faculty Of Civil Engineering, 2017).
- [358] Gisgraphy, *Download server*, (2017).
- [359] Joint Research Centre, *Global land cover 2000*, (2015).
- [360] European Environment Agency, *Legend*, (2011).
- [361] F. J. Gallego, *A population density grid of the European Union*, *Population and Environment* 31, 460 (2010).
- [362] F. J. Gallego, F. Batista, C. Rocha, and S. Mubareka, *Disaggregating population density of the European Union with CORINE land cover*, *International Journal of Geographical Information Science* 25, 2051 (2011).
- [363] C. L. Eicher and C. A. Brewer, *Dasymeric mapping and areal interpolation: Implementation and evaluation*, *Cartography and Geographic Information Science* 28, 125 (2001).

- [364] United Nations, *Demographic Yearbook System*, (2017).
- [365] E. Gløersen and C. Lüer, *Population data collection for European local administrative units from 1960 onwards – final report*, Technical Report (Spatial Foresight GmbH, Luxembourg, 2013).
- [366] United Nations, *World Population Prospects*, (2015).
- [367] A. Haupt, T. T. Kane, and C. Haub, *Population Handbook, 6th edition* (Population Reference Bureau, 2011).
- [368] United Nations, *Compendium of Housing Statistics 1971* (Statistical Office of the United Nations, New York, 1974).
- [369] FAO, *FAOSTAT*, (2017).
- [370] B. R. Mitchell, *European Historical Statistics* (Macmillan, 1981).
- [371] European Union, *European System of Accounts ESA 2010* (Publications Office of the European Union, Luxembourg, 2013).
- [372] International Monetary Fund, *World Economic Outlook Database April 2017*, (2017).
- [373] OECD, *OECD Data*, (2017).
- [374] R. W. Goldsmith, *Comparative National Balance Sheets: A Study of Twenty Countries, 1688-1978* (University of Chicago Press, Chicago, 1985).
- [375] T. Piketty and G. Zucman, *Capital is back: Wealth-income ratios in rich countries 1700–2010*, *The Quarterly Journal of Economics* **129**, 1255 (2014).
- [376] International Organization for Standardization, *Codes for the representation of currencies, ISO 4217:2015*, (2017).
- [377] B. Taylor, *Global history of currencies*, (2004).
- [378] B. L. J. Berry, J. W. Simmons, and R. J. Tennant, *Urban population densities: Structure and change*, *Geographical Review* **53**, 389 (1963).
- [379] A. Anas, R. Arnott, and K. Small, *Urban spatial structure*, *Journal of Economic Literature* **36**, 1426 (1998).
- [380] Y. Y. Papageorgiou, *Population density in a central-place system*, *Journal of Regional Science* **54**, 450 (2014).
- [381] C. Clark, *Population Growth and Land Use* (Macmillan, London, UK, 1967).
- [382] G. Fischer, H. T. van Velthuisen, M. M. Shah, and F. O. Nachtergaele, *Global Agro-ecological Assessment for Agriculture in the 21st Century: Methodology and Results*, Research Report RR-02-02 (IIASA, Laxenburg, Austria, 2002).

- [383] R. Milego and M. J. Ramos, *Disaggregation of socioeconomic data into a regular grid and combination with other types of data*, Technical Report (ESPON EGTC, Luxembourg, 2011).
- [384] K. Klein Goldewijk, *Hyde 3.2*, (2017).
- [385] G. C. Hurtt, L. P. Chini, S. Frolking, R. A. Betts, J. Feddema, G. Fischer, J. P. Fisk, K. Hibbard, R. A. Houghton, A. Janetos, C. D. Jones, G. Kindermann, T. Kinoshita, K. Klein Goldewijk, K. Riahi, E. Shevliakova, S. Smith, E. Stehfest, A. Thomson, P. Thornton, D. P. van Vuuren, and Y. P. Wang, *Harmonization of land-use scenarios for the period 1500–2100: 600 years of global gridded annual land-use transitions, wood harvest, and resulting secondary lands*, *Climatic Change* **109**, 117 (2011).
- [386] J. O. Kaplan, K. M. Krumhardt, and N. E. Zimmermann, *The effects of land use and climate change on the carbon cycle of Europe over the past 500 years*, *Global Change Biology* **18**, 902 (2011).
- [387] K. Klein Goldewijk and P. H. Verburg, *Uncertainties in global-scale reconstructions of historical land use: an illustration using the HYDE data set*, *Landscape Ecology* **28**, 861 (2013).
- [388] J. Pongratz, C. Reick, T. Raddatz, and M. Claussen, *A reconstruction of global agricultural areas and land cover for the last millennium*, *Global Biogeochemical Cycles* **22**, GB3018 (2008).
- [389] N. Ramankutty and J. A. Foley, *Estimating historical changes in global land cover: Croplands from 1700 to 1992*, *Global Biogeochemical Cycles* **13**, 997 (1999).
- [390] A. R. Colson and R. M. Cooke, *Cross validation for the classical model of structured expert judgment*, *Reliability Engineering & System Safety* **163**, 109 (2017).
- [391] R. M. Cooke and L. L. H. J. Goossens, *TU delft expert judgment data base*, *Reliability Engineering & System Safety* **93**, 657 (2008).
- [392] C. Clark, *Urban population densities*, *Journal of the Royal Statistical Society. Series A (General)* **114**, 490 (1951).
- [393] K. Hourihan, *Urban population density patterns and change in Ireland*, *The Economic and Social Review* **13**, 125 (1982).
- [394] J. L. Zêzere, S. Pereira, A. O. Tavares, C. Bateira, R. M. Trigo, I. Quaresma, P. P. Santos, M. Santos, and J. Verde, *DISASTER: a GIS database on hydro-geomorphologic disasters in Portugal*, *Natural Hazards* **72**, 503 (2014).
- [395] Administrația Națională Apele Române, *Studii Privind Determinarea Actiunilor, Masurilor, Optiunilor si Solutiilor Pentru Atingerea Obiectivelor Gestionarii Integrate a Resurselor de Apa Aple Bazinelor Hidrografice Districtul de Bazin Hidrografic Olt, Volumul 6: Managementul Riscului Inundati*, (2009).

ACKNOWLEDGEMENTS

I first encountered flood hazard modelling at a summer school organized by the University of Siena in 2010. One of the lectures was Pieter van Gelder, who at the time held the position of assistant professor for probabilistic design at TU Delft. That was also my first contact with that university. I went on to produce a master thesis related to floods, and then work for University of Szczecin in the field of coastal hazards. Four years after the visit to Italy, I was lecturing at another summer school, this time held in Aveiro (Portugal), and met Oswaldo Morales-Nápoles of TU Delft. After two months, I found myself working for TU Delft, and another four years later I'm at crossroads again. This thesis collects a substantial part of my work of the past few years. All that's good in it is thanks to the many generous collaborators I've worked with in that time. All that's not is my sole responsibility.

First and foremost thanks have to be extended to Oswaldo, my supervisor, for his continuous encouragement, unwavering support and inexhaustible patience (I'm hardly the easiest person to work with). His mathematical knowledge profoundly shaped my work. And he brought me to TU Delft, a which was a landmark event in my life, for sure. For that my promotor, prof. Bas Jonkman, also has to be acknowledged, as he took a big leap of faith in employing me. His experience and knowledge also kept the entire project on track.

Most of the thesis (chapters 2–4) was connected to project RAIN, therefore I send great thanks to all I've worked with in the project. Same goes to colleagues from project BRIGAD, even if none of the work I've done there directly contributed to the thesis. Some of chapter 4 and all of chapter 5 was done during my two stays at the European Commission – Joint Research Centre in Ispra, Italy. For the good collaboration I would like to thank Michalis Vousdoukas, Luc Feyen, Evangelos Voukouvalas, Lorenzo Mentaschi and Lorenzo Alfieri. At TU Delft, the collaboration was somewhat limited due to the topic of my work, but for involvement in the work of chapter 6 thanks go to Antonia Sebastian. Chapter 4 also extensively used data kindly provided by Grigory Nikulin (SMHI), Aimée Slangen (NIOZ) and the employees of Rijkswaterstaat's Nieuwegein unit. I also thank prof. Kazimierz Furmańczyk, for relieving me of my duties at University of Szczecin so I could pursue the research in Delft, and Paweł Terefenko for continued collaboration with Szczecin. The great help of the secretaries - Judith, Agnes and Diana - in keeping the show on the road also needs acknowledgment.

I would also like to sincerely thank Patrycja and François Enet, whose friendship and support from day one was very important to me during my stay at Delft. Of friends and colleagues, a tip of the hat is particularly for Kacper, Nipuni, Jeremy and Qian. Last but absolutely not least, thanks go to my parents, sister and extended family in Szczecin.

*Dominik PAPROTNY
Delft, July 2018*



CURRICULUM VITÆ

Dominik PAPROTNY

27-03-1988 Born in Szczecin, Poland.

EDUCATION

2014–2018 Graduate school
Technische Universiteit Delft, Delft

2010–2012 Master degree in geography, specialization: marine geography
Uniwersytet Szczeciński, Szczecin

2007–2010 Bachelor degree in geography
Uniwersytet Szczeciński, Szczecin

2004–2007 Senior high school
XIII Liceum Ogólnokształcące, Szczecin

WORK EXPERIENCE

X 2014–XI 2018 PhD candidate at Delft University of Technology
with participation in research projects:
“Bridging the Gap for Innovations in Disaster Resilience” (2016–2017)
*“Risk Analysis of Infrastructure Networks in Response
to Extreme Weather”* (2014–2016).

X 2017–II 2018 Trainee researcher at European Commission – Joint Research Centre,
Disaster Risk Management Unit in Ispra, Italy.

III 2013–IX 2014 Researcher at Faculty of Geosciences, University of Szczecin,
research project *“Satellite Monitoring of the Baltic Sea Environment”*

VII–IX 2012 Short-term contract for processing satellite images
at “Fotokart” surveying company in Szczecin.



LIST OF PUBLICATIONS

21. **D. Paprotny**, M. I. Vousdoukas, O. Morales Nápoles, S. N. Jonkman, L. Feyen, *Compound flood potential in Europe*, Hydrology and Earth System Sciences, in review (2018).
20. **D. Paprotny**, *Modern population censuses and progress in counting the world population*, Demographic Research, in review (2018).
19. **D. Paprotny**, O. Morales Nápoles, M. I. Vousdoukas, S. N. Jonkman, G. Nikulin, *Accuracy of pan-European coastal flood mapping*, Journal of Flood Risk Management, early view, e12459 (2018).
18. **D. Paprotny**, A. Sebastian, O. Morales Nápoles, S. N. Jonkman, *Trends in flood losses in Europe over the past 150 years*, Nature Communications **9**, 1985 (2018).
17. P. Terefenko, A. Giza, **D. Paprotny**, A. Kubicki, M. Winowski, *Cliff retreat induced by series of storms at Międzyzdroje (Poland)*, Journal of Coastal Research **SI 85**, 181–185 (2018).
16. **D. Paprotny**, O. Morales Nápoles, S. N. Jonkman, *HANZE: a pan-European database of exposure to natural hazards and damaging historical floods since 1870*, Earth System Science Data **10**, 565–581 (2018).
15. **D. Paprotny**, O. Morales Nápoles, S. N. Jonkman, *Efficient pan-European river flood hazard modelling through a combination of statistical and physical models*, Natural Hazards and Earth System Sciences **17**, 1267–1283 (2017).
14. O. Morales Nápoles, **D. Paprotny**, D. Worm, L. Abspoel-Bukman, W. Courage, *Characterization of precipitation through copulas and expert judgement for risk assessment of infrastructure*, ASCE-ASME Journal of Risk and Uncertainty in Engineering Systems, Part A: Civil Engineering **3**(4), 04017012 (2017).
13. **D. Paprotny**, O. Morales Nápoles, *Estimating extreme river discharges in Europe through a Bayesian Network*, Hydrology and Earth System Sciences **21**, 2615–2636 (2017).
12. **D. Paprotny**, P. Terefenko, *New estimates of potential impacts of sea level rise and coastal floods in Poland*, Natural Hazards **85**(2), 1249–1277 (2017).
11. **D. Paprotny**, O. Morales Nápoles, G. Nikulin, *Extreme sea levels under present and future climate: a pan-European database*, E3S Web of Conferences **7**, 02001 (2016).
10. **D. Paprotny**, *Measuring Central and Eastern Europe's socio-economic development using time lags*, Social Indicators Research **127**(3), 939–957 (2016).
9. J. N. Huibregtse, O. Morales Nápoles, L. Hellebrandt, **D. Paprotny**, M. S. de Wit, *Climate change in asset management of infrastructure: A risk-based methodology applied to disruption of traffic on road networks due to the flooding of tunnels*, European Journal of Transport and Infrastructure Research **16**(1), 98–113 (2016).

8. **D. Paprotny**, O. Morales Nápoles, *A Bayesian Network for extreme river discharges in Europe*, in: L. Podofillini, B. Sudret, B. Stojadinović, E. Zio, W. Kröger (Eds.) *Safety and Reliability of Complex Engineered Systems*, CRC Press/Balkema, 4303–4311 (2015).
7. **D. Paprotny**, *Trends in storm surge probability of occurrence along the Polish Baltic Sea coast*, arXiv pre-print (2014).
6. **D. Paprotny**, P. Andrzejewski, P. Terefenko, K. Furmańczyk, *Application of empirical wave run-up formulas to the Polish Baltic Sea coast*, PLoS ONE **9**(8), e105437 (2014).
5. K. Furmańczyk, P. Andrzejewski, R. Benedyczak, N. Bugajny, Ł. Cieszyński, J. Dudzińska-Nowak, A. Giza, **D. Paprotny**, P. Terefenko, T. Zawiślak, *Recording of selected effects and hazards caused by current and expected storm events in the Baltic Sea coastal zone*, Journal of Coastal Research **SI70**, 338–342 (2014).
4. **D. Paprotny**, *Poziom rozwoju Polski w relacji do państw zachodnich*, Wiadomości Statystyczne, **59**(3), 48–65 (2014).
3. **D. Paprotny**, *Kartowanie ryzyka powodziowego w kontekście rozwiązań europejskich na przykładzie Wybrzeża Trzebiatowskiego*, in: R. K. Borówka, A. Cedro, I. Kavetsky (Eds.). *Współczesne problemy badań geograficznych*. Uniwersytet Szczeciński, Wydział Nauk o Ziemi, Szczecin, 291–302 (2013).
2. **D. Paprotny**, *Modelowanie powodzi w programie SOBEM na przykładzie Wybrzeża Trzebiatowskiego*, in: K. Furmańczyk (Ed.), *Zintegrowane Zarządzenie Obszarami Przybrzeżnymi – stan obecny i perspektywy 4. Zagrożenia i systemy ostrzegania*. Instytut Nauk o Morzu US, Szczecin, 149–161 (2012).
1. **D. Paprotny**, *Zastosowanie GIS w siłach zbrojnych*, in: T. Rydzewski, J. Smutek (Eds.). *Biuletyn Instytutu Geografii Społeczno-Ekonomicznej i Gospodarki Przestrzennej Uniwersytetu im. Adama Mickiewicza w Poznaniu. Seria Rozwój Regionalny i Polityka Regionalna nr 20*, Poznań, 149–162 (2012).